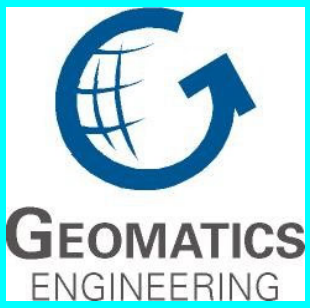

UCGE Reports
Number 20158

Optimising the Use of GPS Multi-Reference Stations for Kinematic Positioning

(URL: http://www.geomatics.ucalgary.ca/links/GradTheses.html)

Department of Geomatics Engineering

By

Luiz Paulo Souto Fortes

April 2002

Calgary, Alberta, Canada

UNIVERSITY OF CALGARY

Optimising the Use of GPS Multi-Reference Stations for Kinematic Positioning

by

Luiz Paulo Souto Fortes

A THESIS

SUBMITTED TO THE FACULTY OF GRADUATE STUDIES

IN PARTIAL FULFILMENT OF THE REQUIREMENTS FOR THE

DEGREE OF DOCTOR OF PHILOSOPHY

DEPARTMENT OF GEOMATICS ENGINEERING

CALGARY, ALBERTA

April, 2002

ABSTRACT

Differential GPS is able to provide cm-level positioning accuracy, as long as the carrier phase ambiguities are resolved to integer values. Classical methods are based on the use of a single reference station located in the vicinity of the rover. Due to the spatial decorrelation of the errors, the distance between the reference station and the user is generally limited to within 20-30 km or even less, mainly depending on the ionosphere. The Multi-Ref method, developed at the University of Calgary, uses a network of reference stations to generate regional code and carrier phase corrections, which can be transmitted to users in order to increase the distance over which integer ambiguity resolution is possible. In the original method, the correlated errors, due to the satellite orbits, troposphere, and ionosphere are modelled together using the L1 and widelane observables.

In this thesis, extensive efforts were carried out towards optimising the Multi-Ref method with the objective of maximising its performance. Data collected in Southeastern Brazil and in the St. Lawrence region, Canada, were used in this research. At first, the impact of using the original covariance functions calculated with different data sets was assessed, showing improvements of up to 15% in the observation domain, depending on the data set used in the computation. A new approach, also using Least-Squares collocation, was then proposed to separately model the correlated errors. An additional effort was carried out in terms of modelling the ionosphere into directional components.

Results of the enhanced method showed the same level of improvement as those obtained using the original covariance functions. However, this new approach has advantages with respect to the transmission of the corrections. Finally, an additional step was taken in terms of applying a Kalman filter to the corrections in order to improve their quality. For cases when the corresponding satellite was setting at low elevations, the filter approach improved results up to 44%. A detailed study about the impact of the various covariance functions on the estimated accuracy of the corrections is also included in this thesis.

PREFACE

This is an unaltered version of the author's Doctor of Philosophy thesis of the same title. This thesis was accepted by the Faculty of Graduate Studies in April, 2002. The faculty supervisor of this work was Dr. M. Elizabeth Cannon, and the other members of the examining committee were Dr. Gérard Lachapelle, Dr. Susan Skone, Dr. David Irvine-Halliday, and Dr. Alfred Leick.

ACKNOWLEDGEMENTS

Many persons and organisations contributed to this doctorate program. I would like to express my gratitude to the following ones in special:

- To Dr. Elizabeth Cannon, my supervisor, for her unconditional support, help and sharp supervision throughout all the phases of the program. I can say that all guidelines she gave me since my very first day at the university were absolutely valuable, not only for the successful completion of the program, but specially for encouraging me to stretch my limits in acquiring knowledge in GPS positioning and navigation;

- To Dr. Gérard Lachapelle, a member of my supervisory committee, for sharing his enormous expertise and experience in the GPS field with me. His ability in generating so many great learning opportunities for me is highly appreciated. Besides, his sense of humour helped me to relieve myself from the tension of the program on many occasions;

- To Dr. Susan Skone, also a member of my supervisory committee, for her support during the entire program, particularly with her expertise in ionospheric topics;

- To Dr. Irvine-Halliday and Dr. Alfred Leick, members of my defence committee, for contributing to the improvement of this thesis research;

- To the Coordenação de Aperfeiçoamento de Pessoal de Nível Superior (CAPES), the Brazilian Federal Government agency that financially supported my PhD program;

- To the Instituto Brasileiro de Geografia e Estatística (IBGE), my employer in Brazil, for giving me this valuable and unique opportunity of high level training;

- To IBGE's Department of Geodesy (DEGED) for the coordination and execution of the GPS campaign that collected important data sets used in this research. I also acknowledge the IBGE partners in the Brazilian Network for Continuous Monitoring of GPS (RBMC), for their participation in the campaign;

- To the Canadian Coast Guard, for releasing the St. Lawrence data sets used in this research;

- To Dr. Michael Sideris, from the Geomatics Engineering, University of Calgary, for helping me to explore the idea of coming to Calgary and for all his help in the initial procedure to apply for it when I was in Brazil;

- To my colleagues from DEGED for all their support and help related not only to the GPS campaign but also in various other stages of the PhD program; I extend this acknowledgement to Edvaldo S. da Fonseca Jr., from the University of São Paulo (USP);

- To my friend Dr. Denizar Blitzkow, from USP, for his continuous support and encouragement;

- To Dr. John Raquet, for many fruitful discussions related to the method he derived. In particular, I would like to thank him for making some of his computer programs available to me at the beginning of my research;

- To all my colleagues of the Navigation Lab, for the nice environment favouring the development of this research. In special, I would like to acknowledge Mark Petovello, Sam Ryan, Paul Alves, Glenn MacGougan, Rakesh Nayak, Jayanta Ray, Kyle O'Keefe, and Junjie Liu for so many fruitful and enriching discussions;

- To my wife, Sandra, and my daughters, Isabela and Luciana, for their love and support. Coming to Calgary was a rich life experience for all of us, but I think it was specially challenging for them, in particular when it was -40°C outside. I am deeply thankful for everything;

- To my parents, Francisco e Maria Regina, for their lifetime care, dedication and support, even when it implied taking their granddaughters away from them for four years;

- To my grandmother, Frelia, for her decisive support in important moments of my life, including when I decided to move abroad to participate in this program;

- To my brothers, for cheering for me;

- To Helena and Gerson, for their incentive and wisdom, specially during hard times;

- To my friends Ceya and Sergio, for their warm welcome in Calgary, their help and friendship all the way through;

- To many other friends and relatives in Brazil who, in one way or another, contributed to this achievement.

DEDICATION

To my parents,

and

to my “girls” Luciana, Isabela, and Sandra.

I would not have made it without you!

TABLE OF CONTENTS

LIST OF TABLES

LIST OF FIGURES

LIST OF SYMBOLS

$1/\beta$	Correlation time in Kalman filter, in seconds
a', a", b', b"	Ionosphere pierce points
B	Double difference matrix
b	Baseline length
C(d)	Covariance function, according to Moritz [1976]
C_0	Value of C(d) for d = 0
C1	L1 code observable (i.e. C/A code)
C_{ll}, C_{ss}, C_{sl}	Covariance matrices of the observations, signals, and cross-covariance matrix between signals and observations in Least-Squares Prediction (Collocation)
$C_{\hat{s}\hat{s}}$	Covariance matrix of the estimated signals $\hat{\mathbf{s}}$ in Least-Squares Prediction (Collocation)
$C_{\delta l}$	Covariance matrix of the observation errors at reference stations
$C_{\delta \hat{l}}$	Covariance matrix of the estimated errors at reference stations
$C_{\delta l_r, \delta l}$	Cross-covariance matrix between the errors at predicted points and at reference stations
$C_{\delta \hat{l}_r}$	Covariance matrix of the estimated errors at predicted points
c	Speed of light in the vacuum (= 299792458.0 m/s)
c_{ab}^{xy}	Covariance between the observation errors δl_a^x and δl_b^y, where **a** and **b** are stations and **x** and **y** are satellites (i.e. element of either the covariance matrix $C_{\delta l}$ or $C_{\delta l_r, \delta l}$)
cor	State vector in Kalman filter (i.e. the Multi-Ref filtered corrections)
D_{ion}	Ionospheric group delay, in metres
d	Distance between two stations, in km
db	Total error in the coordinates of a baseline
d_{ion}	Ionospheric delay in the carrier phase observation, in cycles
d_{trop}	Tropospheric delay, in metres

d^r_{trop}	Tropospheric residual delay after applying a tropospheric model, in metres
$d\rho$	Error in the geometric distance station-satellite, in metres (generally due to satellite orbit errors)
$E\{\ \}$	Expectation operator
$e(x)$	LMV estimator
f_1	L1 GPS frequency (1575.42 MHz)
f_2	L2 GPS frequency (1227.60 MHz)
f_{z_c}	Functional form of the zenith correlated errors
f_{z_u}	Functional form of the zenith uncorrelated errors
GF	Geometric-free observable
H	Design matrix in Kalman filter
I	Variable function of the TEC in the ionosphere (I = 40.3 TEC)
I^x_a	Undifferenced GF scaled to L1 misclosure from station **a** to satellite **x**
$I^x_{a_z}$	Undifferenced GF scaled to L1 misclosure from station **a** to satellite **x** reduced to the zenith
$\hat{I}$	Multi-Ref correction for ionosphere on L1, in metres
IF	Ionospheric-free observable
IS_{L1}	Ionospheric signal on L1 observable
i	Inclination of the satellite orbit
K	Gain matrix in Kalman filter
k_1, k_2	Coefficients of the correlated error functions
k_μ	Coefficient of the mapping functions
k_{1H}, k_{2H}	Coefficients of the variable ΔH in the correlated error function for the troposphere
k_{1N}, k_{2N}, k_{1E}, k_{2E}	Coefficients of the correlated error function for the ionosphere in directional components
L1	L1 carrier phase observable
L2	L2 carrier phase observable
l	Observation vector in Least-Squares Prediction (Collocation)

N	Integer ambiguity, in number of cycles
P	Covariance matrix of state vector in Kalman filter
P2	L2 code observable (i.e. P code on L2)
Q	Process noise matrix in Kalman filter
R	Covariance matrix of the observations in Kalman filter
$R_m(\alpha)$	Rotation matrix (3x3) of angle $\boldsymbol{\alpha}$ around axis **m**
$\hat{r}$	Estimated residual vector in a Least-Squares Condition adjustment
s	Vector of unknown signals in Least-Squares Prediction (Collocation)
$\hat{s}$	Estimate of **s** in Least-Squares Prediction (Collocation)
T_a^x	Undifferenced IF misclosure from station **a** to satellite **x**
T_{a_z}	Undifferenced IF misclosure at station **a** reduced to the zenith
$\hat{T}$	Multi-Ref correction for troposphere and satellite orbits, in metres
v	Residuals in Kalman filter
WL	Widelane phase observable
w	Misclosure vector in a Least-Squares Condition adjustment
$w(t_j)$	White noise sequence in Kalman filter
X_{CM}, Y_{CM}, Z_{CM}	Cartesian coordinates of GPS satellite positions referred to the centre of mass in the ECEF system
X_{PC}, Y_{PC}, Z_{PC}	Cartesian coordinates of GPS satellite positions referred to the antenna phase centre in the ECEF system
x_{CM}, y_{CM}, z_{CM}	Cartesian coordinates of GPS satellite positions referred to the centre of mass in a system parallel to the SCSF system
x_{PC}, y_{PC}, z_{PC}	Cartesian coordinates of GPS satellite positions referred to the antenna phase centre in a system parallel to the SCSF system
x'_{CM}, y'_{CM}, z'_{CM}	Cartesian coordinates of GPS satellite positions referred to the centre of mass in a intermediate system parallel to the SCSF system
x'_{PC}, y'_{PC}, z'_{PC}	Cartesian coordinates of GPS satellite positions referred to the antenna phase centre in an intermediate system parallel to the SCSF system
$\hat{Y}$	LMV estimate of the parameter **Y** from observations **x**
z	Observations in Kalman filter (i.e. the unfiltered Multi-Ref corrections)
Δx, Δy, Δz	GPS satellite antenna phase centre offsets with respect to the satellite centre of mass

$\beta(e)$	Bayesian risk
Δ	Between-receivers single difference operator
ΔN, ΔE, ΔH	North, east and up components of the vector between two stations, in km
Δt	Prediction time interval in Kalman filter
$\Delta\nabla$	Double difference operator
δl	Total error in undifferenced observations (sum of correlated errors and uncorrelated errors), with respect to a reference point $\mathbf{p_0}$
$\delta_c l$ or $\delta_c l(p, p_0)$	Total correlated errors in undifferenced observations, with respect to a reference point $\mathbf{p_0}$
$\delta_u l$	Total uncorrelated errors in undifferenced observations
$\delta\hat{l}$	Estimated observation error at reference stations
$\delta\hat{l}_r$	Estimated observation error at predicted points
$\varepsilon(\Phi)$	Error due to carrier phase multipath and noise, in metres
$\varepsilon(\phi)$	Error due to carrier phase multipath and noise, in cycles
Φ	Carrier phase observation, in metres
$\overline{\Phi}$	Measurement-minus-computed-range observable, in metres
ϕ	Carrier phase observation, in cycles
φ	Argument of latitude of a satellite position
φ_{xx}	Auto-correlation function of a random process
λ	Carrier phase wavelength, in metres
λ_1	L1 wavelength (= 0.1903 m)
λ_2	L2 wavelength (= 0.2442 m)
λ_{IF}	Ionospheric-free wavelength (= 0.4844 m in this thesis)
λ_{WL}	Widelane wavelength (= 0.8619 m)
$\mu(\varepsilon)$	Elevation mapping function
ν	Degrees of freedom or number of condition equations
Θ	Transition matrix in Kalman filter
ρ	Geometric distance station-satellite, in metres
σ^2	Process variance in Kalman filter

$\hat{\sigma}_0^2$	*A posteriori* variance of unit weight
$\sigma_{c_z}^2(p_m, p_n)$	Correlated error function, i.e. variance of the differential zenith errors between points **m** and **n**
$\sigma_{u_z}^2$	Variance of the uncorrelated errors
τ	Time increment in an auto-correlation function of a stationary process
Ω	Longitude of the ascending node of the satellite orbit

LIST OF ABBREVIATIONS

C/A	Coarse/Acquisition code
CCG	Canadian Coast Guard
CGM	Corrected Geomagnetic coordinates
CODE	Centre for Orbit Determination in Europe
CORS	Continuously Operating Reference Stations, USA
DD	Double Difference
DGRF/IGRF	Definite/International Geomagnetic Reference Field
DMA	Defense Mapping Agency, USA
ECEF	Earth-Centred-Earth-Fixed reference system
FARA	Fast Ambiguity Resolution Approach
GF	Geometric-Free observable
GIM	Global Ionospheric Map
GPS	Global Positioning System
GSD	Geodetic Survey Division, Canada
GSI	Geographical Survey Institute, Japan
IBGE	Instituto Brasileiro de Geografia e Estatística, Brazil
IF	Ionospheric-Free observable
IGS	International GPS Service
IS_{L1}	Ionospheric Signal on L1 observable = GF scaled to L1
ITRF	International Terrestrial Reference Frame
LAREG	Laboratory for Research in Geodesy, France
LMV	Linear minimum error variance estimator
NAD83	North American Datum 1983
NASA/GSFC	Goddard Space Flight Center, NASA, USA
NASA/NSSDC	National Space Science Data Center, NASA, USA
NGDC	National Geophysical Data Center, USA
NGS	National Geodetic Survey, USA

NIMA	National Imagery and Mapping Agency, USA
OTF	On-The-Fly
ppm	parts per million
QIF	Quasi Ionospheric-Free ambiguity resolution strategy
RBMC	Brazilian Network for Continuous Monitoring of GPS
RINEX	Receiver Independent Exchange format
RMS	Root Mean Square
SCSF	Satellite-Centred-Satellite-Fixed reference frame
SIDC	Sunspot Index Data Center, Belgium
SIRGAS	Geocentric Reference System for the Americas
SISRE	Signal-In-Space Range Error
SLM	Single Layer Model of the ionosphere
TEC	Total Electron Content
UT	Universal Time
UTC	Universal Time Coordinated
VTEC	Vertical TEC
WGS84	World Geodetic System of 1984
WL	Widelane observable

CHAPTER 1

INTRODUCTION

1.1 Background

The Global Positioning System (GPS) carrier phase observable is the most accurate observation obtained from the system [Wells et al., 1986]. This characteristic is based on the wavelength of both GPS carriers: L1, with a wavelength of 19.03 cm, and L2, with a wavelength of 24.42 cm. It is known that the carrier-phase observation noise can be estimated to within 1% of the signal wavelength, which gives a value of less than 2 mm [Larson, 1996]. This feature has allowed the GPS civilian users to develop several applications obtaining a very high accuracy, at a level much better than the one envisaged by the GPS design group.

The drawback of using the carrier phase observable is that it is an ambiguous measurement since the integer number of cycles at lock-on is not known. Thus it has to be included in the solution model as an additional parameter [Wells et al., 1986; Seeber, 1993; Leick, 1995] and, for each loss of lock (cycle slip) that can not be fixed, there is an

additional integer ambiguity unknown to be resolved. To achieve the best accuracies using the carrier phase in kinematic mode, differential techniques must be used and it is required to resolve the integer ambiguities properly and reliably [Cannon, 1997].

Most GPS errors cancel or reduce through the differential process, as they are correlated between receivers. These correlated errors are the ionospheric and tropospheric delays, and the satellite orbits [Parkinson and Enge, 1996]. However, the greater the distance between the mobile receiver and the reference station(s), the lesser the error correlation, which is known as spatial decorrelation. When this happens, resolving integer ambiguities gets more difficult, due to the fact that they absorb part of the remaining errors. The range over which it is reliable to fix integer ambiguities has been reported to vary from 20 to 30 km [Lachapelle et al., 1999], and can be even less during periods of solar maximum.

In many countries, the institutes responsible for geodetic activities are establishing national active geodetic reference networks, as they represent an economy of resources compared with classical passive geodetic networks [Georgiadou, 1999]. Examples of countries where active networks have been established are: Brazil [Fortes et al., 1998], Canada [McArthur and Steeves, 1988; GSD, 2002], Finland [Kylkilahti et al., 1999], Germany, Israel [Wdowinski, 1999], Japan [GSI, 2002] (this one the most dense in the world, with more than 1000 permanent stations), The Netherlands [van der Marel,

1998], Spain (Catalonia) [Talaya and Bosch, 1999], Mexico, New Zealand [Falvey and Beavan, 1999], Norway, Sweden [Hedling and Jonsson, 1999], Switzerland [Wild et al., 1999], UK [Dodson et al., 1999], and USA [NGS, 2002]. These networks, with inter-station spacing varying from about 20 km in Japan to more than 1000 km in some regions of Brazil and Canada, are creating an important infrastructure to support many applications in addition to geodetic ground control. One of the most promising is to support real-time kinematic services. Several authors have demonstrated the capability of using permanent GPS arrays to model residual errors that affect carrier phase-based GPS positioning, using what is herein referred to as multi-reference station methods. It is expected that ambiguity resolution using corrected observations can be improved in terms of the time required to fix and reliability, as the spatial decorrelation of the errors using corrected observations decreases.

Among the authors who have developed strategies in this field are: Wanninger [1995, 1998, 1999], Wübbena and Seeber [1996], Wübbena et al. [1996, 2001], Gao et al. [1997], Gao and Li [1998], Varner and Cannon [1997], Varner [2000], Raquet [1998], Raquet et al. [1998], van der Marel [1998], Schaer et al. [1999], Vollath et al. [2001], and Landau et al. [2001]. Fotopoulos [2000] classified some of the multi-reference station methods into four main groups according to their underlying correction generation framework: (1) partial derivative algorithms, (2) linear interpolation algorithms, (3) conditional adjustment algorithms, and (4) virtual reference station methods. Each of the

first three techniques defines an actual class of correction generation algorithms, despite the fact that the distinction between the first and the second group is not always clear, as the partial derivative algorithms most of time also correspond to a linear interpolation approach using a bilinear surface (plane). The fourth group corresponds to a geometric transformation of corrections and observations in order to translate them to a fictitious reference station located close to the user position, and can be applied in combination with methods of the first three groups. A description of the general principles of each group can be found in Fotopoulos [2000].

The previously mentioned methods can be classified as follows, according to the categorisation established by Fotopoulos [2000]:

1. Partial derivative algorithms: Wanninger [1995, 1998, 1999], Wübbena and Seeber [1996], Wübbena et al. [1996], Varner and Cannon [1997], Varner [2000], Schaer et al. [1999];
2. Linear interpolation algorithms: Wanninger [1995, 1998, 1999], Gao et al. [1997], Gao and Li [1998];
3. Conditional adjustment algorithms: Raquet [1998], Raquet et al. [1998], van der Marel [1998], Vollath et al. [2001], Landau et al. [2001].

It can be seen that Wanninger references are included in both partial derivative and linear interpolation groups, due to the existing intersection between these groups, as mentioned previously. The conditional adjustment algorithms may be more precisely called Least-Squares Prediction algorithms, as the conditional adjustment is suitable only to compute corrections at the reference stations, whereas a Least-Squares predictor is used to predict corrections at the user position (see Chapter 3 of this thesis). Despite the fact that the algorithm proposed by van der Marel [1998] was not described in detail, it was included in group (3) as it uses a covariance function, which is a characteristic of the Least-Squares prediction methods. Detailed information about the method described by Vollath et al. [2001] and Landau et al. [2001] could not be found either. However, the use of a stochastic model for interpolating the ionospheric errors at the user position indicates that the corresponding method is related to group (3).

Among all mentioned methods, the one derived at the University of Calgary by Raquet [1998], and referred to as Multi-Ref in this thesis, is one of the most rigorous from an optimal estimation theory point of view. It takes into account the stochastic properties of the GPS errors and tries to model them across the region covered by the reference network using covariance functions. It also generates corrections for single (i.e. not differenced) observations collected at the reference stations and at the user positions, which gives a high degree of flexibility in terms of applying these corrections.

This method served as the basis for the proposed optimisation developed in this thesis work.

The Multi-Ref approach was successfully demonstrated using data collected in September 1997 and 1998, in Norway [Raquet, 1998; Townsend et al., 1999]. Significant improvements in the observation, position and ambiguity domains were shown, even for baselines up to 240 km.

This method has taken into account only one covariance function and one mapping function to model all the correlated errors that affect each GPS observation. It is well known that the correlated errors are subject to different spatial decorrelation behaviour, and modelling each one separately on Multi-Ref, analogous to what has been done in Wide Area Differential GPS applications [Mueller, 1994; Aquino, 1999; Skone, 1998], was a necessary investigation, particularly under high ionospheric conditions.

1.2 Objectives

The main proposed objective of this research was to optimise the Multi-Ref approach in order to maximise the ambiguity resolution performance and the accuracy to be obtained in the position domain for kinematic applications. Algorithm design was done to simulate real-time availability of data so that the results are applicable to real-time applications.

In order to implement this idea, the specific objectives of this thesis were to:

- Assess the impact of using different data sets (either geographically and temporally) to compute the original covariance functions derived by Raquet [1998] on Multi-Ref performance; verify the influence of adaptive covariance functions, which follow the observation conditions along the day, on the results. These are important aspects, as they can have a direct influence on the real time operational implementation of Multi-Ref in terms of how often the covariance functions need to be updated;

- Assess the impact of separate modelling of the correlated errors that affect GPS positioning (satellite orbit, tropospheric and ionospheric errors), as it is not expected that they follow the same spatial decorrelation behaviour across the region covered by the reference network;

- Assess the influence of the various covariance functions on the estimated accuracy of the corrections;

- Assess the impact of refining the Multi-Ref corrections through the application of a Kalman filter. In the original method, the corrections for each epoch are

computed using data collected only at that specific epoch, and as such are subject to observability problems, mainly for low satellites which are not observed by all stations of the reference network. Using information from previous epochs could then be used to improve the quality of the corrections.

This work proposed to extend the method derived by Raquet [1998]. As such, its original contributions encompass the derivation of several algorithms, covering the computation of various covariance functions, Multi-Ref corrections (filtered and not filtered) and their covariance matrices. These algorithms were implemented through the development of software packages, some of them based on the NetAdjust computer program developed at the University of Calgary.

All analyses carried out in this thesis were based on data collected in August, 1999, in two different parts of the world, in Southeastern Brazil and in the St. Lawrence region, Canada. Considering the proximity of the solar maximum, the corresponding data sets reflected interesting ionospheric conditions.

1.3 Thesis Outline

This thesis is structured in such a way to cover, along Chapters 2 to 6, the objectives described in the previous section.

In Chapter 2, the correlated errors that affect GPS positioning, namely satellite orbit errors, tropospheric and ionospheric delays, are described in detail, in order to establish a basis for a general understanding of their behaviour and particularly for the generation of the separate covariance functions. Considering the scope of this thesis work, the differential aspects of these errors are emphasised.

Chapter 3 covers the derivation of the Multi-Ref method using Least-Squares Prediction (Collocation). This approach differs from the one used by Raquet [1998] to derive the Multi-Ref correction equations. In addition, the formulation for the estimation of the quality of the corrections, in terms of the computation of their covariance matrix as well as the *a posteriori* variance of unit weight, is also described in this chapter. Finally, the definition of the Multi-Ref original covariance functions and the description of their computation using real data are also included. All these equations are used in subsequent chapters to compute corrections and their estimated accuracy, helping to assess the impact of using various covariance functions and to derive the Kalman filter approach applied to the corrections.

In Chapter 4, the impact of using the original covariance functions computed with different data sets on the Multi-Ref performance is investigated. It starts with a description of the data sets used in this thesis and includes an assessment of the influence of different covariance functions on the estimated accuracy of the corrections.

Chapter 5 describes the derivation of the separate modelling for tropospheric/satellite orbit errors as well as for ionospheric errors and its application to the same data sets. Comparisons of the results obtained using the various covariance functions, including the ones derived in Chapter 4, are shown along this chapter. Some remarks about multipath errors and receiver noise are included in the end, along with a summary of the optimisation of Multi-Ref throughout improving the covariance functions.

The optimisation of Multi-Ref throughout applying a Kalman filter to the tropospheric/satellite orbit corrections and to the ionospheric corrections is treated in Chapter 6. The corresponding system and observation models are derived as well as the approach used to extract, from real corrections, the parameters necessary to define the random processes used. This methodology is then applied to filter the corrections computed using the Brazilian data set and compared with results without applying any filter obtained in Chapter 5.

In Chapter 7, conclusions based on the investigations carried out in Chapters 4, 5, and 6 are listed. Recommendations specifically related to the methods derived and implemented in this thesis are also given, as well as general ones regarding the Multi-Ref approach.

Appendix A re-visits the derivation of the Least-Squares Prediction (Collocation) method and covers the classical properties of the covariance functions, as per Moritz [1976, 1980].

In appendix B, the computation of precise coordinates of reference stations of both networks used in this thesis, as well as the determination of double difference carrier phase integer ambiguities for baselines between reference stations, using Bernese GPS Software, are described. These elements are needed when applying the Multi-Ref method.

Finally, Appendix C lists the GPS satellite antenna phase centre offsets with respect to the satellite centre of mass adopted in the analysis of the quality of broadcast ephemerides carried out in Chapter 2.

CHAPTER 2

DIFFERENTIAL GPS ERROR SOURCES

In this chapter, the GPS error sources that affect GPS positioning are described. Only errors that are present after applying the double difference process are covered, considering that double difference observations are the ones used as input to the Multi-Ref method. Due to this fact, satellite and receiver clock errors are not treated here, as they cancel out in the double difference process. For the remaining errors, the classification proposed by Raquet [1998] is adopted here, in such a way that they are divided into correlated and uncorrelated errors. The first ones correspond to errors that are spatially correlated, i.e. the shorter the baseline formed by two stations the less they are left in the double difference observations. Satellite orbit, tropospheric and ionospheric errors belong to this category. The second ones are associated with characteristics of each site and do not cancel out or reduce in the double difference process; on the contrary they accumulate. These are multipath and receiver noise. Considering that one of the main objectives of this research was to optimise the Multi-Ref approach throughout modelling separately the correlated errors in the covariance function generation, this chapter focuses on their description.

2.1 Satellite Orbit Errors

To use GPS for positioning, it is assumed that the satellite coordinates are known. These coordinates are normally expressed in terms of an ephemeris, which is a mathematical description of where a satellite is at a given time [Roulston et al., 2000].

In order to provide users with ephemeris necessary for real time applications, the GPS design group came up with what is known as broadcast ephemeris. It is available in the navigation message modulated on the GPS carrier signals [Wells et al., 1986], which is uploaded to each satellite at least once per day. A total of 16 pseudo-Keplerian parameters are transmitted, with six describing an elliptical orbit at a specific time t_0, whereas the remaining ones describe the deviations of the actual satellite orbit from the reference ellipse. Each satellite position is a function of time since t_0, being the orbit parameters valid for two hours before and two hours after the reference epoch t_0 [Seeber, 1993]. Initially the computation was based on data collected in five monitor stations, namely, Colorado Springs, Kwajalein, Ascension Island, Hawaii, and Diego Garcia, the first one being also the Master Control Station [Wiederholt and Kaplan, 1996]. Currently one additional monitor station located in Cape Canaveral contributes to the ephemeris computation [U.S. Assistant Secretary of Defense, 2001]. After an initial estimated accuracy at the level of 20 to 50 m [Wells et al., 1986], it was improved to around 2 m

[Beutler, 1997; IGS, 2001a]. The GPS Accuracy Improvement Initiative (AII) [Hay, 2000] focuses on enhancing the quality of the clock and ephemeris parameter values embedded within the navigation message. Once operational in 2005, AII is expected to reduce the signal-in-space range error (SISRE) to 1.30 m RMS [Hay, 2000]. The broadcast ephemeris is referred to the World Geodetic System of 1984 [DMA, 1991].

In order to derive more precise orbits needed for scientific and engineering applications, several groups started to compute what is known as precise ephemeris. Among them there are the official precise orbits computed by the Naval Surface Warfare Center together with National Imagery and Mapping Agency (NIMA), available upon request about 4-8 weeks after the observations [Beutler et al., 1998], and the orbits computed by the International GPS Service (IGS) [IGS, 2001b]. First starting with post-mission precise orbits in 1992, requirements of several applications (some of them real time) led to an increased number of IGS products, which are currently used by a large user community. The IGS orbit products, including satellite ephemerides and Earth rotation parameters, are [IGS ACC, 2001]:

- **IGS Final orbits**: They have the highest quality of all IGS orbits. They are made available on a weekly basis, every Friday, with a delay of 13 to 20 days of the observation day, depending on whether it happened in the last or the first day of the week, respectively;

- **IGS Rapid orbits**: They have a quality comparable to that of the Final orbits. They are made available on a daily basis with a delay of merely 17 hours after the end of the observation day, i.e. the IGS Rapid orbits become available on a daily basis at 17:00 Coordinated Universal Time (UTC). For most applications the user of IGS products will not be able to notice any significant differences between results obtained using the IGS Final and the IGS Rapid orbits;
- **IGS Predicted orbits**: They were the first IGS products available for real time use. IGS stated that the orbit quality was much better than the quality of the GPS broadcast ephemerides in a "median" sense. However, as a consequence of the 36-hour average age of the predictions, the quality of the predicted orbits suffered from a few poorly modelled satellites, which significantly influenced the results. They were discontinued on December 10, 2001, in favour of the new IGS Ultra-Rapid orbits;
- **IGS Ultra-Rapid orbits**: they started to be generated to reduce the age of the Predicted orbits. Like the IGS Predicted orbits, the Ultra rapid ones are available for real time use. However, the Ultra rapid products are provided twice per day, at 03:00 and 15:00 UTC. In this way the average age of the predictions is reduced to 9 hours (compared to the 36 hours for the IGS predicted products). This led to significantly improved orbit predictions. Contrary to all other IGS orbit products, the IGS Ultra rapid orbit files contain 48 hours of orbit. All other orbit products contain 24 hours. The first 24 hours of the IGS Ultra rapid orbit are a "real" orbit, i.e. an orbit based on real GPS data coming from the IGS hourly network. The next 24 hours are a

predicted orbit. The orbits are, however, continuous at the boundary between the real and predicted orbit part. They became official on November 5, 2001, replacing the IGS Predicted ones [Springer, 2000b].

All IGS orbit information is made available at 15-minute intervals in the so-called SP3 format [Remondi, 2001; Haw, 2001] and it was referred to the realisation of the International Terrestrial Reference Frame (ITRF) [LAREG, 2001] available at the computation time until June 3, 2000. After that they are referred to the IGS realisation of ITRF [Ferland, 2000; Springer, 2000a], which is an internally consistent solution. However the underlying reference frame is still ITRF. The current orbit reference is the IGS00, which is the IGS realisation of ITRF2000 [Weber, 2001].

The accuracy of each type of IGS orbit product currently available can be found in IGS [2001a] and is summarised in Table 2.1. The satellite clock estimated accuracies are also included for reference.

In order to actually assess the quality of the broadcast ephemerides during August 1999 (when the data sets used in this thesis were collected – see Sections 4.2.1 and 4.2.2), the satellite coordinates generated using them were compared with the IGS final orbits, assuming the last ones as the “truth”. Satellite positions were computed every 15 minutes using the equations described in Kaplan et al. [1996], in order to allow direct comparison

Table 2.1: Accuracies for satellite coordinates, clocks and other information on the IGS orbit products[1] [IGS, 2001a]

IGS Orbit Product	Accuracy		Latency	Updates
	Orbits	Clocks		
Ultra-Rapid (Predicted)	≈ 25 cm	≈ 5 ns	real time	twice daily
Rapid	5 cm	0.2 ns	17 hours	daily
Final	< 5 cm	0.1 ns	From 13 to 20 days	weekly

1: Accuracy limit based on comparisons with independent laser ranging results. IGS claims that the precision of Rapid and Final orbits is better

without the necessity of interpolating the precise orbits. All comparisons were carried out in the Satellite-Centred-Satellite-Fixed (SCSF) reference frame, which is centred at the satellite centre of mass (Figure 2.1). The satellite coordinates computed using broadcast ephemerides were previously corrected by the satellite antenna offsets (see Appendix C for the adopted values), as they are originally referred to the antenna phase centres. In order to do that, the coordinates were transformed from the Earth-Centred-

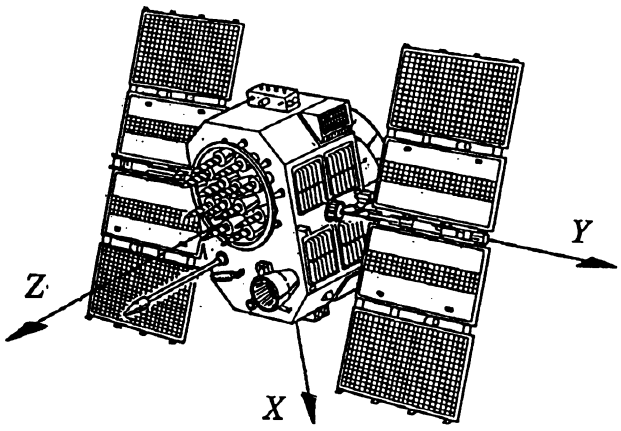

Figure 2.1: Satellite-Centred-Satellite-Fixed (SCSF) reference frame [from Beutler et al., 1998]. X, Y and Z are, respectively, the out-of-plane, along-track and radial components

Earth-Fixed (ECEF) system (WGS84) by applying rotations to make the transformed axes parallel to the SCSF ones, then they were corrected by the antenna offsets, and then transformed back to the ECEF system.

From Figure 2.2, the following angles can be identified:

- **X$\hat{O}$n**, on the equatorial plane: longitude of the ascending node, also known as **Ω**;
- **n$\hat{O}$S**, on the orbital plane: argument of latitude, also known as **φ**;
- between orbital and equatorial planes: inclination of orbit, also known as **i**.

To obtain ECEF-rotated coordinates referred to a system parallel to SCSF, the following formula was applied:

$$\begin{bmatrix} x'_{PC} \\ y'_{PC} \\ z'_{PC} \end{bmatrix}_{// SCSF} = R_3(\varphi)R_1(i)R_3(\Omega)\begin{bmatrix} X_{PC} \\ Y_{PC} \\ Z_{PC} \end{bmatrix}_{ECEF} \quad (2.1)$$

where the subscript **PC** means referred to the satellite antenna phase centre and $\mathbf{R_m(\alpha)}$ represents the 3x3 matrix describing a rotation of angle **α** around axis **m**.

Then the resultant coordinates are corrected for the satellite antenna offsets, according to the following:

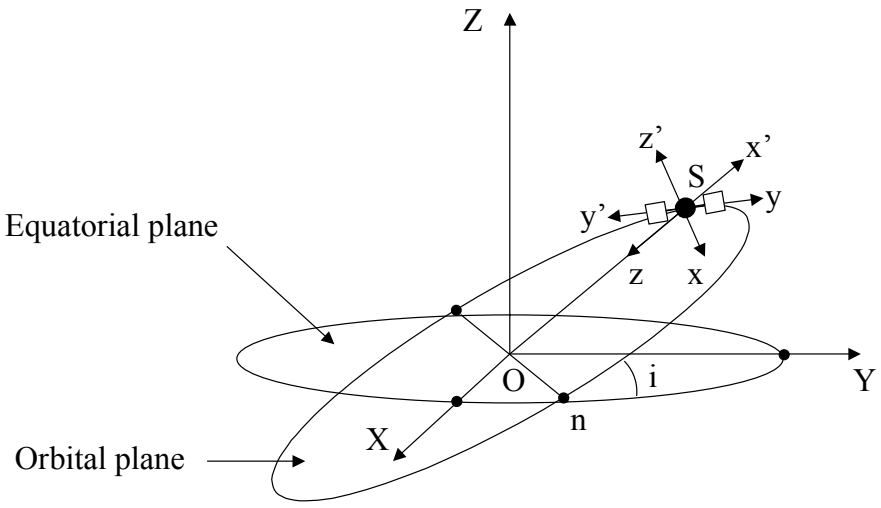

Figure 2.2: ECEF system, with XYZ orthogonal cartesian axes (WGS84), and SCSF system, with xyz axes. O is the Earth's centre of mass (origin of the ECEF system), S is the GPS satellite, x'y'z' is another SCSF auxiliary system, and n is the ascending node

$$\begin{bmatrix} x_{PC} \\ y_{PC} \\ z_{PC} \end{bmatrix}_{// SCSF} = \begin{bmatrix} -z'_{PC} \\ -y'_{PC} \\ -x'_{PC} \end{bmatrix}_{// SCSF} \tag{2.2}$$

$$\begin{bmatrix} x_{CM} \\ y_{CM} \\ z_{CM} \end{bmatrix}_{// SCSF} = \begin{bmatrix} x_{PC} \\ y_{PC} \\ z_{PC} \end{bmatrix}_{// SCSF} + \begin{bmatrix} \Delta x \\ \Delta y \\ \Delta z \end{bmatrix} \tag{2.3}$$

where the subscript **CM** means referred to the satellite centre of mass, and **Δx**, **Δy**, **Δz** are the antenna offsets. The systems with axes **xyz** and **x'y'z'** are Earth-centred and parallel to SCSF. They were translated to the satellite in Figure 2.2 for the sake of clarity (i.e. they represent actual SCSF systems).

The last steps comprised in bringing the $\mathbf{x_{CM}}$, $\mathbf{y_{CM}}$ and $\mathbf{z_{CM}}$ coordinates back to the ECEF system, as given in Equations 2.4 and 2.5.

$$\begin{bmatrix} x'_{CM} \\ y'_{CM} \\ z'_{CM} \end{bmatrix}_{//SCSF} = \begin{bmatrix} -z_{CM} \\ -y_{CM} \\ -x_{CM} \end{bmatrix}_{//SCSF} \tag{2.4}$$

$$\begin{bmatrix} X_{CM} \\ Y_{CM} \\ Z_{CM} \end{bmatrix}_{ECEF} = R_3(-\Omega)R_1(-i)R_3(-\varphi)\begin{bmatrix} x'_{CM} \\ y'_{CM} \\ z'_{CM} \end{bmatrix}_{//SCSF} \tag{2.5}$$

Is should be noticed that the geometry in Figure 2.2 has an approximation. Theoretically, the **z** axis should not intersect the origin **O**, however, doing this causes a negligible error in the correction of the antenna phase centre offset (few millimetres).

$\mathbf{X_{CM}}$, $\mathbf{Y_{CM}}$ and $\mathbf{Z_{CM}}$ coordinates were then compared with the ones obtained using the IGS final precise ephemerides. An additional aspect that has to be considered

when performing the comparison is the reference system adopted in each case. As mentioned before, the broadcast ephemerides are referred to WGS84, whereas the IGS final orbits in August 1999 were referred to ITRF97. However, according to Slater and Malys [1998], the realisation of WGS-84 is coincident with ITRF94 at the 5-cm level. Besides, ITRF94, 96 and 97 are all in the same system (in terms of origin, scale, orientation and time evolution) [LAREG, 2001]. These characteristics show that the differences between WGS84 and ITRF97 are at the centimetre-level, which is two orders of magnitude less than the expected accuracy of the broadcast ephemeris. Therefore, no transformation was applied between satellite coordinates computed with the broadcast and precise ephemeris.

Satellite coordinates were computed for two days, namely August 11 and 13, 1999, using broadcast ephemerides. The differences to the IGS final orbits were transformed from the ECEF system to the SCSF using Equations 2.1 and 2.2. Figure 2.3 shows the differences for each of 27 visible satellites in terms of out-of-plane, along-track and radial components, as well as the total error, for August 11, whereas Table 2.2 lists the corresponding RMS values. From the figure and table it can be seen that the best component was the radial, because the range measurements are more sensitive to the changes in the radial dimension [Zumberge and Bertiger, 1996]. Some satellites had large differences, e.g. PRN 14 (total error of 12.56 m), denoting modelling problems (this

satellite was the first Block II satellite launched [Advanstar, 1999], and decommissioned on April 14, 2000 [NIMA, 2001]).

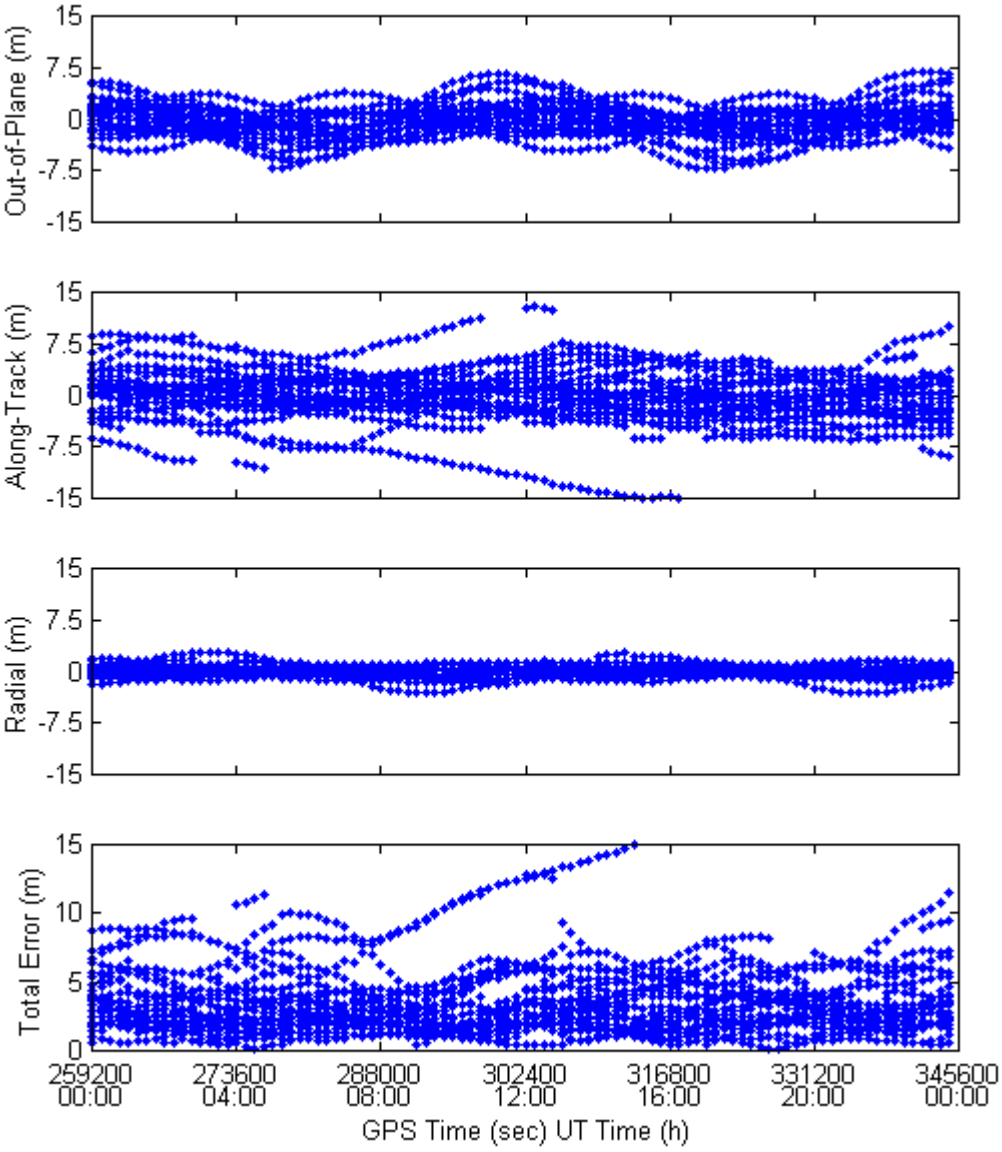

Figure 2.3: Differences between broadcast and IGS final precise ephemeris for each of 27 visible satellites in terms of out-of-plane, along-track and radial components, as well as the total error, for August 11, 1999

Table 2.2: RMS of the differences between broadcast and IGS final precise ephemeris for each of 27 visible satellites in terms of out-of-plane, along-track and radial components, as well as the total error, for August 11, 1999

PRN	BL	Out-of-Plane RMS (m)	Along-Track RMS (m)	Radial RMS (m)	Total Error RMS (m)
1	IIA	2.02	1.81	0.92	2.87
2	II	1.15	2.30	0.39	2.60
3	IIA	1.46	3.36	0.73	3.73
4	IIA	1.11	1.31	0.69	1.85
5	IIA	3.02	2.75	0.53	4.12
6	IIA	4.15	4.61	2.01	6.51
7	IIA	1.20	2.76	0.47	3.05
8	IIA	1.42	3.95	0.68	4.25
9	IIA	0.92	1.07	0.62	1.54
10	IIA	2.08	1.25	0.60	2.50
13	IIR	1.12	1.05	1.21	1.95
14	II	3.15	12.11	1.06	12.56
15	II	1.78	2.39	0.43	3.02
16	II	4.08	3.64	0.41	5.48
17	II	1.11	3.64	0.48	3.84
18	II	4.49	1.81	0.31	4.85
19	II	0.85	1.53	0.45	1.81
21	II	0.68	2.14	0.59	2.32
22	IIA	2.56	1.76	0.19	3.11
23	IIA	0.80	3.96	1.05	4.18
24	IIA	2.53	6.45	0.79	6.98
25	IIA	1.33	1.39	0.45	1.97
26	IIA	1.17	4.65	0.86	4.87
27	IIA	2.08	2.06	0.71	3.01
29	IIA	1.62	2.67	0.67	3.20
30	IIA	1.19	1.47	0.28	1.91
31	IIA	1.50	3.09	0.64	3.49
TOTAL		**2.15**	**3.72**	**0.76**	**4.36**

The RMS of the total error was 4.36 m. Statistics for August 13 were equivalent, with a total error RMS of 4.44 m. Despite the fact that these values are larger than the

expected accuracy (around 2 m), they are slightly smaller than the ones computed by Zumberge and Bertiger [1996], using data collected in 1993, and by Roulston et al. [2000], with data collected in October, 1999, and February, 2000.

Despite the fact that the broadcast ephemerides give errors on the order of few metres, the differential error propagated to baseline components is relatively smaller. According to Beutler et al. [1998], the following approximate relationship holds:

$$\frac{db}{b} = \frac{d\rho}{\rho} \tag{2.6}$$

where **db** is the total error in the coordinates of a baseline of length **b**, **dρ** is the total error in the coordinates of a satellite position, and **ρ** is the mean distance between the stations and the satellite. This fact is considered in Section 5.1, when the impact of orbit error modelling on the Multi-Ref approach is analysed.

2.2 Tropospheric Errors

Conceptually, the troposphere is the layer of the atmosphere that extends from the Earth's surface up to 8-10 km [Spilker Jr., 1996]. However, the meaning of the tropospheric effects on GPS corresponds to the resultant effect caused by atmospheric layers that range up to around 60 km [Lachapelle, 1997]. For GPS frequencies, the tropospheric

propagation delay is independent of frequency, i.e. it is non-dispersive. Hence it can not be corrected using GPS dual frequency measurements [Seeber, 1993].

Usually hydrostatic and wet components express the influence of the troposphere on GPS range measurements. The wet component depends on the distribution of the water vapour in the atmosphere and is harder to model. But it is responsible for only 10 to 20% of the total tropospheric refraction [Lachapelle, 1997]. The dry component can be precisely described (±1%) by models [Seeber, 1993]. Mendes [1999] presents a detailed description and analysis of several models. The zenith dry and wet delays can reach values up to 2.3 m and 0.80 m, respectively [Spilker Jr., 1996], increasing about 10 times near the horizon (at 10° elevation) [Seeber, 1993].

For precise differential positioning, the tropospheric delay is critical, in particular in the height component, as the tropospheric errors are poorly correlated over larger distances. When the baseline length is long or the height difference is large, the local atmospheric conditions are no longer as correlated with one another [Seeber, 1993]. Lachapelle [1997] states that the contribution of the troposphere to the differential positioning error budget varies typically from 0.2 to 0.4 parts per million (ppm), after applying a model. Assuming that most of the tropospheric residual errors are due to the wet component, one can estimate the typical differential contribution of the troposphere

before applying a model as varying from 1 to 4 ppm, which depends strongly on the satellite elevation angle.

2.2.1 The Ionospheric-Free Linear Combination

The ionospheric-free linear combination of the L1 and L2 carrier phase measurements represents a very useful quantity to estimate the double difference tropospheric errors. In general, a linear combination of carrier phase measurements has the form (analogous equation can be applied to code observations as well):

$$\phi_{i,j} = i\phi_1 + j\phi_2 \tag{2.7}$$

where ϕ_1 and ϕ_2 are, respectively, the L1 and L2 carrier phase measurements, in cycles; **i** and **j** are coefficients and $\phi_{i,j}$ is the phase of the resultant linear combination, also measured in cycles. The corresponding wavelength is given by:

$$\lambda_{i,j} = \frac{c}{if_1 + jf_2} \tag{2.8}$$

where $\lambda_{i,j}$ is the wavelength of the combined observable, **c** is the speed of light in the vacuum (299792458.0 m/sec), and f_1 and f_2 are the L1 and L2 GPS frequencies (1575.42 and 1227.60 MHz, respectively).

Depending on how the coefficients **i** and **j** are chosen, the new observation can have interesting properties. For instance, if **i** = 1 and **j** = -1, the so-called widelane (WL) observable is generated. Due to its long wavelength of 86.2 cm (obtained substituting these values for **i** and **j** in Equation 2.8), its use is very popular for ambiguity resolution [Seeber, 1993]. If **i** and **j** are chosen in such a way that:

$$\frac{i}{j} = -\frac{f_1}{f_2} \tag{2.9}$$

the resultant linear combination is free of the first order effects of the ionosphere. Equation 2.9 can be derived considering the total ionospheric effect on the linear combination, based on the individual effects on L1 and L2 (see Section 2.3):

$$d_{ion_{i,j}} = i\, d_{ion_1} + j\, d_{ion_2} = i\frac{-I}{c f_1} + j\frac{-I}{c f_2} = \frac{-I}{c}\left(\frac{i}{f_1} + \frac{j}{f_2}\right) \tag{2.10}$$

where $\mathbf{d_{ion}}$ is the ionospheric error on the respective observable in cycles and **I** is a function of the total electron content in the ionosphere. Hence to have $\mathbf{d_{ion_{i,j}}}$ equal to zero, it is necessary to have the expression between parenthesis in Equation 2.10 also equal to zero, which leads to Equation 2.9.

Some authors consider the following expressions for **i** and **j** when forming the ionospheric-free linear combination [Leick, 1995; Hugentobler et al., 2001]:

$$\begin{aligned} i &= \frac{f_1^2}{f_1^2 - f_2^2} \\ j &= -\frac{f_1 f_2}{f_1^2 - f_2^2} \end{aligned} \tag{2.11}$$

which gives a $\lambda_{i,j}$ (Equation 2.8) equal to the L1 wavelength, i.e. 19.0 cm.

In this thesis, the values adopted by Raquet [1998] were used, namely:

$$\begin{aligned} i &= 1 \\ j &= -\frac{f_2}{f_1} \end{aligned} \tag{2.12}$$

corresponding to a $\lambda_{i,j}$ equal to 48.4 cm. Both sets of **i** and **j** values (Equations 2.11 and 2.12) give equivalent results.

The double difference carrier phase observable can be written as follows [Lachapelle, 1997]:

$$\Delta\nabla\Phi = \Delta\nabla\rho + \Delta\nabla d\rho - \lambda\Delta\nabla d_{ion} + \Delta\nabla d_{trop} + \lambda\Delta\nabla N + \Delta\nabla\varepsilon(\Phi) \qquad (2.13)$$

where $\Delta\nabla$ is the double difference operator and

- Φ carrier phase observation, in metres
- ρ geometric distance between each station and each satellite, in metres
- $d\rho$ error in the geometric distance, in metres
- d_{ion} ionospheric delay, in cycles
- d_{trop} tropospheric delay, in metres
- λ wavelength of the carrier phase signal, in metres
- N integer ambiguity, in number of cycles
- $\varepsilon(\Phi)$ error due to carrier phase multipath and noise, in metres.

In the case of the ionospheric-free observable, obtained substituting **i** and **j** satisfying Equation 2.9 into 2.7, $\mathbf{d_{ion}}$ is equal to zero. If the station coordinates are known,

dρ is due only to satellite orbit errors. Considering that multipath and noise (**ε(Φ)**) are normally much smaller than the tropospheric and satellite orbit errors for baselines greater than 10 km (millimetres versus centimetres), Equation 2.13 can be re-written as follows:

$$\Delta\nabla d_{trop} + \Delta\nabla d\rho = \Delta\nabla\Phi_{IF} - \Delta\nabla\rho - \lambda_{IF}\Delta\nabla N_{IF} \tag{2.14}$$

where the subscript IF means quantities referred to the ionospheric-free observable. If precise orbits are also used, then **Δ∇dρ** can be cancelled and the left side of Equation 2.14 reduces to tropospheric errors only.

$$\Delta\nabla d_{trop} = \Delta\nabla\Phi_{IF} - \Delta\nabla\rho - \lambda_{IF}\Delta\nabla N_{IF} \tag{2.15}$$

The double difference ambiguities (**$\Delta\nabla N_{IF}$**) are not integer in this case, as it is not possible to select integer values for **i** and **j** that satisfy Equation 2.9 (recalling that $\Delta\nabla N_{i,j} = i\,\Delta\nabla N_1 + j\,\Delta\nabla N_2$, where $\Delta\nabla N_1$ and $\Delta\nabla N_2$ are the double difference ambiguities for L1 and L2, respectively). However, if the L1 and L2 ambiguities are resolved previously, then the non-integer values of the ionospheric-free ambiguities can be computed. Consequently Equation 2.15 can be used to estimate the tropospheric double difference errors. In practice, a tropospheric model is applied beforehand, and Equation

2.15 is used to estimate the residual tropospheric errors (the modified Hopfield [1969] model was used in all computations in this thesis).

Raquet [1998], using data collected in Norway, computed RMS of double difference zenith effects of the troposphere (after applying a model) on the order of 0.05 ppm (which could correspond to 0.5 ppm at low, i.e. 5° to 10°, elevations). Similarly, data from the Brazilian network (described in Section 4.2.2) collected on August 11, 1999, were used to compute RMS of the double difference tropospheric errors for 35 baselines. Figure 2.4 plots the computed RMS versus the baseline length. It can be seen that the RMS values increase with the baseline length, as expected. A differential

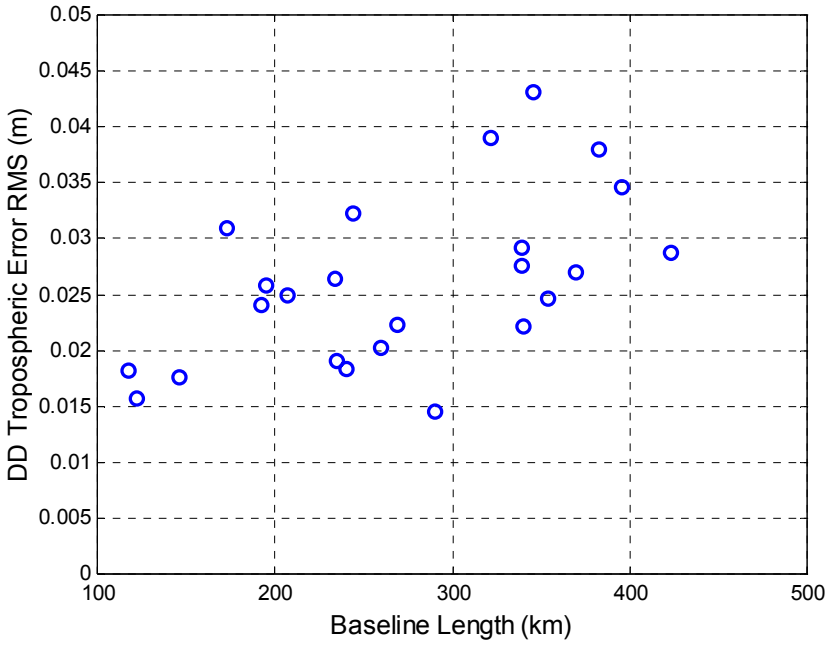

Figure 2.4: Double difference tropospheric error RMS as a function of the baseline length using data collected in Brazil on August 11, 1999

effect of up to 0.2 ppm can be extracted from this figure (0.031 m at 173 km), with an average trend of about 0.1 ppm. These values are larger than those obtained by Raquet [1998] for Norway because of the large wet component in Brazil. Figure 2.5 shows the double difference tropospheric errors for a 146-km baseline.

One aspect that has to be considered when using a linear combination given by Equation 2.7 is the noise (and multipath) propagated into the combined observation. According to Seeber [1993], it can be computed using the following expression:

$$\varepsilon(\phi_{i,j}) = \sqrt{i^2 + j^2}\,\varepsilon(\phi) \tag{2.16}$$

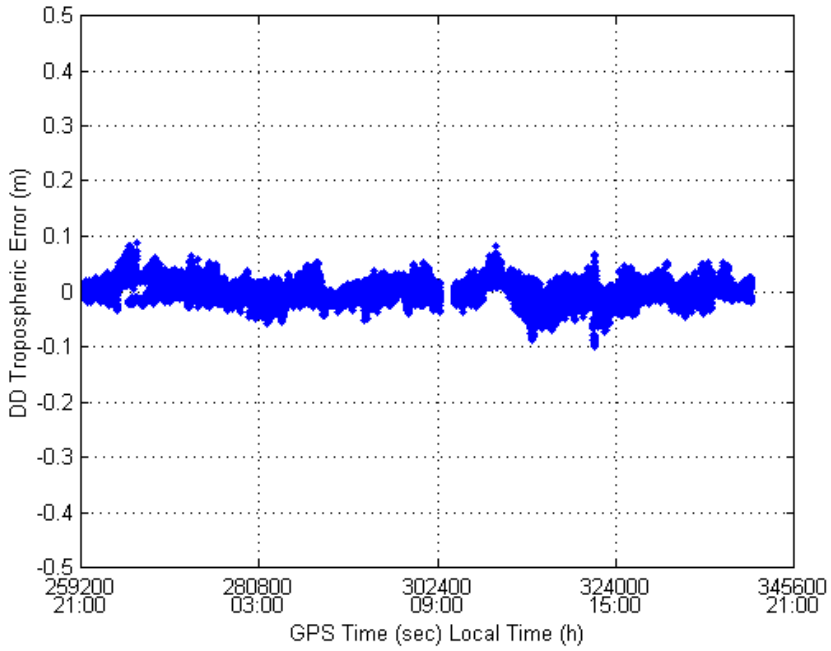

Figure 2.5: Double difference tropospheric errors for a 146-km baseline in Brazil for August 11, 1999

where $\boldsymbol{\varepsilon(\phi)}$ and $\boldsymbol{\varepsilon(\phi_{i,j})}$ are the noise (and multipath) affecting the original signal and the combined one, respectively, in cycles. Substituting $\boldsymbol{\varepsilon(\phi)}$ = 0.01 cycles [Larson, 1996] and **i** and **j** given by Equation 2.12 into 2.16, a nominal value of 0.012677 cycles (equivalent to 0.0061414 m) is obtained for $\boldsymbol{\varepsilon(\phi_{i,j})}$, demonstrating that the ionospheric-free observable is around three times noisier than L1 [Hugentobler et al., 2001]. This corresponds to a variance of 3.7717e-05 m^2. It should be noted that, if another set of **i** and **j** values satisfying Equation 2.9 was chosen (for example, the ones given by Equation 2.11), the same value of noise, in units of length, is propagated into the ionospheric-free observable. This characteristic holds because $\boldsymbol{\lambda_{i,j}\varepsilon(\phi_{i,j})}$ only depends on the ratio between **i** and **j** and not on the individual values of them. From Equations 2.8 and 2.16:

$$\begin{aligned}\lambda_{i,j}\varepsilon(\phi_{i,j}) &= \frac{c}{i f_1 + j f_2}\sqrt{i^2 + j^2}\,\varepsilon(\phi) = \\ &= \frac{c}{i\left(f_1 + \frac{j}{i} f_2\right)} i\sqrt{1 + \frac{j^2}{i^2}}\,\varepsilon(\phi) = \\ &= \frac{c}{f_1 + \frac{j}{i} f_2}\sqrt{1 + \frac{j^2}{i^2}}\,\varepsilon(\phi)\end{aligned} \tag{2.17}$$

which proves that characteristic.

2.3 Ionospheric Errors

The ionosphere is the layer of the ionosphere that extends from 60 to over 1000 km of height above the Earth's surface. In contrast to the troposphere, it is a dispersive medium for the GPS carrier frequencies, allowing users to measure and correct for the first order effect of the ionosphere using the L1 and L2 signals [Klobuchar, 1996]. The ionosphere is formed through the ionisation of the neutral atmosphere by the solar radiation and solar wind, generating ions and electrons [Skone, 1999]. Another difference to the troposphere is that the ionosphere delay can change rapidly, frequently by one order of magnitude during the day, whereas the tropospheric delay generally does not change much, even over long periods of time [Klobuchar, 1996].

The carrier phase first order error (in cycles) caused by the ionosphere is given by the following formula [Klobuchar, 1996]:

$$d_{ion} = -\frac{I}{c\,f} \tag{2.18}$$

where **I** is a function of the total electron content (TEC) in the ionosphere, given by the integration of the electron density along the path from the receiver to the satellite using a 1-m^2 column, and **f** is the frequency. **I** is computed using the following equation:

$$I = 40.3\ TEC \tag{2.19}$$

with **TEC** expressed in number of electrons/m^2 and **I** in cycles•m/s^2. The group delay (code measurement error) is similar to the value given by Equation 2.18, expressed in metres, i.e.:

$$D_{ion} = \frac{I}{f^2} \tag{2.20}$$

where $\mathbf{D_{ion}}$ is the ionospheric group delay.

From Equation 2.19, it can be seen that the magnitude and variability of the ionospheric errors is a function of TEC. The TEC values depend on the rate of ionisation, recombination and transport processes [Skone, 1999]. The rate of the ionisation in a global sense is a function of the solar activity, which follows cycles of approximately 11 years of duration. The number of sunspots observed on the solar disk is correlated with the solar activity [Klobuchar, 1996]. Figure 2.6 shows the monthly and monthly smoothed sunspot numbers for the latest four cycles [SIDC, 2001]. The latest solar maximum occurred during the period 2000-2001. The data sets used in this thesis were collected in August 1999, just before the peak, which means that a strong ionosphere signature is present is the data, as will be shown in Chapter 4.

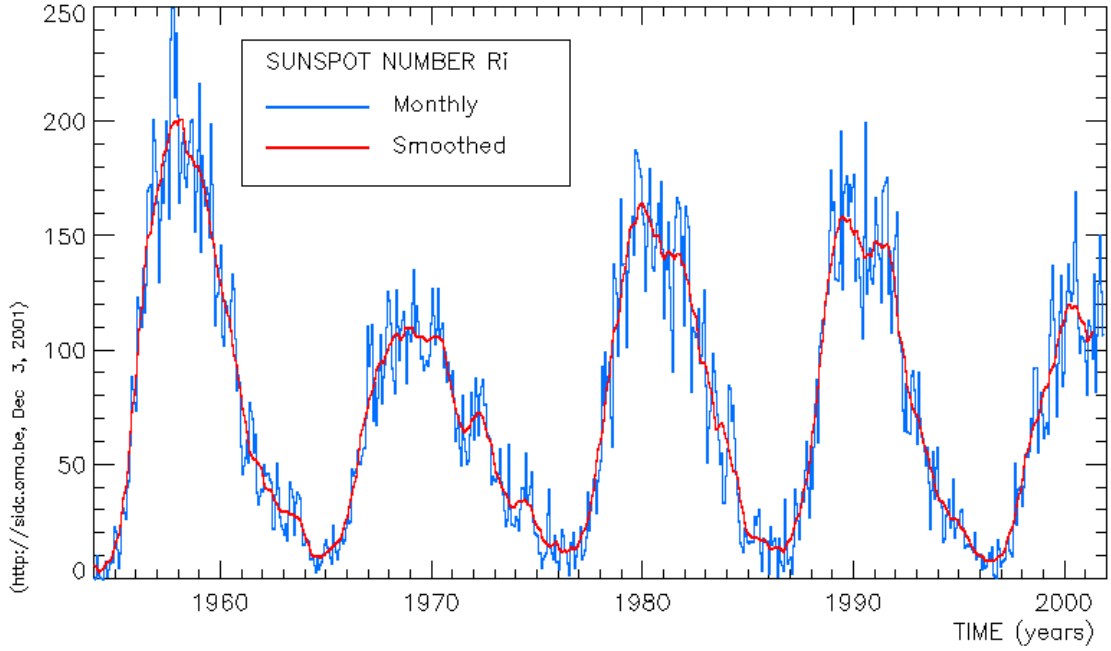

Figure 2.6: The monthly (blue) and monthly smoothed (red) sunspot numbers for the latest four cycles [SIDC, 2001]

In addition to varying with the solar cycle, the TEC presents the following types of variation [Skone, 1999]:

- **Daily**: Maximum around 2:00 p.m. local time, with a possible second maximum around 10:00 p.m. in the equatorial region;
- **Seasonal**: Lowest TEC in the summer (of the Northern Hemisphere); maxima close to the equinoxes (March and September) and in the winter. The TEC is 2 to 3 times higher in the winter than in the summer. These characteristics follow the months of the year, not the season, which means that they are opposite for the Southern

Hemisphere, i.e. lowest in the winter (= summer in the Northern Hemisphere) and maximum in the summer;

- **Geographic**: Two maxima at ±10° from the magnetic equator, in the region under the so-called equatorial anomaly [Appleton, 1954], caused indirectly by the neutral winds. The Brazilian GPS stations that collected data for this thesis work were located under this anomaly.

Figure 2.7 shows a series of 12 Global Ionosphere Maps (GIM), computed for December 25, 2001, in 2-hour intervals starting at 1:00 a.m. Universal Time (UT) (top left subfigure), by the Centre for Orbit Determination in Europe (CODE) IGS Analysis Centre, using about 150 GPS stations. Each map plots the vertical TEC (VTEC) values for the world, obtained using a spherical harmonics expansion up to degree and order 15 [CODE, 2001]. From this figure it can be seen the westward movement of the highest VTEC values (in red), reflecting the apparent movement of the Sun around the Earth. Considering Figure 2.7 (a 4x3 matrix of GIMs), each subfigure can be referred to as an element of a matrix. Hence, the equatorial anomaly can be observed as the two red "eyes" in GIMs (1,1), (4,2) and (4,3). The second daily peak is characterised by the dual "tail" of the spot shown in all subfigures.

Besides the ionospheric delay, another phenomenon that is also related to the electron content of the ionosphere is scintillation. It can be defined as the effect of small-

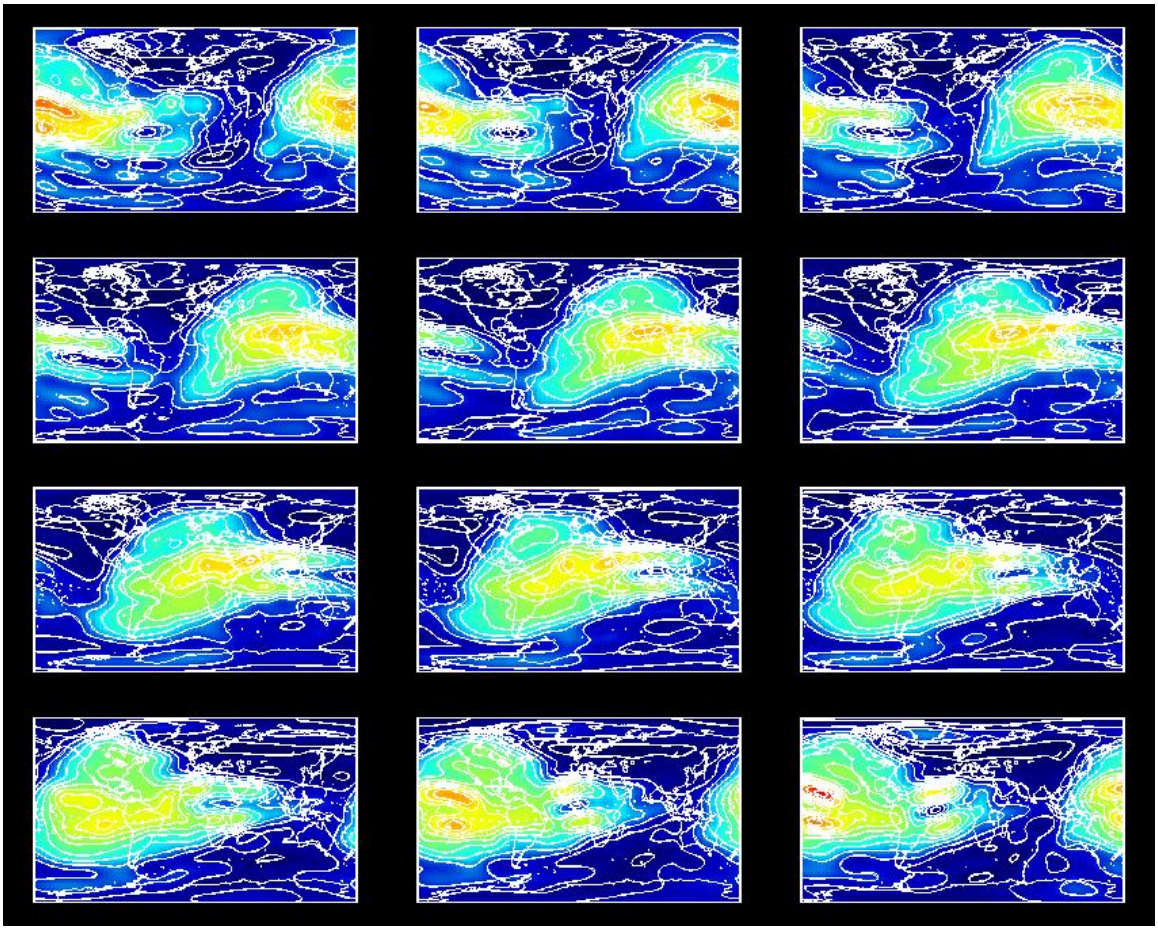

Figure 2.7: Global Ionosphere Maps for December 25, 2001, showing vertical TEC values in 2-hour intervals, starting at 1:00 a.m. (top left subfigure) [CODE, 2001]

scale irregularities in the electron content, which cause amplitude fading and phase fluctuation of the received signals [Wanninger, 1993]. It depends on geomagnetic activity, solar cycle, time of the day, frequency, season and latitude. Aarons [1982] gives a detailed study about the global morphology of ionospheric scintillations. Basically, it happens more often in the polar, auroral [Skone, 1998] and equatorial regions (with the maximum intensity in the last one), whereas its occurrence in mid-latitudes can be

attributed to an extension of the phenomenon from those other regions. In all regions, there is a pronounced nighttime maximum, with a seasonal/longitude dependence: from the Americas to India, effects are stronger between September and March than between April and August, being reversed for the Pacific region [Wanninger, 1993]. Scintillation effects also depend on the 11-year solar cycle. The importance of scintillations for GPS surveys is related to the ability of the receivers to maintain satellite lock, especially in L2. Depending on the technology used for L2 tracking - codeless or semi-codeless - the receiver can be more or less affected by this phenomenon, as the first technique implies a 13dB loss when compared with the second one [Woo, 1999]. Skone and deJong [1999] and Skone [2000a, 2000b] show results of receiver tracking performance in the auroral and equatorial regions. Some statistics related to the campaign that collected the Brazilian data set used in this thesis are also included in Appendix B.

The ionospheric range delay can be a few hundred metres during times of high TEC [Klobuchar, 1996]. Similar to the tropospheric delay, the ionospheric errors also increase with a decrease in the satellite elevation. However, instead of varying between 1 and more than 10 times the value at the zenith, the ionosphere delays increase only up to around 3 times.

The contribution of the ionosphere to the differential positioning error budget is estimated to be 1 to 2 ppm [Seeber, 1993]. However, gradients of up to 10 (15) ppm in

the auroral (trough) region [Skone, 1998] and up to 40 ppm in the equatorial region [Wanninger, 1993] have already been reported.

2.3.1 The Geometric-Free Linear Combination

The geometric-free linear combination represents a very useful quantity to estimate the double difference ionospheric errors. It is obtained by substituting **i** with λ_1 and **j** with $-\lambda_2$ in Equation 2.7, where λ_1 and λ_2 are the L1 and L2 wavelengths, respectively. One then gets:

$$\Phi_{GF} = \lambda_1 \phi_1 - \lambda_2 \phi_2 = \Phi_1 - \Phi_2 \tag{2.21}$$

where GF stands for geometric-free linear combination. It should be noted that this time the result is expressed in metres and not in cycles. Using Equation 2.13 for the L1 frequency and considering Equation 2.18, one obtains:

$$\begin{aligned} \Delta\nabla\Phi_1 &= \Delta\nabla\rho + \Delta\nabla d\rho - \lambda_1 \Delta\nabla d_{ion_1} + \Delta\nabla d_{trop} + \lambda_1 \Delta\nabla N_1 + \Delta\nabla\varepsilon(\Phi_1) = \\ &= \Delta\nabla\rho + \Delta\nabla d\rho - \lambda_1 \frac{\Delta\nabla I}{c f_1} + \Delta\nabla d_{trop} + \lambda_1 \Delta\nabla N_1 + \Delta\nabla\varepsilon(\Phi_1) = \\ &= \Delta\nabla\rho + \Delta\nabla d\rho - \frac{\Delta\nabla I}{f_1^2} + \Delta\nabla d_{trop} + \lambda_1 \Delta\nabla N_1 + \Delta\nabla\varepsilon(\Phi_1) \end{aligned} \tag{2.22}$$

The terms $\Delta\nabla\rho$, $\Delta\nabla d\rho$, and $\Delta\nabla d_{trop}$ do not have the subscript "1", as they do not depend on the frequency. Analogously for the L2:

$$\Delta\nabla\Phi_2 = \Delta\nabla\rho + \Delta\nabla d\rho - \frac{\Delta\nabla I}{f_2^2} + \Delta\nabla d_{trop} + \lambda_2\Delta\nabla N_2 + \Delta\nabla\varepsilon(\Phi_2) \tag{2.23}$$

Applying the double difference operator to Equation 2.21, and substituting Equations 2.22 and 2.23 into the result and cancelling the terms without a subscript (as they are the same), one gets:

$$\begin{aligned}\Delta\nabla\Phi_{GF} &= -\frac{\Delta\nabla I}{f_1^2} + \lambda_1\Delta\nabla N_1 + \Delta\nabla\varepsilon(\Phi_1) - \\ &\quad -\left[-\frac{\Delta\nabla I}{f_2^2} + \lambda_2\Delta\nabla N_2 + \Delta\nabla\varepsilon(\Phi_2)\right] = \\ &= -\Delta\nabla I\left[\frac{1}{f_1^2} - \frac{1}{f_2^2}\right] + \lambda_1\Delta\nabla N_1 - \lambda_2\Delta\nabla N_2 + \\ &\quad + \Delta\nabla\varepsilon(\Phi_1) - \Delta\nabla\varepsilon(\Phi_2)\end{aligned} \tag{2.24}$$

Assuming again that carrier phase multipath and noise are generally much smaller than ionospheric errors for baselines greater than 10 km, Equation 2.24 can be re-written as:

$$-\Delta\nabla I = \left[\frac{f_1^2 f_2^2}{f_2^2 - f_1^2}\right](\Delta\nabla\Phi_{GF} - \lambda_1\Delta\nabla N_1 + \lambda_2\Delta\nabla N_2) \tag{2.25}$$

By substituting Equation 2.25 into the double difference form of Equation 2.18, one gets:

$$\Delta\nabla d_{ion_1} = \frac{1}{c f_1}\left[\frac{f_1^2 f_2^2}{f_2^2 - f_1^2}\right](\Delta\nabla\Phi_{GF} - \lambda_1\Delta\nabla N_1 + \lambda_2\Delta\nabla N_2) \tag{2.26}$$

The final expression for the double difference ionospheric error (or signal) on L1, in metres, in obtained multiplying Equation 2.26 by $\boldsymbol{\lambda_1}$:

$$\Delta\nabla IS_{L1} = \left[\frac{f_2^2}{f_2^2 - f_1^2}\right](\Delta\nabla\Phi_{GF} - \lambda_1\Delta\nabla N_1 + \lambda_2\Delta\nabla N_2) \tag{2.27}$$

where $\mathbf{IS_{L1}}$ stands for ionospheric signal on L1.

An interesting aspect of the geometric-free linear combination arises when computing its wavelength using Equation 2.8: the result is **c/0**, i.e. ∞. This happens because there is no geometric meaning for this linear combination, as all the geometric terms (receiver and satellite coordinates and clocks) are removed.

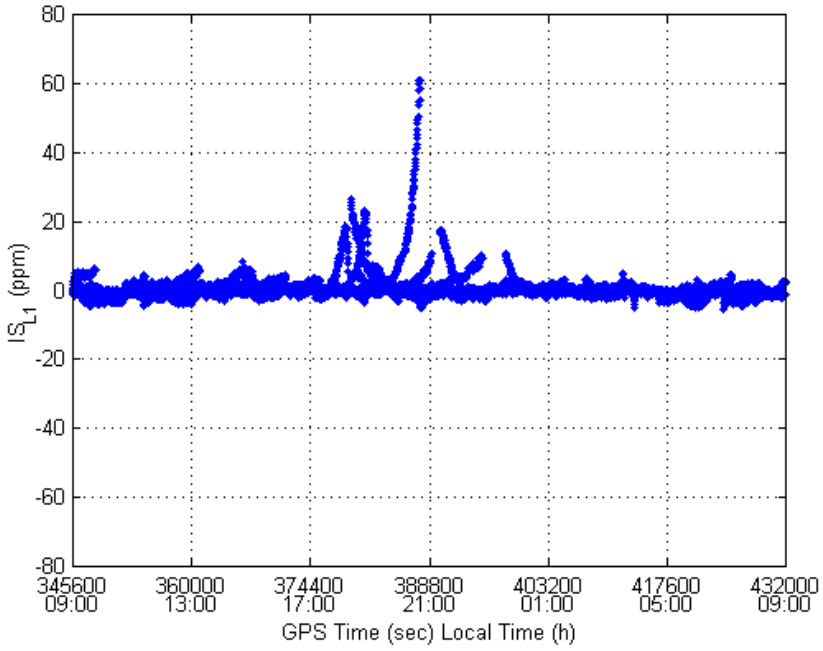

Figure 2.8: Double difference ionospheric signals on L1 for a 19-km baseline in Japan for September 27, 2001, during a geomagnetic storm

Equation 2.27 was used to compute double difference ionospheric signals on L1 for a 19-km baseline in Japan for September 27, 2001, when a magnetic storm occurred. Figure 2.8 shows the results in ppm. It can be seen that values up to 60 ppm were found around 9:00 p.m., local time, i.e. close to the second daily peak (Japan is located under the edge of the equatorial anomaly).

Similar to what was done for the ionospheric-free linear combination, the computation of the noise (and multipath) propagated into the geometric-free scaled to L1

observable was carried out, as this information is also needed in Chapter 5. Using Equation 2.16 with $\mathbf{i} = \lambda_1$, $\mathbf{j} = -\lambda_2$, $\boldsymbol{\varepsilon(\phi)} = 0.01$ cycles, and multiplying the result by the absolute value of the factor $f_2^2/(f_2^2 - f_1^2)$, a nominal value of 0.0047855 m is obtained for $\boldsymbol{\varepsilon(\phi_{i,j})}$, showing that this observable is slightly more than two times noisier than L1. The corresponding variance value is 2.2901e-05 m^2.

CHAPTER 3

THE MULTI-REF METHOD

3.1 Derivation of the Multi-Ref Method Using Least-Squares Prediction (Collocation)

Raquet [1998] came up with a new method to model the errors that affect GPS positioning based on the availability of a network of reference receivers, with known coordinates. Using the constraints given by the network, he developed the NetAdjust method, herein referred as the Multi-Ref approach, which computes the observation errors at each reference receiver and predicts the ones at the rover position. To accomplish this objective, Raquet has derived the solution using a linear minimum error variance (LMV) estimator that minimises the Bayesian risk:

$$\beta(e) = E\{| Y - e(x) |^2\} \tag{3.1}$$

where **Y** is the unknown parameter whose value is to be estimated; **x** are the observations containing information about **Y**; and **e(x)** is an estimator which provides an estimate of **Y** from **x**, according to:

$$\hat{Y} = e(x) \tag{3.2}$$

with $\hat{\mathbf{Y}}$ being the estimate of **x**.

The LMV estimators have the form:

$$e(x) = \alpha + \beta x \, . \tag{3.3}$$

Raquet also mentioned in his work that the same results could be obtained if the Least-Squares Condition case or the Least-Squares Prediction (Collocation) were used. In this section, the second one is used to derive the Multi-Ref method (see Appendix A for re-visiting the Least-Squares Prediction approach).

The problem to be solved consists of using the constraints that exist in a network of reference receivers to model the errors that occur in differential GPS positioning. Once modelled, they are to be used to correct the observations collected at the reference stations as well as at the mobile receiver.

Figure 3.1 schematically illustrates the situation. All the possible baselines between the reference stations are shown just to emphasise the constraints given by the network, but only a set of independent ones [Leick, 1995; Raquet, 1998] should be used in the solution (the use of dependent observations can generate a singular matrix in the normal equation system or artificially change the observation weights, giving a sub-optimal result). The mobile station is connected to the network through one reference station, and the results are the same no matter which one is chosen. More details about this property are given later.

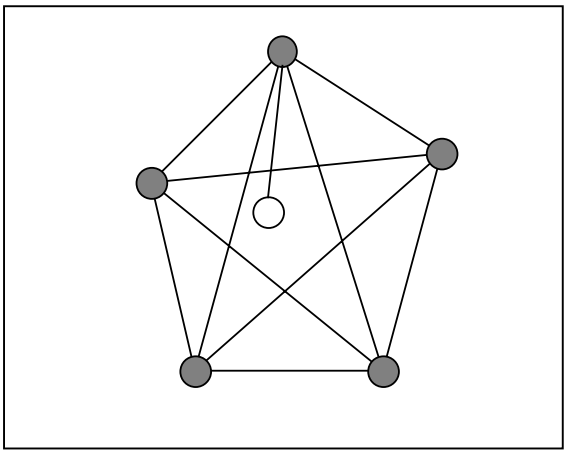

Figure 3.1: A network of reference stations, represented as grey circles, and a rover receiver as a white circle

The double difference measurement-minus-computed-range observable is defined from Equation 2.13 as:

$$\Delta\nabla\overline{\Phi} = \Delta\nabla\Phi - \Delta\nabla\rho = \Delta\nabla d\rho - \lambda\Delta\nabla d_{ion} + \Delta\nabla d^{r}_{trop} + \lambda\Delta\nabla N + \Delta\nabla\varepsilon(\Phi) \qquad (3.4)$$

where the tropospheric delay term $\mathbf{d^{r}_{trop}}$ now represents the residual value after using a model. This observable is useful to isolate the double difference errors, when the station coordinates are known.

The double difference matrix **B** for the network is defined as:

$$B = \frac{\partial\Delta\nabla\overline{\Phi}}{\partial\overline{\Phi}} \quad . \qquad (3.5)$$

Since double difference measurements are direct linear combinations of the measurements themselves, the **B** matrix is made up entirely of the values +1, -1 and 0.

Thus:

$$\Delta\nabla\overline{\Phi} = B\overline{\Phi} \quad . \qquad (3.6)$$

Substituting Equation 3.6 into 3.4 gives:

$$B\overline{\Phi} = \Delta\nabla d\rho - \lambda\Delta\nabla d_{ion} + \Delta\nabla d^{r}_{trop} + \lambda\Delta\nabla N + \Delta\nabla\varepsilon(\Phi) \quad . \tag{3.7}$$

Then:

$$B\overline{\Phi} - \lambda\Delta\nabla N = \Delta\nabla d\rho - \lambda\Delta\nabla d_{ion} + \Delta\nabla d^{r}_{trop} + \Delta\nabla\varepsilon(\Phi) \quad . \tag{3.8}$$

The left side of Equation 3.8 is composed of quantities that are supposed to be known. The double difference measurement-minus-range observable $B\overline{\Phi}$ is computed from the phase observations and the geometric distance between the satellites and the reference stations (based on the fact that their coordinates must be known[1]). The double difference ambiguities between the reference stations have to be known as well, as a requisite for applying the method. On the other hand, the right side of the Equation 3.8 is only comprised of errors. Defining:

$$\Delta\nabla\delta_{c}l = \Delta\nabla d\rho - \lambda\Delta\nabla d_{ion} + \Delta\nabla d^{r}_{trop} \tag{3.9}$$

as double-difference correlated errors and:

$$\Delta\nabla\delta_{u}l = \Delta\nabla\varepsilon(\Phi) \tag{3.10}$$

as double-difference uncorrelated errors, and considering that the double-difference operator $\Delta\nabla$ is a linear operator, Equation 3.8 becomes:

$$B\overline{\Phi} - \lambda\Delta\nabla N = \Delta\nabla\delta_c l + \Delta\nabla\delta_u l = \Delta\nabla(\delta_c l + \delta_u l) = \Delta\nabla\delta l = B\delta l \quad . \tag{3.11}$$

As explained above, the left side of the Equation 3.11 is made up of known quantities. This means that it is possible to compute the values of the double difference errors $B\delta l$ between the reference stations. If $B\delta l$ is known, is it possible to compute the errors δl_r at the rover receiver? The answer is yes, since one can apply the Least-Squares Prediction (Collocation) method. To apply this method it is necessary that both the "measurements" $B\delta l$ and the "signals" δl_r be zero mean. Based on the fact that the vector δl is a misclosure vector, after deducting from the phase observable the geometric distance satellite-receiver, the ambiguity term and the tropospheric modelled error, all the remaining quantities are residual errors and therefore are expected to have zero mean. Raquet [1998] has shown some results obtained using real data that confirm this property. In addition, the needed covariance matrices can be computed using real data, as described in Section 3.2.1.4.

[1] It is estimated that the coordinates of the reference stations must be known with an accuracy of 1-2 cm or better, in order not to impact the ambiguity resolution process in the reference network

Applying the Least-Squares Prediction (Collocation) to the problem (Equation A.25), one obtains:

$$\delta\hat{l}_r = C_{\delta l_r,\Delta\nabla\delta l}\, C^{-1}_{\Delta\nabla\delta l}\, \Delta\nabla\delta l \quad . \tag{3.12}$$

But, using Equation 3.11 and based on the covariance propagation law:

$$\begin{aligned} C_{\Delta\nabla\delta l} &= E\{(\Delta\nabla\delta l)(\Delta\nabla\delta l)^T\} = E\{(B\delta l)(B\delta l)^T\} = \\ &= E\{B\delta l\delta l^T B^T\} = BE\{\delta l\delta l^T\}B^T = BC_{\delta l}B^T \end{aligned} \tag{3.13}$$

and:

$$\begin{aligned} C_{\delta l_r,\Delta\nabla\delta l} &= E\{(\delta l_r)(\Delta\nabla\delta l)^T\} = E\{(\delta l_r)(B\delta l)^T\} = \\ &= E\{(\delta l_r)(\delta l^T B^T)\} = E\{\delta l_r\delta l^T\}B^T = C_{\delta l_r,\delta l}B^T \end{aligned} \tag{3.14}$$

Substituting Equations 3.13 and 3.14 into 3.12 and considering Equation 3.11, the final form for the Multi-Ref solution is obtained:

$$\delta\hat{l}_r = C_{\delta l_r,\delta l}B^T(BC_{\delta l}B^T)^{-1}(B\overline{\Phi} - \lambda\Delta\nabla N) \quad . \tag{3.15}$$

To complete the solution it is also necessary to generate corrections to the observations collected at the reference stations. This derivation is very simple, since one has only to apply Equation 3.15 to the reference stations. Doing that, one obtains:

$$\delta\hat{l} = C_{\delta l} B^T (B C_{\delta l} B^T)^{-1} (B\overline{\Phi} - \lambda \Delta\nabla N) \quad . \tag{3.16}$$

Equations 3.15 and 3.16 form the complete Multi-Ref solution. They are used to correct the measurements collected at the mobile receiver and at the reference stations, respectively. The user has to combine the corrected measurements at the rover with the corrected ones from just one reference receiver in order to form the double differences and to solve for the corresponding baseline components. In this solution, as the user is using observations corrected from the GPS error sources, it is expected that the necessary ambiguities can be solved for over longer distances from the reference station, compared to standard differential carrier phase positioning.

The covariance matrix of the errors can be obtained applying Equation A.26, i.e.:

$$C_{\delta\hat{l}_r} = C_{\delta l_r} - C_{\delta l_r, \Delta\nabla\delta l} C^{-1}_{\Delta\nabla\delta l} C_{\Delta\nabla\delta l, \delta l_r} \tag{3.17}$$

where $C_{\delta\hat{l}_r}$ is the covariance matrix of the errors at the predicted point.

Taking into account Equations 3.13 and 3.14 and then A.18, Equation 3.17 turns into:

$$\begin{aligned} C_{\delta\hat{l}_r} &= C_{\delta l_r} - C_{\delta l_r,\delta l} B^T (BC_{\delta l} B^T)^{-1} BC_{\delta l,\delta l_r} = \\ &= C_{\delta l_r} - C_{\delta l_r,\delta l} B^T (BC_{\delta l} B^T)^{-1} BC_{\delta l_r,\delta l}^T \end{aligned} \tag{3.18}$$

The covariance matrix of the errors at the reference stations is obtained applying Equation 3.18, similarly to what was done to the errors themselves. This gives:

$$C_{\delta\hat{l}} = C_{\delta l} - C_{\delta l} B^T (BC_{\delta l} B^T)^{-1} BC_{\delta l} \quad . \tag{3.19}$$

The fact that the user has to use the corrected observations from just one reference station can be explained by the data encapsulation effect, i.e. the data from the entire network of reference receivers is encapsulated into the corrected measurements of each individual reference receiver. Raquet [1998] explains this by combining explicitly observations from two reference receivers to show that no new information is added. Another way to explain it is noting that Equation 3.16 is also equivalent to the Least-Squares Condition case solution, as also pointed out by Raquet [1998]. Remembering that this solution is of the following form [Krakiwsky, 1990]:

$$\hat{r} = -C_l B^T (B C_l B^T)^{-1} w \tag{3.20}$$

where $\hat{\mathbf{r}}$ is the adjusted residual vector; $\mathbf{C_l}$ is the covariance matrix of the observations; **B** is the design matrix that combines the observations; and **w** is the misclosure vector. The similarity between Equations 3.16 and 3.20 is evident, based on the following relationships:

$\hat{r} \Leftrightarrow -\delta\hat{l}$ (they are symmetric as one is correction and the other is error)

$w \Leftrightarrow B\overline{\Phi} - \lambda\Delta\nabla N$ (the double difference misclosure).

Therefore, as the corrections to the observations collected at the reference stations can be understood as a Least-Squares Condition case solution, any computation including any of the adjusted reference station data gives the same result, no matter the one chosen.

The Multi-Ref solution can also be generated for GPS code observations, with the advantage that it is not necessary to know the ambiguities between the network stations in this case. The term $B\overline{\Phi} - \lambda\Delta\nabla N$ in Equations 3.15 and 3.16 simplifies to $B\overline{p}$, where $\overline{p}$ is the pseudorange measurement-minus-range observable. However, code multipath and noise, much greater than the corresponding ones for the carrier phase, limit the accuracy of this option.

A useful parameter when analysing the quality of the computed errors using Equations 3.15 and 3.16 is the *a posteriori* variance of unit weight. It can be used to scale the covariance matrices of the errors at the predicted points and at the reference stations, given by Equations 3.18 and 3.19, respectively. The mathematical expression for the *a posteriori* variance of unit weight may be obtained from the Least-Squares Condition case [Krakiwsky, 1980; Gemael, 1994]:

$$\hat{\sigma}_0^2 = \frac{\hat{r}^T C_{\delta l}^{-1} \hat{r}}{\nu} \tag{3.21}$$

where:

$\hat{\sigma}_0^2$ is the *a posteriori* variance of unit weight

$\hat{r}$ is the vector of Least-Squares adjusted residuals, given by Equation 3.16 (from Equation 3.20, $\hat{r} = -\delta\hat{l}$)

ν is the degrees of freedom or number of condition equations; in case of Multi-Ref, this is equal to the total number of independent double difference observations formed using all observations collected at the reference stations.

3.2 Role of the Covariance Function in the Multi-Ref Approach

Looking at Equations 3.15 and 3.16 it can be seen that it is necessary to know the covariance matrices $C_{\delta l}$ and $C_{\delta l_r,\delta l}$ to apply the Multi-Ref method (actually, this is a requirement of the Least-Squares Prediction, as it is known). The effectiveness of this approach is dependent on the accuracy of those covariance matrices.

Raquet [1998] has derived a procedure to compute the covariance matrices based on the definition of a covariance function. The corresponding derivation is shown in the next section, in order to set a background for the optimisation implemented in Chapter 5.

3.2.1 The Covariance Function

The covariance function is used to compute the covariance matrices $C_{\delta l}$ and $C_{\delta l_r,\delta l}$ in order to apply the Multi-Ref method.

Each element of these matrices is the covariance between two carrier phase observables δl_a^x and δl_b^y, where **a** and **b** are stations, and **x** and **y** are satellites. The carrier phase observable δl corresponds to the measurement-minus-range observable minus the ambiguity, according to the following equation:

$$\delta l = \Phi - \rho - \lambda N = d\rho - \lambda d_{ion} + d^{r}_{trop} + \varepsilon(\Phi) \tag{3.22}$$

where the terms $d\rho$, $d_{ion,}$ d^{r}_{trop}, and $\varepsilon(\Phi)$ are the same as in Equation 3.4.

The right side of Equation 3.22 is formed only by errors, comprised of the correlated ones (satellite position, ionospheric and tropospheric delays) and by the uncorrelated ones (multipath and noise). Considering that the portion of the correlated errors that is important to the problem is the one that is not cancelled out when forming the double differences, they are expressed in terms of the residual amount to a reference point $\mathbf{p_0}$. Due to the same reason, the satellite and receiver clock errors were not included in Equation 3.22, as they cancel out in the double difference process. Thus, Equation 3.22 becomes:

$$\delta l = \delta_c l(p, p_0) + \delta_u l \tag{3.23}$$

where the term $\delta_c l(p, p_0)$ corresponds to the correlated errors, which depend on the position $\mathbf{p}$ of the receiver where the measurement is taken and on the position of the reference point $\mathbf{p_0}$; and the term $\delta_u l$ corresponds to the uncorrelated ones which depend basically on the station.

Each element of the covariance matrix (c_{ab}^{xy}) is, by definition, expressed according to the following:

$$c_{ab}^{xy} = E\{(\delta l_a^x)(\delta l_b^y)\} \tag{3.24}$$

as E{δl)=0.

Substituting Equation 3.23 into 3.24, the following is obtained:

$$\begin{aligned} c_{ab}^{xy} &= E\{[\delta_c l_a^x(p_a, p_0) + (\delta_u l_a^x)][\delta_c l_b^y(p_b, p_0) + (\delta_u l_b^y)]\} = \\ &= E\{[\delta_c l_a^x(p_a, p_0)\delta_c l_b^y(p_b, p_0) + (\delta_u l_a^x)\delta_c l_b^y(p_b, p_0) + \\ &\quad + \delta_c l_a^x(p_a, p_0)(\delta_u l_b^y) + (\delta_u l_a^x)(\delta_u l_b^y)]\} \end{aligned} \tag{3.25}$$

As there is no correlation between $\delta_c l(p, p_0)$ and $\delta_u l$, Equation 3.25 reduces to:

$$\begin{aligned} c_{ab}^{xy} &= E\{[\delta_c l_a^x(p_a, p_0)\delta_c l_b^y(p_b, p_0) + (\delta_u l_a^x)(\delta_u l_b^y)]\} = \\ &= E\{[\delta_c l_a^x(p_a, p_0)\delta_c l_b^y(p_b, p_0)]\} + E\{[(\delta_u l_a^x)(\delta_u l_b^y)]\} \end{aligned} \tag{3.26}$$

Depending on **a**, **b**, **x** and **y**, Equation 3.26 becomes:

$$c_{ab}^{xy} = \begin{cases} E\{[\delta_c l_a^x(p_a, p_0)\,\delta_c l_a^x(p_a, p_0)]\} + E\{[(\delta_u l_a^x)(\delta_u l_a^x)]\}, \text{ if } a = b \text{ and } x = y \\ E\{[\delta_c l_a^x(p_a, p_0)\,\delta_c l_b^y(p_b, p_0)]\}, \text{ if } a \neq b \text{ and } x = y \\ 0, \text{ otherwise} \end{cases} \tag{3.27}$$

The first line in Equation 3.27 corresponds to the variance of the observation. In the second line, the uncorrelated errors disappear, as there is no correlation between them for different stations. And the covariance reduces to zero for $x \neq y$, as it is reasonable to consider that the correlated errors are uncorrelated for different satellites.

In order to derive the functional form for the errors, it is helpful to use a mapping function to express how the errors at the zenith degrade towards the horizon. Doing that, Equation 3.26 can be expressed in terms of the zenith covariance function as:

$$\begin{aligned} c_{ab}^{xy} &= E\{[\delta_c l_a^x(p_a, p_0)\,\delta_c l_b^y(p_b, p_0)]\} + E\{[(\delta_u l_a^x)(\delta_u l_b^y)]\} = \\ &= \mu^2(\varepsilon) f_z(p_a, p_b, p_0, a, b) = \mu^2(\varepsilon)[f_{z_c}(p_a, p_b, p_0) + f_{z_u}(a, b)] \end{aligned} \tag{3.28}$$

where $\boldsymbol{\mu(\varepsilon)}$ is the mapping function value for the average elevation of the satellites **x** and **y**, respectively $\boldsymbol{\varepsilon^x}$ and $\boldsymbol{\varepsilon^y}$.

Analysing Equation 3.28, it can be seen that the general form of the covariance function c_{ab}^{xy} is multi-dimensional, as it depends on the elevation **ε**, and on the position of the stations **a**, **b** and of the point $\mathbf{p_0}$. Therefore, it can not be easily represented in a graph, as can the traditional covariance functions used in physical geodesy, e.g. Moritz [1976, 1980]. See Appendix A for details of the covariance functions.

3.2.1.1 Functional Form of the Correlated Errors

The functional form associated to the correlated errors corresponds to the function $f_{z_c}(p_a, p_b, p_0)$ in Equation 3.28 and is derived as follows:

$$f_{z_c}(p_a, p_b, p_0) = E\{[\delta_c l_a(p_a, p_0)_z \, \delta_c l_b(p_b, p_0)_z]\} \tag{3.29}$$

where the superscripts related to satellites **x** and **y** have been removed as the errors refer to the zenith.

Considering that the correlated errors express the **residual** error with respect to the reference point $\mathbf{p_0}$:

$$\delta_c l_a(p_a, p_0)_z = \delta_c l_a(p_a)_z - \delta_c l_0(p_0)_z \tag{3.30}$$

Substituting Equation 3.30 into 3.29, one gets:

$$
\begin{aligned}
f_{z_c}(p_a, p_b, p_0) &= E\{[\delta_c l_a(p_a)_z - \delta_c l_0(p_0)_z][\delta_c l_b(p_b)_z - \delta_c l_0(p_0)_z]\} = \\
&= E\{\delta_c l_a(p_a)_z \, \delta_c l_b(p_b)_z - \delta_c l_0(p_0)_z \, \delta_c l_b(p_b)_z - \\
&\quad - \delta_c l_a(p_a)_z \, \delta_c l_0(p_0)_z + [\delta_c l_0(p_0)_z]^2\} = \\
&= E\{(1/2)[\delta_c l_a(p_a)_z - \delta_c l_0(p_0)_z]^2 + \\
&\quad + (1/2)[\delta_c l_b(p_b)_z - \delta_c l_0(p_0)_z]^2 - \\
&\quad - (1/2)[\delta_c l_a(p_a)_z - \delta_c l_b(p_b)_z]^2\} = \\
&= (1/2)E\{[\delta_c l_a(p_a)_z - \delta_c l_0(p_0)_z]^2\} + \\
&\quad + (1/2)E\{[\delta_c l_b(p_b)_z - \delta_c l_0(p_0)_z]^2\} - \\
&\quad - (1/2)E\{[\delta_c l_a(p_a)_z - \delta_c l_b(p_b)_z]^2\}
\end{aligned}
\tag{3.31}
$$

Defining $\sigma^2_{c_z}(p_m, p_n) = E\{[\delta_c l(p_m)_z - \delta_c l(p_n)_z]^2\}$, Equation 3.31 reduces to:

$$
f_{z_c}(p_a, p_b, p_0) = \frac{\sigma^2_{c_z}(p_a, p_0) + \sigma^2_{c_z}(p_b, p_0) - \sigma^2_{c_z}(p_a, p_b)}{2} \tag{3.32}
$$

Considering that $\sigma^2_{c_z}(p_m, p_n)$ represents the differential variance function between points **m** and **n**, it can be described by:

$$\sigma^2_{c_z}(p_m, p_n) = k_1 d + k_2 d^2 \tag{3.33}$$

where **d** is the distance between **m** and **n** and $\mathbf{k_1}$ and $\mathbf{k_2}$ are coefficients to be determined.

3.2.1.2 Functional Form of the Uncorrelated Errors

The functional form associated to the uncorrelated errors is represented by the function $f_{z_u}(a, b)$ in Equation 3.28. This kind of error is only present when **a** = **b**, and has the following form:

$$f_{z_u}(a) = E\{[(\delta_u l_a)_z]^2\} = \sigma^2_{u_z}(a) \tag{3.34}$$

which is a constant that depends only on the receiver and site.

3.2.1.3 Mapping Function

The mapping function has the form [Raquet, 1998]:

$$\mu(\varepsilon) = \frac{1}{\sin\varepsilon} + k_{\mu}\left(0.53 - \frac{\varepsilon}{180^{o}}\right)^{3} \qquad (3.35)$$

where $\mathbf{k_\mu}$ is a coefficient to be determined.

3.2.1.4 Computation of Covariance Function Using Real Data

The coefficients $\mathbf{k_1}$ and $\mathbf{k_2}$ (Equation 3.33), the uncorrelated variances $\sigma^2_{u_z}$ (Equation 3.34) and the coefficient $\mathbf{k_\mu}$ (Equation 3.35) are determined using real data, according to the following approach.

3.2.1.4.1 Determination of the Coefficient k_μ of the Mapping Function

The computation of $\mathbf{k_\mu}$ is done through the following steps (for each baseline in the network - not only those that are independent):

- Computing the double difference measurement-minus-range carrier phase observable minus ambiguities ($\Delta\nabla\delta\mathbf{l}$), given by Equation 3.11;

- Grouping the $\Delta\nabla\delta\mathbf{l}$ in bins depending of the elevation of the lower satellite; each bin has a width of 3^o; using only double differences that have at least one satellite with elevation above 45^o;
- Computing the variance ($\mathbf{E\{(\Delta\nabla\delta l)^2\}}$) of each bin;
- Computing $\boldsymbol{\mu(\varepsilon^{high})}$ averaging the value of the following function ($\boldsymbol{\mu_{nominal}}$) over the time window ($\boldsymbol{\varepsilon}$ is the elevation of the higher satellite for each computed double-difference):

$$\mu_{nominal}(\varepsilon) = [F_I(\varepsilon) + F_T(\varepsilon)] / 2 \tag{3.36}$$

where $\mathbf{F_I(\varepsilon)}$ and $\mathbf{F_T(\varepsilon)}$ are the ionospheric [Klobuchar, 1996] and tropospheric [Spilker Jr, 1996] mapping functions, respectively:

$$F_I(\varepsilon) = 1 + 16\,(0.53 - \varepsilon / 180°)^3 \tag{3.37}$$

$$F_T(\varepsilon) = 1 / \sin\varepsilon \tag{3.38}$$

- Computing the term $\mathbf{E\{(\Delta\nabla\delta l_z)^2\}}$ substituting $\boldsymbol{\varepsilon}$ by 90° in the function:

$$g(\varepsilon) = n_1\, F_I(\varepsilon) + n_2\, F_T(\varepsilon) \tag{3.39}$$

where the coefficients $\mathbf{n_1}$ and $\mathbf{n_2}$ are determined by a Least-Squares adjustment using the variance of each bin as the observations;

- Computing $\boldsymbol{\mu(\varepsilon)}$ for each bin using the following expression (the terms on the right side computed previously):

$$\mu(\varepsilon) = \sqrt{\frac{2E\{(\Delta\nabla\delta l)^2\}}{E\{(\Delta\nabla\delta l_z)^2\}} - \mu^2(\varepsilon^{high})} \tag{3.40}$$

Finally, the Mapping Function **$\mu(\varepsilon)$** is determined throughout the computation of the $\mathbf{k_\mu}$ coefficient by a Least-Squares adjustment using Equation 3.35 as the mathematical model and the mean values of **$\mu(\varepsilon)$** for each bin (computed using the values for all baselines calculated by Equation 3.40) as observations.

3.2.1.4.2 Determination of the Covariance Function's Coefficients k_1, k_2 and the Variance $\sigma^2_{u_z}$

The computation of $\mathbf{k_1}$, $\mathbf{k_2}$ and $\sigma^2_{u_z}$ is done through the steps:

- Scaling each double difference measurement-minus-range carrier phase observable minus ambiguities (**$\Delta\nabla\delta l$**), given by Equation 3.11, to the zenith using the following expression:

$$\Delta\nabla\delta l^{xy}_{ab_z} = \Delta\nabla\delta l^{xy}_{ab}\left[\frac{\mu(\varepsilon^x) + \mu(\varepsilon^y)}{2}\right]^{-1} \tag{3.41}$$

where $\mu(\varepsilon^x)$ and $\mu(\varepsilon^y)$ are the mapping function values computed substituting the elevation of the base (**x**) and remote (**y**) satellites, respectively, into Equation 3.35, considering that $\mathbf{k}_\mu$ was computed in the previous step;

- For each baseline in the network, computing the variance of $\Delta\nabla\delta\mathbf{l}^{\mathbf{xy}}_{\mathbf{ab_z}}$;

- Computing $\mathbf{k_1}$, $\mathbf{k_2}$ and the variance $\boldsymbol{\sigma}^2_{\mathbf{u_z}}$, based on a Least-Squares adjustment using the following mathematical model and the variances of $\Delta\nabla\delta\mathbf{l}^{\mathbf{xy}}_{\mathbf{ab_z}}$ as observations:

$$E\{(\Delta\nabla\delta l^{xy}_{ab_z})^2\} = 2(k_1 d_{ab} + k_2\, d^2_{ab}) + 2\sigma^2_{u_z}(a) + 2\sigma^2_{u_z}(b) \qquad (3.42)$$

3.2.1.5 Properties of the Covariance Functions

Traditionally, covariance functions and their associated stochastic processes should satisfy the properties of isotropy, homogeneity, harmonicity, positive definiteness, stationarity, and ergodicity, which are described in Appendix A. However, considering that these properties were studied in applications of the Earth's gravity field [Moritz, 1976], it is expected that they do not necessarily need to be fulfilled in the Multi-Ref application. In the present case, the quantities to be modelled are GPS errors. Due to the ionosphere and its temporal and spatial variability, these errors may not be stationary or ergodic, although they could be bounded in time intervals during which these properties could still be valid. In addition, if one thinks again about the ionosphere, isotropy and

homogeneity are properties that may not be satisfied, in particular in the equatorial region. On the other hand, positive definiteness is a very necessary characteristic, considering that the covariance matrices to be generated and used in Multi-Ref must be positive definite. Some results mentioned in Chapter 4 and 5 indicate that, depending on the correlated error function chosen (Equation 3.29), this is not always the case.

CHAPTER 4

OPTIMISING MULTI-REF THROUGH COMPUTING THE ORIGINAL COVARIANCE FUNCTIONS WITH DIFFERENT DATA

4.1 Introduction

Raquet [1998] states that the effectiveness of the Multi-Ref approach depends on the accuracy of the covariance matrix. As seen in the last chapter, the covariance matrix in Multi-Ref is computed based on the derivation of covariance functions that express how the various errors that affect differential GPS positioning, sorted into correlated and uncorrelated ones, behave in the region covered by the reference network. So it is necessary to investigate what is the actual influence of the covariance functions in the corrections computation using Equations 3.15 and 3.16. With respect to this matter, two aspects needed to be analysed:

- Using the original covariance functions described in Section 3.2.1, Raquet [1998] derived covariance functions for L1 and WL observables, as the objective was to generate corrections for these two kinds of observables. Taking into account that

these two covariance functions are evaluated using real data, according to the procedure described in Section 3.2.1.4, it was necessary to assess the impact of using different data sets for the covariance functions determination. This is an important aspect, as it can have a direct influence on the real time operational implementation of Multi-Ref. If the corrections show to be very dependent on the covariance matrices (i.e. on the covariance functions), this creates a necessity of implementing some kind of adaptive approach for the covariance functions evaluation, recomputing them every day, or every week, for instance, in order to follow the changes of the error behaviour in the region. On the other hand, if the corrections are not sensitive to the covariance functions, this facilitates real time operation, as there is no need to update them very often. Moritz [1972] mentions that the results of the Least-Squares collocation are not very sensitive with respect to the covariance function, in the same way as the results of ordinary Least-Squares adjustment do not depend strongly on the weights. However, as the theory of collocation was first derived to deal with an application of physical geodesy, it was necessary to verify if that characteristic holds in the context of the Multi-Ref application;

- It is not expected that each of the correlated errors that affect GPS positioning shows the same spatial decorrelation across the region covered by the reference network. For instance, if one thinks about the characteristics of the ionosphere as

well as of the troposphere, described in Chapter 2, it is evident that those characteristics imply different influences on the double difference observations. Hence, the idea of modelling separately the correlated errors in Multi-Ref arises, as a way to improve the quality of the corrections. In particular, ionospheric errors vary with local time, geographic location, season and solar cycle. Independent modelling of the ionospheric errors should allow for statistical characterisation of such variations. This is a significant issue for the current period of solar maximum, and for the regions where the reference networks used in this thesis are located: Southeastern Brazil - under the equatorial anomaly -, and the St. Lawrence region - where enhanced ionospheric activity will be associated with geomagnetic storms over subsequent years.

In this chapter, the analyses described in the first item above are carried out. Section 4.3 covers the optimisation in terms of using different data sets to evaluate the L1 and WL covariance functions. In Chapter 5, ionospheric errors are modelled separately, using the geometric-free observable scaled to L1, as well as tropospheric and satellite orbit errors, using the ionospheric-free observable.

All analyses carried out herein are based on data collected in Southeastern Brazil and in the St. Lawrence region, Canada. Section 4.2 summarises the data used in Section 4.3 and in Chapters 5 and 6.

4.2 Data Sets Used for Refining the Covariance Functions

In order to compute the covariance functions, real data is needed to supply the procedure describe in Section 3.2.1.4. Basically, the necessary information includes the double difference misclosures computed for baselines in the reference network, according to Equation 3.11, and re-written below:

$$B\overline{\Phi} - \lambda\Delta\nabla N = \Delta\nabla\delta_c l + \Delta\nabla\delta_u l = \Delta\nabla(\delta_c l + \delta_u l) = \Delta\nabla\delta l = B\delta l \qquad (4.1)$$

This information is the same needed to apply the Multi-Ref method, with the difference that for covariance function computations not only independent baselines are considered, as the objective here is to try to model how the errors decorrelate with distance and consequently the baseline lengths must cover enough of a range to allow proper error modelling.

Analysing Equation 4.1, it is clear that geodetic coordinates and double difference integer ambiguities are necessary in order to compute the misclosure for every epoch of each baseline of interest. This task was carried out for both test networks using either the Bernese GPS Software, Version 4.0 [Rothacher and Mervart, 1996] or Version 4.2 [Hugentobler et al., 2001], depending on which version was available at the time of

processing. Details about the geodetic coordinates computation as well as the double difference integer ambiguities determination are given in Appendix B. An elevation mask of 15° and an observation rate of 15 seconds were used in all processing carried out in this thesis.

4.2.1 St. Lawrence Network

The St. Lawrence Seaway is a constricted navigation channel that requires the highest possible level of positioning accuracy. From Québec City to the Great Lakes, the riverbed is very shallow and the navigation channel requires dredging along numerous and long stretches. A campaign was carried out in August 1999 along the St. Lawrence Seaway taking advantage of the existing GPS network infra-structure in order to assess the Multi-Ref approach. From August 2 to 7 four temporary NovAtel MiLLennium™ GPS receivers were used in Grand-Mère, Deschaillons, Thetford Mines and Sorel, in addition to Canadian Coast Guard (CCG) radiobeacons equipped with Ashtech Z-12™ receivers, located in Lauzon, Trois-Rivières and St-Jean-sur-Richelieu (Figure 4.1). Short baselines, ranging from 30 to 82 km, were involved in this test, as a way to overcome possible ionospheric residual effects, considering the proximity to the solar maximum around year 2000. Data was collected at 1 Hz.

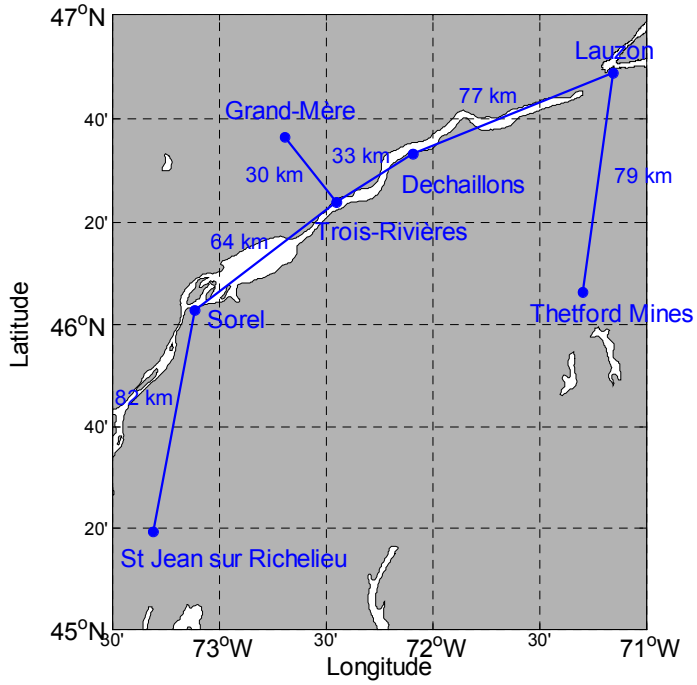

Figure 4.1: St. Lawrence's reference network

Double difference (DD) misclosures for 18 baselines connecting reference stations were calculated at each 15-second epoch for August 4, generating around 30,000 misclosure values per baseline. As these misclosures are to be used for the computation of several covariance functions, and it is necessary to verify how the errors decorrelate with distance, the 18-baseline set includes not only independent ones, but also others covering a range from 30 to 235 km. Table 4.1 shows the processed baselines and the corresponding lengths. Each station is identified with a 4-character acronym, which can be easily correlated to the station names in Figure 4.1.

Table 4.1: St. Lawrence network's baselines for which DD misclosures were computed using data collected on August 4, 1999

From	To	Length (km)
GMER	TRIV	30
DCHA	TRIV	33
GMER	DCHA	46
SORE	TRIV	64
SORE	GMER	70
DCHA	LAUZ	77
LAUZ	TMIN	79
TMIN	DCHA	79
RICH	SORE	82
TMIN	TRIV	95
SORE	DCHA	97
LAUZ	TRIV	109
GMER	LAUZ	119
RICH	TRIV	137
SORE	TMIN	140
RICH	DCHA	166
RICH	TMIN	179
RICH	LAUZ	235

Various types of misclosures were computed, depending on the observable used in the computation: C/A code (C1), L2 P code (P2), L1 phase (L1), L2 phase (L2), wide-lane (WL), ionospheric free (IF) and ionospheric signal in L1 phase (IS_{L1}). Figures 4.2 and 4.3 show these misclosures values for a short baseline (Grand-Mère to Deschaillons, 46 km) and for a long one (St. Jean sur Richelieu to Lauzon, 235 km), respectively.

Comparing these figures it can be seen that the DD L1, L2, WL, IF and IS_{L1} misclosures increase with the baseline length, as the longer the baseline, the less the ionospheric, tropospheric and satellite position errors cancel out. As Figure 4.3 shows larger errors, it can be seen that the misclosures appear like a track, which correspond to

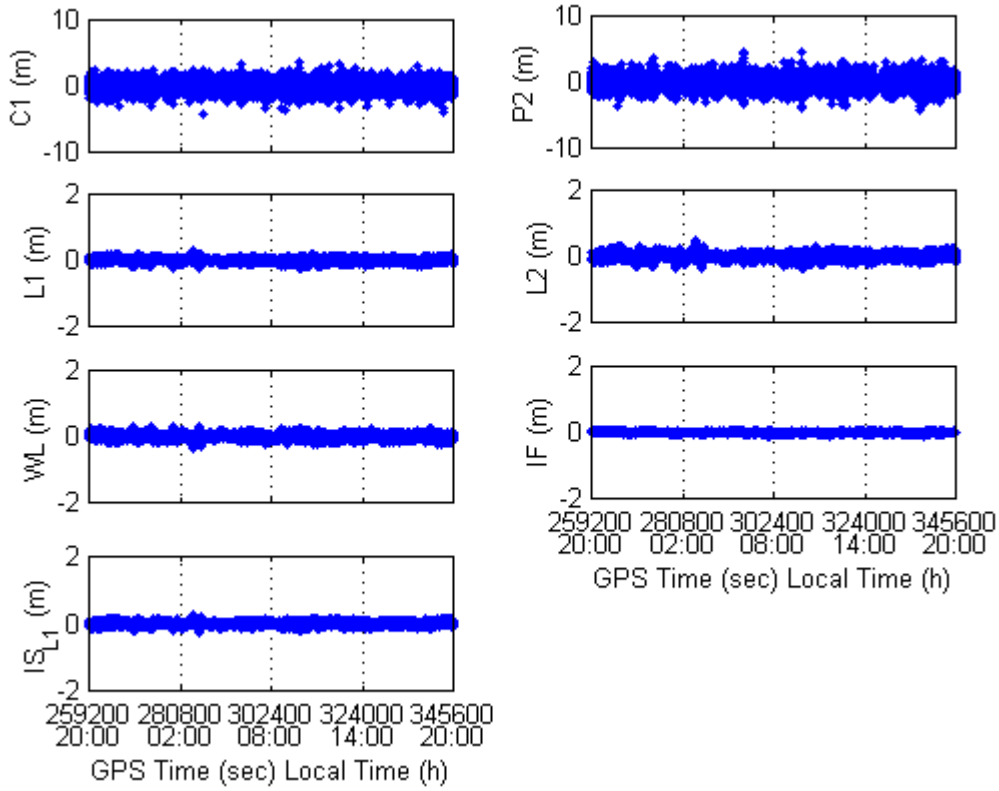

Figure 4.2: Double Difference C1, P2, L1, L2, WL, IF and IS_{L1} misclosures for a short baseline (Grand-Mère to Deschaillons, 46 km) for August 4, 1999

values from a remote satellite setting or rising at low elevations. These misclosures are larger between 20:00 and 05:00 local time (0 to 9 UT), indicating that the ionosphere was slightly enhanced during this time. Figure 4.4 shows the K_p values for this day [NGDC, 2001], confirming moderate values (between 3 and 4) for this index during the first 9 hours of the day, as opposed to very low values in the rest of the day. From Figure 4.3 it also can be seen that the ionosphere was the main source of error during the campaign, when one compares L1 and IS_{L1} graphs. Figure 4.5 shows the same Figure 4.3 IS_{L1} graph, but expressed in ppm. It can be seen that the double difference residual effect of the

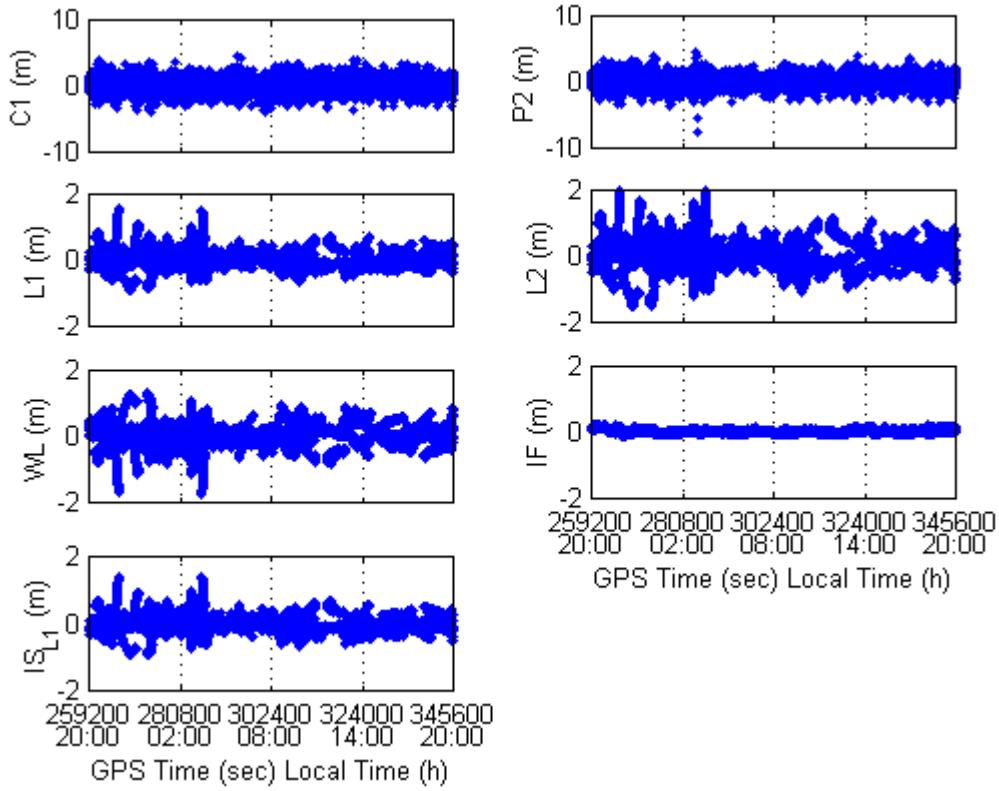

Figure 4.3: Double Difference C1, P2, L1, L2, WL, IF and IS_{L1} misclosures for a long baseline (St. Jean sur Richelieu to Lauzon, 235 km) for August 4, 1999

ionosphere reached values of up to 6 ppm. On the other hand, the first order effect of the ionosphere is eliminated from the IF misclosures, resulting in much smaller residuals.

Figure 4.6 shows the RMS values of all misclosures for the 18 baselines. The vertical axes in this figure are not the same for all types of observables, in order to properly emphasise the correlation of the DD L1, L2, WL, IF and IS_{L1} misclosures with distance. Regarding C1 and P2, it is evident that this correlation does not exist, as noise and multipath dominates this kind of observable.

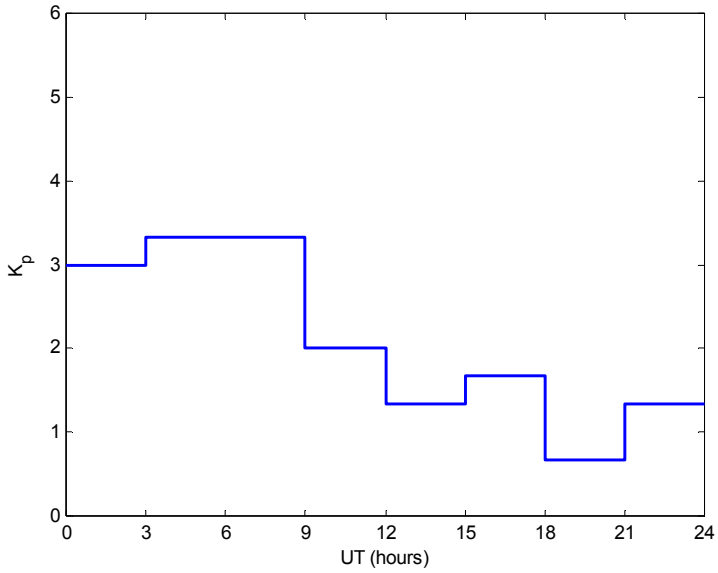

Figure 4.4: K_p values for August 4, 1999

In order to assess the quality of the improvement brought by the Multi-Ref method with respect to various tests performed in this thesis, it was necessary to have a "reference" to compare with. Hence in all networks used herein, a station from the reference network was put aside when computing corrections using Equations 3.15 and 3.16 in order to play the role of a "rover" receiver. The closest reference station out of the remaining ones was then used to form the baseline analysed in the observation, position and ambiguity domains. Each configuration of a rover receiver together with the remaining reference stations along with the baseline formed between the former and closest reference station represents a test scenario.

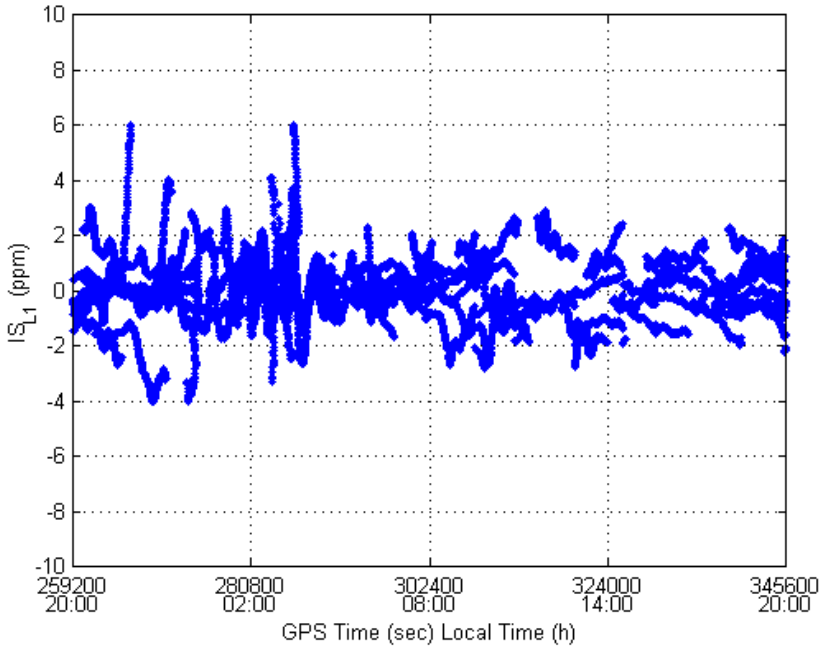

Figure 4.5: Double Difference IS_{L1} misclosures for a long baseline (St. Jean sur Richelieu to Lauzon, 235 km) for August 4, 1999

For the St. Lawrence network, two test scenarios were adopted: in the first one (Figure 4.7), Trois-Rivières was treated as the "rover" receiver and all the remaining stations acted as reference stations. Since Grand-Mère is the closest station to Trois-Rivières, the 30 km baseline defined by these two stations was processed using raw and corrected observations (actually the selection of the closest reference station is necessary only in terms of the single-reference on-the-fly – OTF - processing using raw data, since using any reference station with corrected observations gives the same results due to the encapsulation effect mentioned in Section 3.1). The second configuration (Figure 4.8), implemented in order to test the impact of the method on a longer baseline, consisted of choosing Deschaillons as the "rover" and all the remaining stations but Trois-Rivières

were used to compute network corrections. Grand-Mère was again the closest station to Deschaillons and then the 46-km baseline formed by them was processed using raw and corrected observations.

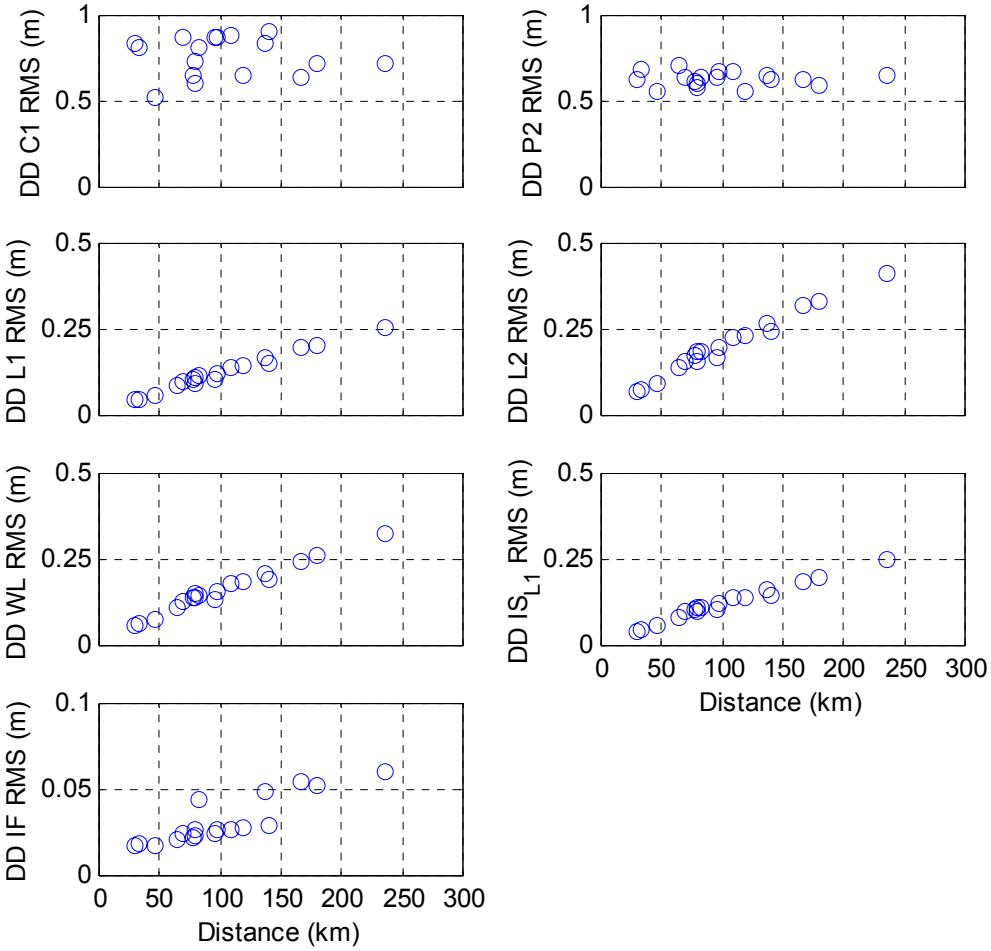

Figure 4.6: Double Difference C1, P2, L1, L2, WL, IF and IS_{L1} misclosures RMS for all baselines for August 4, 1999

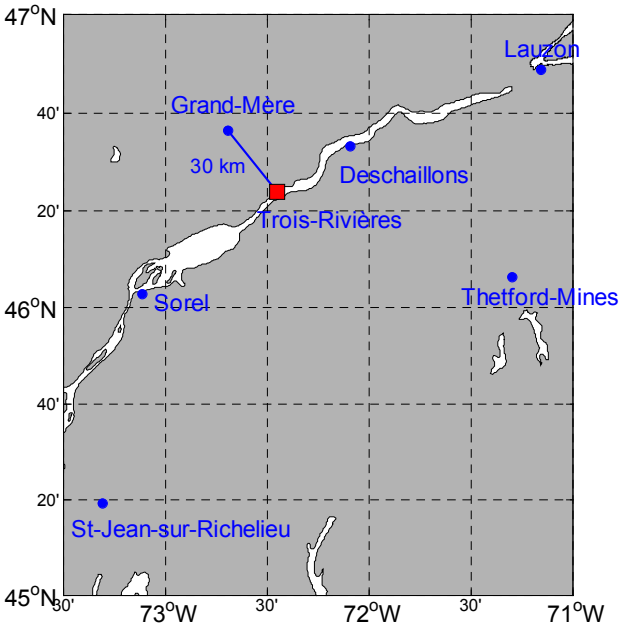

Figure 4.7: First scenario used to perform various tests using the Multi-Ref method in the St. Lawrence Network. The "rover" station is represented as a square and a line connects it to the closest reference network station

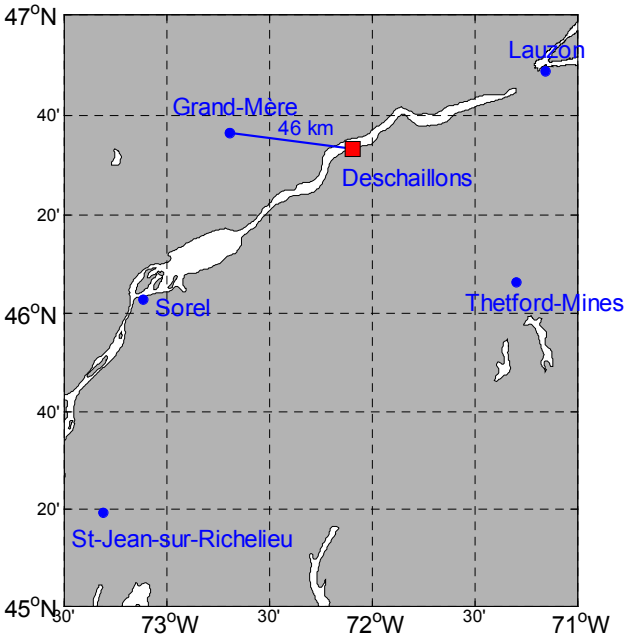

Figure 4.8: Second scenario used to perform various tests using the Multi-Ref method in the St. Lawrence Network. The "rover" station is represented as a square and a line connects it to the closest reference network station

There were two days for which all seven stations were simultaneously tracking GPS satellites (August 4 and 5), which were then selected for processing and analysis in all tests performed.

4.2.2 Brazilian Network

The Brazilian Network for Continuous Monitoring of GPS (RBMC) [Fortes et al., 1998] is an active geodetic network, established in Brazil to support 3-D post-processing positioning. Considering the dimensions of the country and the network's national coverage, the inter-station spacing ranges from 400 to more than 1000 km, supporting mainly static carrier phase applications as well as differential code positioning (Figure 4.9). All collected data contribute to the International GPS Service [IGS, 2001b] densification network in South America, and two stations (BRAZ and FORT) belong to the IGS global network. This existing infrastructure has enormous potential to contribute to the establishment of RTK services. As the baselines are too long for carrier phase RTK positioning, a 5-day densification campaign was carried out from August 11 to 15, 1999 in Southeastern Brazil, in order to assess the feasibility of the Multi-Ref method in a region very much affected by the ionosphere. Code and carrier phase data were acquired from ten temporary stations, in addition to four stations belonging to the RBMC network, namely BRAZ, PARA, UEPP and VICO. Except for the receiver located at UEPP, which

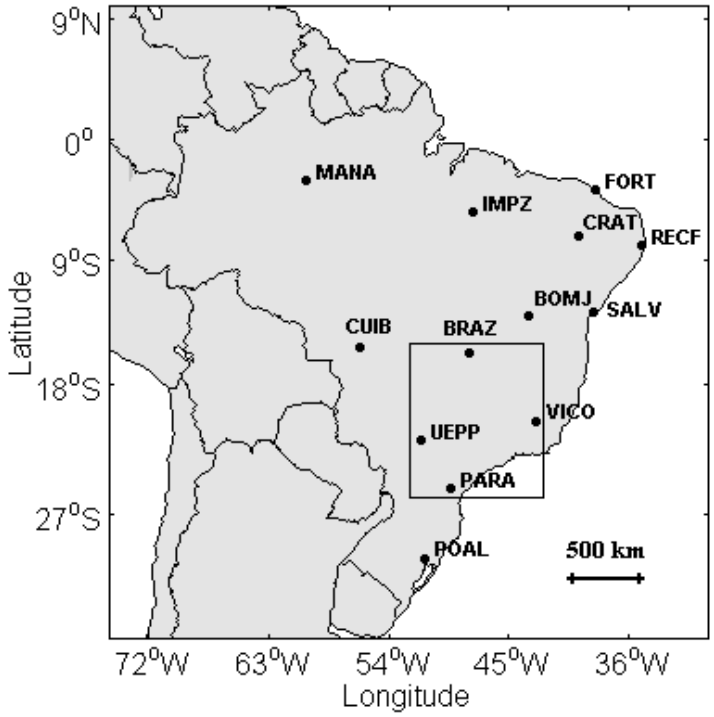

Figure 4.9: The Brazilian network for Continuous Monitoring of GPS (RBMC). The rectangle shows the region where the densification campaign was carried out in August 1999.

collected data at a 15-second data rate, all the others collected data every 5 seconds. The observed elevation mask was set to 5°. Figure 4.10 shows the stations occupied during the campaign as well as the receiver used at each one.

Due to logistical problems, some stations did not function during the whole duration of the campaign. Therefore August 11 and 13 data were selected for processing and analysis, corresponding to days when most of the stations tracked the GPS satellites during the entire 24-hour period. August 11 had an additional feature, as it was the day when a solar eclipse occurred.

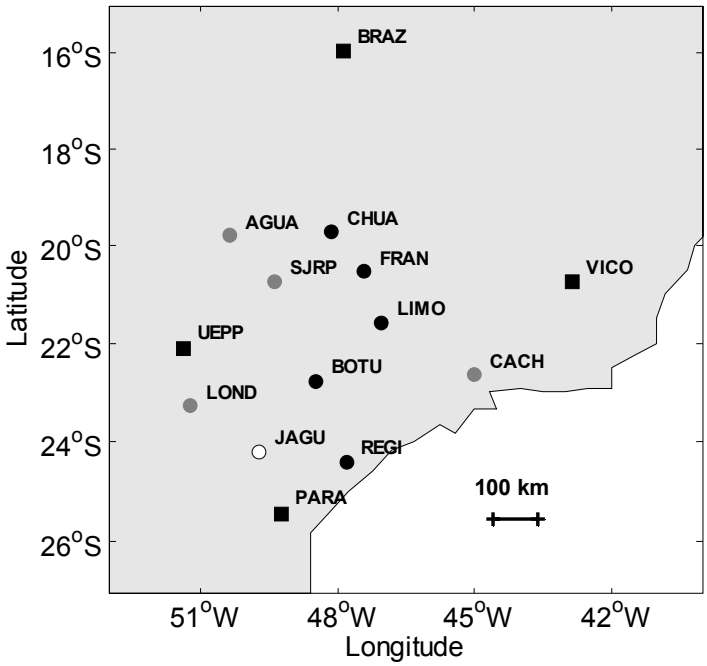

Figure 4.10: Stations occupied during the RBMC densification campaign, held from August 11 to 15, 1999. Stations represented as a square belong to the RBMC national structure. Stations in black (9) were occupied with Trimble 4000SSi receivers; in grey (4), with Ashtech Z-XII receivers; and in white (1) with Javad Legacy receiver

The solar eclipse on August 11, 1999. The Solar eclipse occurred approximately between 09:00 and 13:00 UT (06:00 to 10:00, local time in the test region). The total eclipse was visible from within a narrow corridor, which traversed the Eastern Hemisphere. The path of the Moon's umbral shadow began in the Atlantic and crossed central Europe, the Middle East, and India where it ended. A partial eclipse was seen within the much broader path of the Moon's penumbral shadow, which included north-eastern North America, all of Europe, northern Africa and the western half of Asia

[NASA/GSFC, 2001]. Although the zone of totality nor partiality did not cover any part of South America, as can be seen in Figure 4.11, it was interesting to check if there was any impact on the GPS measurements, considering that during almost four hours part of the atmosphere did not receive rays from the Sun. This is especially significant when one thinks about the effect of the solar emissions on the ionosphere.

Double difference misclosures for several baselines connecting reference stations were calculated at each 15-second epoch for August 11 and 13, generating around 30,000

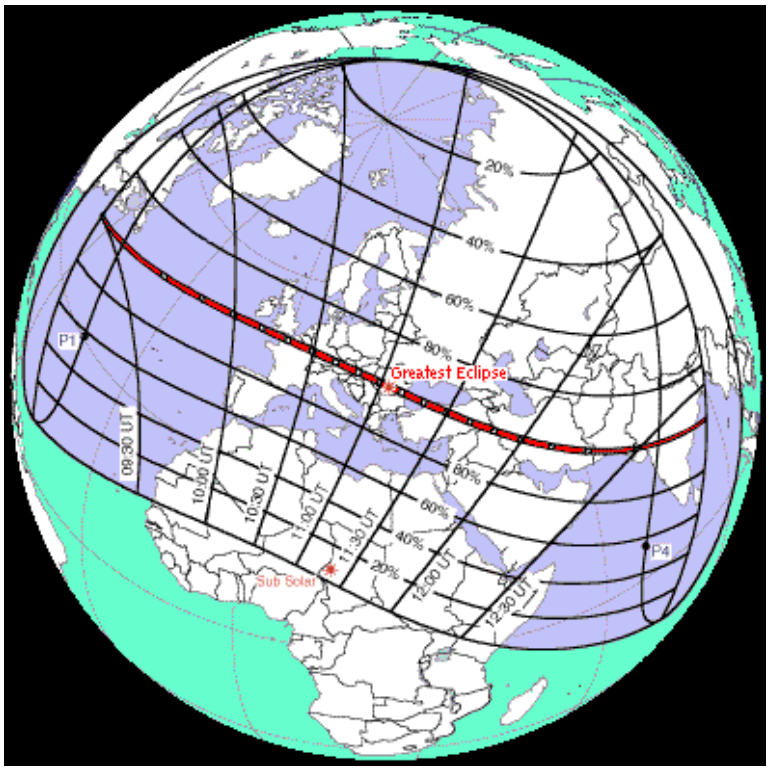

Figure 4.11: Map of the area covered by the partial eclipse (blue) and the much narrower track of the total eclipse (red) on August 11, 1999. The north/south lines show how far the centre of the eclipse zone have progressed at various times, shown in Universal Time [from Hermit, 2001]

misclosure values per baseline. Analogous to what was done using the St. Lawrence data, the baseline sets include not only independent baselines, but also others covering a range from 118 to 423 km. Figure 4.12 shows the RMS values of the double difference misclosures for each kind of observable C1, P2, L1, L2, WL, IF and IS_{L1}, for 24 baselines observed on August 11, as a function of the baseline length. It can again be seen that the code noise and multipath dominate C1 and P2, as a correlation with distance is not seen (only slightly for L2 code, as the ionospheric error is greater for this frequency). For all other observables, the correlation with distance is evident, mainly due to the ionosphere, except obviously for the ionospheric-free observable case (the graph for this observable is shown twice, one following the same scale as the others, for comparison purposes, and another one with a greater scale in the vertical axis, to show that the correlation with distance is still present).

Figure 4.13 shows the same type of graphs, for 35 baselines observed on August 13. A direct comparison of results in both figures shows a slightly larger spatial gradient of the ionospheric residual errors (DD IS_{L1}) on August 13, in addition to a higher noise (see DD IF on the right). In order to confirm that the quieter behaviour of the ionosphere on August 11 could be justified by the solar eclipse, data collected on a third day, August 14, 1999, was processed in the same way. Figure 4.14 shows the corresponding results for 30 baselines. It can be seen that the level of the ionosphere was as high as in the second day, with observations even noisier. Table 4.2 lists the baselines

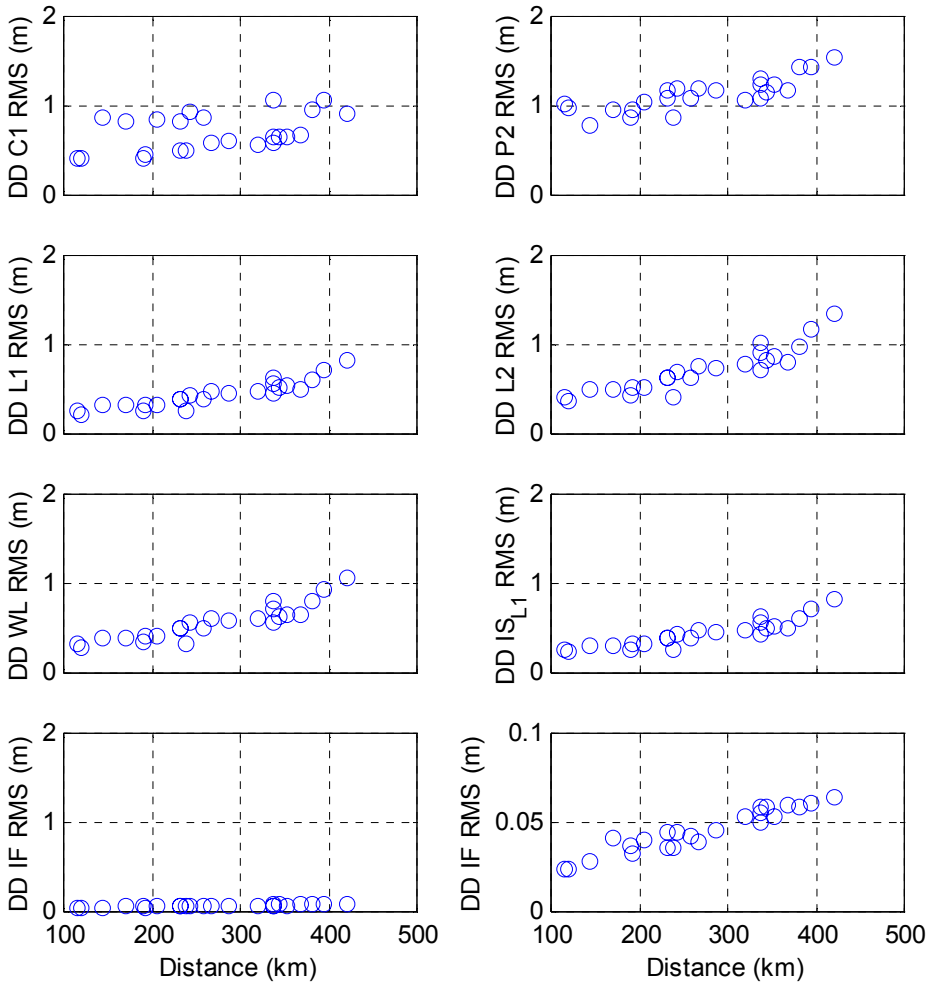

Figure 4.12: Double difference misclosure RMS values for each kind of observable, for 24 baselines observed on August 11, 1999, as a function of baseline length

processed using data collected on August 11, 13 and 14 and their corresponding lengths. Figures 4.15 and 4.16 show the DD misclosures for all observable types for AGUA to SJRP baseline (143 km), for August 11 and 13, respectively. Analysing these two figures, it can be seen again that the ionosphere is the major contributor to the final errors, when one correlates the graphs of L1 and IS_{L1}. For August 11 (Figure 4.15), the ionospheric errors peaked around 10:00 p.m. local time (of the previous day) and 2:00 p.m. local

time, almost disappearing after 3:00 a.m. in the night time. However, the night peak did not occur again at 10:00 p.m. local time of August 11. One could relate that to a probable late effect of the solar eclipse on the ionosphere. This reduction of the ionospheric activity on that day after 9:00 a.m. UT onward was also reported by Feltens and Schaer [2000], who analysed GPS data collected at high rate (1-3 sec.) using about 60 ground stations of the global IGS tracking network located along the eclipse path from the east coast of North America, over Europe to the Middle East. For August 13 (Figure 4.16), the highest ionospheric residuals occurred in the night time, around 10:00 p.m. local time (of the previous day and of that day), which often happens in regions located under the equatorial anomaly, such as this one.

Figures 4.17 and 4.18 show the ISL1 DD misclosures of Figures 4.15 and 4.16, respectively, zoomed in and expressed in ppm. It can be seen that the ionosphere reached values of up to 11 ppm on August 11, and up to 23 ppm on August 13, confirming once more that the ionosphere was quieter on August 11.

Three scenarios, whose meaning was described in Section 4.2.1, were used in this thesis when applying the various Multi-Ref method's optimisations to the Brazilian network. These three scenarios for August 13, 1999, are shown in Figure 4.19, each one corresponding to different baseline distances to the closest reference station in the network.

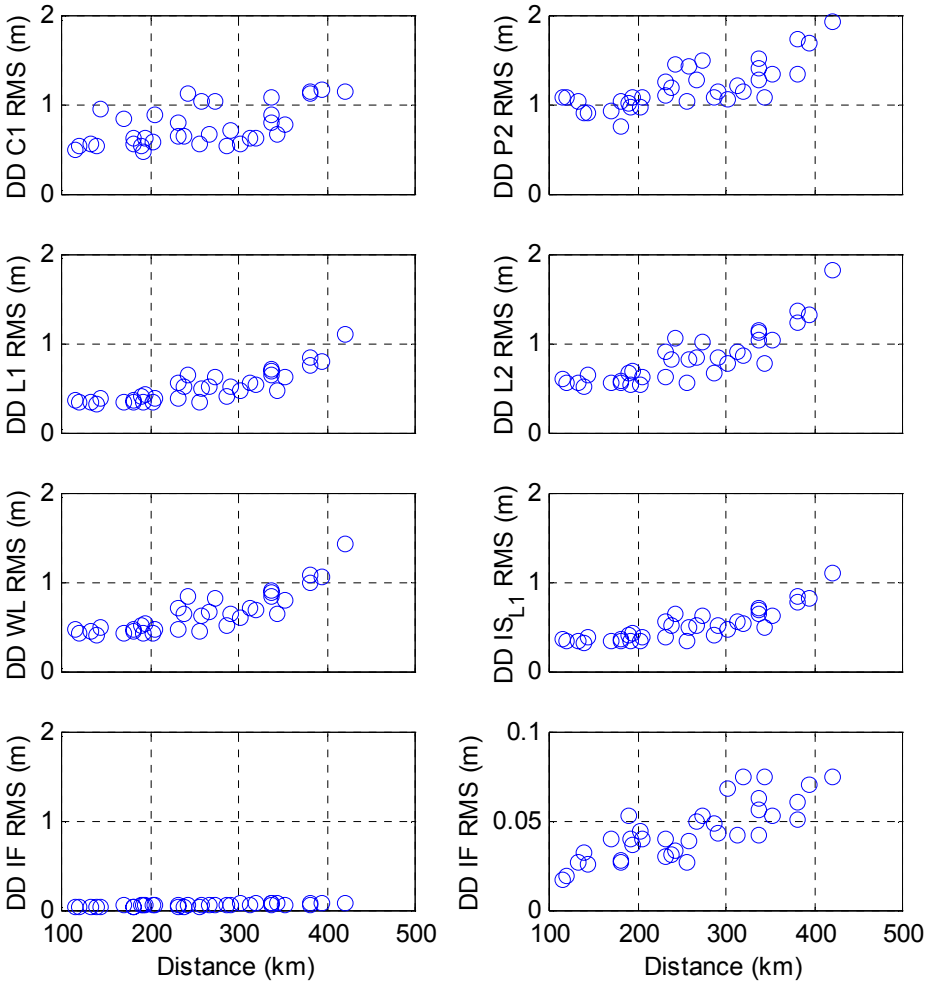

Figure 4.13: Double difference misclosure RMS values for each kind of observable, for 35 baselines observed on August 13, 1999, as a function of baseline length

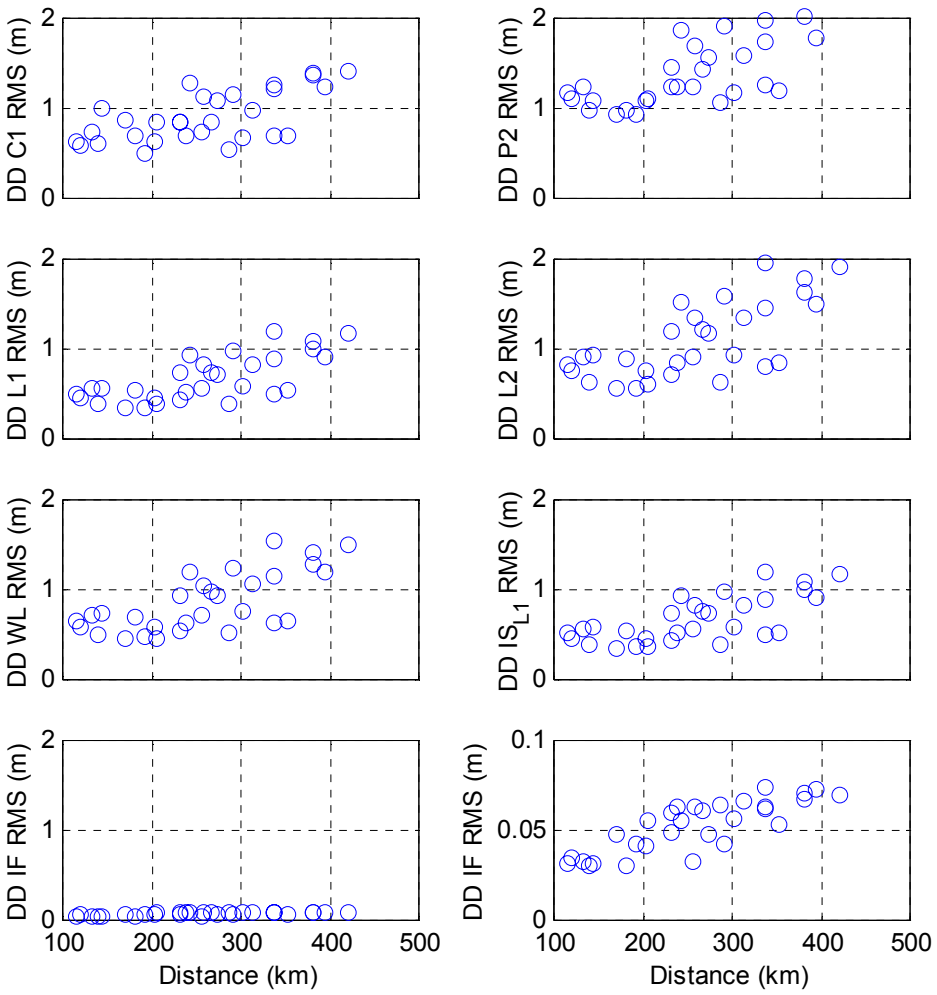

Figure 4.14: Double difference misclosure RMS values for each kind of observable, for 30 baselines observed on August 14, 1999, as a function of baseline length

Table 4.2: Brazilian network's baselines for which DD misclosures were computed using data collected on August 11, 13 and/or 14, 1999. The processing of a baseline using data collected in a specific day is indicated by the symbol "√"

From	To	Length (km)	Day of August 1999		
			11	13	14
CHUA	FRAN	118	√	√	√
FRAN	LIMO	122	√	√	√
LOND	UEPP	135		√	√
JAGU	PARA	142		√	√
AGUA	SJRP	146	√	√	√
CHUA	SJRP	173	√	√	√
JAGU	LOND	183		√	√
PARA	REGI	184		√	
BOTU	REGI	193	√	√	
BOTU	LIMO	195	√	√	√
JAGU	REGI	196		√	
BOTU	JAGU	206		√	√
FRAN	SJRP	207	√	√	√
AGUA	CHUA	234	√	√	√
CHUA	LIMO	235	√	√	√
CACH	LIMO	240	√	√	√
BOTU	SJRP	244	√	√	√
SJRP	UEPP	259		√	√
LIMO	SJRP	260	√	√	√
BOTU	FRAN	269	√	√	√
AGUA	UEPP	276		√	√
BOTU	LOND	290	√	√	√
JAGU	UEPP	293		√	√
BOTU	PARA	304		√	√
BOTU	UEPP	316		√	√
LIMO	REGI	322	√	√	
BOTU	CHUA	339	√	√	√
LOND	SJRP	339	√	√	√
CACH	FRAN	340	√	√	√
CACH	REGI	346	√	√	
BOTU	CACH	354	√	√	√
LOND	REGI	370	√		
AGUA	BOTU	383	√	√	√
JAGU	SJRP	384		√	√
AGUA	LOND	396	√	√	√
BRAZ	CHUA	423	√	√	√
Total number of processed baselines			**24**	**35**	**30**

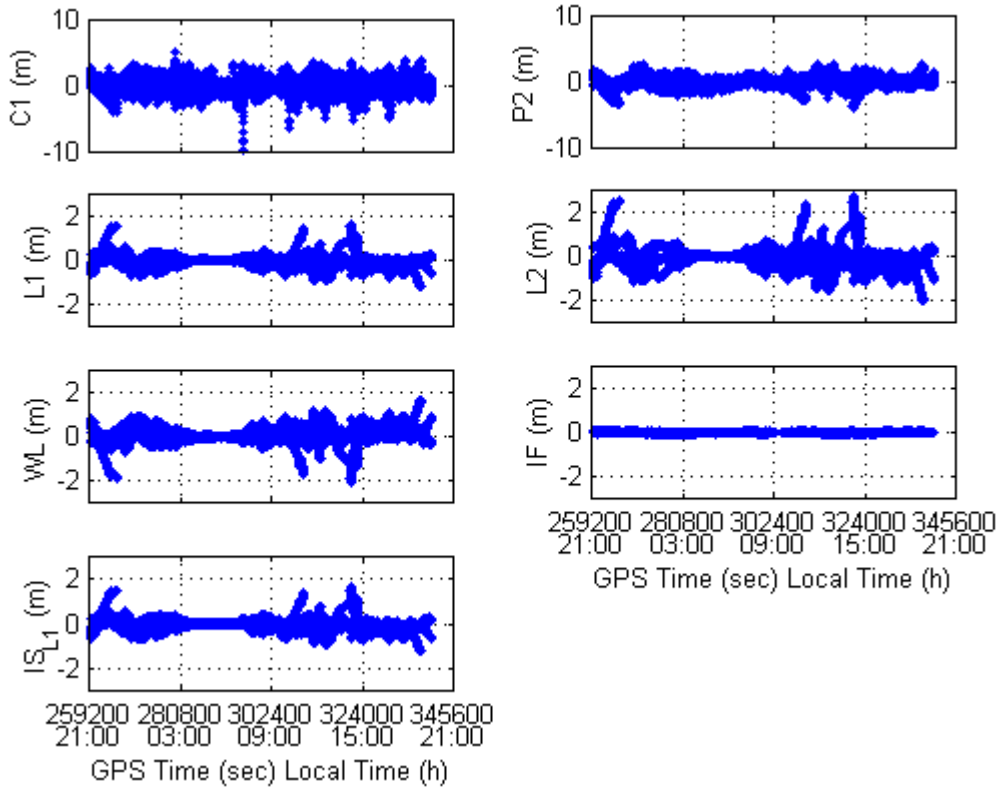

Figure 4.15: Double Difference C1, P2, L1, L2, WL, IF and IS_{L1} misclosures for AGUA to SJRP baseline (146 km) for August 11, 1999

In the first scenario, LIMO is the rover, at 122 km from FRAN, the closest reference station. In the second one, SJRP is the rover, at 146 km from AGUA. In the third one, BOTU is the rover, at 193 km from REGI. The scenarios used for August 11, 1999, are basically the same, except JAGU, PARA and UEPP were not included, since they did not collect data for 24 hours on that day.

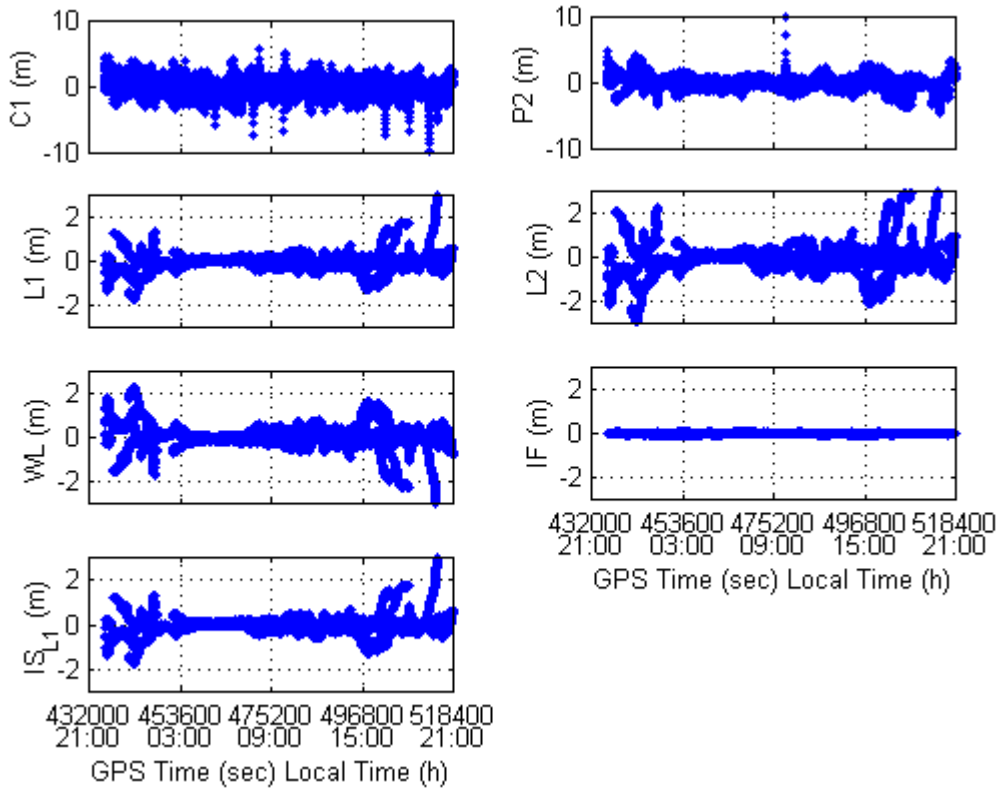

Figure 4.16: Double Difference C1, P2, L1, L2, WL, IF and IS_{L1} misclosures for AGUA to SJRP baseline (146 km) for August 13, 1999

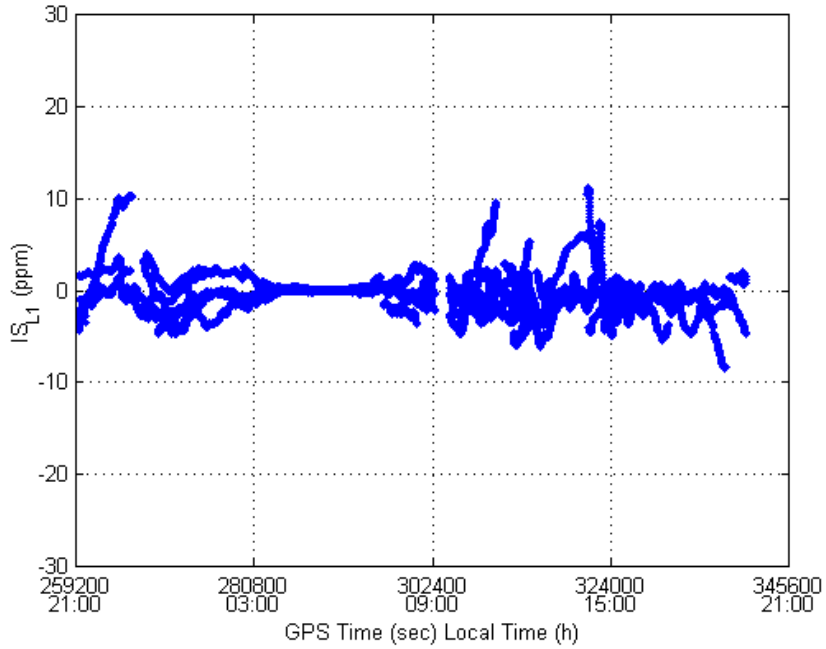

Figure 4.17: Double Difference IS_{L1} misclosures for AGUA to SJRP baseline (146 km) for August 11, 1999

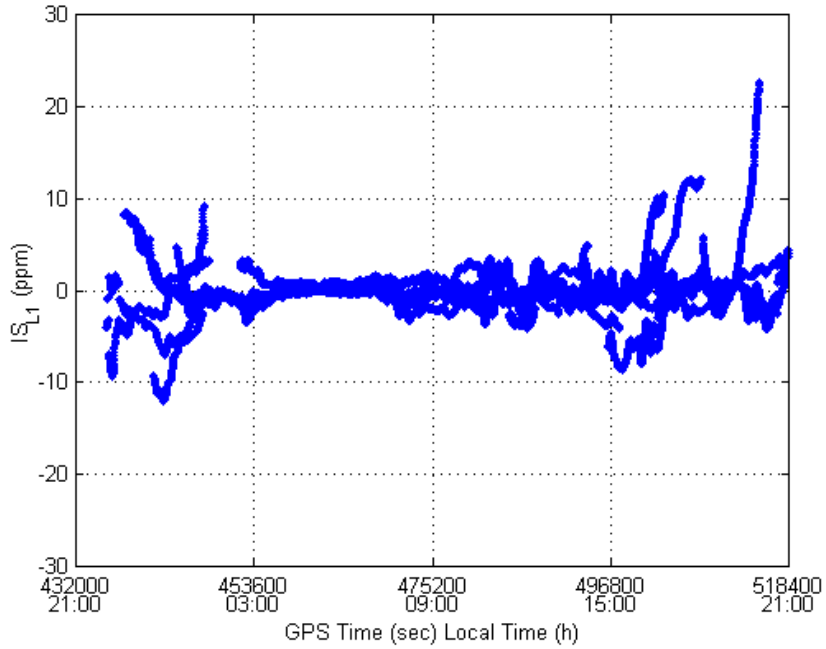

Figure 4.18: Double Difference IS_{L1} misclosures for AGUA to SJRP baseline (146 km) for August 13, 1999

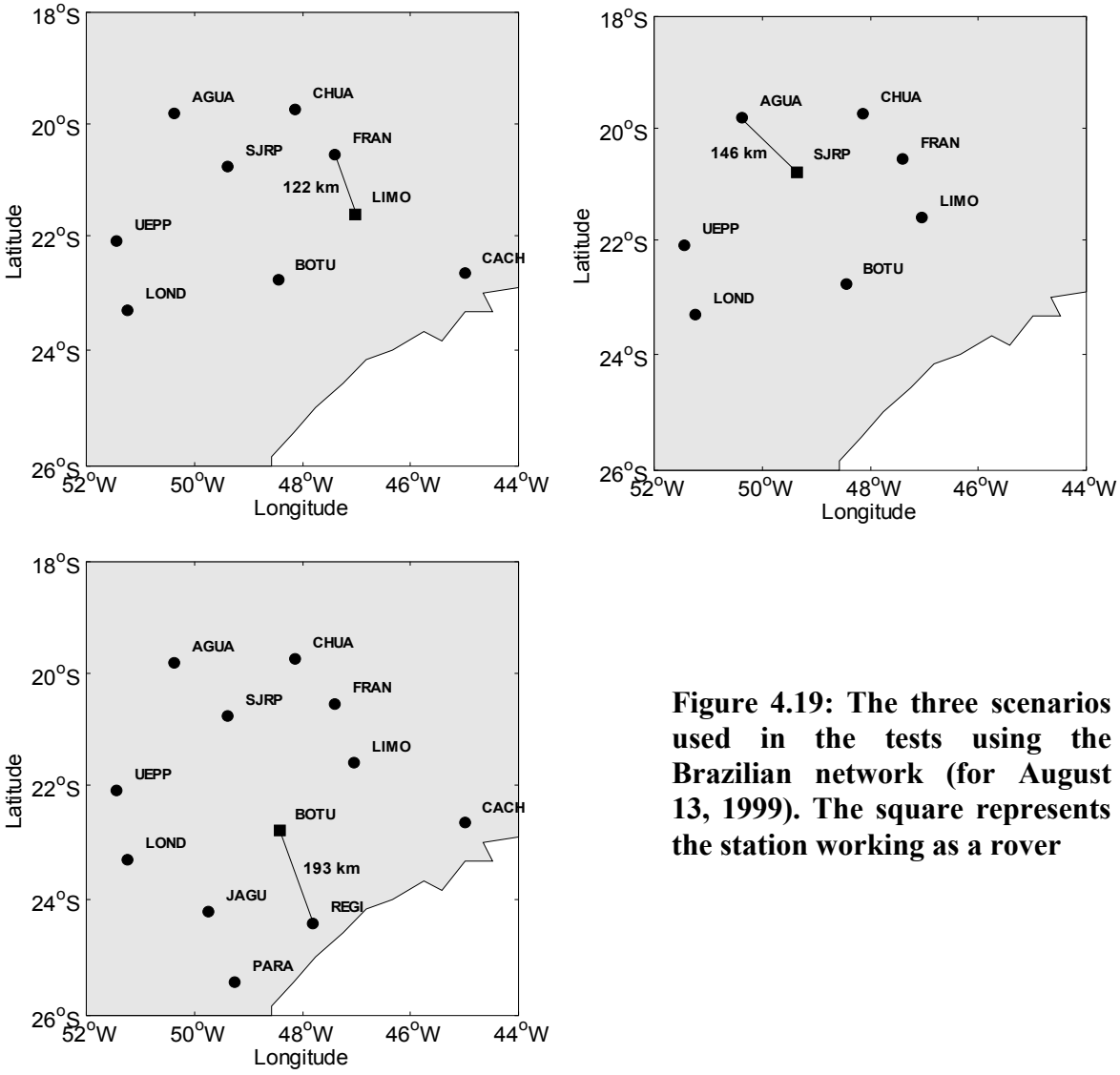

Figure 4.19: The three scenarios used in the tests using the Brazilian network (for August 13, 1999). The square represents the station working as a rover

4.3 Refinement of the Original Covariance Functions

In this section, the use of different data sets to compute the original L1 and WL covariance functions, and their impact on applying the Multi-Ref approach, is assessed. Both the St. Lawrence and the Brazilian networks were processed using covariance

functions computed with data collected on November 27, 1998 in the same St. Lawrence region, but not by exactly the same network as described in Section 4.2.1 (only Lauzon, Trois-Rivières and St-Jean-sur-Richelieu stations were common). Details about those covariance functions can be found in Fortes et al. [2000]. Table 4.3 lists the November 1998 L1 and WL covariance functions' coefficients computed according to the procedure described in Section 3.2.1.4. The $\mathbf{k_\mu}$ coefficient, used to compute the mapping function described by Equation 3.35, is greater for WL than for L1, as WL observations are noisier than L1 (even when measured in cycles) and noise increases for lower elevations. The $\mathbf{k_1}$ and $\mathbf{k_2}$ coefficients, which implicitly define how the zenith differential error variances increase with distance (Equation 3.33), are greater for L1 than for WL. Considering that the dominant error on November 27, 1998 was also due to the ionosphere [Fortes et al., 2000], the ratio between WL and L1 values given by Equation 3.33 are, as expected, at the same order of magnitude as the ratio between the ionospheric effect on WL and L1 (in cycles) squared (i.e. $0.283^2 = 0.080$ – see Raquet [1998]). The values for $\sigma^2_{u_z}$ listed in Table 4.3 were obtained by Raquet [1998], as they can only be determined using very short baselines (few metres), criterion that was not fulfilled by any baseline in the network.

Sections 4.3.1 and 4.3.2 describe, for the two test networks, respectively, the Multi-Ref results in the observation, position and ambiguity domains, obtained using the November 1998 covariance functions; the re-computation of the covariance functions

Table 4.3: k_1, k_2 and k_μ coefficients and variances of the uncorrelated errors at the zenith ($\sigma^2_{u_z}$) computed using data collected in the St. Lawrence region on November 27, 1998 [Fortes et al., 2000]

Coefficient	L1	WL
k_1 [a]	5.90069e-04	3.04498e-05
k_2 [b]	1.16116e-06	2.90428e-08
k_μ [c]	18.005	27.485
$\sigma^2_{u_z}$ [d]	4.4273e-05	3.0794e-05

a: cycles^2/km; b: cycles^2/km^2; c: unitless; d: cycles^2

using data collected in the respective campaigns carried out in the St. Lawrence and Southeastern Brazil, in August 1999; and the Multi-Ref results when the new covariance functions are applied.

4.3.1 St. Lawrence Network

4.3.1.1 Results of Applying the Multi-Ref Approach Using the November 1998 Covariance Functions

The two scenarios described in Section 4.2.1 were used to assess how much improvement the Multi-Ref approach brought in the observation, position and ambiguity domains, using data collected on August 4 and 5, 1999, and the November 1998 covariance functions.

In the observation domain, the L1 and WL double difference raw carrier phase misclosures were compared with those generated after applying the Multi-Ref corrections. For this purpose, corrections generated using Equation (3.16) were applied to the reference station observations at the Grand-Mère station (for the two scenarios), while corrections using Equation (3.15) were computed for the Trois-Rivières "rover" position, in the first scenario, and for the Deschaillons "rover" position in the second scenario. The root mean square (RMS) of the raw and Multi-Ref-corrected double difference misclosures for Grand-Mère to Trois-Rivières (30 km) and Grand-Mère to Deschaillons (46 km), as well as the improvement percentage, are shown in Table 4.4. The agreement between the two days is excellent. The improvement obtained using the Multi-Ref approach reached up to 47%. Figure 4.20 shows the double difference L1 and WL misclosures using raw and Multi-Ref-corrected observations for Grand-Mère to Deschaillons on August 5. It can be seen the improvement brought by the Multi-Ref approach in reducing the double difference misclosures.

Table 4.4: Raw and Multi-Ref-corrected double difference misclosures RMS and respective improvement for Grand-Mère to Trois-Rivières (GM-TR) and Grand-Mère to Deschaillons baselines (GM-D) for August 4 and 5, 1999

Baseline	Length (km)	L1 (m)			WL (m)		
		Raw	Corr.	Improv.	Raw	Corr.	Improv.
GM-TR	30						
August 4		0.045	0.024	47%	0.060	0.034	43%
August 5		0.041	0.023	44%	0.059	0.033	44%
GM-D	46						
August 4		0.058	0.034	41%	0.074	0.046	38%
August 5		0.056	0.034	39%	0.076	0.043	43%

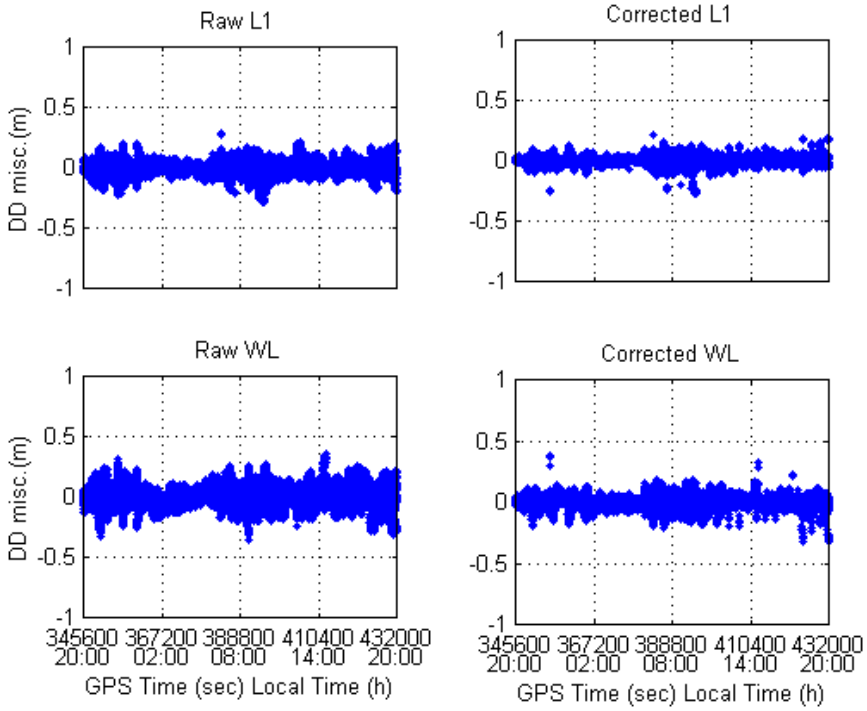

Figure 4.20: Raw and Multi-Ref-corrected L1 and WL double difference misclosures for Grand-Mère to Deschaillons baseline (46 km) for August 5, 1999

In the position domain, the known double difference integer ambiguities (resolved previously with Bernese – see Appendix B) were used, since the objective was to verify how much improvement the method brings independent of the ambiguity fixing process. Raw and Multi-Ref–corrected observations were used in FLYKIN™, an OTF software program developed at the University of Calgary [Lu et al., 1994]. In order to use the known ambiguities, the software was modified to read ambiguities from a file instead of trying to resolve them. Coordinates of Trois-Rivières (first scenario) and Deschaillons (second scenario), computed by FLYKIN™ using raw and corrected observations for August 4 and 5 were compared with the known values. The results are summarised in

Table 4.5. The Multi-Ref approach resulted in an improvement of up to 64%. The height component had the least improvement, as it is generally the least accurate in GPS positioning. In order to assess the influence of the ionosphere in the position domain, results of a third solution using the IF linear combination are also included in Table 4.5. The double difference ambiguities are not integer numbers in the IF case, but they are computed using the known L1 and L2 integer ambiguities (see Section 2.2.1). This can only be done if both the L1 and L2 integer ambiguities can be resolved, which was the case. The level of improvement obtained with the IF solution is not as high as with L1 and WL, because the raw error was already relatively small. Among all three solutions, the IF is the most accurate one, as it can be seen from Table 4.5.

Table 4.5: Raw and Multi-Ref position differences RMS and respective improvement for August 4 and 5, 1999

Coord.	L1 (m)			WL (m)			IF (m)		
Component	Raw	Corr.	Imp.	Raw	Corr.	Imp.	Raw	Corr.	Imp.
Grand-Mère → Trois-Rivières (30 km), August 4									
Latitude	0.049	0.023	53%	0.069	0.034	51%	0.019	0.015	21%
Longitude	0.031	0.015	52%	0.043	0.023	47%	0.012	0.010	17%
Height	0.076	0.049	36%	0.084	0.054	36%	0.042	0.031	26%
Grand-Mère → Trois-Rivières (30 km), August 5									
Latitude	0.052	0.019	63%	0.070	0.035	50%	0.021	0.016	24%
Longitude	0.031	0.014	55%	0.042	0.021	50%	0.012	0.009	25%
Height	0.069	0.047	32%	0.085	0.059	31%	0.051	0.037	27%
Grand-Mère → Deschaillons (46 km), August 4									
Latitude	0.048	0.032	33%	0.059	0.042	29%	0.017	0.013	24%
Longitude	0.066	0.029	56%	0.077	0.036	53%	0.013	0.011	15%
Height	0.081	0.066	19%	0.105	0.089	15%	0.039	0.027	31%
Grand-Mère → Deschaillons (46 km), August 5									
Latitude	0.045	0.035	22%	0.054	0.043	20%	0.021	0.016	24%
Longitude	0.062	0.026	58%	0.077	0.028	64%	0.015	0.013	13%
Height	0.081	0.046	43%	0.115	0.071	38%	0.043	0.029	33%

For the ambiguity domain test, the baselines in each of the two scenarios were processed using FLYKIN Suite™ [GEOsurv, 1999], using raw and Multi-Ref-corrected observations. Due to the longer wavelength of the WL, FLYKIN Suite™ was set to perform a WL ambiguity search first and then try to convert the fixed WL ambiguities to L1 in a second step. In order to generate statistics to actually measure the improvement in the ambiguity domain, it was necessary to force FLYKIN Suite™ to re-start the WL ambiguity search at fixed time intervals, to generate enough samples for each session. Thus almost every ten minutes a new ambiguity set was searched. Sometimes ten minutes was not enough to fix the corresponding ambiguities, so FLYKIN Suite™ was left running for an extra 10-minute interval. This procedure generated about 144 samples for each 24-hour session per baseline. The ambiguities computed by FLYKIN Suite™ were then compared with the ones solved by the batch Bernese solution. Table 4.6 shows the results in terms of percentage of corrected fixes, mean time to fix ambiguities and percentage of WL ambiguities reliably converted to L1. It can be seen that, using the Multi-Ref approach, improvements in all three types of comparisons were achieved. The percentage of corrected fixes, even using raw observations, was above 88%, which can be explained by the use of WL observables over relatively short baselines. The conversion to L1 ambiguities is important if one wants to derive IF solutions. Resolution of L1 integer ambiguities is however relatively difficult due to an unfavourable ratio between wavelength and differential errors. This is why the success rate was only 21% or less

when using raw observations. The use of the Multi-Ref approach improved L1 ambiguity resolution by about 10%.

Table 4.6: Ambiguity domain improvement for Grand-Mère to Trois-Rivières (GM-TR) and Grand-Mère to Deschaillons (GM-D) baselines for August 4 and 5, 1999

Baseline	Length	% of corrected fixes of WL ambiguities		Mean number of epochs (@ 15 sec.) to fix WL ambiguities		% of WL ambiguities reliably converted to L1	
		Raw	Corr.	Raw	Corr.	Raw	Corr.
GM-TR	30 km						
August 4		92%	98%	9	7	17%	28%
August 5		93%	98%	12	8	17%	28%
GM-D	46 km						
August 4		93%	94%	10	9	21%	32%
August 5		88%	91%	17	13	20%	25%

One alternative to explore in the method is to not maintain the integer nature of the ambiguities, determining them as real numbers (float ambiguities). Fortes et al. [2000] showed that when float ambiguities are determined between two stations in a reference network, the Multi-Ref final results in the position domain were degraded by an average of only 5% to 7%. When float ambiguities were also used to position the rover, an additional average degradation of 8 to 9% occurred, totalling up to a 16% degradation when using float ambiguities in the reference network and to the rover versus using integer ambiguities everywhere. However, these results were obtained after the float ambiguities converged. During the convergence time, the use of float ambiguities can be very problematic, as they tend to absorb errors.

To complete the analysis of the St. Lawrence data set using the November 1998 covariance functions, it was necessary to assess the quality of the L1 and WL corrections, based on the covariance matrices of the predicted corrections and those of the reference stations, computed using Equations 3.18 and 3.19, respectively. For the sake of simplicity, the $\mathbf{p_0}$ point, introduced in Section 3.2.1, was always made coincident with the predicted points (Trois-Rivières or Deschaillons) in the two scenarios analysed. The selection of the $\mathbf{p_0}$ point is needed in order to convert the relative nature of the observations used in Equations 3.15 and 3.16, embedded in the double difference misclosures, into single observation errors (or corrections). When the predicted point coincides with $\mathbf{p_0}$, the correlated error function between any reference station and the predicted point ($f_{z_c}(p_a, p_b, p_0)$), given by Equation 3.32, is zero for any satellite. This causes the cross-covariance matrix, $C_{\delta l_r}$, to be zero and, consequently, the predicted corrections and the covariance matrix of them are also zero. Due to this reason, only covariance matrices of the reference stations' corrections were computed here. Despite this fact, the conclusions derived here can be applied to the predicted corrections, as both are computed based on the same covariance matrix of the reference stations' observations $C_{\delta l}$.

The covariance matrix of the reference stations' corrections was computed for every epoch of data. Its diagonal elements are the variances of the corrections to the independent (carrier phase) observations collected at the reference stations. The mean of

the diagonal elements was then taken in order to have a sole number to represent the quality of the corrections for each epoch. This procedure was carried out for the two days of data, for each scenario and for L1 and WL. The results are shown on the top graphs of Figures 4.21 to 4.24, respectively for the first and second scenarios, August 4; and first and second scenarios, August 5. As it is known that the covariance matrix of the adjusted quantities normally reflects the internal precision of the observations, the mentioned

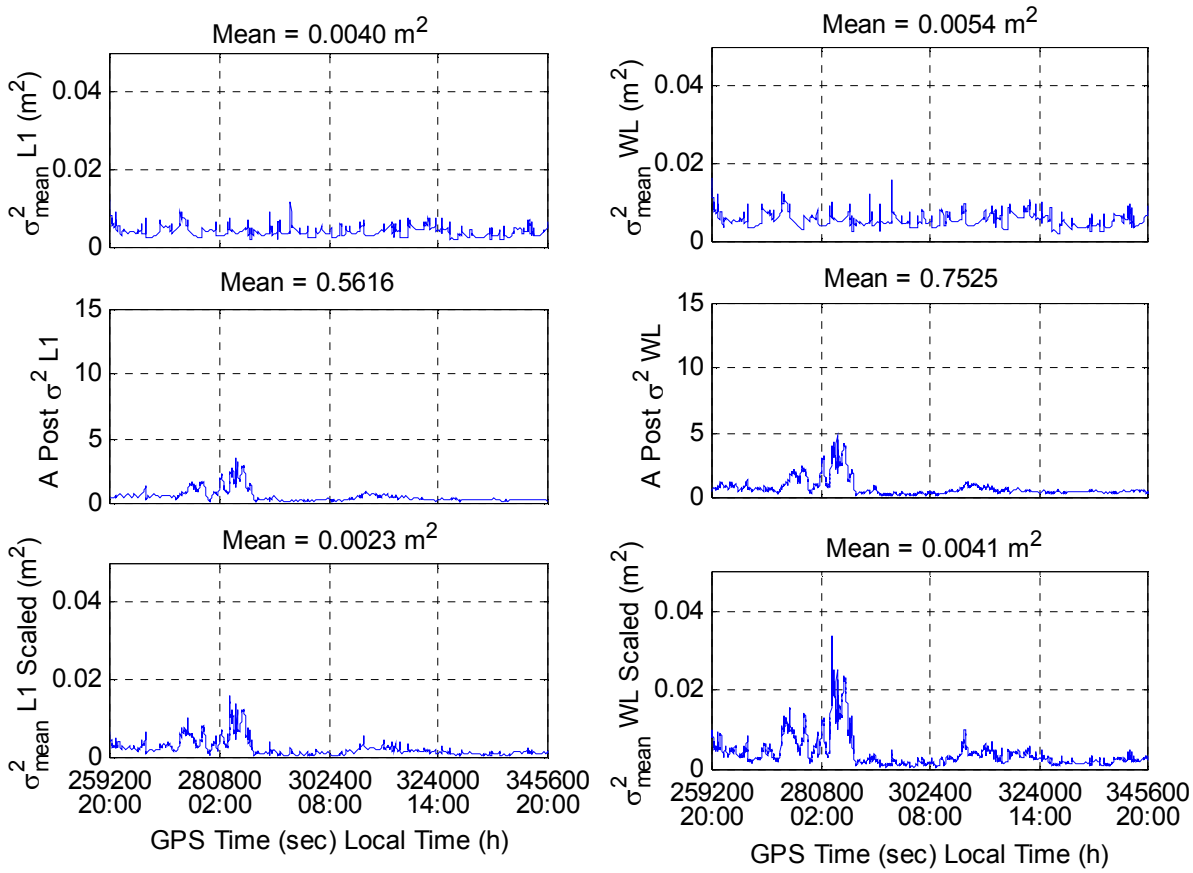

Figure 4.21: Quality estimation of the reference station's corrections for L1 and WL for the first scenario (Trois-Rivières as rover) for August 4, 1999: mean variance (top graphs), *a posteriori* variance of unit weight (graphs in the middle), and mean variance scaled by the *a posteriori* variance (bottom graphs)

figures also include the *a posteriori* variance of unit weight (graphs in the middle), computed for each epoch of the four cases using Equation 3.21. The *a posteriori* variances of unit weight were then used to scale the variances in order to generate an estimate of the external precision. The mean of the scaled variances is shown in the graphs at the bottom of Figures 4.21 to 4.24. On the top of each graph, the mean of each quantity over time is also listed.

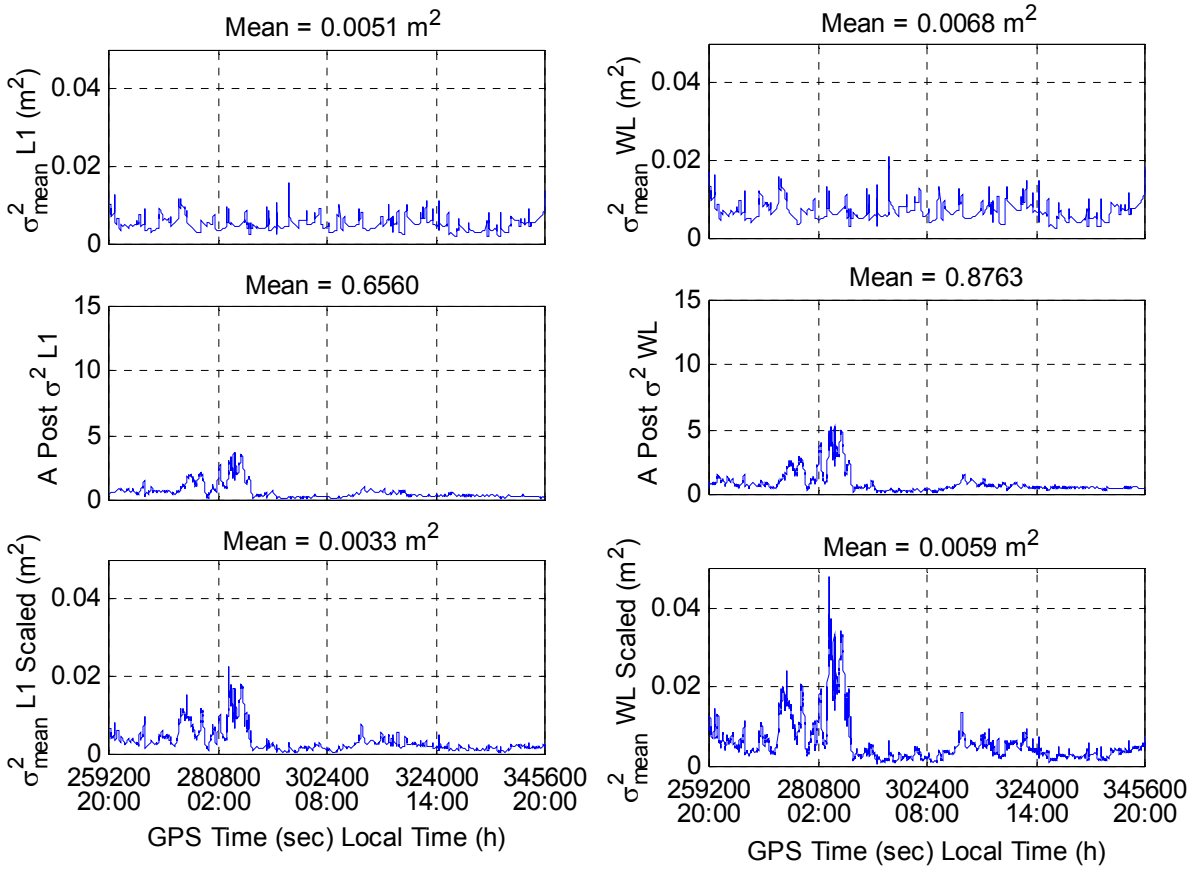

Figure 4.22: Quality estimation of the reference station's corrections for L1 and WL for the second scenario (Deschaillons as rover) for August 4, 1999: mean variance (top graphs), *a posteriori* variance of unit weight (graphs in the middle), and mean variance scaled by the *a posteriori* variance (bottom graphs)

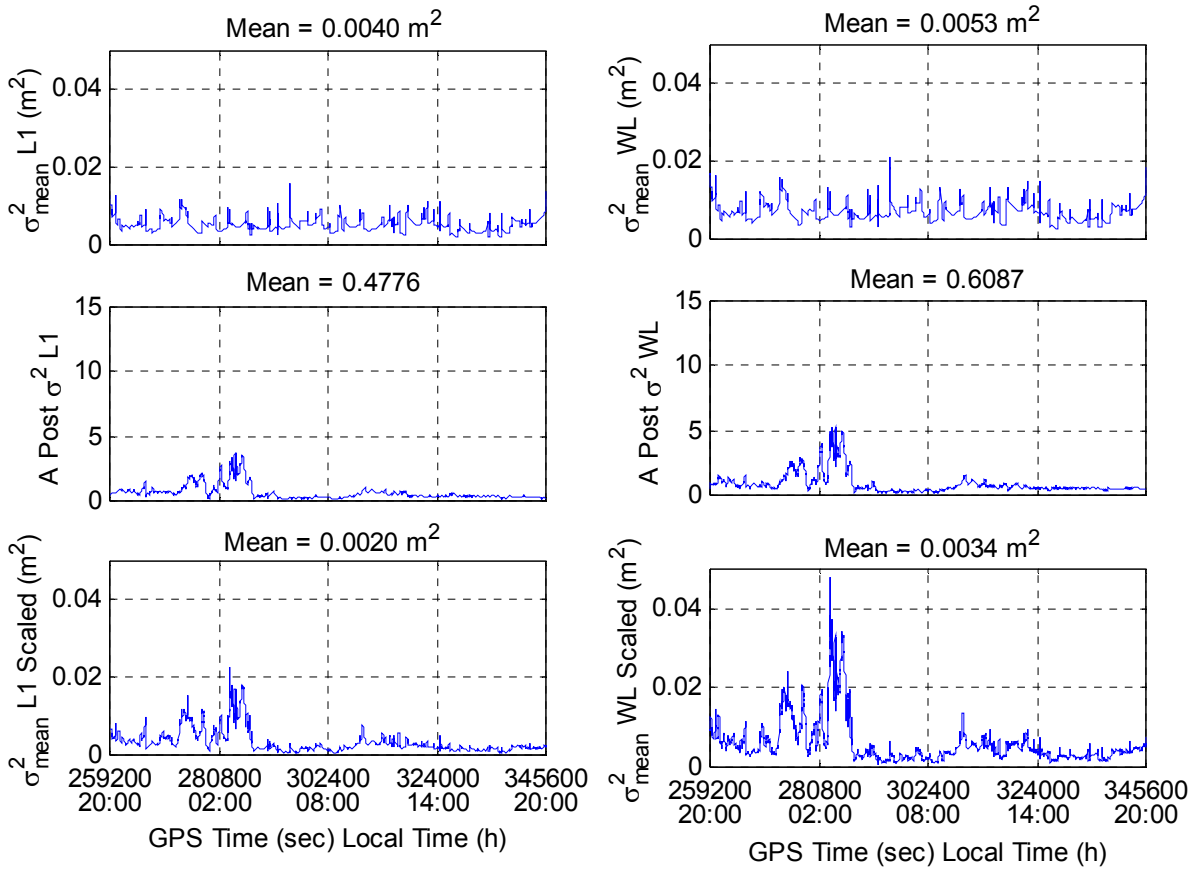

Figure 4.23: Quality estimation of the reference station's corrections for L1 and WL for the first scenario (Trois-Rivières as rover) for August 5, 1999: mean variance (top graphs), *a posteriori* variance of unit weight (graphs in the middle), and mean variance scaled by the *a posteriori* variance (bottom graphs)

Analysing these figures, it can be seen that the values for WL variances are generally greater than the ones for L1, as expected, considering that WL observables are noisier and more affected by the ionosphere than L1. The top two graphics correspond basically to the propagation of the observation covariance matrix (computed using the covariance functions) into the corrections. Its time variation can be justified by the changes in the satellite constellation and geometry.

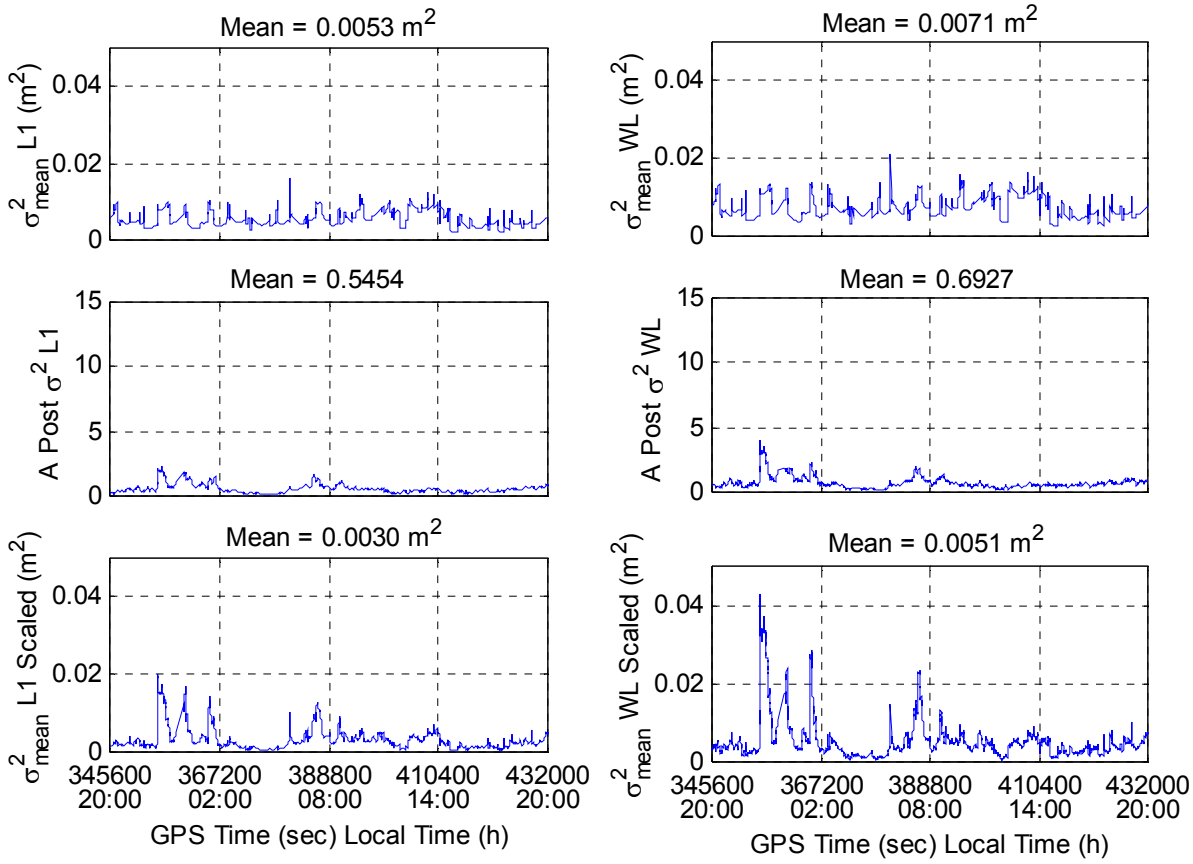

Figure 4.24: Quality estimation of the reference station's corrections for L1 and WL for the second scenario (Deschaillons as rover) for August 5, 1999: mean variance (top graphs), *a posteriori* variance of unit weight (graphs in the middle), and mean variance scaled by the *a posteriori* variance (bottom graphs)

An important aspect is that the values of the covariance matrix of the corrections are somehow arbitrary, as they strongly depend on the selection of $\mathbf{p_0}$. But if a location close to the centre of the network is chosen for $\mathbf{p_0}$, minimising the distances involved in the computation of the covariance matrix of the observations, reasonable values are computed from an absolute point of view. Due to this reason, the variances for the second

scenario are always slightly bigger than the ones for the first scenario, as the second scenario implies in a sparser network and, as such, with longer distances from any reference station to $\mathbf{p_0}$ (which coincides with Deschaillons station, as mentioned before).

An interesting feature can be observed on the *a posteriori* variance of unit weight graphs: its value increases after 2:00 a.m. local time on Figures 4.21 and 4.22. The expected value for the ratio between the *a posteriori* and the *a priori* variances of unit weight is 1 [Leick, 1995]. Considering that the *a priori* variance of unit weight was implicitly chosen as equal to 1 in the tests (as the observation weight matrix was made equal to the inverse of the covariance matrix of the observations), the expected value for the *a posteriori* variance of unit weight is also 1. If it is greater than 1, this means that the observation variances were optimistic. If it is smaller than 1, then the variances were pessimistic. Therefore the greater values of *a posteriori* variance after 2:00 a.m. local time indicates that the observation variances were smaller than they should be during that time, when compared with the actual residuals. This happened for both scenarios on August 4 and it is consistent with the double difference misclosures shown in Figure 4.3. So one can conclude that the active ionosphere during this time (as stated before) was detected by the *a posteriori* variance values. This behaviour is propagated into the scaled mean variance values, shown in the bottom graphs. This kind of *a posteriori* variance values variation is also observed on both scenarios on August 5, but not as bad, indicating that the ionosphere was slightly less active on this day.

As mentioned before, the results generated in this section were computed using covariance functions derived using data collected in the St. Lawrence region on November 1998. Fortes et al. [2000] reported that during that time the double difference effects of the ionosphere reached values of up to 10 ppm, thus a higher level than the 6 ppm found in August 1999. This fact can be seen if one analyses the *a posteriori* variance of unit weight in all cases reported in Figures 4.21 to 4.24. The mean values over time were systematically less than 1, indicating that the covariance functions (computed using November 1998 data) gave observation variances greater than the actual residual values. More about the interpretation of the estimated accuracy of the corrections is mentioned later in this chapter.

4.3.1.2 Re-computation of the Original Covariance Functions Using Data Collected in August 4, 1999

Using L1 and WL misclosures for August 4, 1999, described in Section 4.2.1, and the procedure described in Section 3.2.1.4, the covariance functions given by Equations 3.33, 3.34 and 3.35 were re-evaluated. Table 4.7 includes de $\mathbf{k_1}$, $\mathbf{k_2}$ and $\mathbf{k_\mu}$ coefficients as well the variance of the uncorrelated errors at the zenith that were obtained. As happened with the November, 1998 data set, the variances of the uncorrelated errors at the zenith included in this table correspond to values obtained from Raquet [1998] and constrained

during the Least-Squares adjustment process. A comparison of these coefficients with the ones computed using the November, 1998 data set (Table 4.3) is done graphically in Figure 4.29 later in this section.

Table 4.7: k_1, k_2 and k_μ coefficients and variances of the uncorrelated errors at the zenith ($\sigma^2_{u_z}$) computed using data collected in St. Lawrence on August 4, 1999

Coefficient	L1	WL
k_1 [a]	1.71331e-04	1.37359e-05
k_2 [b]	3.98211e-06	2.96245e-07
k_μ [c]	12.277	13.493
$\sigma^2_{u_z}$ [d]	4.4273e-05	3.0794e-05

a: cycles^2/km; b: cycles^2/km^2; c: unitless; d: cycles^2

Figures 4.25 and 4.26 show the statistics of the $\mathbf{k_\mu}$ computation for the L1 and WL observables, respectively. The circles are mean values of $\boldsymbol{\mu(\varepsilon)}$ computed for each bin of each of the 18 baselines using Equation 3.40; the dashed lines show the 1-σ envelope around the mean values of $\boldsymbol{\mu(\varepsilon)}$ considering the 18 baselines; and the continuous line shows the fit of Equation 3.35 to the data. In general, the curves show a good fit to the data.

Figures 4.27 and 4.28 show plots of the function fit for the determination of the $\mathbf{k_1}$ and $\mathbf{k_2}$ coefficients for L1 and WL, respectively. Each small circle represents the actual "observation" used in the fit, formed by the variances of the double difference

misclosures reduced to the zenith for each baseline at the corresponding baseline length. It can be seen that the quality of the fit was very good.

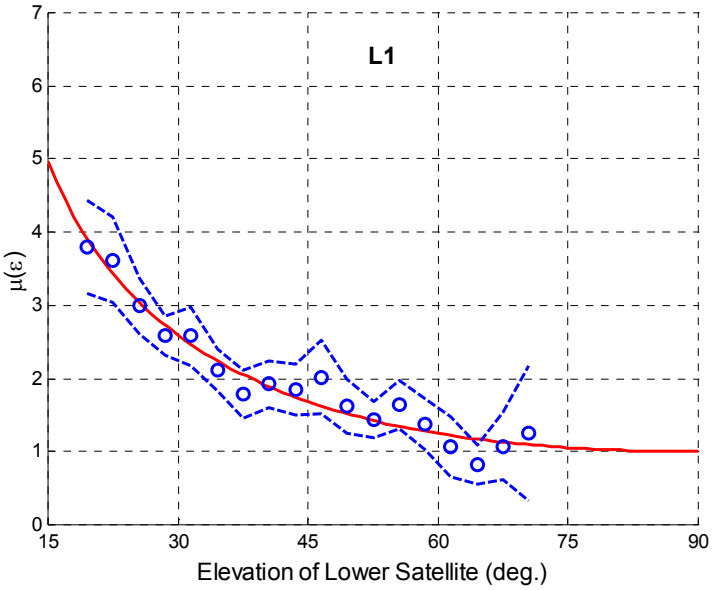

Figure 4.25: Statistics of the k_μ computation for the L1 observable

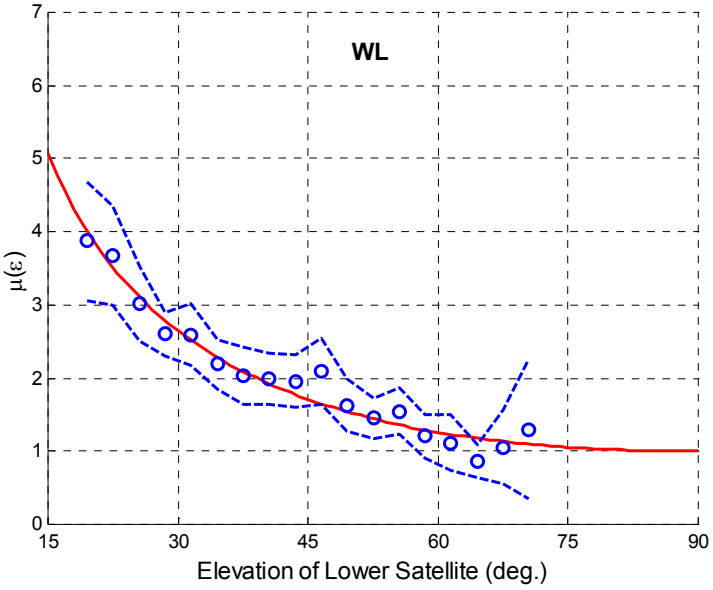

Figure 4.26: Statistics of the k_μ computation for the WL observable

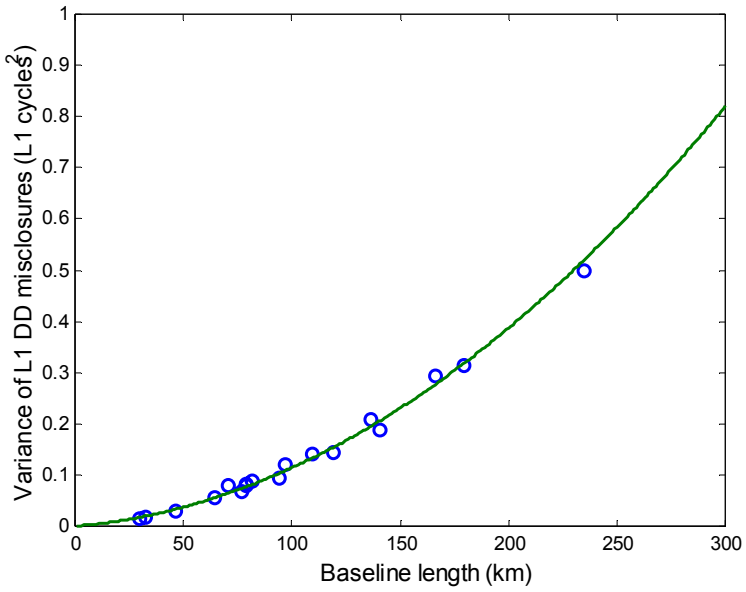

Figure 4.27: Function fit after determining k_1 and k_2 coefficients for the L1 observable

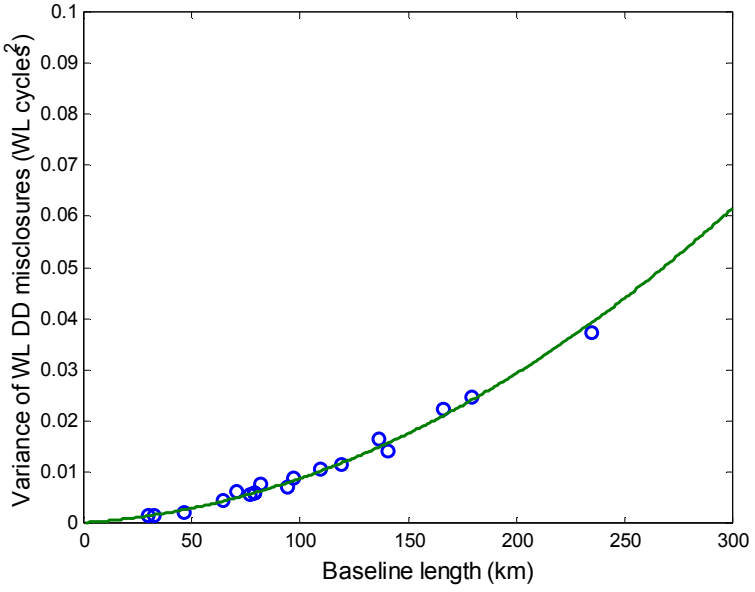

Figure 4.28: Function fit after determining k_1 and k_2 coefficients for the WL observable

The corresponding covariance and mapping functions given by Equations 3.33 and 3.35, respectively, are given in Figure 4.29. For the sake of comparison, the functions obtained using data collected in November, 1998, are also shown in the figure. For November, 1998, the zenith correlated errors seem to be smaller, but this could have been

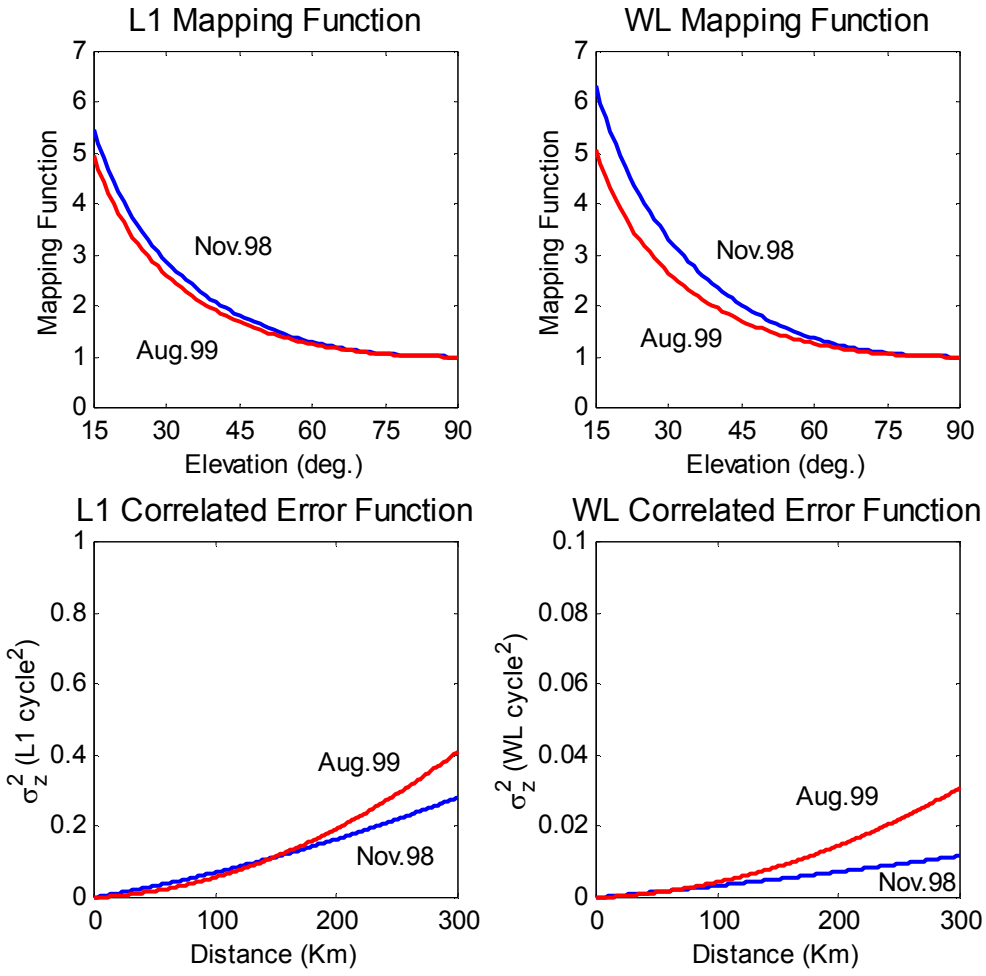

Figure 4.29: Mapping functions (top figures) and correlated error functions (bottom figures) for L1 and WL using November 27, 1998 (blue), and August 4, 1999 (red) data from the St. Lawrence region

compensated by a steeper mapping function, in such a way that the final covariance matrix elements of the observations were in general greater than the ones computed using the August, 1999 covariance functions. It can be seen again that the ratio between the correlated error function values for WL and L1 are at the same order of magnitude as the ratio between the ionospheric effect on WL and L1 (in cycles) squared (i.e. 0.080). The different shapes for the functions validate testing their use to assess the impact on the improvement brought by the Multi-Ref method.

4.3.1.3 Improvement Brought by the Multi-Ref Method Using the Original Covariance Functions Computed With Data Collected on August 4, 1999

Using the covariance functions computed in the last section (whose coefficients were listed in Table 4.7), the improvement brought by the Multi-Ref method was computed in the observation domain for the two scenarios described previously. The results are included in Table 4.8. Figure 4.30 shows the raw and corrected double difference L1 and WL misclosures for the Grand-Mère to Deschaillons baseline (46 km) for August 5, 1999.

Comparing values in Table 4.8 with the ones in Table 4.4, it can be seen that they are not significantly different. This means that in this case the use of covariance functions computed using data of the campaign improved the results at only the millimetre level.

Due to the similarity of the results, the tests in the position and ambiguity domains were not repeated using the August 4, 1999, original covariance functions.

Table 4.8: Raw and Multi-Ref-corrected double difference misclosures RMS and respective improvement for Grand-Mère to Trois-Rivières (GM-TR) and Grand-Mère to Deschaillons baselines (GM-D) for August 4 and 5, 1999, using August 4, 1999, covariance functions

Baseline	Length (km)	L1 (m)			WL (m)		
		Raw	Corr.	Improv.	Raw	Corr.	Improv.
GM-TR	30						
August 4		0.045	0.024	47%	0.060	0.034	43%
August 5		0.041	0.023	44%	0.059	0.032	46%
GM-D	46						
August 4		0.058	0.033	43%	0.074	0.045	39%
August 5		0.056	0.033	41%	0.076	0.042	45%

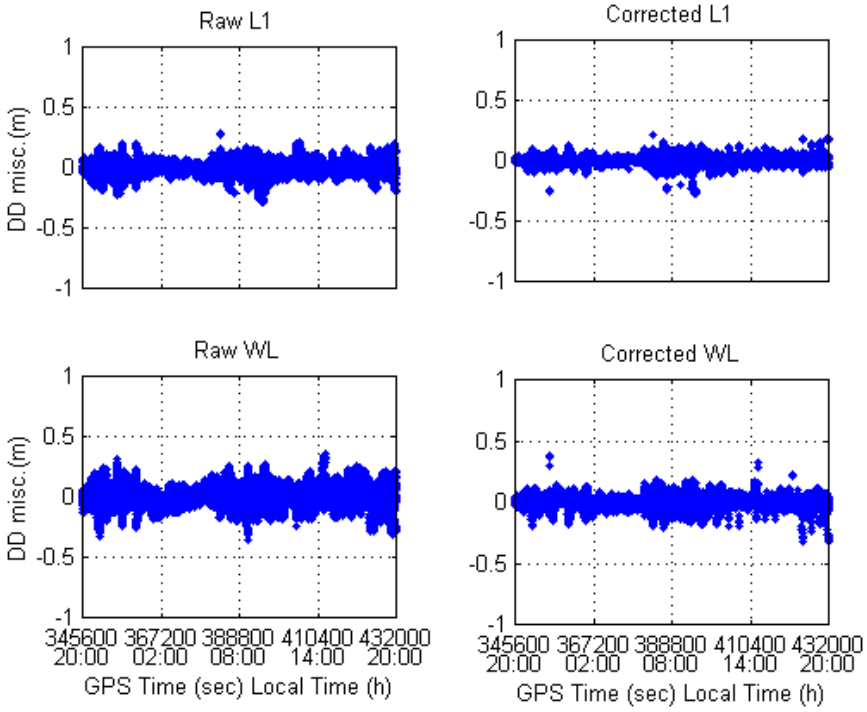

Figure 4.30: Raw and Multi-Ref-corrected L1 and WL double difference misclosures for Grand-Mère to Deschaillons baseline (46 km) for August 5, 1999, using August 4, 1999, original covariance functions

Comparing Figures 4.30 with 4.20 (both refer to the same baseline), one can see that they look basically the same, except for the position of the isolated dots (in the corrected misclosures graphs), which are in general closer to the y-axis origin in Figure 4.30. These dots correspond to corrected double difference misclosure values for epochs when the remote satellite was setting or rising, caused by the fact that the satellite was observed by only a few reference stations. These occurrences are addressed in Chapter 6. Figure 4.31 shows the corrected misclosures of Figures 4.20 and 4.30 for the interval 22:00-23:00 local time in order to emphasise that, using more appropriate covariance functions, these isolated cases were improved. However, the number of occurrences of these cases are too small (compared with the total number of misclosures - around 30,000) in order to have an impact on the overall corrected misclosure computed RMS.

To complete the analysis of the impact of using the August 4, 1999, original covariance functions, it was necessary to compute the covariance matrix of the reference stations' corrections and the *a posteriori* variance of unit weight, similarly to what was done for the November, 1998 covariance functions. Figures 4.32 to 4.35 show the mean variance for every epoch for both scenarios for both days (on the top). These figures also show the *a posteriori* variance (in the middle) and the corresponding scaled mean variances at the bottom. On the top of each graph, the mean of each quantity over time is

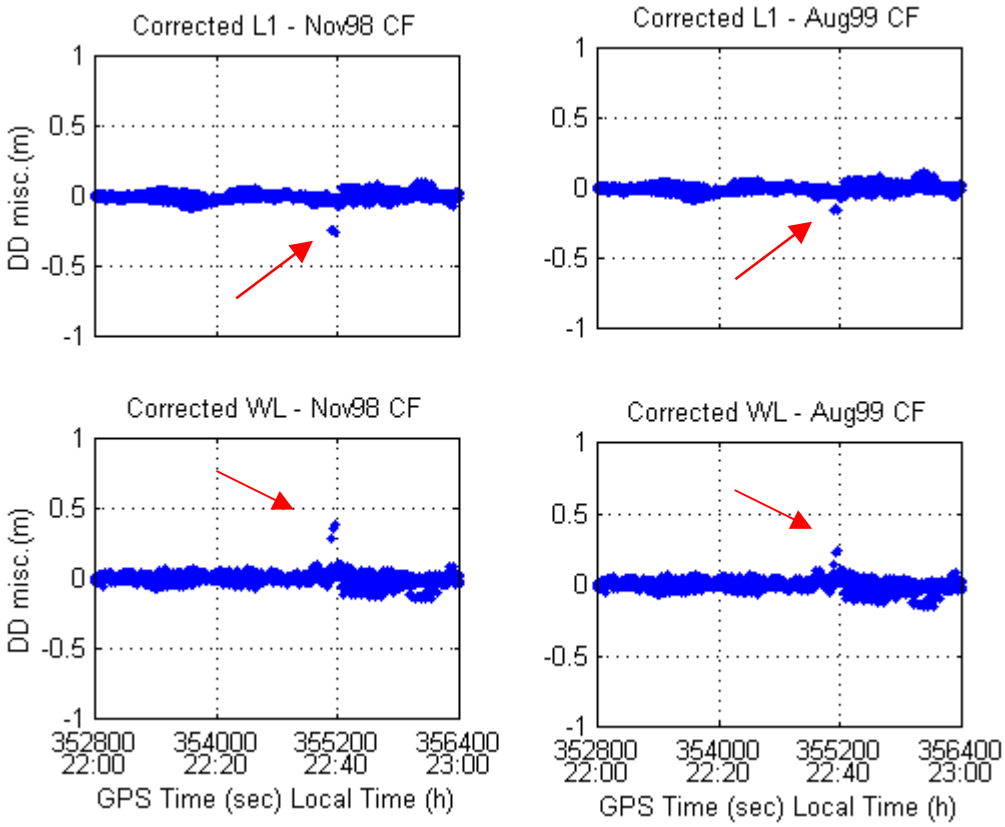

Figure 4.31: Multi-Ref-corrected L1 and WL double difference misclosures for Grand-Mère to Deschaillons baseline (46 km) for August 5, 1999, using November, 1998 (on the left) and August 4, 1999 (on the right) original covariance functions. The arrows point towards the isolated dots improved with the August, 1999, covariance functions

also listed. These figures are analogous to Figures 4.21 to 4.24, respectively. Comparing the corresponding ones (i.e. 4.21 and 4.32; 4.22 and 4.33; 4.23 and 4.34; 4.24 and 4.35), one can see that the mean variance values (on the top) are smaller when the August 4, 1999 covariance functions are used. This is because the relative errors during the August 1999 campaign were smaller than the ones of November 1998, as seen in Figure 4.29 (the variance of the corrections are based on the covariance matrix of the observations - $C_{\delta l}$ -, which were computed using the August 4, 1999 covariance functions). The comparison

of the *a posteriori* variances of unit weight (in the middle) shows that the corresponding values are closer to 1 for August 1999, as expected. This means that the weighting scheme used for August 1999 is better than the one for November 1998, as it should be, considering that it was based on covariance functions computed using the data from the very campaign. The values larger than 1 are justified by the influence, in the final mean, of the spikes present in the figures. As explained before, these spikes are due to an increased ionospheric activity during those periods of time.

Table 4.9 summarises the mean of each quantity over time in Figures 4.21 to 4.24 and 4.32 to 4.35. Analysing this table, it can be seen that, depending on the covariance functions used, the mean variances vary considerably (in some cases, the values using the August 4, 1999 covariance functions are less than 50% of the values obtained using the November 98 ones). These results agree with Moritz [1976], who stated that changes to the correction variances occur when different covariance functions are used, despite the fact that this influence may not affect the corrections themselves. However, scaling the variances by the *a posteriori* variance of the unit weight compensates those differences, generating very close estimated correction variances in all cases. This was somehow expected, assuming that the *a posteriori* variance converts the precision of the corrections (internal), based on the covariance functions, to an estimation of their accuracy (external), based on the real data. Other results later in Chapter 6 confirm that the scaled

standard deviation of the corrections is a very good estimate of the real error of the corrections.

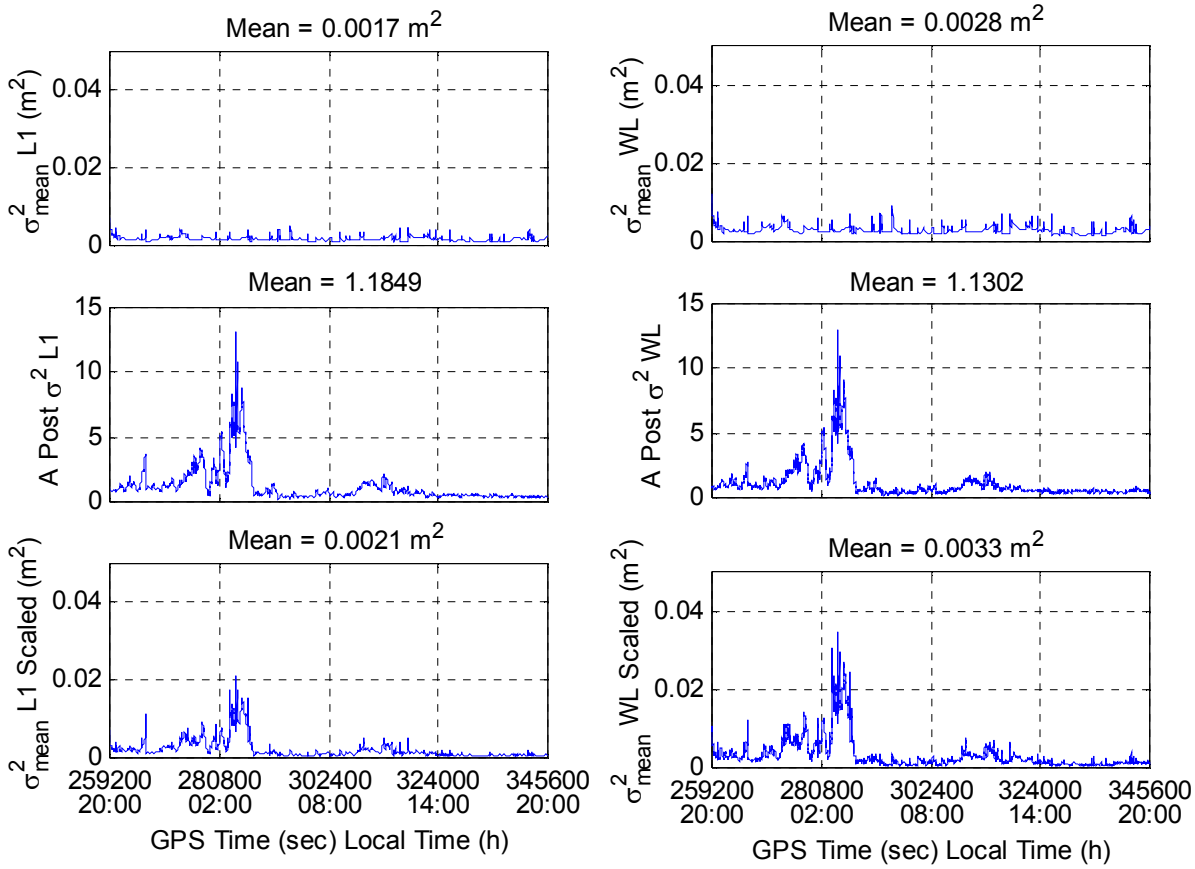

Figure 4.32: Quality estimation of the reference station's corrections for L1 and WL for the first scenario (Trois-Rivières as rover) for August 4, 1999, using the August 4, 1999 covariance functions: mean variance (top graphs), *a posteriori* variance of unit weight (graphs in the middle), and mean variance scaled by the *a posteriori* variance (bottom graphs)

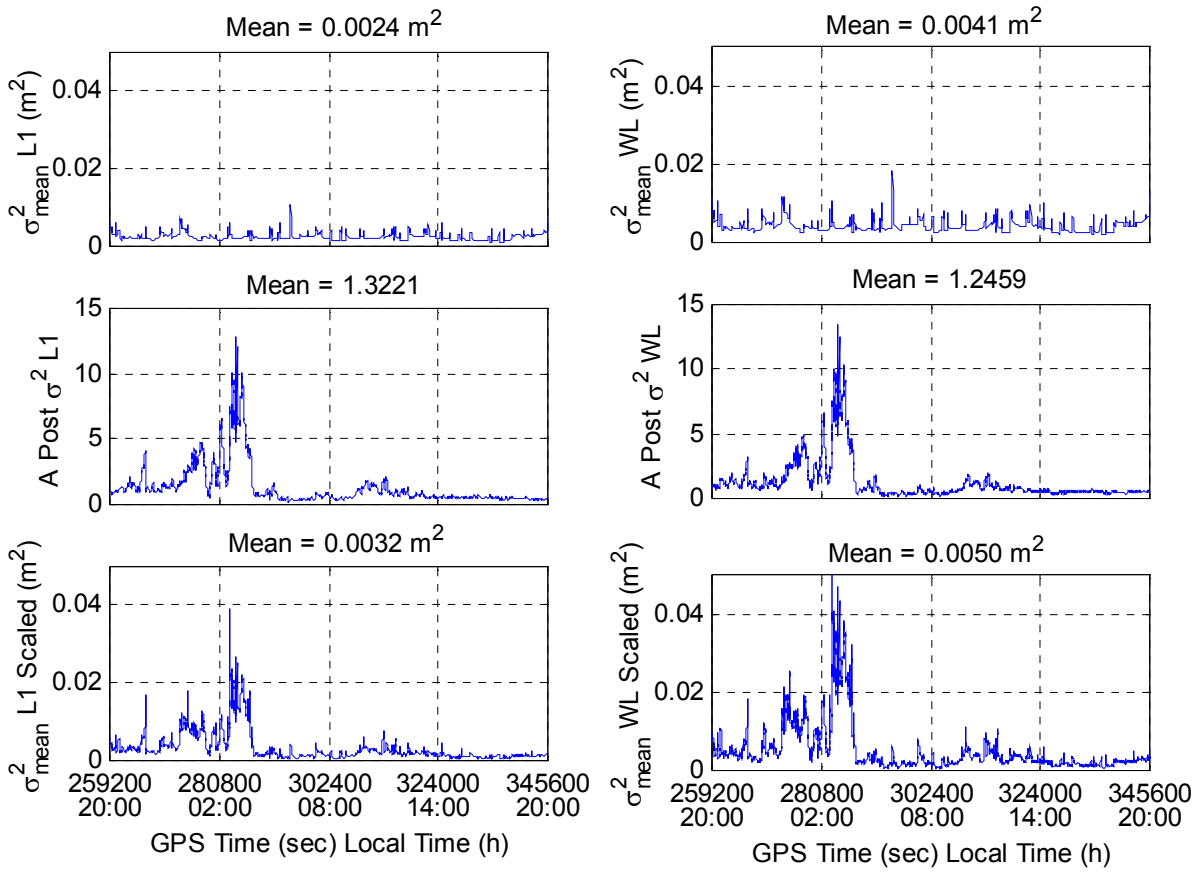

Figure 4.33: Quality estimation of the reference station's corrections for L1 and WL for the second scenario (Deschaillons as rover) for August 4, 1999, using the August 4, 1999 covariance functions: mean variance (top graphs), *a posteriori* variance of unit weight (graphs in the middle), and mean variance scaled by the *a posteriori* variance (bottom graphs)

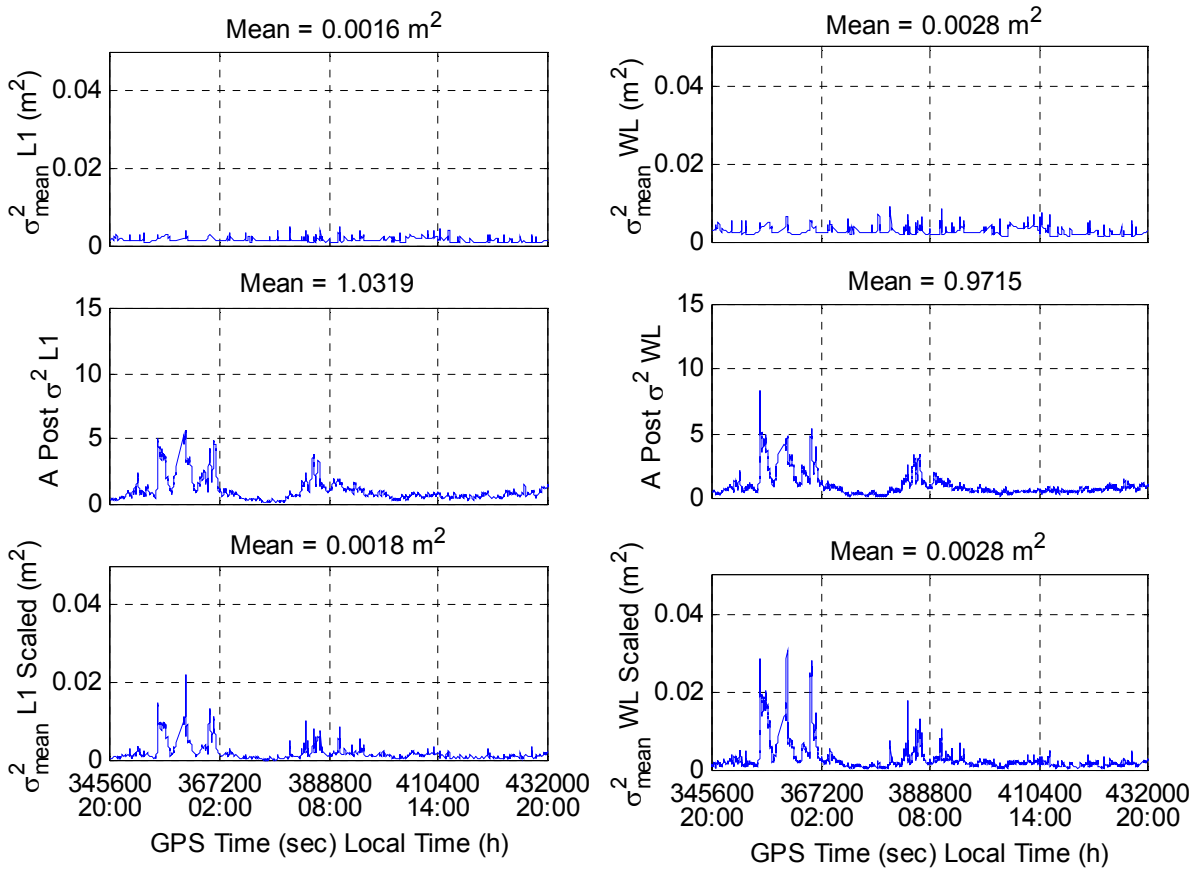

Figure 4.34: Quality estimation of the reference station's corrections for L1 and WL for the first scenario (Trois-Rivières as rover) for August 5, 1999, using the August 4, 1999 covariance functions: mean variance (top graphs), *a posteriori* variance of unit weight (graphs in the middle), and mean variance scaled by the *a posteriori* variance (bottom graphs)

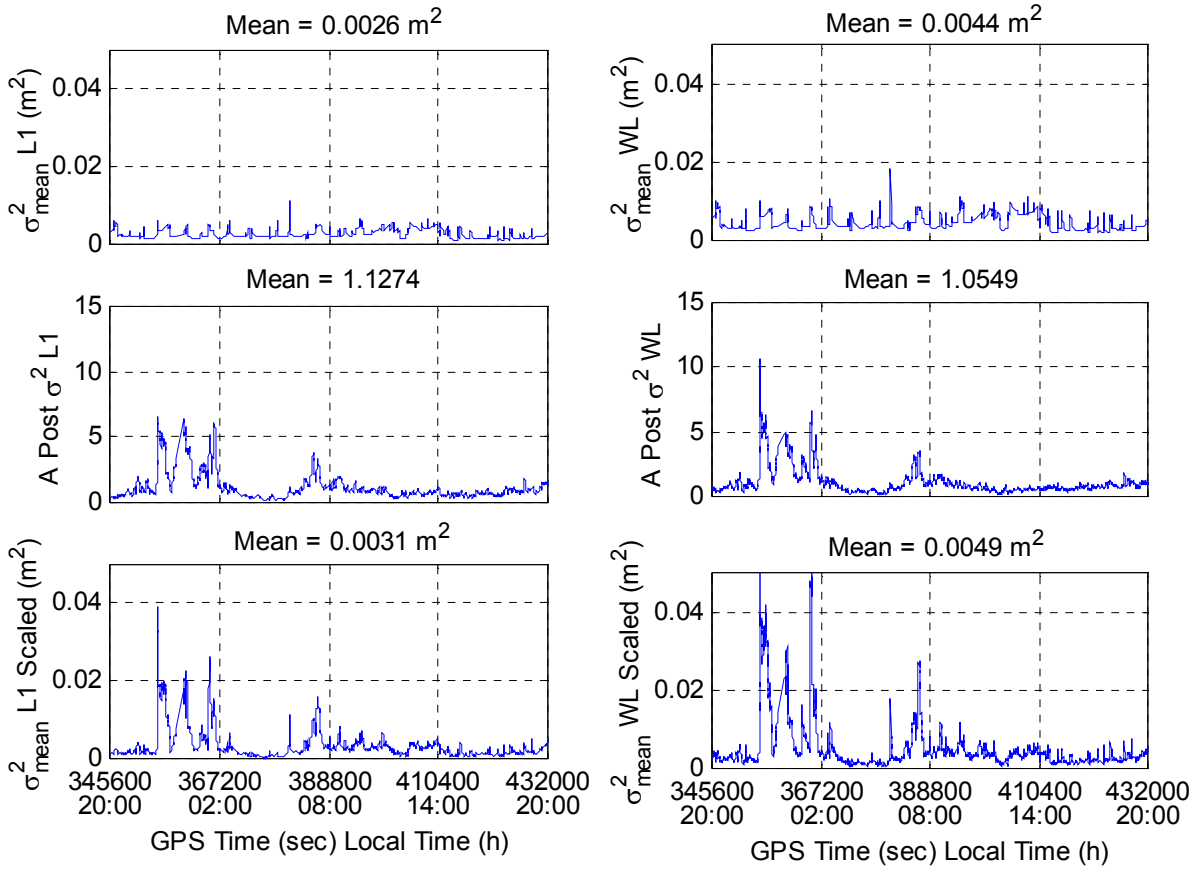

Figure 4.35: Quality estimation of the reference station's corrections for L1 and WL for the second scenario (Deschaillons as rover) for August 5, 1999, using the August 4, 1999 covariance functions: mean variance (top graphs), *a posteriori* variance of unit weight (graphs in the middle), and mean variance scaled by the *a posteriori* variance (bottom graphs)

Table 4.9: Mean values over time of the mean variance, the *a posteriori* variance and the scaled mean variance of the reference station's corrections for L1 and WL using the November 1998 (in blue) and the August 4, 1999 (in red) covariance functions

Baseline	Length (km)	Mean Variance (m^2)		*A Posteriori* Variance		Mean Variance Scaled (m^2)	
		L1	WL	L1	WL	L1	WL
GM-TR	30						
August 4		0.0040	0.0054	0.5616	0.7525	0.0023	0.0041
		0.0017	0.0028	1.1849	1.1302	0.0021	0.0033
August 5		0.0040	0.0053	0.4776	0.6087	0.0020	0.0034
		0.0016	0.0028	1.0319	0.9715	0.0018	0.0028
GM-D	46						
August 4		0.0051	0.0068	0.6560	0.8763	0.0033	0.0059
		0.0024	0.0041	1.3221	1.2459	0.0032	0.0050
August 5		0.0053	0.0071	0.5454	0.6927	0.0030	0.0051
		0.0026	0.0044	1.1274	1.0549	0.0031	0.0049

4.3.2 Brazilian Network

4.3.2.1 Results of Applying the Multi-Ref approach using the November 1998 Covariance Functions

The three scenarios described in Section 4.2.2 were used to assess how much improvement the Multi-Ref approach brought in the observation, position and ambiguity domains, using data collected in Southeastern Brazil in August, 1999, and the November, 1998 covariance functions.

In the observation domain, the L1 and WL double difference raw carrier phase misclosures were compared with those generated after applying the Multi-Ref corrections, similarly to what was done with the St. Lawrence data. The root mean square (RMS) of the raw and corrected double difference residuals for each scenario was computed, as well as the percentage improvement for August 11 and 13. The results are shown in Table 4.10. The improvement reached up to 61%, which is at the same level as the ones reported in other studies applying the same method to networks in different parts of the world [Raquet, 1998; Townsend et al., 1999]. However, the absolute values of the raw double difference carrier phase misclosures were very high in this campaign due to a very active ionosphere. Even with corrected observations, RMS values of 0.181 m in L1 and 0.250 m in WL still remain, which are too large for ambiguity resolution. This will be addressed again later, when the results in the ambiguity domain are presented. It should be noticed that the residuals obtained using raw (and corrected) observations are systematically higher in the second day, confirming that the ionosphere was more active on that day.

Figure 4.36 shows raw and corrected L1 and WL double difference carrier phase residuals for the AGUA to SJRP baseline for August 13, 1999. It can be seen that the method did an effective job correcting the observations, even those related to very large residuals. However, some double difference residuals with absolute values up to 1 metre still remain. The isolated residuals greater than 1 metre in the corrected observation

graphs are explained by the fact that during these epochs the corresponding remote satellite (normally at low elevation) was not observed by a significant number of reference stations of the network.

Table 4.10: Raw and Multi-Ref-corrected double difference misclosures RMS and respective improvement for FRAN to LIMO, AGUA to SJRP, and REGI to BOTU baselines for August 11 and 13, 1999

Baseline	Length (km)	L1 (m)			WL (m)		
		Raw	Corr.	Improv.	Raw	Corr.	Improv.
FRAN - LIMO	122						
August 11		0.191	0.116	39%	0.258	0.170	34%
August 13		0.327	0.181	45%	0.418	0.250	40%
AGUA - SJRP	146						
August 11		0.284	0.119	58%	0.364	0.159	56%
August 13		0.350	0.138	61%	0.440	0.186	58%
REGI - BOTU	193						
August 11		0.239	0.128	46%	0.312	0.180	42%
August 13		0.407	0.162	60%	0.516	0.199	61%

In the position domain, raw and corrected observations were used in the modified version of FLYKIN™ (the one that reads ambiguities from a file instead of trying to resolve them – see Section 4.3.1.1). For each scenario, coordinates of the rover, using raw and corrected L1 and WL observations for August 11 and 13, were compared with the known values. The RMS values of the differences are shown in Table 4.11. The ionospheric-free (IF) linear combination solution is also included. It is important to note that, even with known ambiguities and raw observations, the RMS of the solution in height is as large as 1.073 metres for L1 and 1.264 m for WL. Despite the fact that the method brought improvements up to 70% for the L1 and WL observables, the residuals

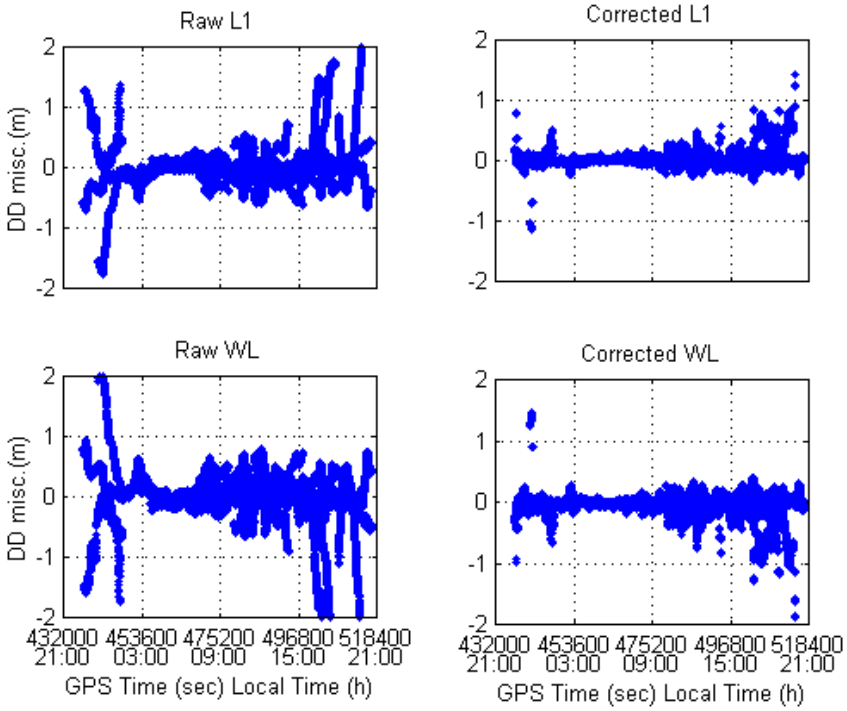

Figure 4.36: Raw and Multi-Ref-corrected L1 and WL double difference misclosures for AGUA to SJRP baseline (146 km) for August 13, 1999

using raw observations were too high to be fully corrected by the error model implemented. The percentage improvements for the IF solution are lower than the ones for the other two observables, and even negative in some cases, corresponding to differences between raw and corrected RMS at the level of the carrier phase noise. The raw RMS in the IF case, encompassing mainly troposphere and orbit errors, were already very small, except for the REGI to BOTU baseline, which has a significant height difference between both stations (700 m), contributing to a higher residual tropospheric delay.

Table 4.11: Raw and Multi-Ref position differences RMS and respective improvement for August 11 and 13, 1999

Coord. Component	L1 (m)			WL (m)			IF (m)		
	Raw	Corr.	Imp.	Raw	Corr.	Imp.	Raw	Corr.	Imp.
FRAN → LIMO (122 km), August 11									
Latitude	0.204	0.096	53%	0.268	0.137	49%	0.019	0.021	-11%
Longitude	0.130	0.080	38%	0.164	0.106	35%	0.018	0.015	17%
Height	0.386	0.263	32%	0.496	0.356	28%	0.057	0.065	-14%
FRAN → LIMO (122 km), August 13									
Latitude	0.329	0.129	61%	0.422	0.174	59%	0.026	0.023	12%
Longitude	0.275	0.189	31%	0.352	0.269	24%	0.027	0.018	33%
Height	0.642	0.422	34%	0.699	0.551	21%	0.051	0.058	-14%
AGUA → SJRP (146 km), August 11									
Latitude	0.249	0.049	62%	0.312	0.114	63%	0.015	0.014	7%
Longitude	0.186	0.106	43%	0.229	0.140	39%	0.021	0.013	38%
Height	0.495	0.251	49%	0.653	0.354	46%	0.059	0.055	7%
AGUA → SJRP (146 km), August 13									
Latitude	0.271	0.113	58%	0.372	0.157	58%	0.027	0.019	30%
Longitude	0.320	0.095	70%	0.389	0.160	59%	0.032	0.019	41%
Height	0.690	0.364	47%	0.717	0.514	28%	0.053	0.052	2%
REGI → BOTU (193 km), August 11									
Latitude	0.260	0.105	60%	0.331	0.151	54%	0.027	0.021	22%
Longitude	0.194	0.106	45%	0.241	0.139	42%	0.023	0.013	43%
Height	0.467	0.283	39%	0.633	0.444	30%	0.095	0.078	18%
REGI → BOTU (193 km), August 13									
Latitude	0.368	0.129	65%	0.453	0.163	64%	0.037	0.022	41%
Longitude	0.337	0.153	55%	0.385	0.193	50%	0.054	0.031	43%
Height	1.073	0.489	54%	1.264	0.591	53%	0.153	0.091	41%

For the ambiguity domain test, the baselines in each of the three scenarios were processed using FLYKIN Suite™ using raw and corrected observations. This software was set to perform a WL ambiguity search first and then try to convert the WL ambiguities to L1. Similar to what was done with the St. Lawrence data, FLYKIN Suite™

was forced to re-start the WL ambiguity search at fixed time intervals, to generate enough samples for each session. Thus almost every twenty minutes a new ambiguity set was searched. Sometimes twenty minutes was not enough to fix the corresponding ambiguities, so FLYKIN Suite™ was left running for an extra 20-minute interval. This procedure generated about 72 samples for each 24-hour session per baseline. The ambiguities computed by FLYKIN Suite™ were then compared with the ones solved by the batch Bernese solution. Table 4.12 shows the results in terms of percentage of corrected fixes, mean time to fix ambiguities and percentage of WL ambiguities reliably converted to L1. It can be seen that, using the Multi-Ref approach, improvements in all three types of comparisons were achieved. However, the percentage of success in fixing WL ambiguities was never greater than 65%, even using corrected data, which means that, despite the fact that the method has largely reduced the errors present in the observations (mainly ionosphere), the remaining ones still have an impact on the ambiguity resolution process.

To complete the analysis of the results using the November, 1998, covariance functions, the covariance matrices of the L1 and WL reference stations' corrections were computed using Equation 3.19. Similar to what was done for the St. Lawrence test, the $\mathbf{p_0}$ point was always made coincident with the predicted points (LIMO, SJRP and BOTU) in the three scenarios analysed, zeroing the predicted corrections and the covariance matrices. However, the conclusions derived here can be applied to the predicted

Table 4.12: Ambiguity domain improvement for AGUA to SJRP, FRAN to LIMO, and REGI to BOTU baselines for August 11 and 13, 1999

Baseline	Length	% of corrected fixes of WL ambiguities		Mean number of epochs (@ 15 sec.) to fix WL ambiguities		% of WL ambiguities reliably converted to L1	
		Raw	Corr.	Raw	Corr.	Raw	Corr.
FRAN -LIMO	122 km						
Aug. 11		60%	65%	20	18	9%	12%
Aug. 13		53%	66%	23	13	5%	11%
AGUA -SJRP	146 km						
Aug. 11		47%	63%	18	11	4%	6%
Aug. 13		48%	49%	24	21	7%	6%
REGI - BOTU	193 km						
Aug. 11		64%	59%	20	17	8%	15%
Aug. 13		51%	58%	26	22	5%	13%

corrections, as they are computed based on the same covariance matrix of the reference stations' observations, $C_{\delta l}$.

The covariance matrix of the reference stations' corrections was computed for every epoch of data. The mean of the diagonal elements was then taken in order to have a sole number to represent the quality of the corrections for each epoch. This procedure was carried out for the two days of data, for each scenario and for L1 and WL. The results are shown on the top graphs of Figures 4.37 to 4.42, respectively for the first, second, and third scenarios, August 11; and first, second, and third scenarios, August 13. The mentioned figures also include the *a posteriori* variance of unit weight (graphs in the middle), computed for each epoch of the six cases using Equation 3.21. The *a posteriori* variances of unit weight were then used to scale the variances in order to generate an

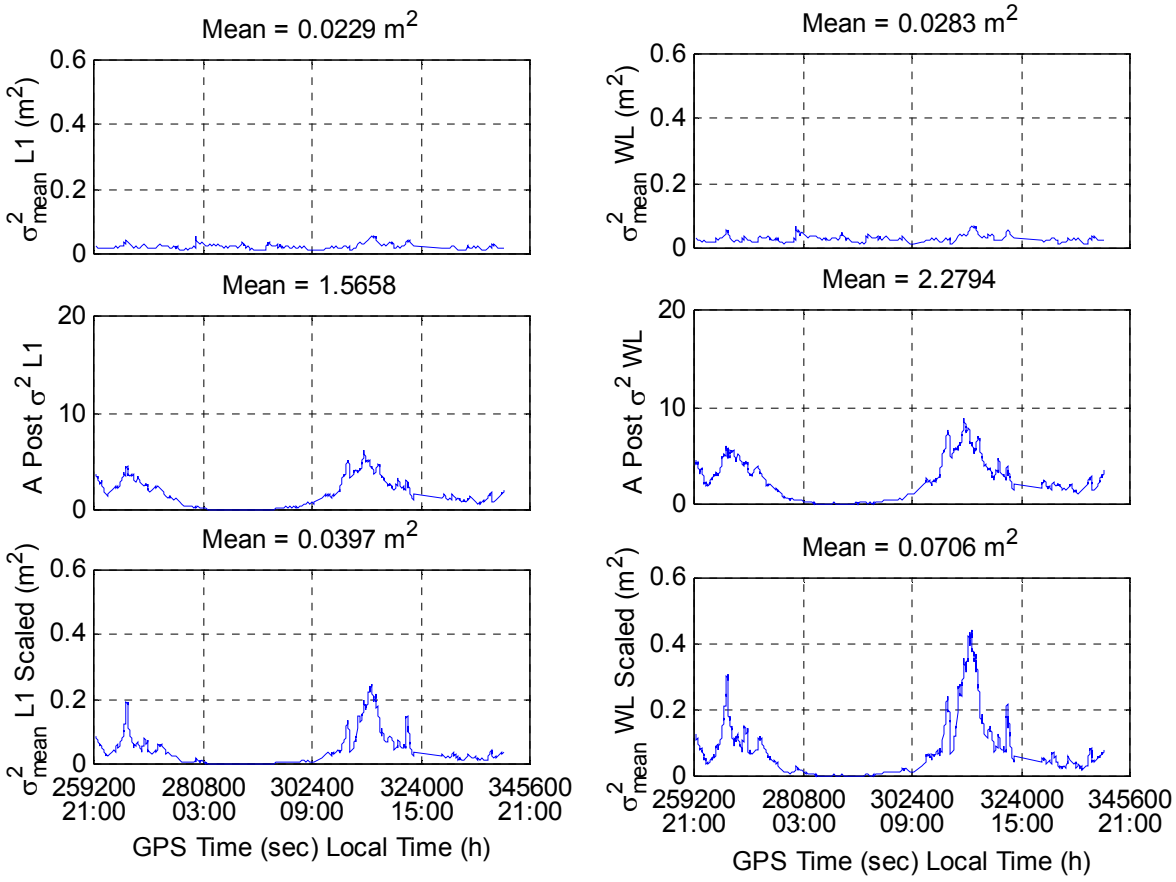

Figure 4.37: Quality estimation of the reference station's corrections for L1 and WL for the first scenario (LIMO as rover) for August 11, 1999: mean variance (top graphs), *a posteriori* variance of unit weight (graphs in the middle), and mean variance scaled by the *a posteriori* variance (bottom graphs)

estimate of the external precision. The mean of the scaled variances is shown in the graphs at the bottom of the figures. On the top of each graph, the mean of each quantity over time is also listed.

Analysing these figures, one can see that the values for the WL variances are systematically greater than the ones for L1, considering that the WL observables are

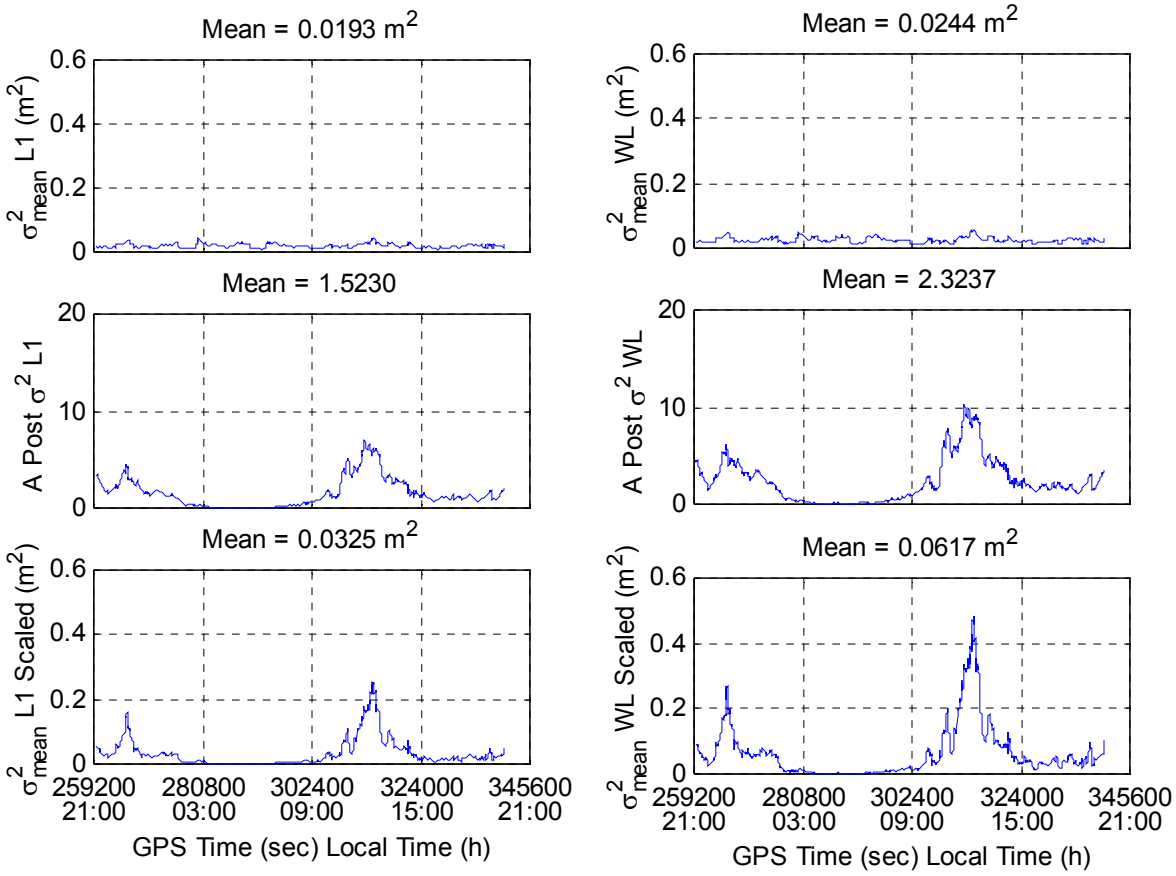

Figure 4.38: Quality estimation of the reference station's corrections for L1 and WL for the second scenario (SJRP as rover) for August 11, 1999: mean variance (top graphs), *a posteriori* variance of unit weight (graphs in the middle), and mean variance scaled by the *a posteriori* variance (bottom graphs)

noisier and more affected by the ionosphere. The variances shown in the graphs on the top correspond to propagation of the observation covariance matrix into the corrections, as seen in the St. Lawrence test. The variances for the Brazilian network are always greater than the ones for the St. Lawrence one, as the Brazilian one involves much longer baselines.

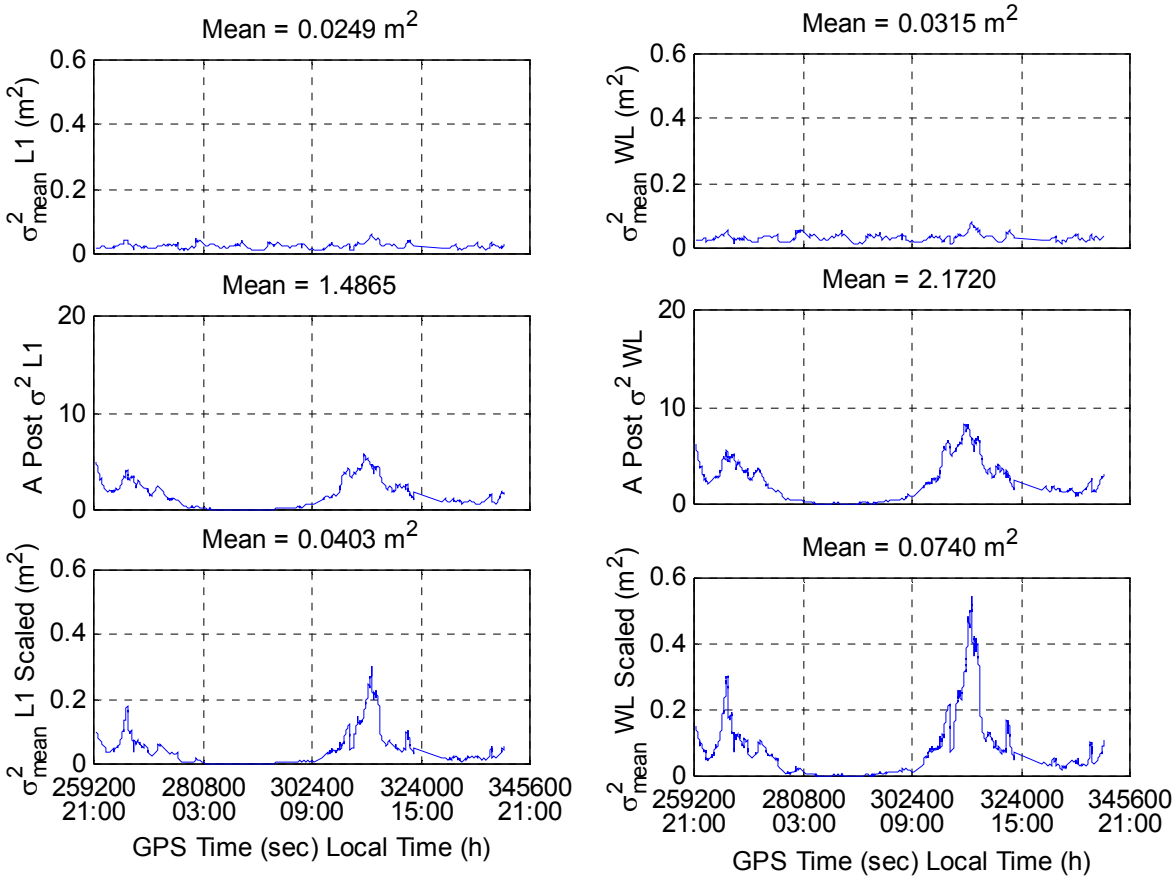

Figure 4.39: Quality estimation of the reference station's corrections for L1 and WL for the third scenario (BOTU as rover) for August 11, 1999: mean variance (top graphs), *a posteriori* variance of unit weight (graphs in the middle), and mean variance scaled by the *a posteriori* variance (bottom graphs)

It is interesting to compare the time variation of the *a posteriori* variance of unit weight (graphs in the middle) in Figures 4.38 and 4.41 with the time variation of the L1 and WL double difference misclosures in Figures 4.15 and 4.16, respectively. The correlation is evident, confirming that the *a posteriori* variance is a very good indicator of the behaviour of the misclosures, both significantly increasing during periods of high ionosphere (21:00-3:00 and 9:00-15:00 local time in case of August 11) and decreasing

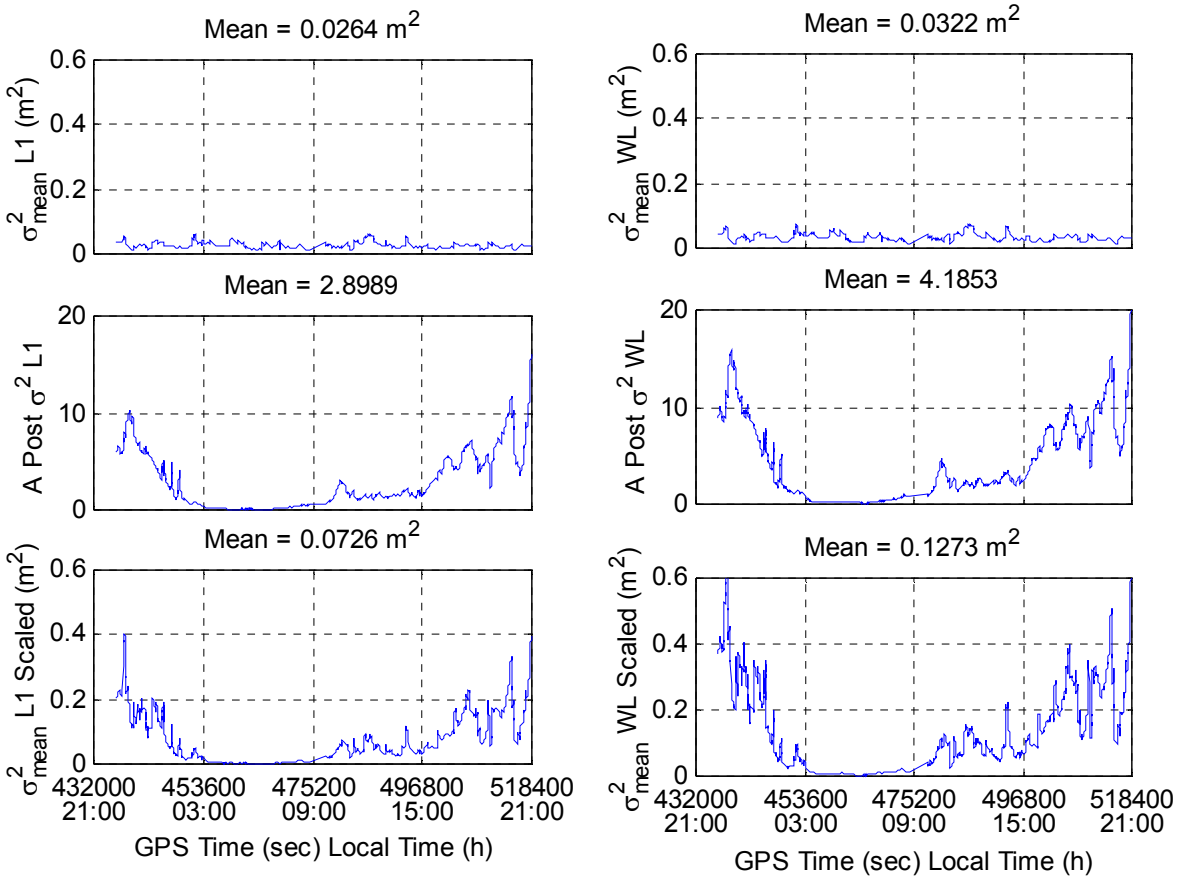

Figure 4.40: Quality estimation of the reference station's corrections for L1 and WL for the first scenario (LIMO as rover) for August 13, 1999: mean variance (top graphs), *a posteriori* variance of unit weight (graphs in the middle), and mean variance scaled by the *a posteriori* variance (bottom graphs)

during quiet periods (3:00-9:00 and 15:00-21:00 in case of August 11). It therefore seems that the *a posteriori* variance is a "single" number that can be used in a real time service to monitor the magnitude of the misclosures, which is mostly affected by the ionospheric activity in the region covered by the reference network.

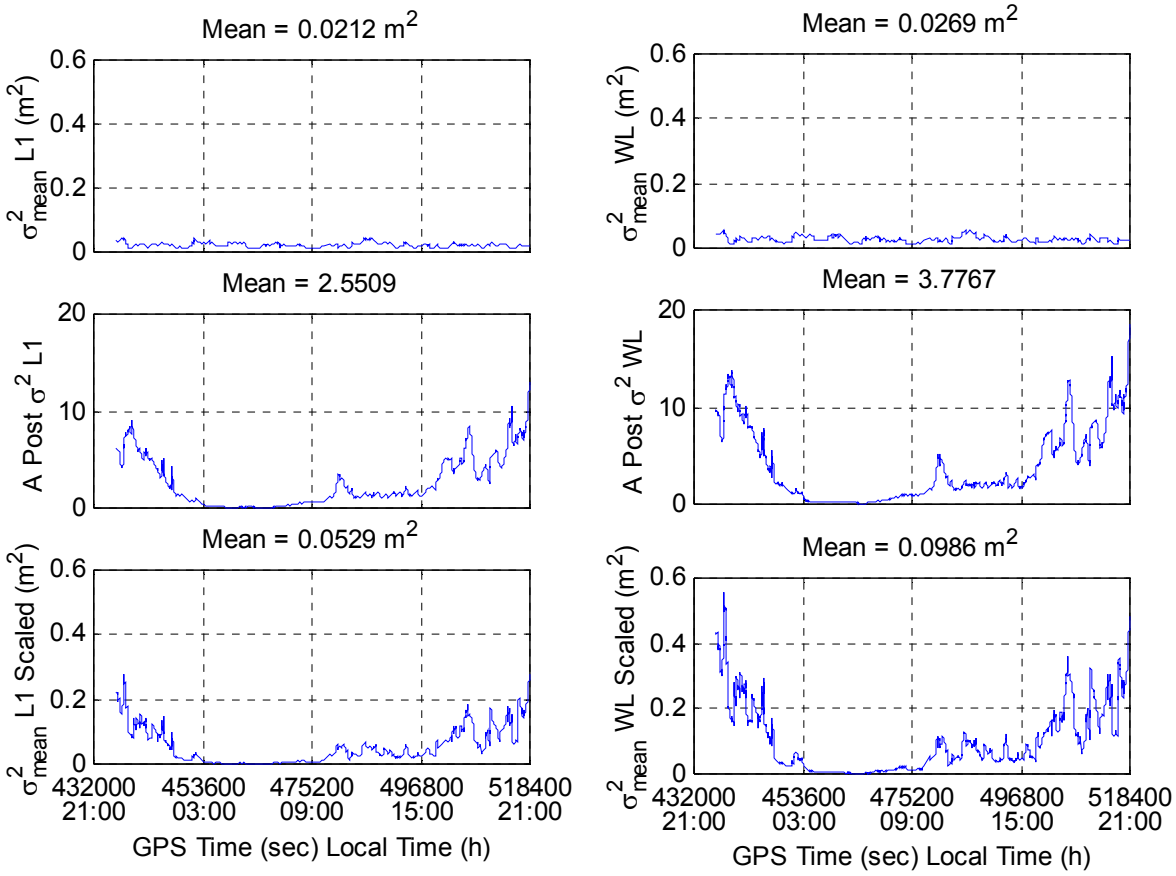

Figure 4.41: Quality estimation of the reference station's corrections for L1 and WL for the second scenario (SJRP as rover) for August 13, 1999: mean variance (top graphs), *a posteriori* variance of unit weight (graphs in the middle), and mean variance scaled by the *a posteriori* variance (bottom graphs)

The mean *a posteriori* variance over time is always greater than 1, indicating that the observation weights (given by the covariance functions) were too optimistic. Indeed, the November 1998 covariance functions, used herein, were computed using a data set collected under ionospheric conditions as large as 10 ppm [Fortes et al., 2000], whereas the Brazilian data was collected under ionospheric spatial gradients of up to 11 ppm on August 11 (the eclipse day) and up to 23 ppm on August 13 (see Section 4.2.2).

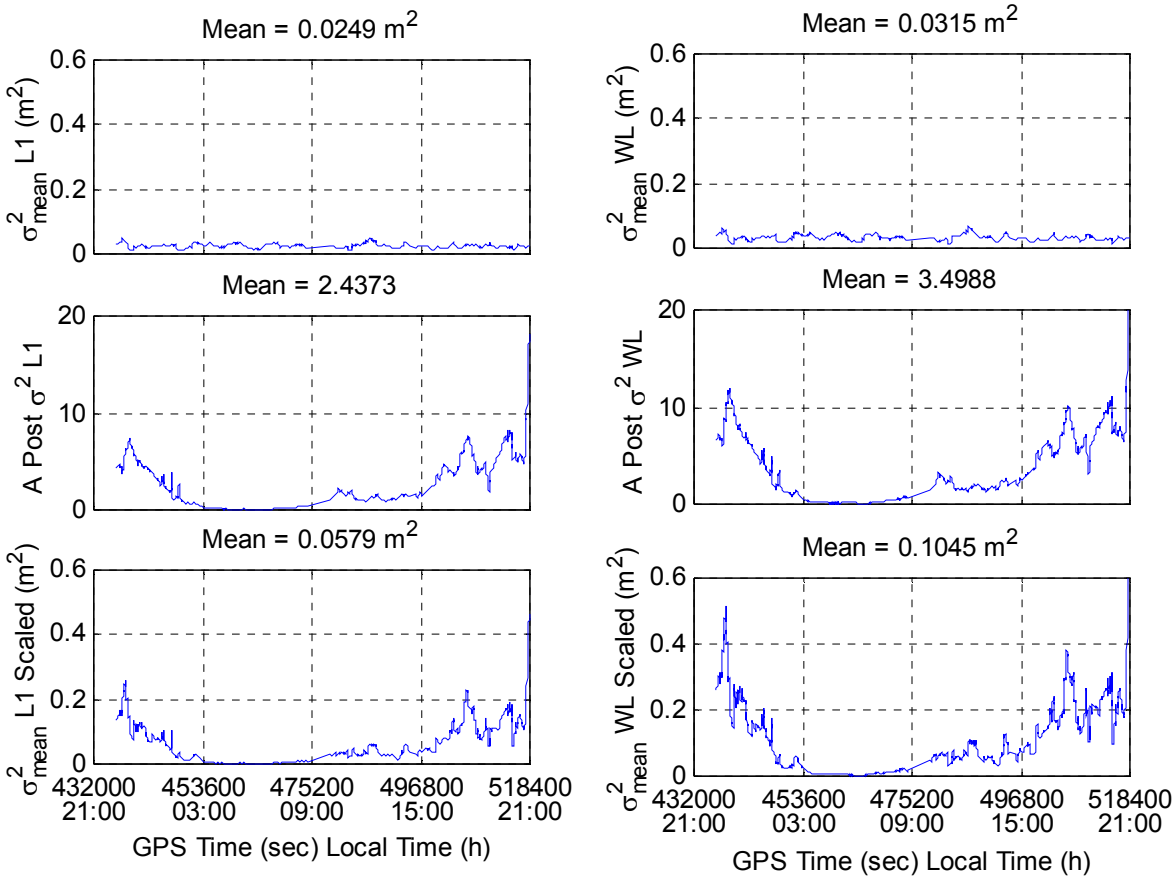

Figure 4.42: Quality estimation of the reference station's corrections for L1 and WL for the third scenario (BOTU as rover) for August 13, 1999: mean variance (top graphs), *a posteriori* variance of unit weight (graphs in the middle), and mean variance scaled by the *a posteriori* variance (bottom graphs)

The *a posteriori* variance mean values for August 11 range from 1.4865 to 1.5658 for L1 and from 2.1720 to 2.2794 for the WL, whereas they range from 2.4373 to 2.8989 for L1 and from 3.4988 to 4.1853 for the WL for August 13, confirming again that the double difference misclosures were smaller during the eclipse day, corresponding to a

less active ionosphere (an *a posteriori* variance greater than one implies that the misclosures were greater than the values predicted by the covariance functions).

4.3.2.2 Re-computation of the Original Covariance Functions Using Data Collected on August 13, 1999

Using L1 and WL misclosures for August 13, 1999, described in Section 4.2.2, and the procedure described in Section 3.2.1.4, the covariance functions given by Equations 3.33 to 3.35 were re-evaluated. Table 4.13 includes the $\mathbf{k_1}$, $\mathbf{k_2}$ and $\mathbf{k_\mu}$ coefficients that were computed. As happened in the St. Lawrence case, the variances of the uncorrelated errors at the zenith included in this table correspond to values obtained from Raquet [1998] and constrained during the Least-Squares adjustment process. A comparison of these

Table 4.13: k_1, k_2 and k_μ coefficients and variances of the uncorrelated errors at the zenith ($\sigma^2_{u_z}$) computed using data collected in Southeastern Brazil on August 13, 1999

Coefficient	L1	WL
k_1 [a]	4.82219e-04	3.11958e-05
k_2 [b]	7.95499e-06	5.97788e-07
k_μ [c]	26.680	31.221
$\sigma^2_{u_z}$ [d]	4.4273e-05	3.0794e-05

a: cycles^2/km; b: cycles^2/km^2; c: unitless; d: cycles^2

coefficients with the ones computed using the November, 1998 data set (Table 4.3) is done graphically in Figure 4.47 later in this section.

Figures 4.43 and 4.44 show the statistics of the $\mathbf{k_\mu}$ computation for the L1 and WL observables, respectively. The circles are mean values of $\boldsymbol{\mu(\varepsilon)}$ computed for each bin for the 35 baselines using Equation 3.40; the dashed lines show the 1-σ envelope around the mean values of $\boldsymbol{\mu(\varepsilon)}$ considering the 35 baselines; and the continuous line shows the fit of Equation 3.35 to the data. In general, the curves do not fit to the data as good as in the St. Lawrence case. In the Brazilian case, the steeper behaviour of the $\boldsymbol{\mu(\varepsilon)}$ values, reaching values less than 1 for elevations greater than 60° for both L1 and WL, does not seem to be right. Therefore the procedure described in Section 3.2.1.4.1 to evaluate the $\boldsymbol{\mu(\varepsilon)}$ values, based on averaging the mapping functions for troposphere and ionosphere, is not adequate is this case, indicating that the use of different mapping functions for each type of error, as proposed in Chapter 5, is more appropriate.

Figures 4.45 and 4.46 show, respectively, plots of the L1 and WL functions' fit to the data when determining the corresponding $\mathbf{k_1}$ and $\mathbf{k_2}$ coefficients. Each small circle represents the variances of the double difference misclosures reduced to the zenith for each baseline at the corresponding baseline length. It can be seen that the quality of the fit was good, despite the fact that the circles were more dispersed than in the St. Lawrence case. The isolated circle at the top right of the plots correspond to the longest baseline in

the network (BRAZ – CHUA, with 423 km), and consequently the most problematic one when resolving ambiguities using Bernese (see Appendix B).

The corresponding covariance and mapping functions given by Equations 3.33 and 3.35, respectively, are given in Figure 4.47. For the sake of comparison, the functions obtained using data collected in St. Lawrence in November 1998, whose Multi-Ref results are described in Section 4.3.2.1, are also shown in the figure. It is evident that the correlated errors are much larger in the Brazilian case and they degrade slightly faster towards the horizon, mainly due to the fact that the Brazilian network is located under a region more affected by the ionosphere, with greater spatial gradients. Considering the huge differences in the covariance functions, it was worth to assess the Multi-Ref performance using the updated covariance functions. One may verify again that the ratio between the correlated error function values for WL and L1 are at the same order of magnitude as the ratio between the ionospheric effect on WL and L1 (in cycles) squared (i.e. 0.080).

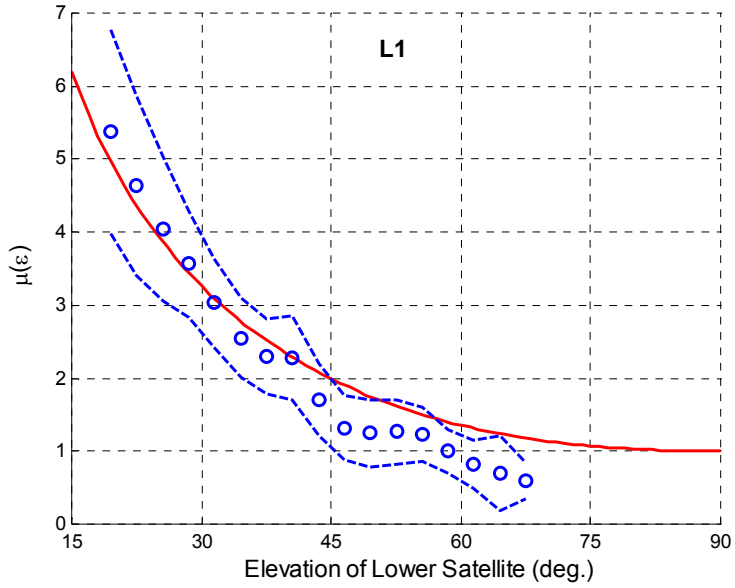

Figure 4.43: Statistics of the k_μ computation for the L1 observable, using Brazilian data collected on August 13, 1999

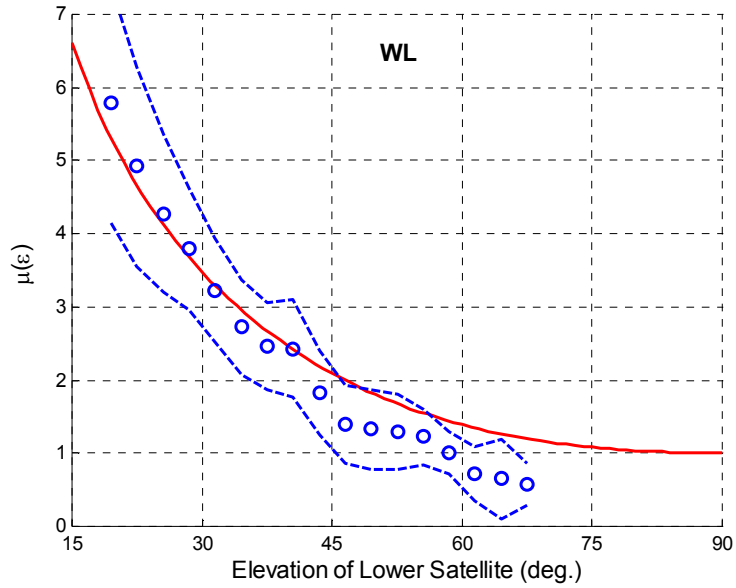

Figure 4.44: Statistics of the k_μ computation for the WL observable, using Brazilian data collected on August 13, 1999

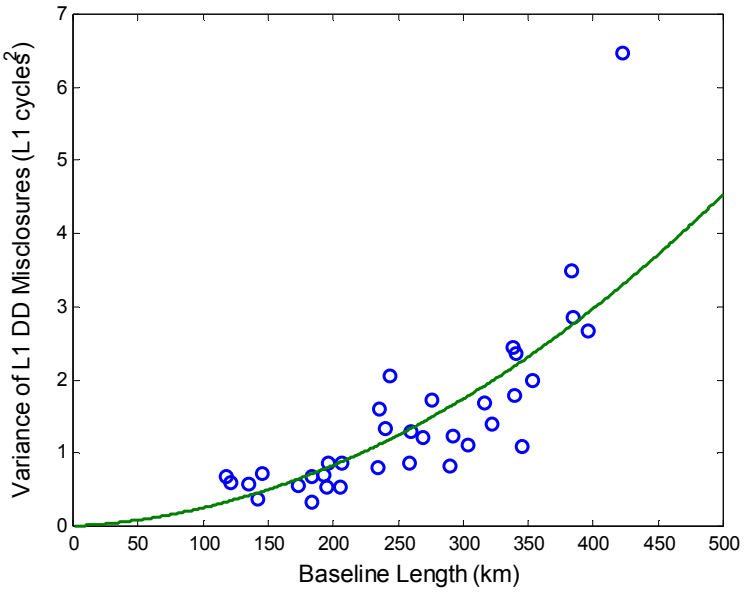

Figure 4.45: Function fit after determining k_1 and k_2 coefficients for the L1 observable using Brazilian data collected on August 13, 1999

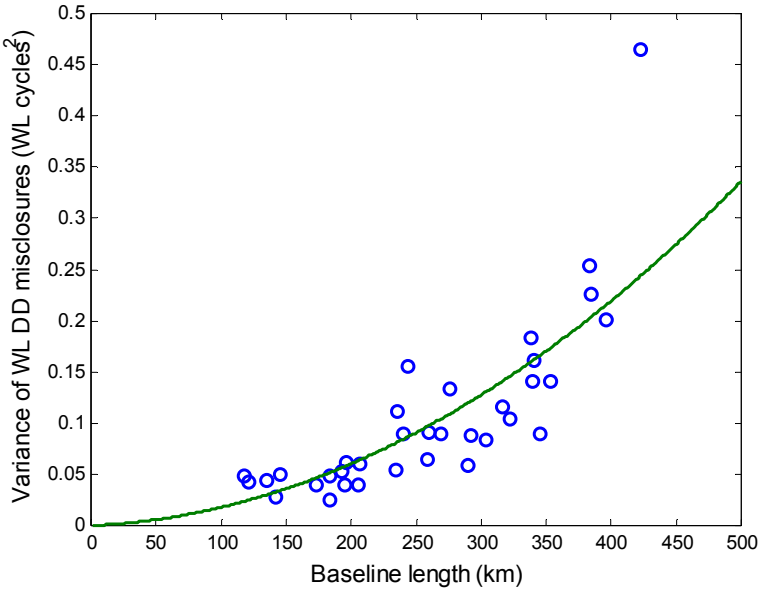

Figure 4.46: Function fit after determining k_1 and k_2 coefficients for the WL observable using Brazilian data collected on August 13, 1999

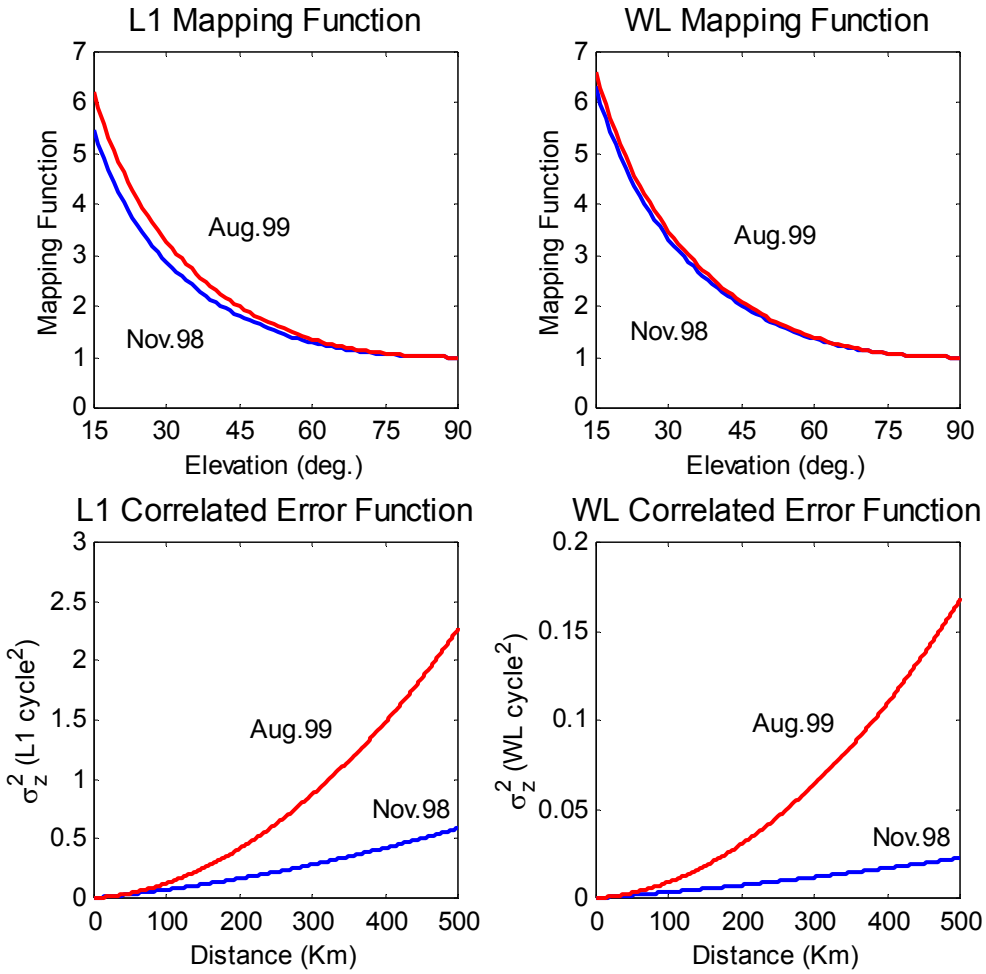

Figure 4.47: Mapping functions (top figures) and correlated error functions (bottom figures) for L1 and WL using data collected on November 27, 1998 in St. Lawrence region (blue), and data collected on August 13, 1999 in Southeastern Brazil (red)

4.3.2.3 Improvement Brought by the Multi-Ref Method Using the Original Covariance Functions Computed With Data Collected on August 13, 1999

Using the covariance functions computed in the last section (whose coefficients were listed in Table 4.13), the improvement brought by the Multi-Ref method was computed in the observation domain for the three scenarios described before. The results are included in Table 4.14.

Table 4.14: Raw and Multi-Ref-corrected double difference misclosures RMS and respective improvement for FRAN to LIMO, AGUA to SJRP, and REGI to BOTU baselines for August 11 and 13, 1999, using August 13, 1999, covariance functions

Baseline	Length (km)	L1 (m)			WL (m)		
		Raw	Corr.	Improv.	Raw	Corr.	Improv.
FRAN - LIMO	122						
August 11		0.191	0.101	47%	0.258	0.131	49%
August 13		0.327	0.150	54%	0.418	0.192	54%
AGUA - SJRP	146						
August 11		0.284	0.108	62%	0.364	0.142	61%
August 13		0.350	0.130	63%	0.440	0.170	61%
REGI - BOTU	193						
August 11		0.239	0.119	50%	0.312	0.163	48%
August 13		0.407	0.178	56%	0.516	0.217	58%

Table 4.15 lists the differences between the improvement brought by the Multi-Ref method using the November 1998 covariance functions (results from Table 4.10) and using the August 13, 1999 covariance functions (results from Table 4.14). Analysing this table, it can be seen that using updated covariance functions improved the results by as much as 9%, 0.031 m in double differences L1 RMS, and 14%, 0.058 m in WL. In one

case the results were worse than the ones obtained using the November 1998 covariance functions. A satellite at low elevation (PRN 21) which was observed only by few reference stations when rising at the horizon mostly caused this fact. As briefly mentioned in Section 4.3.1.3, the quality of the corrections deteriorates in this situation, and this is addressed in Chapter 6. In this specific case, the November, 1998, covariance functions seem to have given better results by chance. When the double difference misclosures related to this satellite are removed, the August 13, 1999 covariance functions also give better performance, as can be seen in Table 4.15.

Table 4.15: Differences between Multi-Ref-corrected double difference misclosures RMS and respective improvement for FRAN to LIMO, AGUA to SJRP, and REGI to BOTU baselines for August 11 and 13, 1999, using November 1998 and August 13, 1999, covariance functions[1]

Baseline	Length (km)	L1 (m)		WL (m)	
		Corr. Diff.	Imp. Diff.	Corr. Diff.	Imp. Diff.
FRAN - LIMO	122				
August 11		-0.015	8%	-0.039	15%
August 13		-0.031	9%	-0.058	14%
AGUA - SJRP	146				
August 11		-0.011	4%	-0.017	5%
August 13		-0.008	2%	-0.016	3%
REGI - BOTU	193				
August 11		-0.009	4%	-0.017	6%
August 13		0.016	-4%	0.018	-3%
August 13[2]		-0.013	3%	-0.023	4%

1: a positive improvement difference means better performance using the August 13, 1999 covariance functions

2: double difference misclosures with PRN 21 as a remote satellite removed

In this case the use of covariance functions computed using data of the campaign improved the results at the centimetre level. This can be justified by the fact that the previous results were generated using data collected in another region of the world (at high latitudes - St. Lawrence region, Canada) and consequently under completely different ionospheric conditions. In addition, the baselines in the three Brazilian scenarios were much longer than the two in the St. Lawrence ones, which may have "amplified" the impact of the covariance functions. Despite the fact that the magnitude of the changes are not large, it suggests that it is better to be conservative and compute the covariance functions using data collected by the very reference network when starting this kind of service. After that, recomputing them about three times during each 11-year solar cycle (at the peak, in the middle and at the bottom of the cycle) is probably enough. At this point, one could think about the benefits of an adaptive approach where the covariance functions would be recomputed several times a day to follow the variations of the ionosphere. This topic is further discussed in Section 5.2.1 when analysing the covariance function for the ionosphere.

Considering that the differences in the observation domain were at the centimetre level only, no further tests were conducted in the position and ambiguity domains.

Figure 4.48 shows the raw and corrected double difference L1 and WL misclosures for AGUA to SJRP baseline (146 km) for August 13, 1999. Comparing this

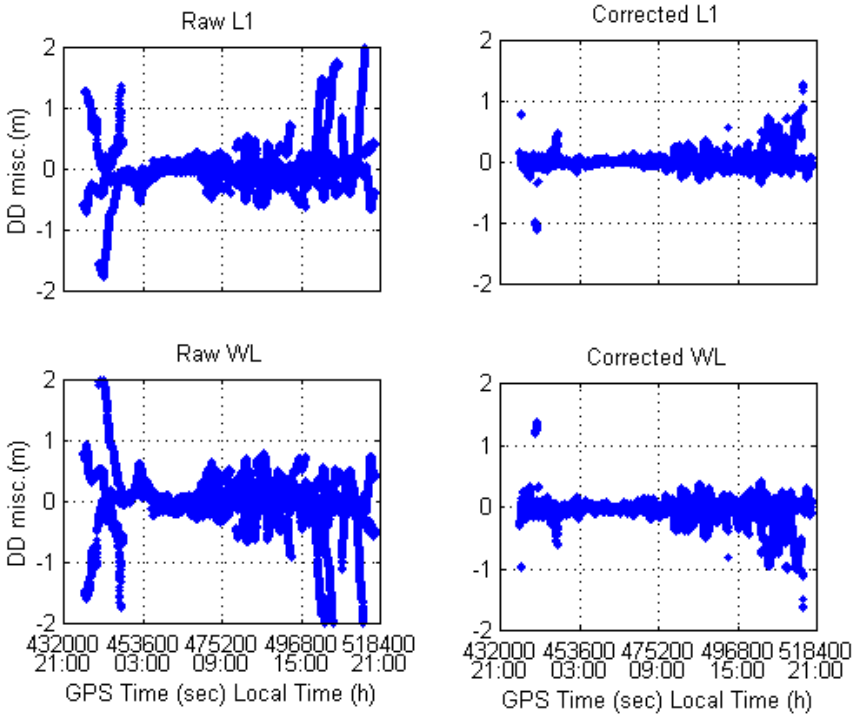

Figure 4.48: Raw and Multi-Ref-corrected L1 and WL double difference misclosures for AGUA to SJRP baseline (146 km) for August 13, 1999, using August 13, 1999, original covariance functions

figure with Figure 4.36 (both refer to the same baseline), one can see that they look very similar, with the corrected double difference misclosures slightly less spread around the y-axis in Figure 4.48. The isolated dots correspond to corrected values for epochs when the remote satellite was setting or rising, resulted in this satellite being observed by only a few reference stations. These dots are generally closer to the y-axis in Figure 4.48, a fact that had already been observed in the St. Lawrence test. Chapter 6 addresses these occurrences. Figure 4.49 shows the corrected misclosures of Figures 4.36 and 4.48 for the interval 23:00-00:00 local time in order to emphasise that, using more appropriate covariance functions, these isolated cases were improved. An interesting aspect on Figure

4.49 is the discontinuity of the isolated "track". The two segments correspond to misclosures for the same satellite pair (PRN 3, base, and PRN 15, remote). Satellite 15 was rising above the 15° elevation mask at the beginning of the track. During these epochs, this satellite was observed by only two baselines out of six from the reference network. The discontinuity occurred exactly at epoch 442080, when this satellite started to be observed by one more baseline, totalling three out of six. This clearly shows the impact of the observability on the computed corrections. The updated covariance

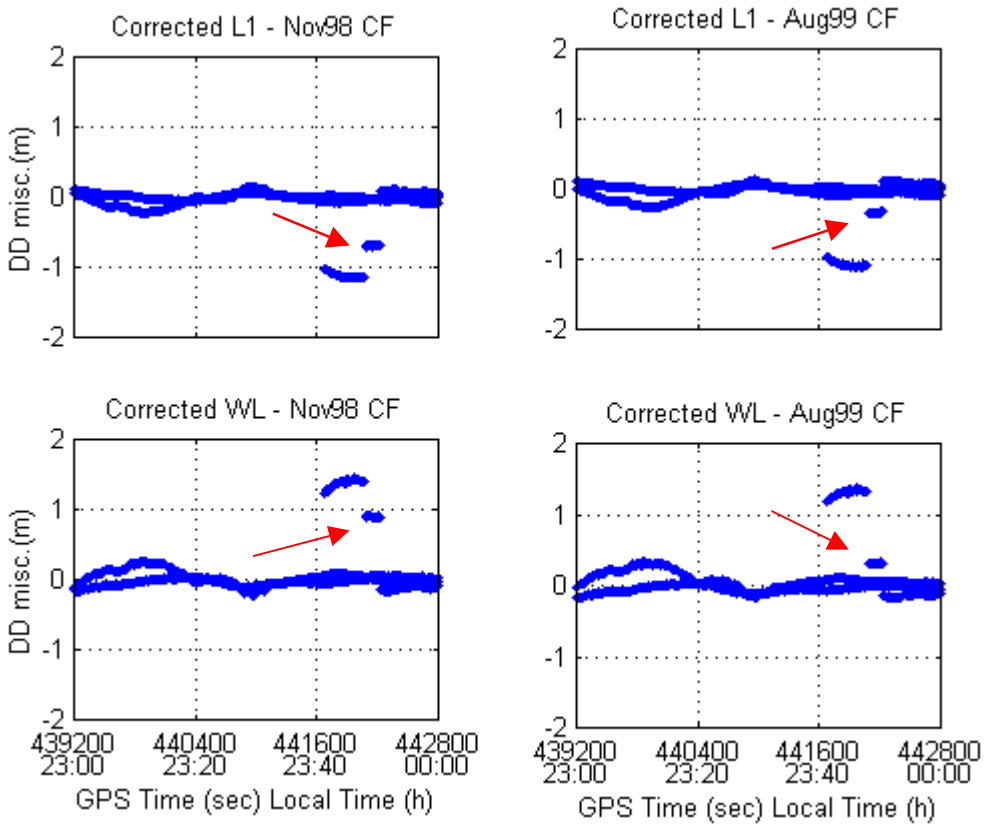

Figure 4.49: Multi-Ref-corrected L1 and WL double difference misclosures for AGUA to SJRP baseline (146 km) for August 13, 1999, using November 1998 (on the left) and August 13, 1999 (on the right) original covariance functions. The arrows point towards the isolated dots improved with the August 1999 covariance functions

functions performed better than the November 1998 ones when only 3 baselines were observing PRN 15. With two baselines, there was no difference between both cases.

To complete the analysis of the impact of using the August 4, 1999, original covariance functions, it was necessary to compute the covariance matrix of the reference stations' corrections and the *a posteriori* variance of unit weight, similar to what was done for the November, 1998, covariance functions. Figures 4.50 to 4.55 show the mean variance for every epoch for the three scenarios for both days (on the top). These figures also show the *a posteriori* variance (in the middle) and the corresponding scaled mean variances at the bottom. On the top of each graph, the mean of each quantity over time is also listed. These figures are analogous to Figures 4.37 to 4.42, respectively. Comparing the corresponding ones (i.e. 4.37 and 4.50; 4.38 and 4.51; 4.39 and 4.52; 4.40 and 4.53; 4.41 and 4.54; 4.42 and 4.55), it can be seen that the mean variance values (on the top) are larger when the August 13, 1999, covariance functions are used. This is because the relative errors during the August, 1999, campaign were significantly larger than the ones of November, 1998, as seen in Figure 4.47. A comparison of the *a posteriori* variances of unit weight (in the middle) shows that the corresponding values are closer to 1 for August 1999, as expected. This means that the weighting scheme used for August 1999 is better than the one for November, 1998, as it should be, considering that it was based on covariance functions computed using the data from the very campaign. The values larger than 1 are justified by the influence, in the final mean, of the spikes present in the figures.

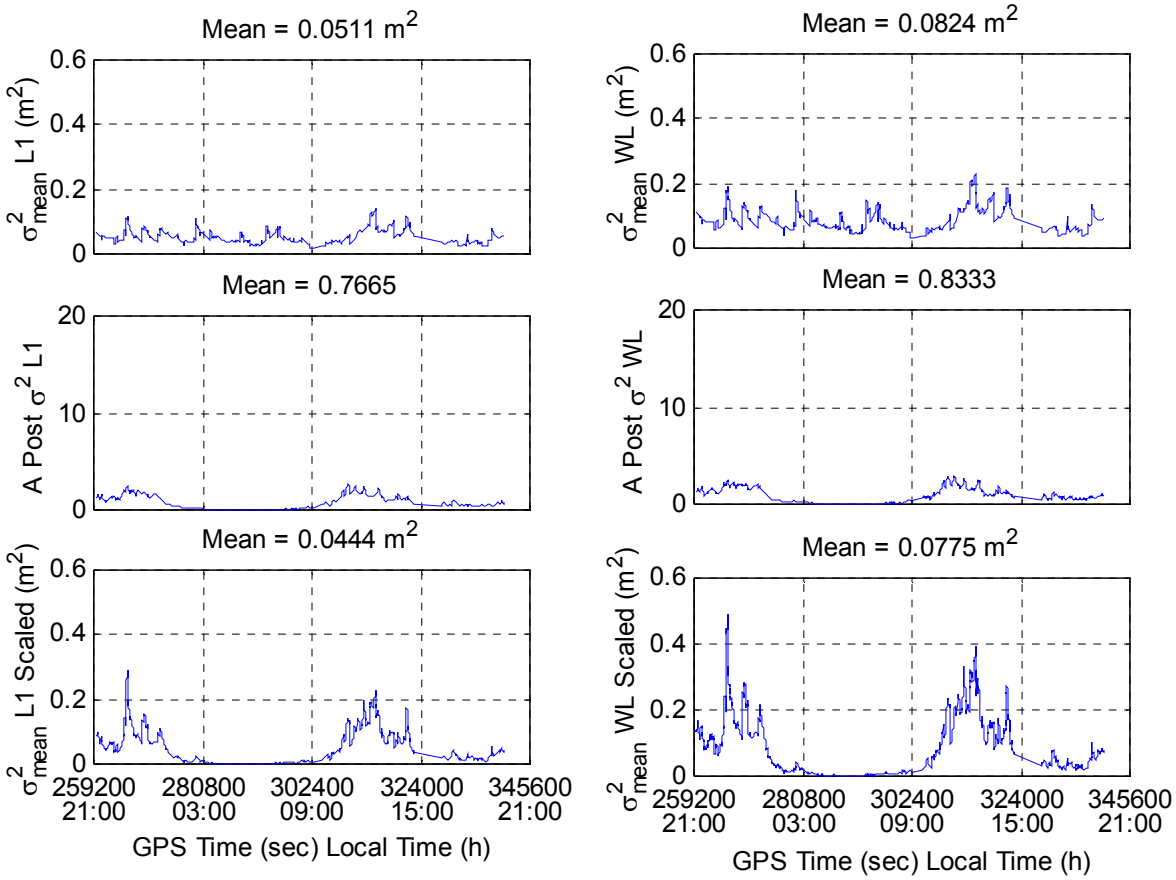

Figure 4.50: Quality estimation of the reference station's corrections for L1 and WL for the first scenario (LIMO as rover) for August 11, 1999, using the August 13, 1999 covariance functions: mean variance (top graphs), *a posteriori* variance of unit weight (graphs in the middle), and mean variance scaled by the *a posteriori* variance (bottom graphs)

As explained before, these spikes are due to an increased ionospheric activity during those periods of time.

Table 4.16 summarises the mean of each quantity over time in Figures 4.37 to 4.42 and 4.50 to 4.55. Analysing this table, it can be seen that, depending on the covariance functions used, the mean variances vary considerably (in some cases, the

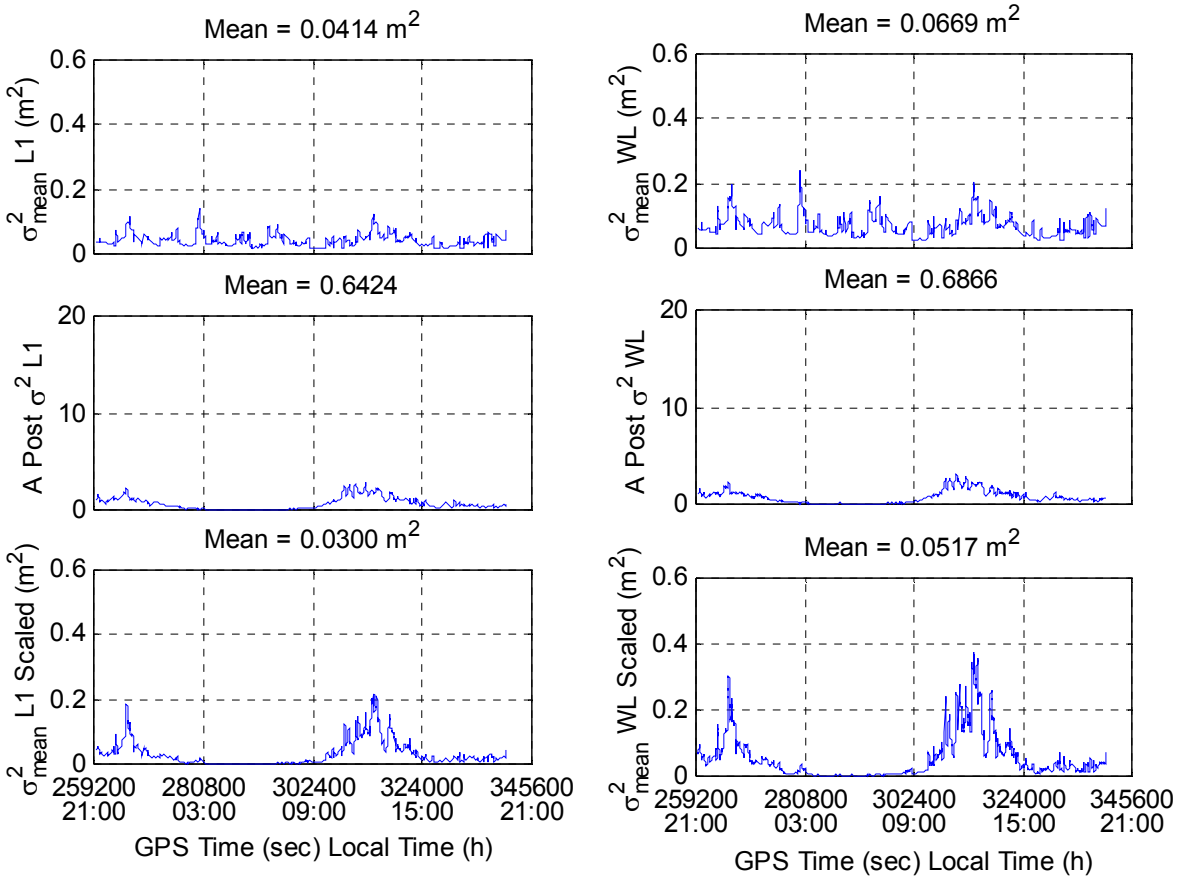

Figure 4.51: Quality estimation of the reference station's corrections for L1 and WL for the second scenario (SJRP as rover) for August 11, 1999, using the August 13, 1999 covariance functions: mean variance (top graphs), *a posteriori* variance of unit weight (graphs in the middle), and mean variance scaled by the *a posteriori* variance (bottom graphs)

values using the August 13, 1999 covariance functions are between 2 and 3 times larger than the values obtained using those from November 1998). These results agree with Moritz [1976], who stated that changes to the correction variances occur when different covariance functions are used, despite this influence may not affect the corrections themselves. However, scaling the variances by the *a posteriori* variance of the unit

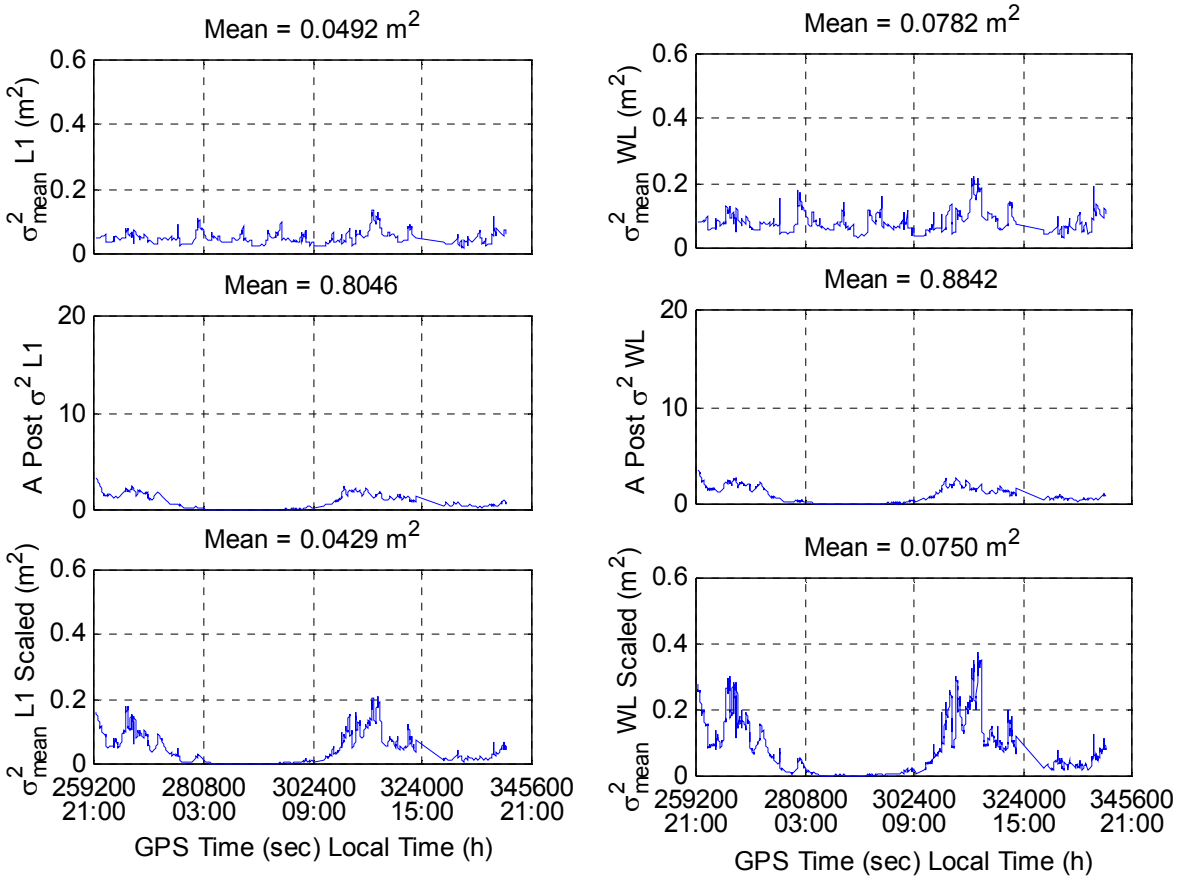

Figure 4.52: Quality estimation of the reference station's corrections for L1 and WL for the third scenario (BOTU as rover) for August 11, 1999, using the August 13, 1999 covariance functions: mean variance (top graphs), *a posteriori* variance of unit weight (graphs in the middle), and mean variance scaled by the *a posteriori* variance (bottom graphs)

weight compensates those differences, generating very close estimated correction variances in all cases, as it had already been seen in the analogous St. Lawrence results.

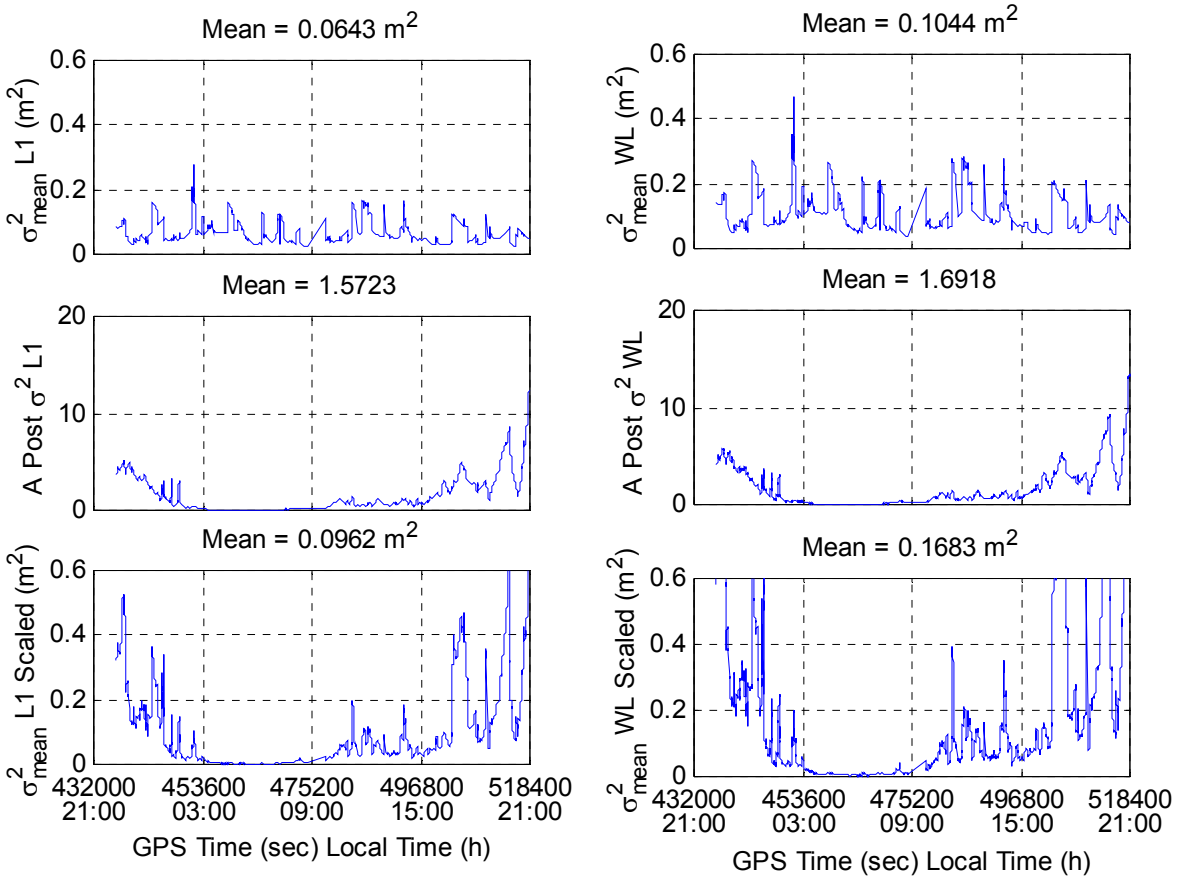

Figure 4.53: Quality estimation of the reference station's corrections for L1 and WL for the first scenario (LIMO as rover) for August 13, 1999, using the August 13, 1999 covariance functions: mean variance (top graphs), *a posteriori* variance of unit weight (graphs in the middle), and mean variance scaled by the *a posteriori* variance (bottom graphs)

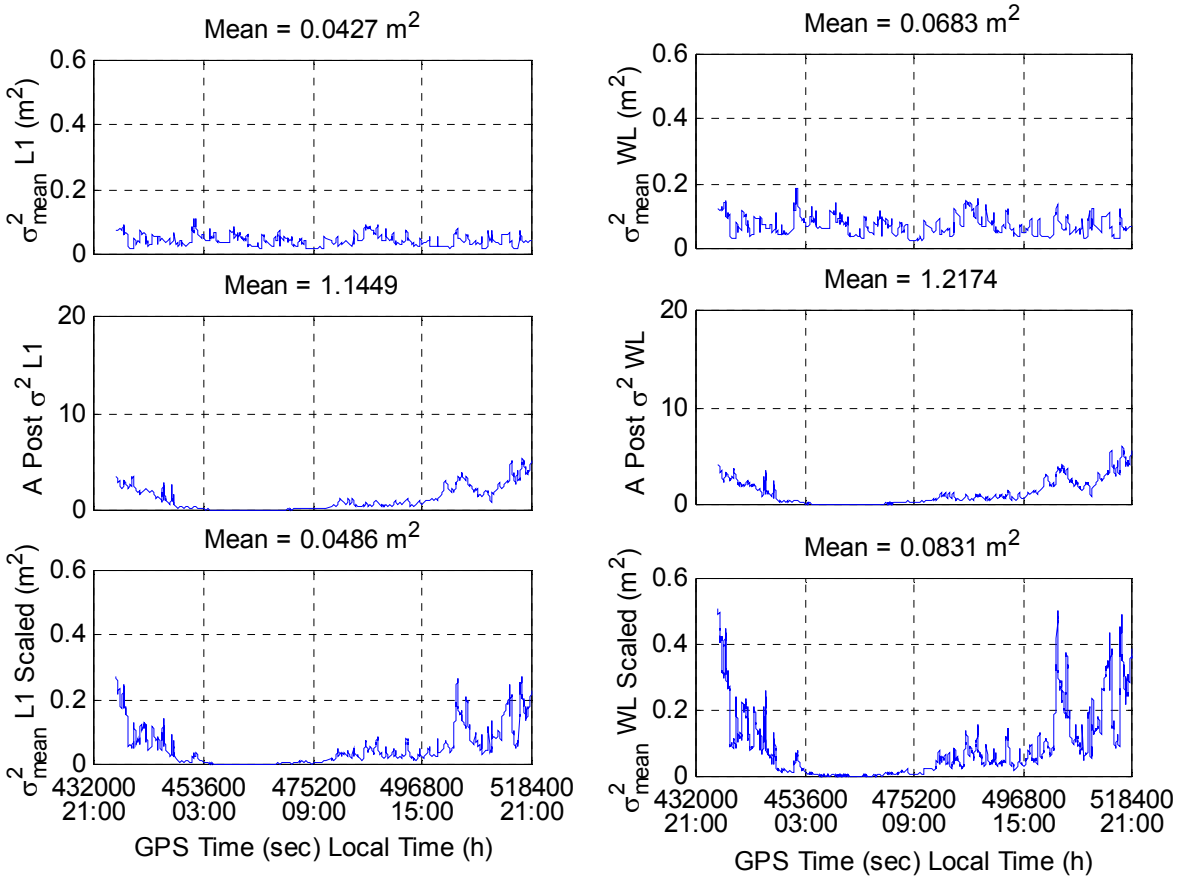

Figure 4.54: Quality estimation of the reference station's corrections for L1 and WL for the second scenario (SJRP as rover) for August 13, 1999, using the August 13, 1999 covariance functions: mean variance (top graphs), *a posteriori* variance of unit weight (graphs in the middle), and mean variance scaled by the *a posteriori* variance (bottom graphs)

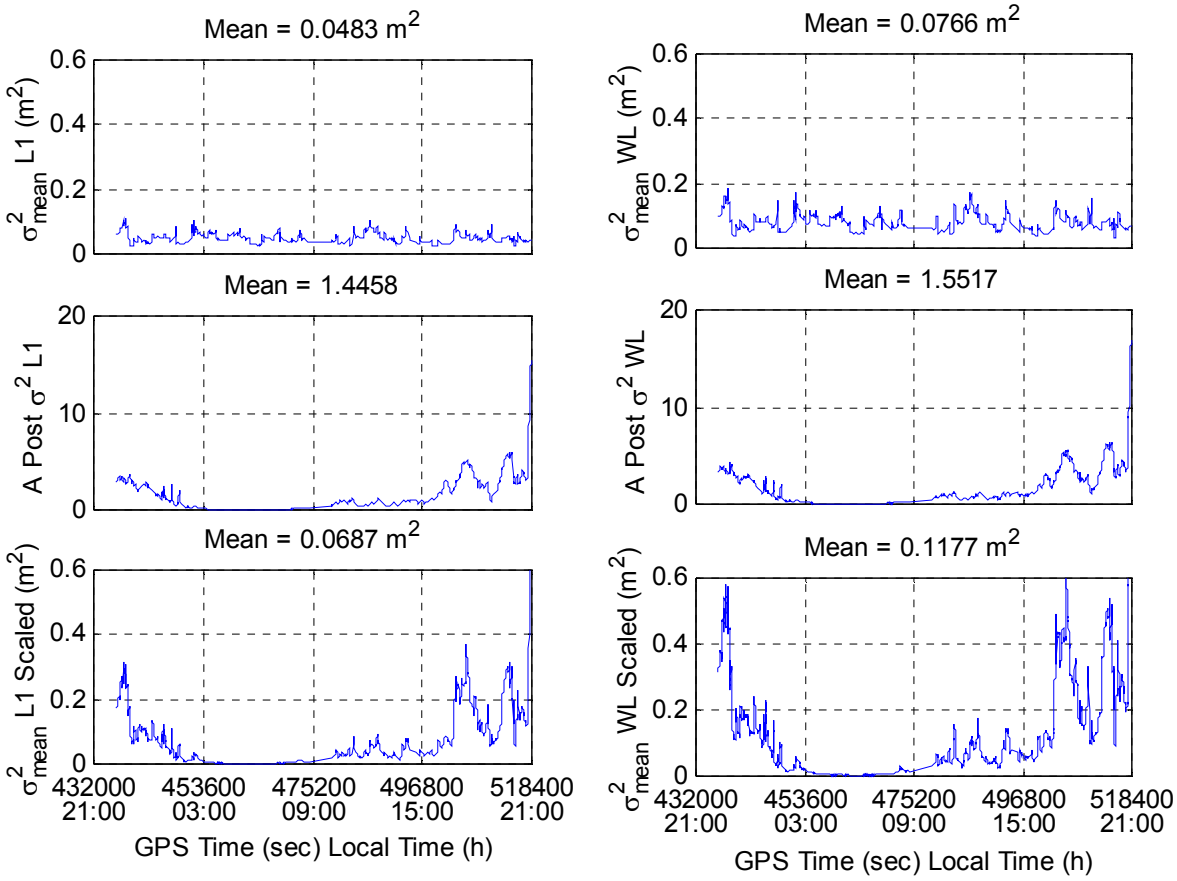

Figure 4.55: Quality estimation of the reference station's corrections for L1 and WL for the third scenario (BOTU as rover) for August 11, 1999, using the August 13, 1999 covariance functions: mean variance (top graphs), *a posteriori* variance of unit weight (graphs in the middle), and mean variance scaled by the *a posteriori* variance (bottom graphs)

Table 4.16: Mean values over time of the mean variance, the *a posteriori* variance and the scaled mean variance of the reference station's corrections for L1 and WL using the November 1998 (in blue) and the August 13, 1999 (in red) covariance functions

Baseline	Length (km)	Mean Variance (m^2)		*A Posteriori* Variance		Mean Variance Scaled (m^2)	
		L1	WL	L1	WL	L1	WL
FRAN-LIMO	122						
August 11		0.0229	0.0283	1.5658	2.2794	0.0397	0.0706
		0.0511	0.0824	0.7665	0.8333	0.0444	0.0775
August 13		0.0264	0.0322	2.8989	4.1853	0.0726	0.1273
		0.0643	0.1044	1.5723	1.6918	0.0962	0.1683
AGUA-SJRP	146						
August 11		0.0193	0.0244	1.5230	2.3237	0.0325	0.0617
		0.0414	0.0669	0.6424	0.6866	0.0300	0.0517
August 13		0.0212	0.0269	2.5509	3.7767	0.0529	0.0986
		0.0427	0.0683	1.1449	1.2174	0.0486	0.0831
REGI-BOTU	193						
August 11		0.0249	0.0315	1.4865	2.1720	0.0403	0.0740
		0.0492	0.0782	0.8046	0.8842	0.0429	0.0750
August 13		0.0249	0.0315	2.4373	3.4988	0.0579	0.1045
		0.0483	0.0766	1.4458	1.5517	0.0687	0.1177

4.3.2.4 Improvement Brought by the Multi-Ref Method Using Extreme Cases of the Original Covariance Functions

The results obtained using the original covariance functions recomputed using data collected in August 1999 indicate that the Multi-Ref method is not very sensitive to the covariance functions used, except for some few cases corresponding to remote satellites at very low elevations. As the covariance functions used in this chapter were computed using real data and, as such, limited by the actual observation conditions, it was necessary to verify if that low sensitivity also held in very extreme cases. Therefore covariance functions were simulated in order to reproduce extremely high and low error conditions. Table 4.17 lists the corresponding $\mathbf{k_1}$ and $\mathbf{k_2}$ coefficients for these two extreme cases. The values for L1 were chosen to generate variances that were orders of magnitude larger and smaller than the ones computed using the real data, whereas the coefficient values for WL were computed multiplying the L1 values by 0.080, which corresponds to the ratio between the ionospheric effect on WL and L1 (in cycles) squared. Special care was taken in order not to select coefficients that would be multiples of those computed using real data, as the corrections computed using Equations 3.15 and 3.16 do not change if the covariance matrices are multiplied by a scalar. Figure 4.56 shows the corresponding L1 (on the left) and WL (on the right) correlated error functions (given by Equation 3.33) for both extreme cases and for the November 1998, and August 13, 1999, covariance functions (this last two are the same ones shown at the bottom of Figure 4.47). Due to the

large differences between the functions, the plots are shown twice (on the top and at the bottom), since it was necessary to vary the y-axis scale to see them all.

Table 4.17: k_1 and k_2 coefficients for extreme cases of the correlated error functions

Coefficient	L1	WL
Extreme high		
k_1[a]	1.00000e-01	8.00000e-03
k_2[b]	1.00000e-02	8.00000e-04
Extreme low		
k_1[a]	1.00000e-07	8.00000e-09
k_2[b]	1.00000e-08	8.00000e-10

a: $cycles^2/km$; b: $cycles^2/km^2$

Using the coefficients listed in Table 4.17 along with the $\mathbf{k_\mu}$ coefficients for the L1 and WL mapping functions computed previously using the Brazilian data (listed in Table 4.13), the Multi-Ref approach was applied to the second scenario (i.e. with SJRP station as the rover – see Figure 4.19) for August 13, 1999. The improvement in the observation domain is shown in Table 4.18 for both extreme cases. For the sake of comparison, the results using the original covariance functions computed using data collected on August 13, 1999 (from Table 4.14) are also included in this table. In can be seen that the Multi-Ref performance changes only at the millimetre level when the extreme cases of the correlated error functions are used, confirming the low sensitivity of the method to the covariance functions utilised. Figures 4.57 and 4.58 show, for the

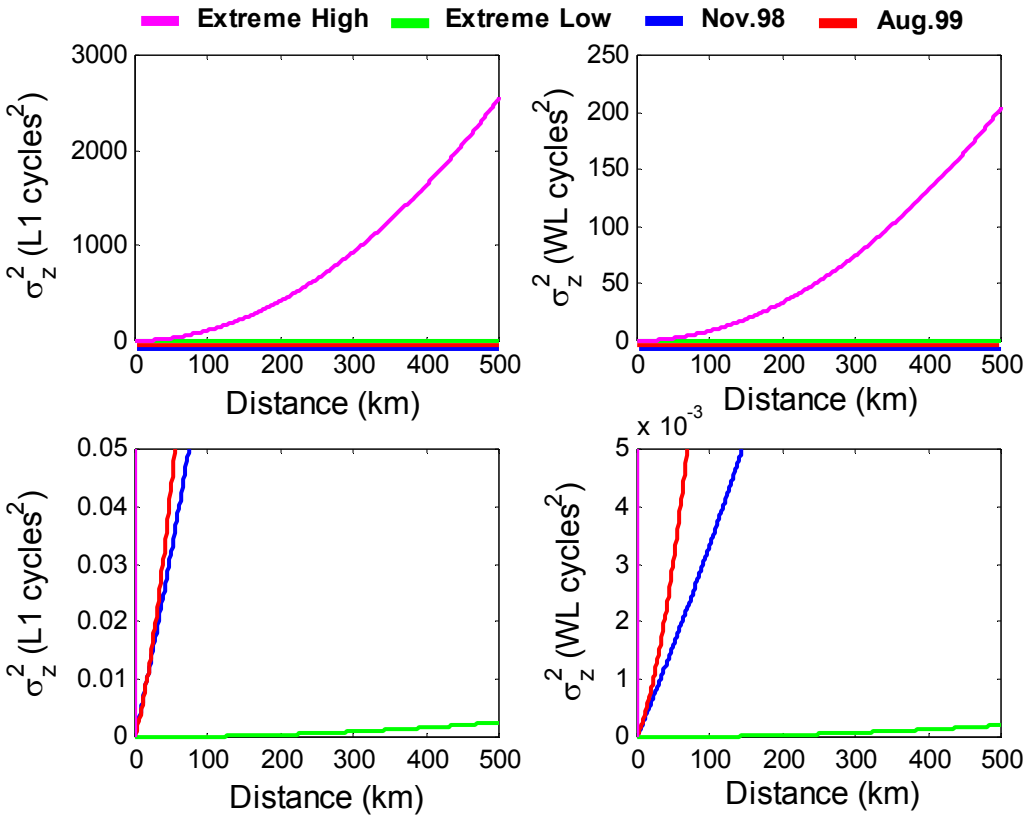

Figure 4.56: Extreme high (in magenta) and low (in green) cases of the correlated error functions, shown twice (on the top and at the bottom) with different y-axis scales. The corresponding functions computed using November 1998 St. Lawrence data (in blue), and August 13, 1999, Brazilian data (in red) are also shown

extreme high and low cases, respectively, the raw and corrected double difference L1 and WL misclosures for that baseline (AGUA to SJRP). Comparing with Figure 4.48, which corresponds to the original covariance functions computed with data collected on August 13, 1999, it can be seen that they are all very similar, except for the position of isolated dots.

Table 4.18: Raw and Multi-Ref-corrected double difference misclosures RMS and respective improvement for AGUA to SJRP baseline (146 km) for August 13, 1999, using the extreme high and low cases of the correlated error functions. The results using the original covariance functions computed using data collected on August 13, 1999 are also included

Baseline	Length (km)	L1 (m)			WL (m)		
		Raw	Corr.	Improv.	Raw	Corr.	Improv.
AGUA-SJRP	146						
Extreme high		0.350	0.127	64%	0.440	0.166	62%
Extreme low		0.350	0.123	65%	0.440	0.176	60%
August 13		0.350	0.130	63%	0.440	0.170	61%

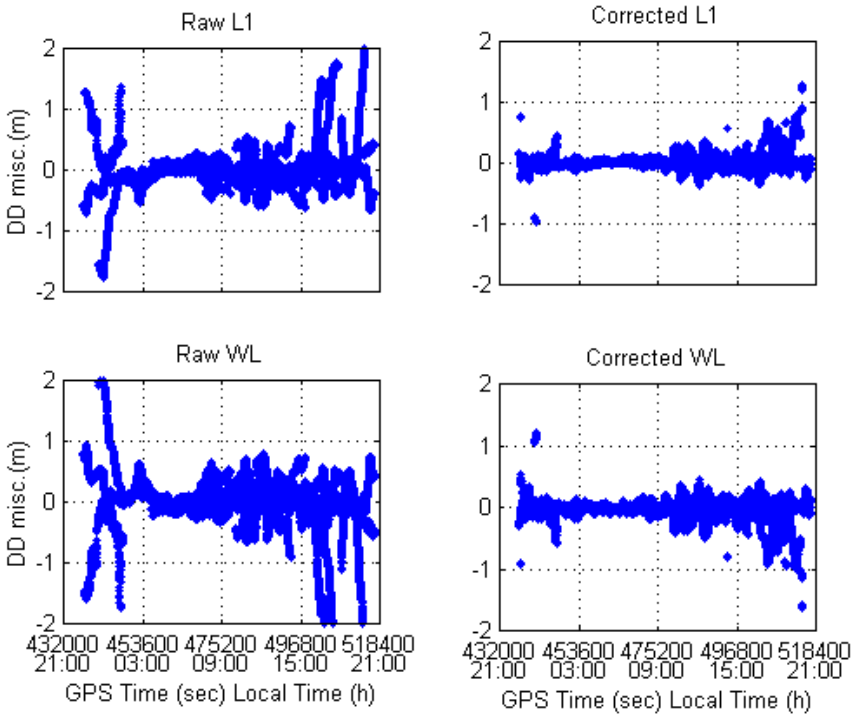

Figure 4.57: Raw and Multi-Ref-corrected L1 and WL double difference misclosures for AGUA to SJRP baseline (146 km) for August 13, 1999, using the extreme high case of the correlated error functions

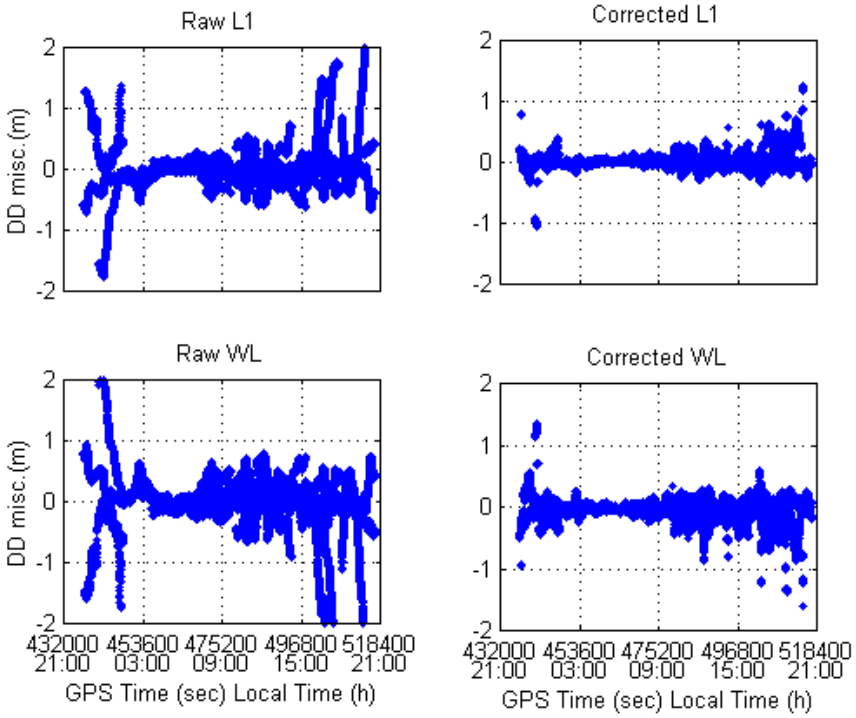

Figure 4.58: Raw and Multi-Ref-corrected L1 and WL double difference misclosures for AGUA to SJRP baseline (146 km) for August 13, 1999, using the extreme low case of the correlated error functions

CHAPTER 5

OPTIMISING MULTI-REF THROUGH MODELLING THE ERRORS SEPARATELY IN THE COVARIANCE FUNCTIONS

From Chapter 2, it could be seen that the behaviour of each correlated error that affects GPS positioning is not expected to be the same over the region covered by the reference network. Hence an attempt was made in this chapter to separately model the differential ionosphere, troposphere and satellite orbits, in order to assess how much improvement this could bring to the quality of the Multi-Ref results.

Separate modelling of the errors was carried out by generating different covariance functions for each kind of observable that "isolates" the correlated errors. So, the ionospheric-free linear combination was used to model the troposphere together with the satellite orbit errors, whereas the geometric-free linear combination scaled to L1 was used to model the ionosphere signal on L1 (see Chapter 2 for a description of these linear combinations).

5.1 Covariance Function for Tropospheric and Satellite Orbit Errors

As previously mentioned, the ionospheric-free linear combination was used here. This linear combination eliminates the first order effect of the ionosphere, with the tropospheric and satellite orbit errors, in addition to noise and multipath, remaining. Ideally, it would be better to not have more than one type of correlated error modelled by the observable used. This could be achieved if IGS final precise orbits were used, according to the approach derived by Zhang [1999]. However, as the intent is to ultimately generate corrections for a real time service, these orbits would not be available to the service provider. Another option would be using the IGS ultra-rapid orbits, which include post-processed and predicted satellite positions, as seen in Chapter 2 (the predicted positions would be used then). Despite the fact that these orbits are not as accurate as the final ones ($\approx \pm$ 25 cm as opposite to $< \pm 5$ cm accuracy – see Table 2.1), they represent a significant improvement over the broadcast ones ($\pm$ 436 cm accuracy – see Table 2.2) and would have very little impact on the double difference observations. On the other hand, its real time use implies the necessity of implementing its transmission to the users. In addition, one of the big advantages of the Multi-Ref approach is to generate corrected observations that could be input to an off-the-shelf processing software by the user, which could not be the case if ultra-rapid orbits were used. The last option would be to use the broadcast orbits. Despite the fact that its accuracy can be more than ten times worse than the one given by the ultra-rapid orbits, the differential error

propagated to the baseline components is relatively small, according to Equation 2.6, rewritten below:

$$\frac{db}{b} = \frac{d\rho}{\rho} \tag{5.1}$$

Considering an orbit error (**dρ**) of 4.36 m, and 20,000 km for **ρ**, a **db/b** equal to 0.22 ppm is obtained. Then, for a 100-km baseline, this gives an error of 2.2 cm in the coordinates of the baseline due to the orbital errors. This is sometimes considered pessimistic in terms of the observation domain, as Equation 5.1 estimates the propagated error in the position domain. The actual error in the observation domain is expected to be 4 to 10 times smaller [Beutler et al., 1998]. Hence the residual satellite orbit errors, as they are not excessive even using broadcast ephemerides, can be modelled together with the tropospheric ones using the ionospheric-free linear combination.

To generate the covariance function for the ionospheric-free observable, a proper mapping function to reduce the observations to the zenith needed to be selected. In addition, a different formula than the one shown in Equation 3.41 was derived, as using the average of the mapping function values computed using the base and remote satellite elevations seemed to have simplified the approach (the idea behind the optimisation was to avoid approximations as much as possible). The following procedure was therefore used:

$$\Delta\nabla T_{ab}^{xy} = T_a^x - T_a^y - (T_b^x - T_b^y) = \\ = \mu_a^x T_{a_z}^x - \mu_a^y T_{a_z}^y - (\mu_b^x T_{b_z}^x - \mu_b^y T_{b_z}^y) \tag{5.2}$$

where $\Delta\nabla T_{ab}^{xy}$ is the double difference misclosure for the baseline defined by stations **a** and **b** and satellites **x** and **y** for the ionospheric-free observables; T_a^x is the undifferenced misclosure from station **a** to satellite **x** (analogously for station **b** and satellite **y**); $T_{a_z}^x$ is the undifferenced misclosure from station **a** to satellite **x** reduced to the zenith using the μ_a^x mapping function (analogously for station **b** and satellite **y**). Considering that one can assume that the zenith errors are independent of the satellite and that for baseline lengths in regional networks the mapping function values computed to the same satellite from different stations are the same, the following equalities can be written:

$$T_{a_z}^x = T_{a_z}^y = T_{a_z} \tag{5.3}$$

$$T_{b_z}^x = T_{b_z}^y = T_{b_z} \tag{5.4}$$

$$\mu_a^x = \mu_b^x = \mu^x \tag{5.5}$$

$$\mu_a^y = \mu_b^y = \mu^y \tag{5.6}$$

Substituting Equations 5.3 to 5.6 into 5.2, the following is obtained:

$$\Delta\nabla T_{ab}^{xy} = (\mu^x - \mu^y)(T_{a_z} - T_{b_z}) \tag{5.7}$$

Then:

$$\Delta T_{ab_z} = T_{a_z} - T_{b_z} = (\mu^x - \mu^y)^{-1} \Delta\nabla T_{ab}^{xy} \tag{5.8}$$

which gives the relationship between the double difference misclosure and the differential error between stations **a** and **b** reduced to the zenith. In applying Equation 5.8, special care has to be taken to select double differences for which the absolute value of the term $(\mu^x - \mu^y)$ is not too small (> 0.2), in order to avoid numerical problems, similar to what was shown by Zhang [1999].

The following mapping function was used for the ionospheric-free observables, valid for elevations greater than 10°:

$$\mu(\varepsilon) = \frac{1}{\sin\varepsilon} \tag{5.9}$$

where ε is the satellite elevation. Zhang [1999] used real data to fit a mapping function based on Equation 5.9, similar to what Raquet [1998] had done for the lumped case, and practically obtained the same as Equation 5.9. So, in addition to representing the basic mapping function for the troposphere, it was validated using real data. More sophisticated functions could have been used (see Mendes [1999], for a vast list of possibilities), but considering the magnitude of the errors to be modelled (a few centimetres) and that generally the largest differences between models occur below a 15-degree elevation, the impact of the extra sophistication on the Multi-Ref results would be negligible.

A second degree polynomial was used again for the correlated error function (Equation 3.33).

The following steps were followed in order to compute the covariance function for the tropospheric and satellite orbit errors:

- For each double difference misclosure of each baseline, compute the corresponding differential error between stations **a** and **b** reduced to the zenith ($\mathbf{\Delta T_{ab_z}}$) using Equation 5.8 and the mapping function given by Equation 5.9;
- For each baseline in the network, compute the variance of $\mathbf{\Delta T_{ab_z}}$;
- Compute $\mathbf{k_1}$ and $\mathbf{k_2}$ coefficients based on a Least-Squares adjustment using the variances of $\mathbf{\Delta T_{ab_z}}$ as observations in the following mathematical model:

$$E\{(\Delta T_{ab_z})^2\} = k_1 d_{ab} + k_2 d_{ab}^2 + \sigma_{u_z}^2(a) + \sigma_{u_z}^2(b) \quad (5.10)$$

where $\mathbf{d_{ab}}$ is the 3-D distance between points **a** and **b**.

Analogous to what was done in previous cases, the variances of the uncorrelated errors ($\boldsymbol{\sigma}_{\mathbf{u_z}}^{\mathbf{2}}$) in Equation 5.10 were not estimated, but a nominal value for the ionospheric-free linear combination equal to 3.7717e-05 m^2 (see Section 2.2.1) was used instead.

One can see that Equation 5.10 is similar to 3.42, except that in the latter the quantity modelled is based on double differences and thus the entire formula is multiplied by a factor of 2. Equation 5.10 can be derived as follows.

The total error (correlated plus uncorrelated) present in an observable is given by (see Section 3.2.1):

$$\delta l = \delta_c l(p, p_0)_z + \delta_u l_{p_z} = \delta_c l(p)_z - \delta_c l(p_0)_z + (\delta_u l_p)_z \quad (5.11)$$

Using Equation 5.11, the differential tropospheric error ($\boldsymbol{\Delta T_{ab_z}}$) between stations **a** and **b** reduced to the zenith can then be expressed by:

$$
\begin{aligned}
\Delta T_{ab_z} &= \delta_c l(p_a, p_0)_z + (\delta_u l_a)_z - [\delta_c l(p_b, p_0) + (\delta_u l_b)_z] = \\
&= \delta_c l(p_a)_z - \delta_c l(p_0)_z + (\delta_u l_a)_z - \\
&- [\delta_c l(p_b)_z - \delta_c l(p_0)_z + (\delta_u l_b)_z] = \\
&= \delta_c l(p_a)_z - \delta_c l(p_0)_z + (\delta_u l_a)_z - \\
&- \delta_c l(p_b)_z + \delta_c l(p_0)_z - (\delta_u l_b)_z = \\
&= \delta_c l(p_a)_z - \delta_c l(p_b)_z + (\delta_u l_a)_z - (\delta_u l_b)_z
\end{aligned}
\tag{5.12}
$$

The variance of $\mathbf{\Delta T_{ab_z}}$ is obtained using Equation 5.12, as follows:

$$
E\{(\Delta T_{ab_z})^2\} = E\{[\delta_c l(p_a)_z - \delta_c l(p_b)_z + (\delta_u l_a)_z - (\delta_u l_b)_z]^2\} \tag{5.13}
$$

Recalling that the uncorrelated errors are not correlated with anything else except themselves, the expectation of the product between them and any other term on Equation 5.13 cancels when the square is performed, giving:

$$
\begin{aligned}
E\{(\Delta T_{ab_z})^2\} &= E\{[\delta_c l(p_a)_z - \delta_c l(p_b)_z]^2\} + \\
&+ E\{[(\delta_u l_a)_z]^2\} + E\{[(\delta_u l_b)_z]^2\}
\end{aligned}
\tag{5.14}
$$

Remembering that $\sigma^2_{c_z}(p_m, p_n) = E\{[\delta_c l(p_m)_z - \delta_c l(p_n)_z]^2\}$ (see Section 3.2.1.1) and taking into account Equations 3.33 and 3.34 in 5.14, Equation 5.10 is obtained.

Once the $\mathbf{k_1}$, $\mathbf{k_2}$ coefficients are computed, they are used along with $\boldsymbol{\sigma}^2_{\mathbf{u}_z}$ in Equation 3.27 to derive the covariance matrices, which are necessary to calculate the Multi-Ref corrections using Equations 3.15 and 3.16. It is important to note that the Multi-Ref corrections refer to the type of observable that is used in those equations. So, if one uses L1 or WL, as in the previous cases, the values obtained are corrections to be applied to the L1 and WL observations. If one uses the ionospheric-free observable, the corrections are related to this observable, which means that they are values to correct for tropospheric and satellite orbit errors (actually, the corrections also accounted for multipath and noise, which normally represent the smallest portion of the error budget). After computed, these corrections are applied to any observable, according to the following:

L1 code: $$Cl_T = Cl + \hat{T} \tag{5.15}$$

L1 phase: $$Ll_T = L1 + \frac{\hat{T}}{\lambda_1} \tag{5.16}$$

L2 phase: $$L2_T = L2 + \frac{\hat{T}}{\lambda_2} \tag{5.17}$$

Widelane: $$WL_T = WL + \frac{\hat{T}}{\lambda_{WL}} \quad (5.18)$$

Ionospheric-free: $$IF_T = IF + \frac{\hat{T}}{\lambda_{IF}} \quad (5.19)$$

Where $\hat{T}$ represents the Multi-Ref correction for troposphere and satellite orbits expressed in metres and the subscript T indicates an observable corrected for these errors (in metres, for C1, and in cycles for the remaining ones).

5.2 Covariance Function for Ionospheric Errors

The geometric-free linear combination scaled to L1 was used in this case. As seen in Chapter 2, this linear combination eliminates the tropospheric and satellite orbit errors, with the ionospheric errors affecting the L1 observables remaining, in addition to noise and multipath.

Analogous to what was done when modelling the tropospheric and satellite orbit errors, a proper mapping function to reduce the observations to the zenith needed to be selected in order to generate the covariance function for the geometric-free observable. An equation analogous to 5.8, used for the troposphere and orbit case, was also derived herein, in substitution to Equation 3.41. There is a conceptual difference behind the derivation of Equation 5.8 and the procedure that follows: in the first case, the equalities

shown in Equations 5.3 and 5.4 hold, as the observations reduced to the zenith are valid at the reference stations **a** and **b**; however, the same is not true for the ionospheric case. Figure 5.1 shows the single layer model of the ionosphere. In this model it is assumed that all free electrons are concentrated in a shell of infinitesimal thickness at a certain altitude, H [Schaer, 1999]. When the mapping function is applied to the undifferenced misclosures I_a^x, I_a^y, I_b^x, and I_b^y, the resultant values reduced to the zenith $I_{a_z}^x$, $I_{a_z}^y$, $I_{b_z}^x$ and $I_{b_z}^y$ are referred to the ionospheric pierce points **a'**, **a"**, **b'**, and **b"**, respectively (the arrows at these points in Figure 5.1 are verticals pointing towards the zenith), as the ionospheric refraction occurs at the shell.

From Figure 5.1:

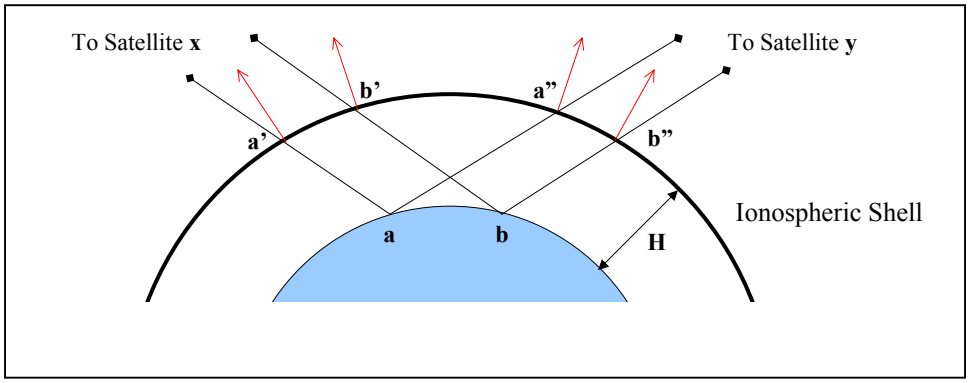

Figure 5.1: The single layer model of the ionosphere, with a double-difference observation (from stations a and b to satellites x and y) shown

$$\begin{aligned}\Delta\nabla I_{ab}^{xy} &= I_a^x - I_a^y - (I_b^x - I_b^y) = \\ &= \mu_a^x I_{a_z}^x - \mu_a^y I_{a_z}^y - (\mu_b^x I_{b_z}^x - \mu_b^y I_{b_z}^y)\end{aligned} \tag{5.20}$$

where $\Delta\nabla I_{ab}^{xy}$ is the double difference misclosure for the baseline defined by stations **a** and **b** and satellites **x** and **y** for the geometric-free observables; $I_{a_z}^x$ is the undifferenced misclosure from station **a** to satellite **x** reduced to the zenith using the μ_a^x mapping function (analogously for station **b** and satellite **y**). Considering that for baseline lengths in regional networks the mapping function values computed to the same satellite from different stations are practically the same, the following equalities can be written:

$$\mu_a^x = \mu_b^x = \mu^x \tag{5.21}$$

$$\mu_a^y = \mu_b^y = \mu^y \tag{5.22}$$

Substituting Equations 5.21 and 5.22 into 5.20, the following one is obtained:

$$\begin{aligned}\Delta\nabla I_{ab}^{xy} &= \mu^x I_{a_z}^x - \mu^y I_{a_z}^y - (\mu^x I_{b_z}^x - \mu^y I_{b_z}^y) = \\ &= \mu^x (I_{a_z}^x - I_{b_z}^x) - \mu^y (I_{a_z}^y - I_{b_z}^y)\end{aligned} \tag{5.23}$$

Squaring Equation 5.23 and applying the expectation operator, one gets:

$$
\begin{aligned}
E\{(\Delta\nabla I_{ab}^{xy})^2\} &= E\{[\mu^x(I_{a_z}^x - I_{b_z}^x) - \mu^y(I_{a_z}^y - I_{b_z}^y)]^2\} = \\
&= E\{[\mu^x(I_{a_z}^x - I_{b_z}^x)]^2 - \\
&\quad - 2\mu^x\mu^y(I_{a_z}^x - I_{b_z}^x)(I_{a_z}^y - I_{b_z}^y) + \\
&\quad + [\mu^y(I_{a_z}^y - I_{b_z}^y)]^2\} = \\
&= (\mu^x)^2 E\{(I_{a_z}^x - I_{b_z}^x)^2\} - \\
&\quad - 2\mu^x\mu^y E\{(I_{a_z}^x - I_{b_z}^x)(I_{a_z}^y - I_{b_z}^y)\} + \\
&\quad + (\mu^y)^2 E\{(I_{a_z}^y - I_{b_z}^y)^2\}
\end{aligned}
\tag{5.24}
$$

As, by definition, $\Delta I_{ab_z}^x = I_{a_z}^x - I_{b_z}^x$, Equation 5.24 becomes:

$$
\begin{aligned}
E\{(\Delta\nabla I_{ab}^{xy})^2\} &= (\mu^x)^2 E\{(\Delta I_{ab_z}^x)^2\} - \\
&\quad - 2\mu^x\mu^y E\{(\Delta I_{ab_z}^x)(\Delta I_{ab_z}^y)\} + \\
&\quad + (\mu^y)^2 E\{(\Delta I_{ab_z}^y)^2\}
\end{aligned}
\tag{5.25}
$$

The term $E\{(\Delta I_{ab_z}^x)(\Delta I_{ab_z}^y)\}$ represents the covariance between the ionospheric differential errors on L1 between the pierce points **a' - b'** and **a" - b**". Assuming that

these differential errors normally correspond to physically independent portions of the ionosphere, it is reasonable to consider for now that there is no correlation between them. Consequently, Equation 5.25 becomes:

$$E\{(\Delta\nabla I_{ab}^{xy})^2\} = (\mu^x)^2 E\{(\Delta I_{ab_z}^{x})^2\} + (\mu^y)^2 E\{(\Delta I_{ab_z}^{y})^2\} \tag{5.26}$$

In addition, Equation 5.14, derived for the tropospheric and satellite orbit errors, is valid if the correlated errors are considered over the ionosphere shell. Then, the following expressions can be written:

$$\begin{aligned} E\{(\Delta I_{ab_z}^{x})^2\} = {} & E\{[\delta_c l(p_{a'})_z - \delta_c l(p_{b'})_z]^2\} + \\ & + E\{[(\delta_u l_a)_z]^2\} + E\{[(\delta_u l_b)_z]^2\} \end{aligned} \tag{5.27}$$

$$\begin{aligned} E\{(\Delta I_{ab_z}^{y})^2\} = {} & E\{[\delta_c l(p_{a''})_z - \delta_c l(p_{b''})_z]^2\} + \\ & + E\{[(\delta_u l_a)_z]^2\} + E\{[(\delta_u l_b)_z]^2\} \end{aligned} \tag{5.28}$$

Taking into account Equations 3.33 (for a second degree polynomial for the correlated error function) and 3.34, Equations 5.26 and 5.27 become:

$$E\{(\Delta I_{ab_z}^{x})^2\} = k_1 d_{a'b'} + k_2 d_{a'b'}^2 + \sigma_{u_z}^2(a) + \sigma_{u_z}^2(b) \tag{5.29}$$

$$E\{(\Delta I^{y}_{ab_z})^2\} = k_1 d_{a''b''} + k_2\, d^2_{a''b''} + \sigma^2_{u_z}(a) + \sigma^2_{u_z}(b) \tag{5.30}$$

Substituting Equations 5.29 and 5.30 into 5.26, one gets:

$$\begin{aligned} E\{(\Delta\nabla I^{xy}_{ab})^2\} = {} & (\mu^x)^2[k_1 d_{a'b'} + k_2\, d^2_{a'b'} + \sigma^2_{u_z}(a) + \sigma^2_{u_z}(b)] + \\ & + (\mu^y)^2[k_1 d_{a''b''} + k_2\, d^2_{a''b''} + \sigma^2_{u_z}(a) + \sigma^2_{u_z}(b)] \end{aligned} \tag{5.31}$$

And factoring Equation 5.31 to isolate $\mathbf{k_1}$ and $\mathbf{k_2}$ coefficients:

$$\begin{aligned} E\{(\Delta\nabla I^{xy}_{ab})^2\} = {} & [(\mu^x)^2 d_{a'b'} + (\mu^y)^2 d_{a''b''}]\, k_1 + \\ & + [(\mu^x)^2\, d^2_{a'b'} + (\mu^y)^2\, d^2_{a''b''}]\, k_2 + \\ & + [(\mu^x)^2 + (\mu^x)^2][\sigma^2_{u_z}(a) + \sigma^2_{u_z}(b)] \end{aligned} \tag{5.32}$$

Equation 5.32 represents the observation equation to be used in a Least-Squares adjustment to determine the coefficients $\mathbf{k_1}$ and $\mathbf{k_2}$. Despite being derived rigorously, its application is very difficult because the distances $\mathbf{d_{a'b'}}$ and $\mathbf{d_{a''b''}}$ computed on the shell vary at every data epoch due to the satellite motion. Hence it is not possible to average the values of $\mathbf{(\Delta\nabla I^{xy}_{ab})^2}$ for each baseline in order to estimate $\mathbf{E\{(\Delta\nabla I^{xy}_{ab})^2\}}$. As a result, each individual value of $\mathbf{(\Delta\nabla I^{xy}_{ab})^2}$ for each baseline has to be used in the adjustment,

generating one observation equation. For the 35 baselines used in the Brazilian network, this corresponded to 902,594 observation equations in total. And, as the individual values of $(\Delta\nabla \mathbf{I}_{\mathbf{ab}}^{\mathbf{xy}})^{\mathbf{2}}$ are poor estimates of $\mathbf{E}\{(\Delta\nabla \mathbf{I}_{\mathbf{ab}}^{\mathbf{xy}})^{\mathbf{2}}\}$, the quality of the adjustment was not satisfactory, generating coefficients that, when applied to compute Multi-Ref corrections, performed worse than the original November, 1998, covariance functions (Section 4.3.2.1). In order to overcome the difficulties discussed above, an approximation had to be implemented. Despite the fact that the single layer model of the ionosphere is closer to reality, a more simplified model was used which assumed that the relative ionospheric errors are valid between stations on the Earth surface, analogous to what was carried out for the tropospheric and satellite orbit errors. Therefore, instead of Equation 5.32, the following was used:

$$E\{(\Delta I_{ab_z})^2\} = k_1 d_{ab} + k_2 d_{ab}^2 + \sigma_{u_z}^2(a) + \sigma_{u_z}^2(b) \tag{5.33}$$

where $\mathbf{d_{ab}}$ is the 3-D distance between points **a** and **b** located at the surface of the Earth.

The derivation of Equation 5.33 is absolutely analogous to 5.10 (presented in Section 5.1), using a second degree polynomial for the correlated error function.

The mapping function used for the geometric-free observable is [Skone, 1998; Schaer, 1999]:

$$\mu(\varepsilon') = \frac{1}{\sin \varepsilon'} \tag{5.34}$$

where **ε'** is the satellite elevation measured at the ionospheric pierce point. According to the geometric elements shown in Figure 5.2, Skone [1998] and Schaer [1999] translated Equation 5.34 into another one as a function of the satellite elevation measured at the station on the ground (**ε**). The resultant mapping function is:

$$\mu(\varepsilon) = \left[1 - \left(\frac{\cos(\varepsilon)}{1 + \frac{H}{R}} \right)^2 \right]^{-\frac{1}{2}} \tag{5.35}$$

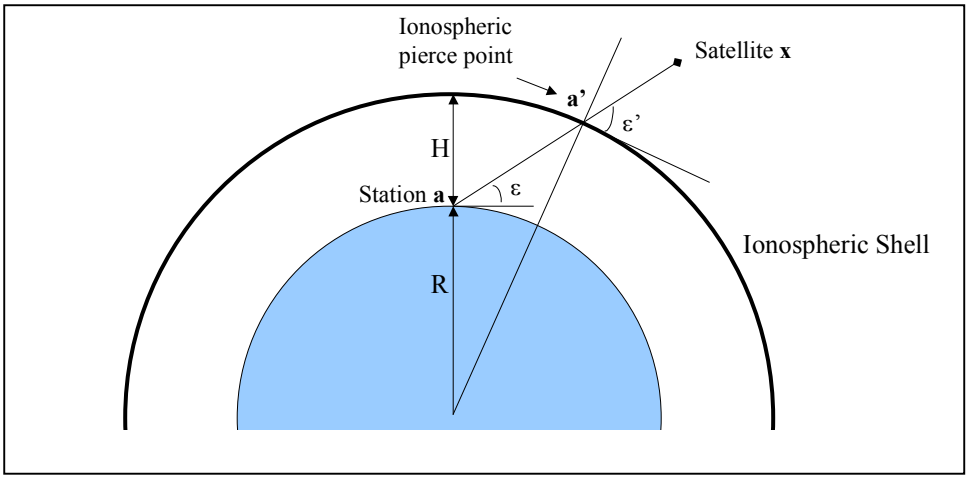

Figure 5.2: The single layer model of the ionosphere, with satellite elevation angles ε (from station a) and ε' (from the pierce point a') shown

where **H** is the height of the ionospheric shell and **R** (≈ 6371 km) is the mean radius of the Earth. **H** is normally chosen to be a value between 350 and 450 km. Schaer [1999] used data from global IGS stations collected from January, 1995, to March, 1998, to compute global ionospheric maps, treating **H** as an additional unknown parameter. The average adjusted **H** was approximately equal to 450 km, and then this value was used in this thesis. Another possibility for the mapping function would be to use the one suggested by Klobuchar [1996] for the broadcast ionospheric model (Equation 3.37). Figure 5.3 shows four different mapping functions for comparison purposes: the single layer model (SLM) with H = 350 km; SLM with H = 450 km; the Klobuchar [1996]

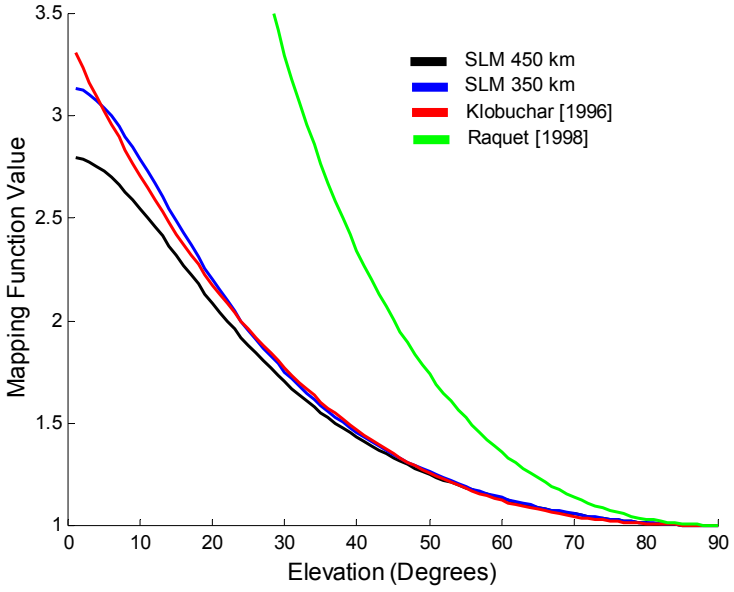

Figure 5.3: Three mapping functions for the ionosphere: the single layer model with H = 350 and 450 km, and the Klobuchar model. The Raquet mapping function (with $k_\mu = 27$) was also included for comparison

model; and the Raquet [1998] model (Equation 3.35), with k_μ = 27 in this example. Figure 5.4 shows the ratio between the SLM 350 km, the Klobuchar model and the Raquet model with respect to the SLM 450 km. Based on these figures, it can be seen that the Klobuchar mapping function approximates the SLM with **H** = 350 km. In addition, the SLM 450 km gives values only slightly smaller than the ones given by the SLM 350 km (which means that the choice of **H** in the Multi-Ref context is not so significant). The difference between the Raquet model and all the others is significant, as expected, as the former one is driven by the tropospheric mapping function (1/sin ε). Considering that the ionosphere was the dominant correlated error in both the St. Lawrence and the Brazilian data sets, the analysis of these figures suggests that the use of the Raquet mapping function in Multi-Ref was not adequate, justifying modelling the errors separately.

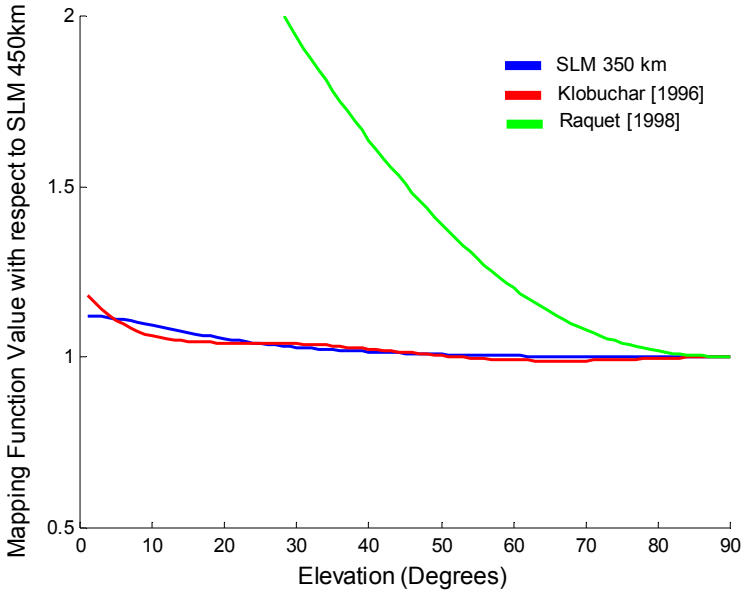

Figure 5.4: Ratio of the SLM 350 km, the Klobuchar and the Raquet mapping functions to the SLM 450 km one

The following steps were followed in order to compute the covariance function for the ionospheric errors:

- For each double difference misclosure of each baseline, compute the corresponding differential error between stations **a** and **b** reduced to the zenith ($\mathbf{\Delta I_{ab_z}}$) using the following equation (with the derivation being analogous to the one used to obtain Equation 5.8), and the mapping function given by Equation 5.35:

$$\Delta I_{ab_z} = I_{a_z} - I_{b_z} = (\mu^x - \mu^y)^{-1} \Delta\nabla I_{ab}^{xy} \tag{5.36}$$

  Again, only satellite pairs for which the absolute value of the difference $(\mu^x - \mu^y)$ was greater than 0.2 were considered;

- For each baseline in the network, compute the variance of $\mathbf{\Delta I_{ab_z}}$;
- Compute $\mathbf{k_1}$ and $\mathbf{k_2}$ coefficients based on a Least-Squares adjustment using the variances of $\mathbf{\Delta I_{ab_z}}$ as observations in the mathematical model given by Equation 5.33.

Analogous to what was done in previous cases, the variances of the uncorrelated errors ($\mathbf{\sigma^2_{u_z}}$) in Equation 5.33 were not estimated, but a nominal value for the geometric-free linear combination equal to 2.2901e-05 m^2 (see Section 2.3.1) was used instead.

The corrections to the geometric-free observations scaled to L1 are values to correct for ionospheric errors on L1 phase observations (actually, the corrections also accounted for multipath and noise, which normally represent the smallest portion of the error budget). After being computed, these corrections are applied to any observable, according to the following:

L1 code: $$Cl_I = Cl - \hat{I} \quad (5.37)$$

L1 phase: $$Ll_I = Ll + \frac{\hat{I}}{\lambda_1} \quad (5.38)$$

L2 phase: $$L2_I = L2 + (f_1^2 / f_2^2)\frac{\hat{I}}{\lambda_2} \quad (5.39)$$

Widelane: $$WL_I = WL - (f_1 / f_2)\frac{\hat{I}}{\lambda_{WL}} \quad (5.40)$$

Geometric-free scaled to L1: $$IS_{Ll_I} = IS_{L1} + \hat{I} \quad (5.41)$$

where $\hat{I}$ represents the Multi-Ref correction for the ionosphere expressed in metres and the subscript I indicates an observable corrected for these errors (in metres, for C1 and IS_{L1}, and in cycles for the remaining ones).

5.2.1 Variations in the Ionospheric Correlated Error Function

In the derivations of the procedure to compute the covariance function for the ionosphere, a second degree polynomial was implicitly used as the correlated error function. This function, given by Equation 3.33 and re-written below, proved to be a basic function that gave good results when used in both the original covariance functions (for L1 and WL) and the ones that model the errors separately (for troposphere/satellite orbits and for ionosphere).

$$\sigma^2_{c_z}(p_m, p_n) = k_1 d + k_2 d^2 \tag{5.42}$$

As far as separate modelling of the errors is concerned, the magnitude and behaviour of the ionospheric errors justified trying other options for the shape of the correlated error function, as a way to improve the final results obtained by the Multi-Ref approach.

Especially in regions under the equatorial anomaly, as the one where the Brazilian network is located, the occurrence of strong ionospheric gradients in periods close to the solar maximum, normally greater in north-south directions than in east-west ones, are expected. In order to investigate the directional dependency of the ionospheric gradients in the Brazilian data (which could justify the design of the covariance functions with

directional components), correlation coefficients were computed for every baseline pair using data collected on August 13. The procedure used was the following:

- All possible pairs extracted from the total number of 35 baselines that collected data on August 13 (see Table 4.2) were considered (595 baseline pairs in total);
- For each double difference misclosure of each baseline in the pair, compute the differential ionospheric error reduced to the zenith ($\mathbf{\Delta I_{ab_z}}$) using Equations 5.35 and 5.36. As before, only satellite pairs for which the absolute value of the difference $(\mu^x - \mu^y)$ was greater than 0.2 were considered;
- For each baseline pair, compute the covariance between the ionospheric differential errors according to the following equation:

$$\sigma_{(ab)(cd)} = \frac{1}{n}\sum_{i=1}^{n}(\Delta I_{ab_z})(\Delta I_{cd_z}) \tag{5.43}$$

where $\mathbf{\sigma_{(ab)(cd)}}$ is the covariance between baselines **a** to **b** and **c** to **d**; $\mathbf{\Delta I_{ab_z}}$ and $\mathbf{\Delta I_{cd_z}}$ are the individual differential ionospheric errors reduced to the zenith computed for each epoch in each baseline using common satellite pairs, i.e.:

$$\Delta I_{ab_z} = (\mu^x - \mu^y)^{-1}\Delta\nabla I_{ab}^{xy} \tag{5.44}$$

$$\Delta I_{cd_z} = (\mu^x - \mu^y)^{-1}\Delta\nabla I_{cd}^{xy} \tag{5.45}$$

and **n** is the total number of terms in the summation;

- Compute the correlation coefficient for each baseline pair according to the following equation [Maybeck, 1994]:

$$\rho_{(ab)(cd)} = \frac{\sigma_{(ab)(cd)}}{\sigma_{(ab)}\sigma_{(cd)}} \tag{5.46}$$

where $\boldsymbol{\rho_{(ab)(cd)}}$ is the correlation coefficient; $\boldsymbol{\sigma_{(ab)(cd)}}$ is given by Equation 5.43; and $\boldsymbol{\sigma_{(ab)}}$ and $\boldsymbol{\sigma_{(ab)}}$ are the standard deviations of $\boldsymbol{\Delta I_{ab_z}}$ and $\boldsymbol{\Delta I_{cd_z}}$, respectively, computed independently for each baseline (and using the same differential error values that participated in the calculation of the covariance in Equation 5.43).

Figure 5.5 shows the correlation coefficients for all 595 baseline pairs, computed according to the procedure described above, as a function of the azimuth difference of the baselines in each pair. It is clear that there is a strong correlation between the ionospheric differential errors for baselines with similar azimuths, and almost no correlation for baselines with 90-degree azimuth difference. Based on this fact, it seemed worth to try using a correlated error function that modelled the ionospheric errors into directional components. The following function corresponds to this model:

$$\sigma^2_{c_z}(p_m, p_n) = k_{1N}\Delta N + k_{2N}\Delta N^2 + k_{1E}\Delta E + k_{2E}\Delta E^2 \tag{5.47}$$

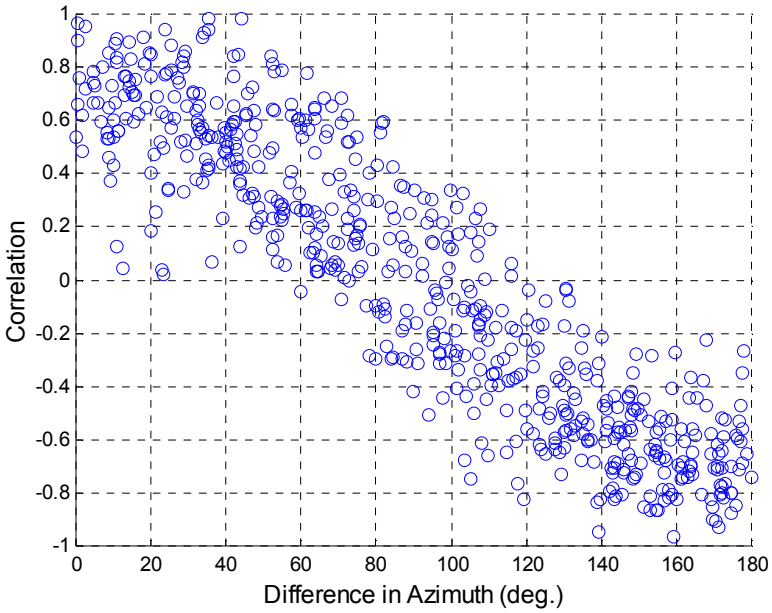

Figure 5.5: Differential zenith ionospheric error correlations between any two baselines in the Brazilian network as a function of the difference in azimuth of the baselines, computed using data collected on August 13, 2001

where **ΔN** and **ΔE** are, respectively, the north and east components of the baseline, and $\mathbf{k_{1N}}$, $\mathbf{k_{2N}}$, $\mathbf{k_{1E}}$, $\mathbf{k_{2E}}$ are the coefficients to be determined in a Least-Squares adjustment using the following observation equation:

$$\begin{aligned} E\{(\Delta I_{ab_z})^2\} = {} & k_{1N}\Delta N_{ab} + k_{2N}\,\Delta N_{ab}^2 + \\ & + k_{1E}\Delta E_{ab} + k_{2E}\,\Delta E_{ab}^2 + \\ & + \sigma_{u_z}^2(a) + \sigma_{u_z}^2(b) \end{aligned} \tag{5.48}$$

Equations 5.47 and 5.48 are equivalent to 5.42 and 5.33, respectively. The difference is that the baseline distance **d** in Equations 5.42 and 5.33 was split into north and east components (**ΔN** and **ΔE**, respectively) in order to model different ionospheric gradients along those directions. The concept of using directional error functions was used by some authors, for example Varner and Cannon [1997], Varner [2000], and Wanninger [1999].

In addition to the directional correlated error function given by Equation 5.47, other ones were tested using the Brazilian data set. One based on a third degree polynomial function was tried, giving very poor results. The RMS of the Multi-Ref–corrected misclosures computed using a third degree polynomial was worse than the one of the raw misclosures, indicating that this function was not appropriate. Later, it was found out that the normal matrix to be inverted to compute the corrections (term $BC_{\delta l}B^T$ in Equations 3.15 and 3.16) was not positive definite. Another one, based on the second degree polynomial (Equation 5.42), was also tested, this time in an adaptive context. Considering the variation of the ionospheric effects with local time, an attempt was made in terms of computing coefficients that changed with time. In this case, a different set of coefficients was calculated for every 30 or 60 minutes. The improvement brought by the Multi-Ref method was worse than using the original November, 1998, covariance functions (Section 4.3.2.1). This can be explained by the fact that the adjustment performed for every range of time was not satisfactory, probably due to the lack of

redundant observations (instead of about 30,000 observations – present in 24 hours - to compute the variance of the differential ionospheric errors - $\mathbf{E\{(\Delta I_{ab_z})^2\}}$ - only about 625 were used to compute coefficients every 30 minutes, for instance). Figure 5.6 shows the ionospheric error functions computed every 30 minutes using data collected on August 13, 1999. It can be seen their variability along the day, which depends on the ionospheric conditions in each 30-minute time interval. As mentioned previously, the quality of each function was not enough to produce an improvement with respect to the function computed using 24 hours of data (also shown in the figure).

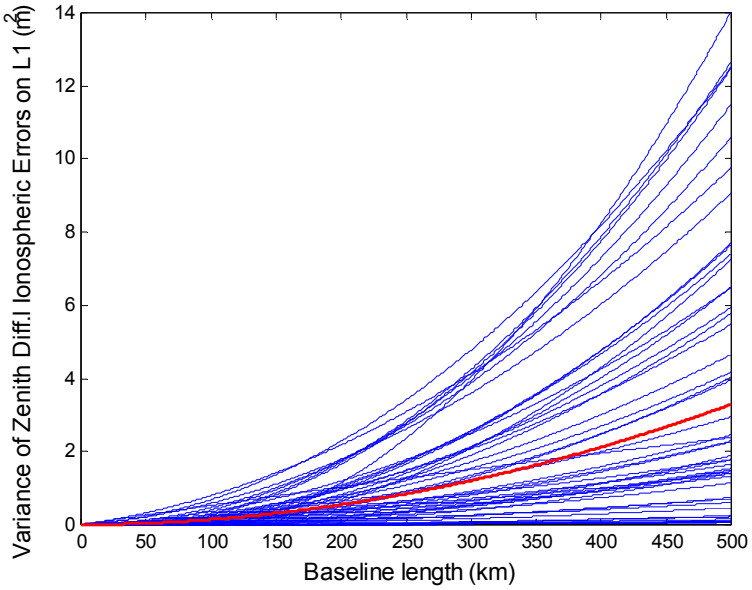

Figure 5.6: Ionospheric error functions computed for every 30 minutes (in blue) and for 24 hours (in red) using data collected in Brazil on August 13, 1999

Hence only results using the directional correlated error function (Equation 5.47), besides the ones obtained with the basic second degree polynomial (Equation 5.42), are shown in the subsequent sections using the St. Lawrence and the Southeastern Brazil data sets.

5.3 St. Lawrence Network

5.3.1 Computation of the Covariance Function for the Troposphere and Satellite Orbits Using Data Collected on August 4, 1999

Using ionospheric-free (IF) misclosures for August 4, 1999, described in Section 4.2.1, and the procedure described in Section 5.1, the covariance function given by Equation 5.42 was evaluated in order to represent the decorrelation of tropospheric and satellite orbit errors with distance. Table 5.1 includes the $\mathbf{k_1}$ and $\mathbf{k_2}$ coefficients that were obtained, as well as the variance of the uncorrelated errors at the zenith that was used in the data processing.

Figure 5.7 shows the function fit for the determination of the $\mathbf{k_1}$ and $\mathbf{k_2}$ coefficients (Equation 5.33). Each small circle represents the actual "observation" used in the fit, formed by the variances of the differential tropospheric and satellite orbit errors

Table 5.1: k_1, k_2 coefficients and variances of the uncorrelated errors at the zenith ($\sigma^2_{u_z}$) for the ionospheric-free observable computed using data collected in St. Lawrence on August 4, 1999

Coefficient	IF
k_1 [a]	1.03268e-05
k_2 [b]	8.83740e-08
$\sigma^2_{u_z}$ [c]	3.7717e-05

a: m^2/km; b: m^2/km^2; c: m^2

reduced to the zenith (ΔT_{ab_z}) for each baseline at the corresponding baseline length. It can be seen that the quality of the fit was very good.

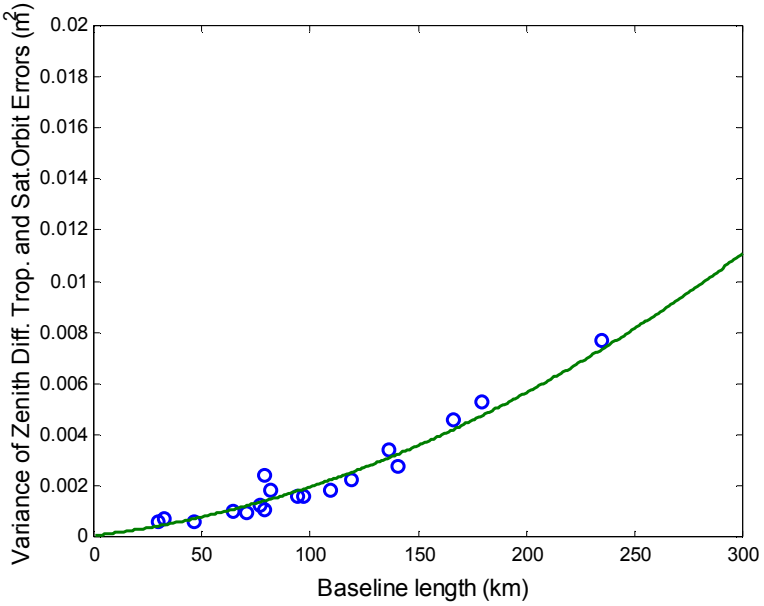

Figure 5.7: Function fit after determining k_1 and k_2 coefficients for the ionospheric-free observable

5.3.2 Computation of the Covariance Function for the Ionosphere Using Data Collected on August 4, 1999

Using geometric-free misclosures scaled to L1 for August 4, 1999 (IS_{L1}, described in Section 4.2.1), and the procedure described in Section 5.2, the covariance functions given by Equations 5.42 (second degree polynomial) and 5.47 (second degree polynomial in directional components) were evaluated in order to represent the decorrelated ionospheric errors with respect to distance. Table 5.2 includes the $\mathbf{k_1}$ and $\mathbf{k_2}$ coefficients that were obtained, as well as the variance of the uncorrelated errors that was used in the processing, corresponding to Equation 5.42, whereas Table 5.3 lists the $\mathbf{k_{1N}}$, $\mathbf{k_{2N}}$, $\mathbf{k_{1E}}$, and $\mathbf{k_{2E}}$ coefficients corresponding to Equation 5.47. For the sake of completeness, the variance of the uncorrelated errors at the zenith is also included. It can be shown that the coefficients in Table 5.2 combined with the ones for the troposphere and satellite orbits (Table 5.1) generate a covariance function equivalent to the L1 one (Figure 4.27), taking into account the difference in the mapping functions used (mainly between Equation 5.35 and 3.35). The coefficients on Table 5.3 correspond to a parameterisation of the values in Table 2 into directional components.

Figure 5.8 shows the function fit for the determination of the $\mathbf{k_1}$ and $\mathbf{k_2}$ coefficients. Each small circle represents the actual "observation" used in the fit, formed by the variances of the differential ionospheric errors reduced to the zenith ($\mathbf{\Delta I_{ab_z}}$) for

each baseline at the corresponding baseline length. It can be seen that the quality of the fit was very good.

Table 5.2: k_1, k_2 coefficients and variances of the uncorrelated errors at the zenith ($\sigma^2_{u_z}$) for the geometric-free observable scaled to L1 computed using data collected in St. Lawrence on August 4, 1999

Coefficient	IS_{L1}
k_1 [a]	1.74958e-04
k_2 [b]	3.21288e-06
$\sigma^2_{u_z}$ [c]	2.2901e-05

a: m^2/km; b: m^2/km^2; c: m^2

Table 5.3: k_{1N}, k_{2N}, k_{1E}, k_{2E} coefficients and variances of the uncorrelated errors at the zenith ($\sigma^2_{u_z}$) for the geometric-free observable scaled to L1 computed using data collected in St. Lawrence on August 4, 1999

Coefficient	IS_{L1}
k_{1N} [a]	2.51319e-04
k_{2N} [b]	2.86767e-06
k_{1E} [a]	2.29866e-05
k_{2E} [b]	3.55075e-06
$\sigma^2_{u_z}$ [c]	2.2901e-05

a: m^2/km; b: m^2/km^2; c: m^2

Figure 5.9 shows the north-south and east-west covariance functions based on the computed coefficients, according to Equations 5.49 and 5.50, respectively. These two

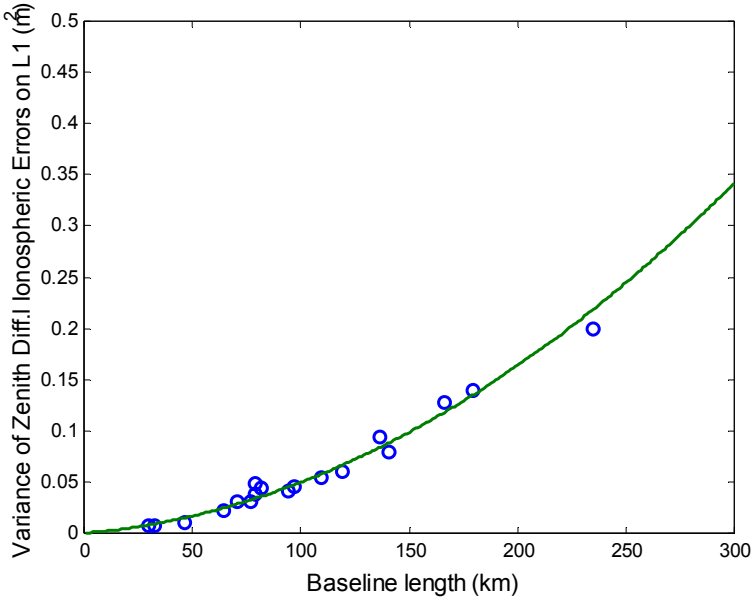

Figure 5.8: Function fit after determining k_1 and k_2 coefficients for the geometric-free scaled to L1 observable

equations were obtained breaking down Equation 5.47 into the corresponding directional components, in order to see if different gradients occurred along the north-south and east-west directions, respectively, in the St. Lawrence network. Based on this figure, it can be seen that the ionospheric errors along the north-south direction were only slightly larger than the ones along the east-west direction, indicating that no trough [Skone, 1998] occurred over the network on August 4, 1999.

$$\sigma^2_{c_{zN}} = k_{1N}\Delta N + k_{2N}\Delta N^2 \tag{5.49}$$

$$\sigma^2_{c_{zE}} = k_{1E}\Delta E + k_{2E}\Delta E^2 \tag{5.50}$$

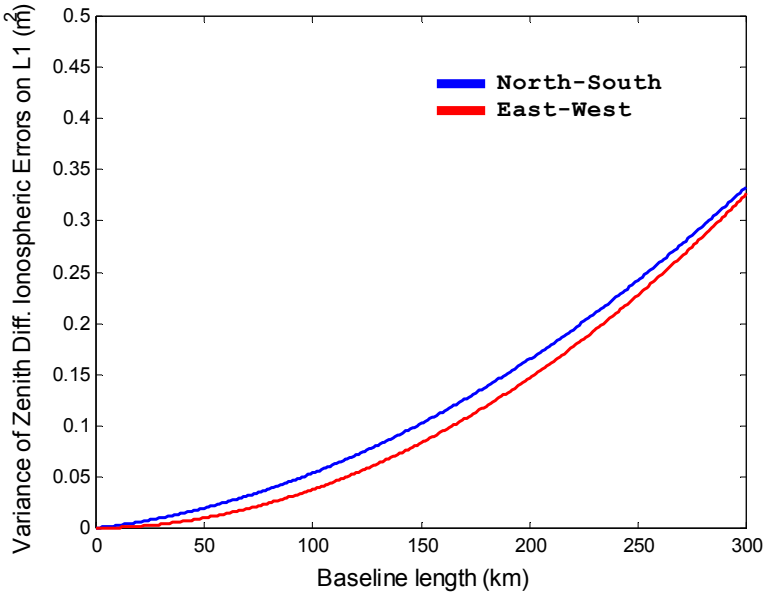

Figure 5.9: North-South and East-West ionospheric covariance functions using August 4, 1999, data

5.3.3 Improvement Brought by the Multi-Ref Method Using the Covariance Functions Computed for Troposphere/Satellite Orbits and Ionosphere With Data Collected on August 4, 1999

Using the covariance functions computed in Sections 5.3.1 and 5.3.2 (whose coefficients were listed in Tables 5.1 to 5.3), corrections for ionospheric-free and geometric-free scaled to L1 observables were calculated. After that, observables were corrected using a combination of Equations 5.15 to 5.19, and 5.37 to 5.41, according to the following:

L1 code: $$Cl_{T/I} = C1 + \hat{T} - \hat{I} \quad (5.51)$$

L1 phase: $$Ll_{T/I} = L1 + \frac{\hat{T} + \hat{I}}{\lambda_1} \quad (5.52)$$

L2 phase: $$L2_{T/I} = L2 + \frac{\hat{T} + (f_1^2/f_2^2)\hat{I}}{\lambda_2} \quad (5.53)$$

Widelane: $$WL_{T/I} = WL + \frac{\hat{T} - (f_1/f_2)\hat{I}}{\lambda_{WL}} \quad (5.54)$$

Ionospheric-free: $$IF_{T/I} = IF + \frac{\hat{T}}{\lambda_{IF}} \quad (5.55)$$

Geometric-free scaled to L1: $$IS_{Ll_{T/I}} = IS_{L1} + \hat{I} \quad (5.56)$$

where $\hat{T}$ and $\hat{I}$ represents the Multi-Ref corrections for troposphere/satellite orbit and ionosphere, respectively, expressed in metres; and the subscript T/I indicates an observable corrected for these errors (in metres, for C1 and IS_{L1}, and in cycles for the remaining ones).

As two different covariance functions were computed for the ionosphere, two sets of results are presented here: results using the covariance function for the troposphere and satellite orbits (coefficients in Table 5.1) and the covariance function for the ionosphere (coefficients in Table 5.2); and results using the same covariance function for the troposphere and satellite orbits (coefficients in Table 5.1) and the covariance function for the ionosphere with directional components (coefficients in Table 5.3). The improvement

brought by the Multi-Ref method was computed in the observation domain for the two scenarios described in Section 4.2.1. The results for the two sets of covariance functions are included in Tables 5.4 and 5.5, respectively. All results are shown in terms of the improvement in L1 and WL (after applying corrections using Equations 5.52 and 5.54, respectively), in order to compare with previous results obtained using other covariance functions.

Table 5.4: Raw and Multi-Ref-corrected double difference misclosures RMS and respective improvement for the Grand-Mère to Trois-Rivières (GM-TR) and Grand-Mère to Deschaillons baselines (GM-D) for August 4 and 5, 1999, using August 4, 1999, covariance functions for the troposphere, satellite orbits and ionosphere in non-directional components

Baseline	Length (km)	L1 (m)			WL (m)		
		Raw	Corr.	Improv.	Raw	Corr.	Improv.
GM-TR	30						
August 4		0.045	0.024	47%	0.060	0.034	43%
August 5		0.041	0.023	44%	0.059	0.032	46%
GM-D	46						
August 4		0.058	0.033	43%	0.074	0.045	39%
August 5		0.056	0.033	41%	0.076	0.041	46%

Comparing values in Tables 5.4 with the ones in Table 4.8, it can be seen that they are practically identical. This means that, in this case, modelling separately the correlated errors that affect GPS positioning does not improve the results when compared with the ones obtained using the original covariance functions. Table 5.6 summarises the differences between the Multi-Ref-corrected double difference misclosures RMS and the respective improvement when using the non-directional and the directional covariance functions for the ionosphere (i.e. Table 5.5 versus 5.4). It can be seen that, in general, the

directional components slightly improved the results, but only at the millimetre level, i.e. at the level of the carrier phase noise. The baselines involved in this test are probably too short to be sensitive to any change in the covariance function. Besides, the north-south and east-west covariance functions shown in Figure 5.9 do not significantly differ from each other, and this also contributed to the small differences shown in Table 5.6.

Table 5.5: Raw and Multi-Ref-corrected double difference misclosures RMS and respective improvement for the Grand-Mère to Trois-Rivières (GM-TR) and Grand-Mère to Deschaillons baselines (GM-D) for August 4 and 5, 1999, using August 4, 1999, covariance functions for the troposphere, satellite orbits and ionosphere in directional components

Baseline	Length (km)	L1 (m)			WL (m)		
		Raw	Corr.	Improv.	Raw	Corr.	Improv.
GM-TR	30						
August 4		0.045	0.024	47%	0.060	0.033	45%
August 5		0.041	0.024	41%	0.059	0.032	46%
GM-D	46						
August 4		0.058	0.030	48%	0.074	0.042	43%
August 5		0.056	0.032	43%	0.076	0.040	47%

Table 5.6: Differences between Multi-Ref-corrected double difference misclosures RMS and respective improvement for the Grand-Mère to Trois-Rivières (GM-TR) and Grand-Mère to Deschaillons baselines (GM-D) for August 4 and 5, 1999, using the non-directional and the directional covariance functions for the ionosphere[1]

Baseline	Length (km)	L1 (m)		WL (m)	
		Corr. Diff.	Imp. Diff.	Corr. Diff.	Imp. Diff.
GM-TR	30				
August 4		0.000	0%	-0.001	2%
August 5		0.001	-3%	-0.000	0%
GM-D	46				
August 4		-0.003	5%	-0.003	4%
August 5		-0.001	2%	-0.001	1%

1: a positive improvement difference means better performance using the directional covariance function for the ionosphere

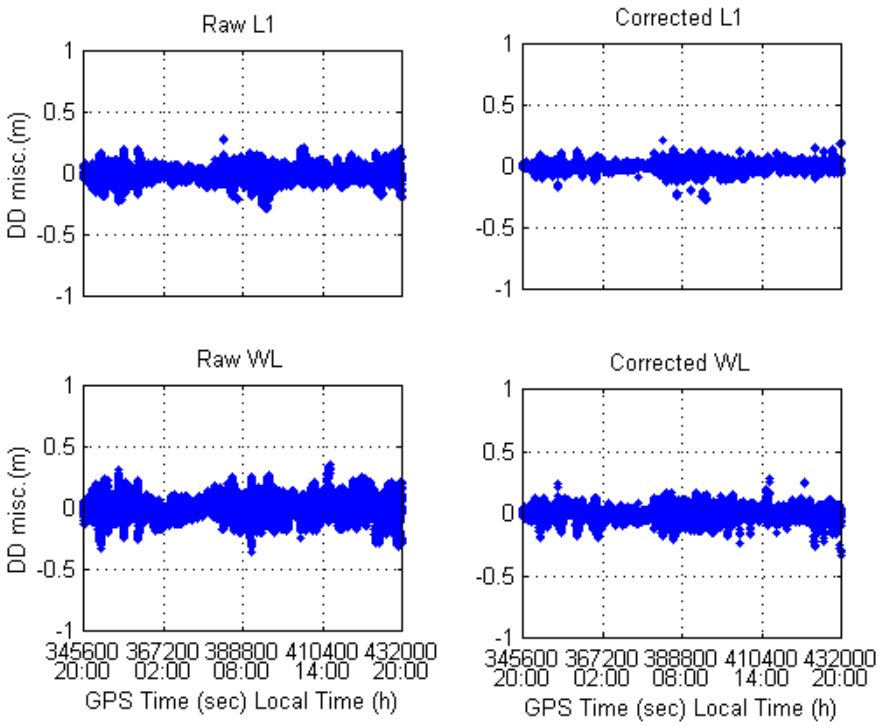

Figure 5.10: Raw and Multi-Ref-corrected L1 and WL double difference misclosures for the Grand-Mère to Deschaillons baseline (46 km) for August 5, 1999, using August 4, 1999, covariance functions for the troposphere, satellite orbits and ionosphere in non-directional components

Figures 5.10 and 5.11 show the raw and corrected double difference L1 and WL misclosures for the Grand-Mère to Deschaillons baseline (46 km) for August 5, 1999, using the two sets of covariance functions. Comparing with Figure 4.30 (they correspond to the same baseline), one can see that they look basically the same, except for the position of some isolated dots in the corrected misclosure graphs.

Similar to what was done for the original covariance function's cases, the covariance matrix of the reference stations' corrections and the *a posteriori* variance of

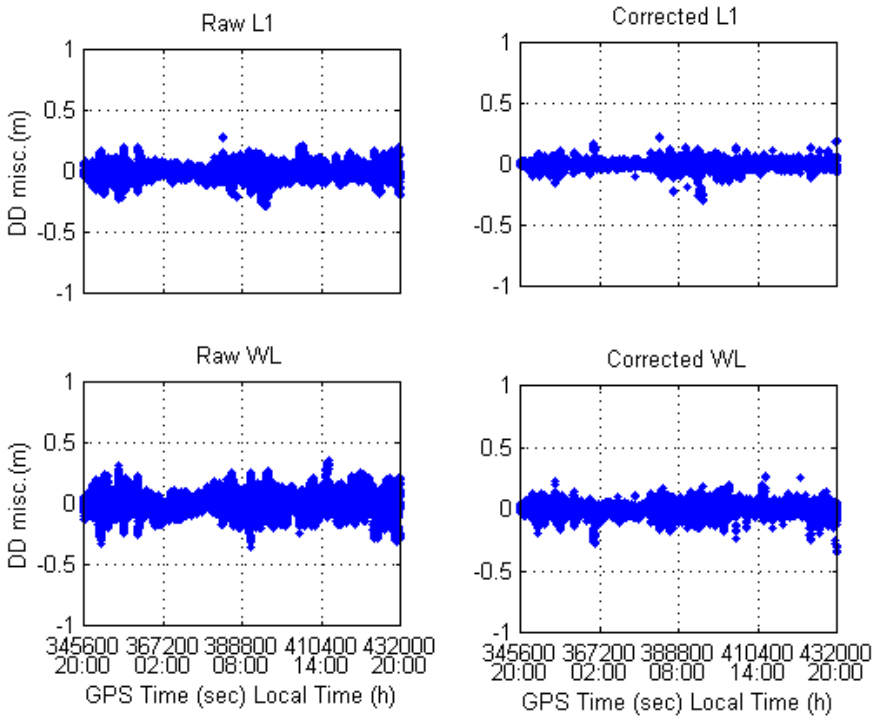

Figure 5.11: Raw and Multi-Ref-corrected L1 and WL double difference misclosures for the Grand-Mère to Deschaillons baseline (46 km) for August 5, 1999, using August 4, 1999, covariance functions for the troposphere, satellite orbits and ionosphere in directional components

unit weight were also computed when using the covariance functions for the troposphere/satellite orbits and ionosphere in non-directional components. Figures 5.12 to 5.15 show the mean variance for every epoch for the two scenarios for both days (on the top). These figures also show the *a posteriori* variance (in the middle) and the corresponding scaled mean variances at the bottom. On the top of each graph, the mean of each quantity over time is also listed.

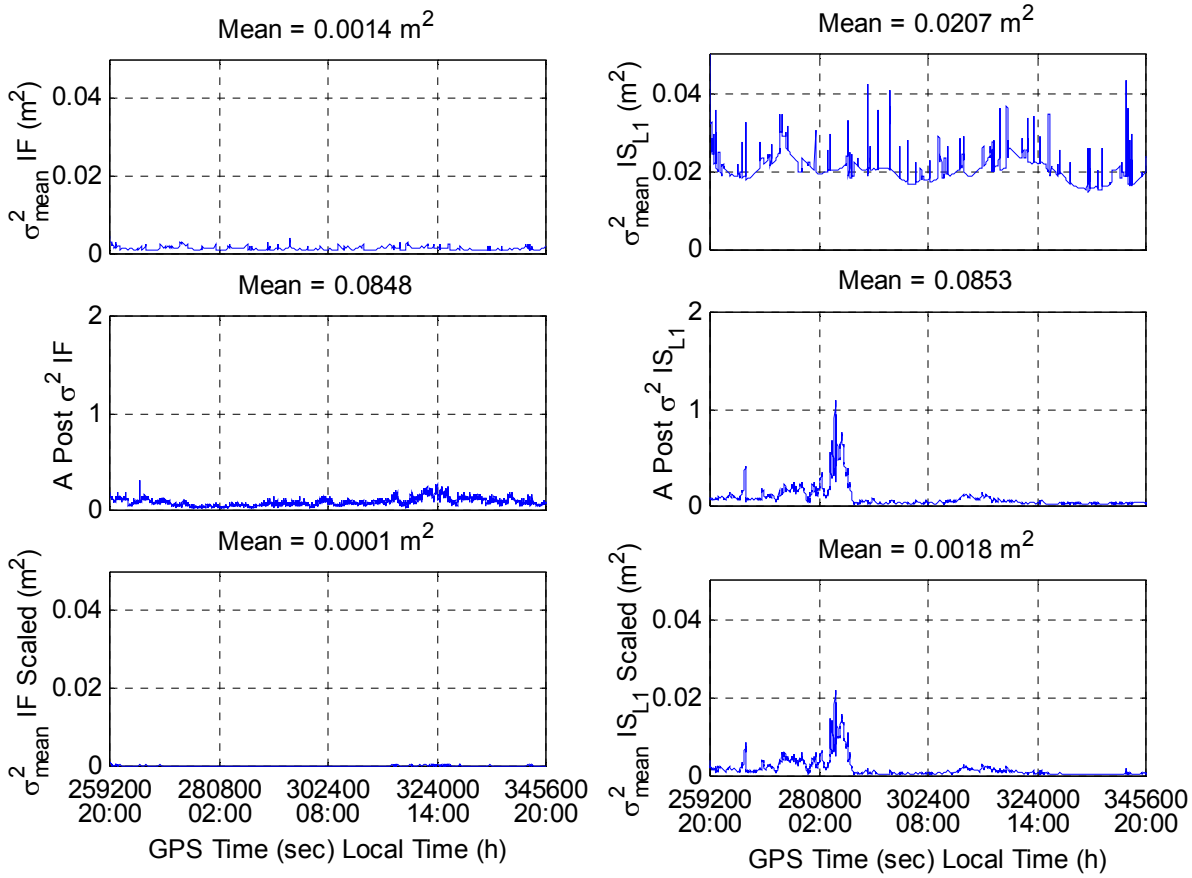

Figure 5.12: Quality estimation of the reference station's corrections for IF and IS_{L1} for the first scenario (Trois-Rivières as rover) for August 4, 1999, using the August 4, 1999, covariance functions for the troposphere/satellite orbits and ionosphere in non-directional components: mean variance (top graphs), *a posteriori* variance of unit weight (graphs in the middle), and mean variance scaled by the *a posteriori* variance (bottom graphs)

Analysing these figures, it can be seen that the correction variances (graphs on the top and at the bottom) for IF observables are around one order of magnitude smaller than the ones for IS_{L1}, as expected, as the tropospheric and satellite orbit errors are much smaller than the ionospheric ones in this case. These figures are analogous to Figures 4.32 to 4.35, respectively, except for the fact that instead of values for L1 and

WL, the values for the IF and IS_{L1} observables are reported. In order to compare them, one has to use the L1 plots on the left side of Figures 4.32 to 4.35 and the IS_{L1} on the right side of figures 5.12 to 5.15 (actually, all types of correlated errors are accounted for in the L1 plots, but as the ionosphere was the main contributor, comparing them with the IS_{L1} ones is a reasonable approximation). One can then see that the mean variances for

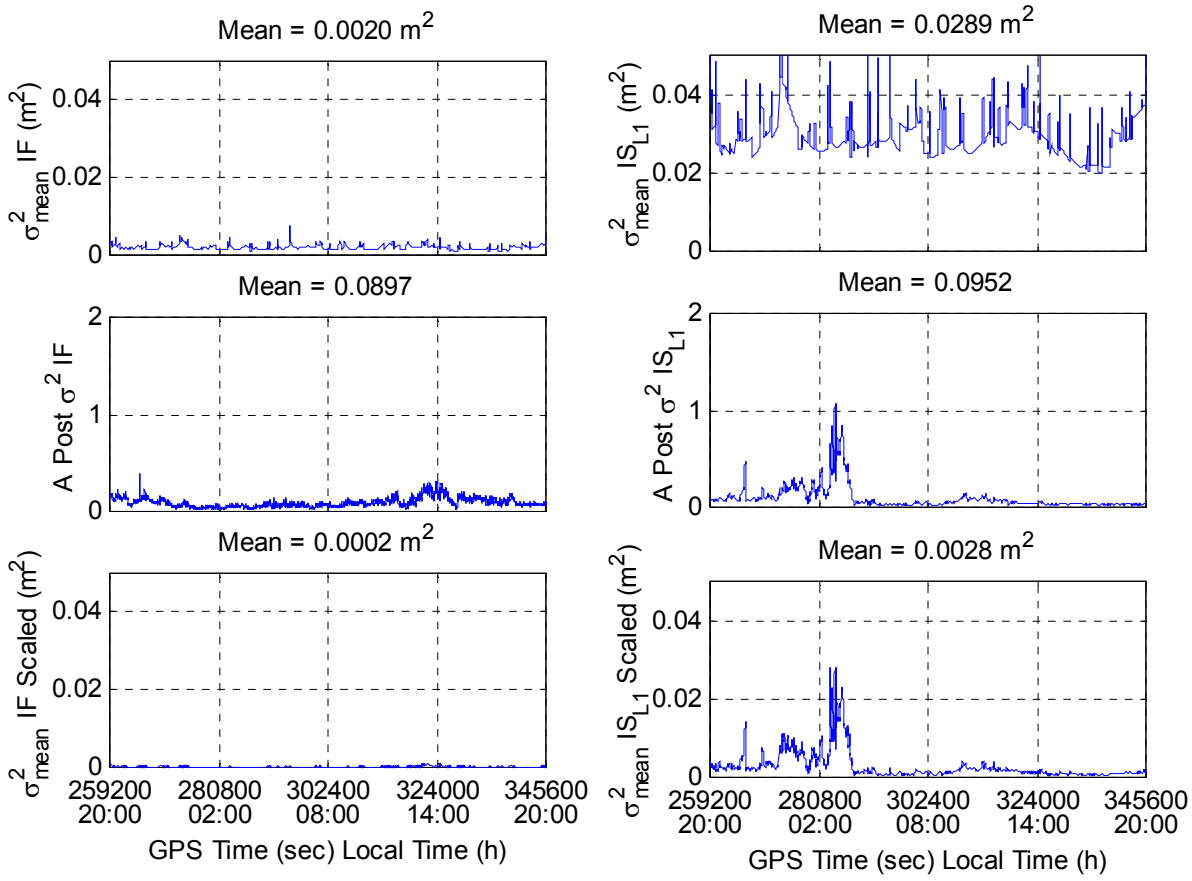

Figure 5.13: Quality estimation of the reference station's corrections for IF and IS_{L1} for the second scenario (Deschaillons as rover) for August 4, 1999, using the August 4, 1999, covariance functions for the troposphere/satellite orbits and ionosphere in non-directional components: mean variance (top graphs), *a posteriori* variance of unit weight (graphs in the middle), and mean variance scaled by the *a posteriori* variance (bottom graphs)

the IS_{L1} are much larger than the ones for L1 (graphs on the top). This can be explained by the fact that, in the IF and IS_{L1} cases, the quantity used to fit the covariance function was the differential error, whereas the double difference was used in the L1 case (and the correction mean variances, shown on the top graphs, are a function of the observation variances given by the covariance functions). It seems that converting from double difference misclosures to differential error, using Equations 5.8 and 5.36 for IF and IS_{L1},

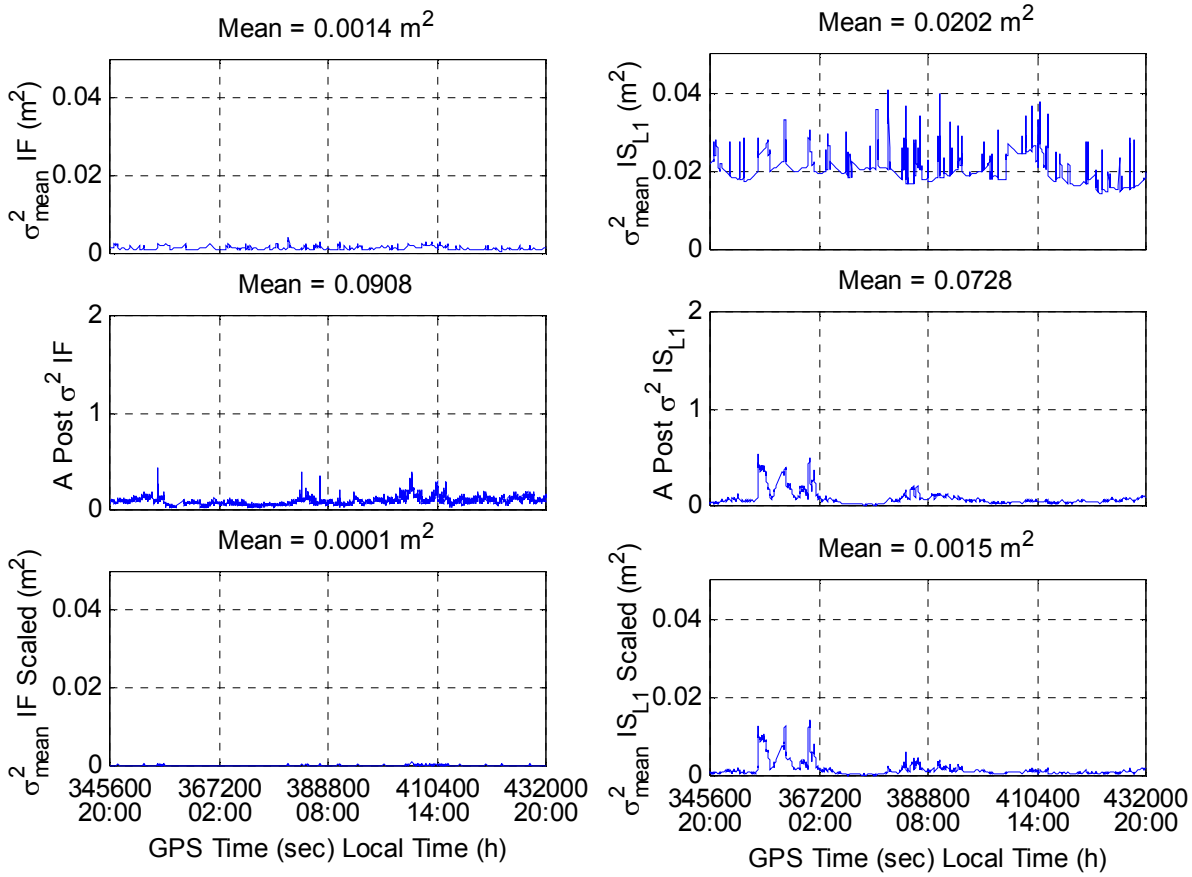

Figure 5.14: Quality estimation of the reference station's corrections for IF and IS_{L1} for the first scenario (Trois-Rivières as rover) for August 5, 1999, using the August 4, 1999 covariance functions for the troposphere/satellite orbits and ionosphere in non-directional components: mean variance (top graphs), *a posteriori* variance of unit weight (graphs in the middle), and mean variance scaled by the *a posteriori* variance (bottom graphs)

respectively, the resulting errors were higher than they should be. As mentioned in Sections 5.1 and 5.2, only double differences for which the absolute value of the term $(\mu^x - \mu^y)$ was greater than 0.2 were used, in order to avoid numerical problems. Hence, the differential errors obtained were somehow a function of the 0.2 factor, which seemed to have been too small, generating differential errors that were too large. This can be

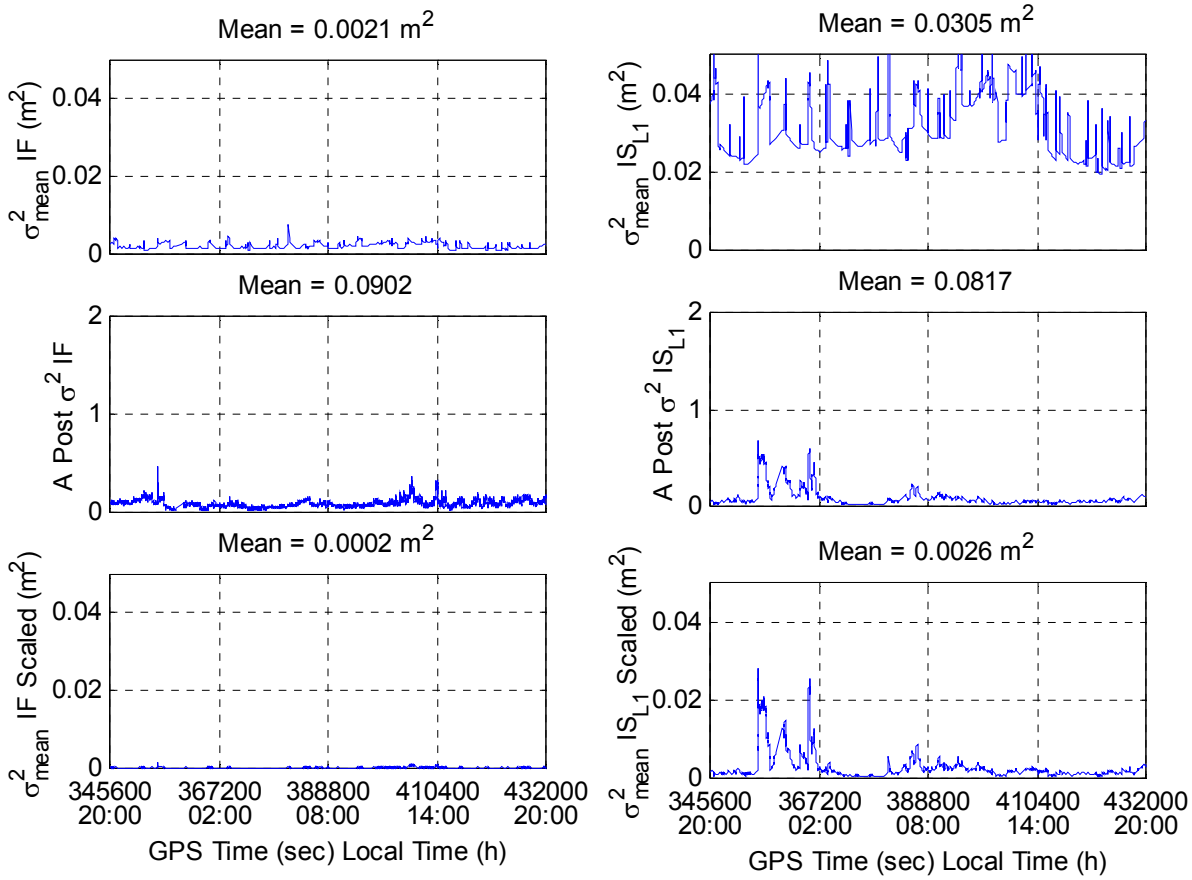

Figure 5.15: Quality estimation of the reference station's corrections for IF and IS_{L1} for the second scenario (Deschaillons as rover) for August 5, 1999, using the August 4, 1999 covariance functions for the troposphere/satellite orbits and ionosphere in non-directional components: mean variance (top graphs), *a posteriori* variance of unit weight (graphs in the middle), and mean variance scaled by the *a posteriori* variance (bottom graphs)

observed both in the IF and in the IS_{L1} cases. The computed *a posteriori* variance of unit weight values (in the middle graphs) confirm this fact, as they were systematically smaller than 1 in the IF and IS_{L1} cases, indicating that the observation weights (given by the inverse of the observation variances) were too small for both observables. However, when the correction variances are scaled by the *a posteriori* variances, the resultant values (given in the bottom graphs) are very similar for the L1 and IS_{L1} cases (see a comparison between the bottom left graph in Figures 4.32 to 4.35 and the bottom right ones in Figures 5.12 to 5.15).

Analogous to what was seen in the *a posteriori* variance plots for L1 and WL, the values for the IS_{L1} also mirror the situation of the ionosphere at each epoch, showing spikes during periods of time when an increased ionospheric activity occurred. On the other hand, the *a posteriori* variances for the IF case show the lower variability of the actual tropospheric errors, when compared with the ionospheric values.

The covariance matrix of the reference stations' corrections and the *a posteriori* variance of unit weight were also computed when using the covariance function for the ionosphere in directional components. As the results were very similar to the ones with the non-directional case, the corresponding figures are not shown here. Table 5.7 summarises the correction variance means scaled by the *a posteriori* variances for L1 and IS_{L1} using the three covariance functions computed for the St. Lawrence network using

data collected on August 4, 1999, namely the original one for L1 (from Figures 4.32 to 4.35), the one for the ionosphere in non-directional components (from Figures 5.12 to 5.15), and the one for the ionosphere in directional components. Analysing this table, it can be seen that the values are very similar, with the IS_{L1} (both) in general slightly smaller than the L1 ones, as these last ones also include tropospheric and orbit errors. In summary, no matter which model was used for the covariance function, the estimated correction variances are very similar.

Table 5.7: Correction variance means scaled by the *a posteriori* variances for L1 and IS_{L1} using the three covariance functions (CF) computed for the St. Lawrence network using data collected on August 4, 1999

Baseline	Length (km)	Original CF for L1 (m^2)	CF for the Ionosphere in Non-directional Components (m^2)	CF for the Ionosphere in Directional Components (m^2)
GM-TR	30			
August 4		0.0021	0.0018	0.0022
August 5		0.0018	0.0015	0.0019
GM-D	46			
August 4		0.0032	0.0028	0.0025
August 5		0.0031	0.0026	0.0024

5.4 Brazilian Network

5.4.1 Computation of the Covariance Function for the Troposphere and Satellite Orbits Using Data Collected on August 13, 1999

Using ionospheric-free (IF) misclosures for August 13, 1999, described in Section 4.2.2, and the procedure described in Section 5.1, the covariance function for the troposphere and satellite orbits given by Equation 5.42 was evaluated. Table 5.8 lists the $\mathbf{k_1}$ and $\mathbf{k_2}$ coefficients that were obtained, as well as the variance of the uncorrelated errors at the zenith that was used in the processing.

Table 5.8: k_1, k_2 coefficients and variances of the uncorrelated errors at the zenith ($\sigma^2_{u_z}$) for the ionospheric-free observable computed using data collected in Southeastern Brazil on August 13, 1999

Coefficient	IF
k_1 [a]	1.00000e-06
k_2 [b]	1.12124e-07
$\sigma^2_{u_z}$ [c]	3.7717e-05

a: m^2/km; b: m^2/km^2; c: m^2

Figure 5.16 shows the function fit (Equation 5.10) for the determination of the $\mathbf{k_1}$ and $\mathbf{k_2}$ coefficients. The y-axis represents the variances of the differential tropospheric and satellite orbit errors reduced to the zenith ($\mathbf{\Delta T_{ab_z}}$) for each baseline, whereas the

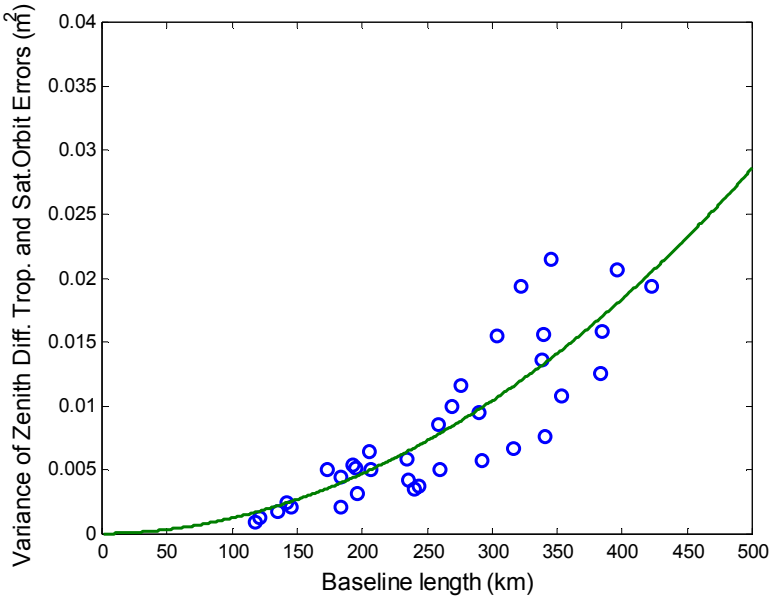

Figure 5.16: Function fit after determining k_1 and k_2 coefficients for the ionospheric-free observable

corresponding baseline length is represented along the x-axis. It can be seen that the quality of the fit was good. When comparing with Figure 5.7, which is the analogous one for the St. Lawrence case, it can be seen that the general trend is the same (i.e. a differential variance of around 0.01 m^2 at 300 km, for instance). However, the adjustment residuals are larger in the Brazilian case, due to longer baselines involved and possibly to a more non-homogeneous troposphere.

An attempt was made in terms of modelling the troposphere in the Brazilian case by considering the height difference between the baseline stations as an additional parameter, besides the baseline length. The corresponding function to be determined was:

$$\sigma^2_{c_z}(p_m, p_n) = k_{1d}d + k_{2d}d^2 + k_{1H}\Delta H + k_{2H}\Delta H^2 \qquad (5.57)$$

As the height of the stations in the network (from 44 to 1005 m) did not cover a range of values large enough to model the height dependency in a proper way, statistical meaningful values for coefficients $\mathbf{k_{1H}}$ and $\mathbf{k_{2H}}$ in Equation 5.57 could not be computed. Schaer et al. [1999] found similar results, mentioning the insensitivity of the differential residual tropospheric delays to height differences, when modelling this kind of error using the AGNES network in Switzerland (which covers a much larger range of height values - from 378 to 3635 m).

5.4.2 Computation of the Covariance Function for the Ionosphere Using Data Collected on August 13, 1999

Using geometric-free misclosures scaled to L1 (IS_{L1}, described in Section 4.2.2) for August 13, 1999, and the procedure described in Section 5.2, the $\mathbf{k_1}$ and $\mathbf{k_2}$ coefficients (Equation 5.42) and the $\mathbf{k_{1N}}$, $\mathbf{k_{2N}}$, $\mathbf{k_{1E}}$, and $\mathbf{k_{2E}}$ ones (Equation 5.47) were calculated. Table 5.9 includes the first ones, corresponding to a second degree polynomial, as well as the variance of the uncorrelated errors used in the data processing, whereas Table 5.10 lists the second ones, corresponding to a second degree polynomial in directional components. The variance of the uncorrelated errors at the zenith is also included in Table 5.10.

Table 5.9: k_1, k_2 coefficients and variances of the uncorrelated errors at the zenith ($\sigma^2_{u_z}$) for the geometric-free observable scaled to L1 computed using data collected in Southeastern Brazil on August 13, 1999

Coefficient	IS_{L1}
k_1 [a]	1.89365e-04
k_2 [b]	1.27916e-05
$\sigma^2_{u_z}$ [c]	2.2901e-05

a: m^2/km; b: m^2/km^2; c: m^2

Table 5.10: k_{1N}, k_{2N}, k_{1E}, k_{2E} coefficients and variances of the uncorrelated errors at the zenith ($\sigma^2_{u_z}$) for the geometric-free observable scaled to L1 computed using data collected in Southeastern Brazil on August 13, 1999

Coefficient	IS_{L1}
k_{1N} [a]	1.17319e-04
k_{2N} [b]	1.84220e-05
k_{1E} [a]	5.58387e-04
k_{2E} [b]	6.14085e-06
$\sigma^2_{u_z}$ [c]	2.2901e-05

a: m^2/km; b: m^2/km^2; c: m^2

Similar to the results obtained for the St. Lawrence network (Section 5.3), it can be shown that the coefficients in Table 5.9 combined with the ones for the troposphere and satellite orbits (Table 5.8) generate a covariance function equivalent to the L1 one

(Figure 4.45), taking into account the difference in the mapping functions used (mainly between Equation 5.35 and 3.35).

The coefficients included in Table 5.10 were computed after transforming the geodetic coordinates of the stations to corrected geomagnetic ones (CGM) [Gustafsson et al., 1992]. As the Earth's magnetic field plays an important role in the alignment of the free electrons in the ionosphere (which tend to follow its lines of force), it is expected that the direction over which the ionospheric errors decorrelate more (in the equatorial region) is along the north-south *geomagnetic* one and not the geodetic one. Besides, the strong correlation of the differential ionospheric errors with the azimuth of the baseline shown in Figure 5.5 justified using CGM coordinates to maximise the directional components modelling (which did not occur with the St. Lawrence data set). Figure 5.17 shows some CGM parallels and meridians over Brazil. By definition, the CGM coordinates (latitude, longitude) of a point in space are computed by tracing the DGRF/IGRF magnetic field line (in the present case given by the Definite/International Geomagnetic Reference Field - DGRF/IGRF - model for Epoch's years 1945, 1950, ..., 2000, and the secular variation model for 1995-2005), through the specified point to the dipole geomagnetic equator, then returning to the same altitude along the dipole field line and assigning the obtained dipole latitude and longitude as the CGM coordinates to the starting point [NASA/NSSDC, 2001a]. This transformation was performed using a

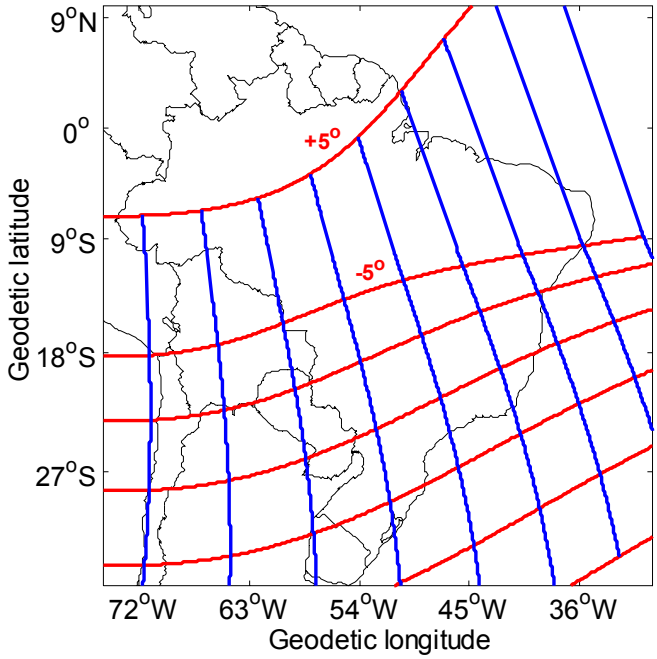

Figure 5.17: CGM parallels (in red) and meridians (in blue) over Brazil, every 5°. The CGM equator is not represented as it can not be defined at certain regions

computer program made available by Papitashvili [2001], which is behind the MODELWeb online computation service provided by NASA/NSSDC [2001b].

Figure 5.18 shows the function fit (Equation 5.33) for the determination of the $\mathbf{k_1}$ and $\mathbf{k_2}$ coefficients. The y-axis represents the variances of the differential ionospheric errors reduced to the zenith ($\mathbf{\Delta I_{ab_z}}$) for each baseline, whereas the corresponding baseline length is represented along the x-axis. It can be seen that the quality of the fit was reasonably good. When comparing with Figure 5.8, which is the analogous one for the St. Lawrence case, it can be seen that the curve for the Brazilian data set is steeper, corresponding to a more active ionosphere (6 ppm, versus 23 ppm, at the double

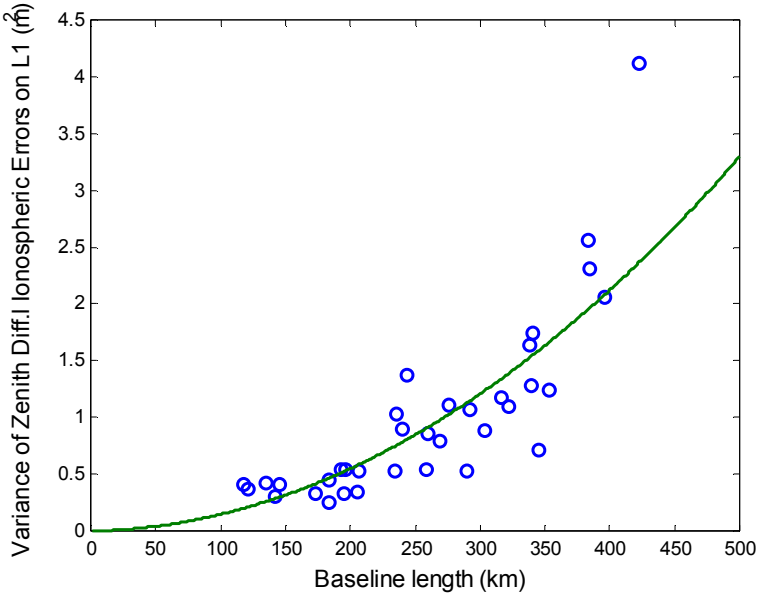

Figure 5.18: Function fit after determining k_1 and k_2 coefficients for the geometric-free observable

difference level, according to Sections 4.2.1 and 4.2.2, respectively). Besides, the adjustment residuals are larger in the Brazilian case, due probably to a more non-homogeneous ionosphere.

Figure 5.19 shows the function fit (Equation 5.48) for the determination of the $\mathbf{k_{1N}}$, $\mathbf{k_{2N}}$, $\mathbf{k_{1E}}$, and $\mathbf{k_{2E}}$ coefficients. The z-axis represents the variances of the differential ionospheric errors reduced to the zenith ($\mathbf{\Delta I_{ab_z}}$) for each baseline, whereas the corresponding baseline $\mathbf{\Delta N}$ and $\mathbf{\Delta E}$ (in CGM coordinates) are represented along the horizontal axes. In this case, Equation 5.48 represents a 3-D surface, as it expresses the relationship of three quantities ($\mathbf{\Delta I_{ab_z}}$, $\mathbf{\Delta N}$ and $\mathbf{\Delta E}$). Circles represent the data points

used in the fit (corresponding to 35 baselines). Not all data points can be seen, as some are located underneath the surface.

Observing the curves generated by intersecting the 3-D surface in Figure 5.19 with planes ΔN-z and ΔE-z, it can be seen that the ionospheric error decorrelation along the geomagnetic north-south direction was slightly more than twice the decorrelation along the east-west direction, as expected for a region located under the equatorial anomaly.

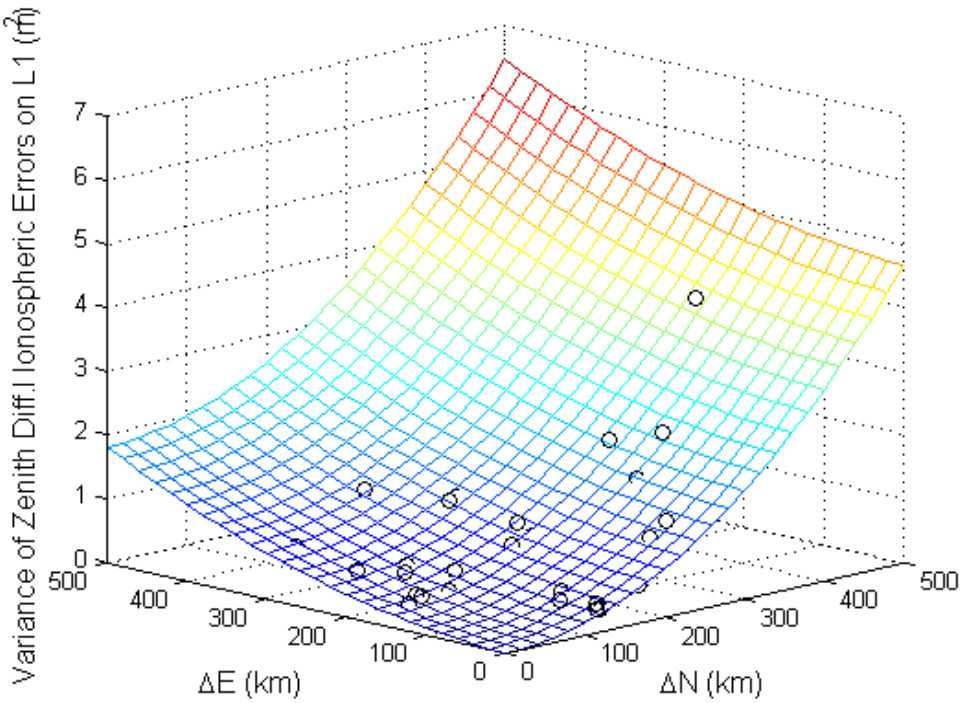

Figure 5.19: Function fit after determining k_{1N}, k_{2N}, k_{1E}, and k_{2E} coefficients for the geometric-free observable

5.4.3 Improvement Brought by the Multi-Ref Method Using the Covariance Functions Computed for the Troposphere/Satellite Orbits and Ionosphere With Data Collected on August 13, 1999

Using the covariance functions computed in Sections 5.4.1 and 5.4.2 (whose coefficients were listed in Tables 5.8, 5.9 and 5.10), corrections for ionospheric-free and geometric-free scaled to L1 observables were calculated. After that, observables were corrected using Equations 5.51 to 5.56.

Two sets of results are presented here: results using the covariance function for the troposphere and satellite orbits (coefficients in Table 5.8) and the covariance function for the ionosphere (coefficients in Table 5.9); and results using the same covariance function for the troposphere and satellite orbits (coefficients in Table 5.8) and the covariance function for the ionosphere with directional components (coefficients in Table 5.10). In order to apply this latter covariance function, geodetic coordinates were converted to CGM, as the coefficients in Table 5.10 refer to this system. The improvement brought by the Multi-Ref method was computed in the observation domain for the three scenarios described in Section 4.2.2. The results for the two sets of covariance functions are included in Tables 5.11 and 5.12, respectively. All results are shown in terms of improvement in L1 and WL (after applying corrections using

Equations 5.52 and 5.54, respectively), in order to compare with previous results obtained using other covariance functions.

Table 5.11: Raw and Multi-Ref-corrected double difference misclosures RMS and respective improvement for FRAN to LIMO, AGUA to SJRP, and REGI to BOTU baselines for August 11 and 13, 1999, using August 13, 1999, covariance functions for the troposphere, satellite orbits and ionosphere in non-directional components

Baseline	Length (km)	L1 (m)			WL (m)		
		Raw	Corr.	Improv.	Raw	Corr.	Improv.
FRAN - LIMO	122						
August 11		0.191	0.108	43%	0.258	0.137	47%
August 13		0.327	0.151	54%	0.418	0.195	53%
AGUA - SJRP	146						
August 11		0.284	0.104	63%	0.364	0.135	63%
August 13		0.350	0.123	65%	0.440	0.161	63%
REGI - BOTU	193						
August 11		0.239	0.120	50%	0.312	0.163	48%
August 13		0.407	0.172	58%	0.516	0.209	59%

Table 5.12: Raw and Multi-Ref-corrected double difference misclosures RMS and respective improvement for FRAN to LIMO, AGUA to SJRP, and REGI to BOTU baselines for August 11 and 13, 1999, using August 13, 1999, covariance functions for the troposphere, satellite orbits and ionosphere in directional components

Baseline	Length (km)	L1 (m)			WL (m)		
		Raw	Corr.	Improv.	Raw	Corr.	Improv.
FRAN - LIMO	122						
August 11		0.191	0.107	44%	0.258	0.133	48%
August 13		0.327	0.166	49%	0.418	0.212	49%
AGUA - SJRP	146						
August 11		0.284	0.099	65%	0.364	0.131	64%
August 13		0.350	0.133	62%	0.440	0.174	60%
REGI - BOTU	193						
August 11		0.239	0.125	48%	0.312	0.170	46%
August 13		0.407	0.182	55%	0.516	0.224	57%

Table 5.13 summarises the differences between the RMS of the Multi-Ref-corrected double difference misclosures and the respective improvement when using the original covariance functions and the ones derived in this chapter for the Brazilian network (i.e. Table 4.14 versus Tables 5.11 and 5.12). Analysing these results, it can be seen that separate modelling of the correlated errors that affect GPS positioning does not improve the results when compared with the ones obtained using the original covariance functions, similar to what was observed with the St. Lawrence data set. Differences at the millimetre level only (i.e. at the level of the carrier phase noise), either negative (improvement) or positive (deterioration), were obtained, indicating the equivalence of those results. Surprisingly, the more sophisticated model, represented by the directional components of the ionospheric error in CGM coordinates, did not systematically perform better than the others, even with the errors notably behaving differently along the north-south and east-west directions, indicating that the Multi-Ref approach is not sensitive to this kind of model. This is further discussed in Section 5.6.

Figures 5.20 and 5.21 show the raw and corrected double difference L1 and WL misclosures for the AGUA to SJRP baseline (146 km) for August 13, 1999, using the two sets of covariance functions. Comparing with Figure 4.48 (they correspond to the same baseline), one can see that they look basically the same, except again for the position of some isolated dots in the corrected misclosures graphs.

Table 5.13: Differences between RMS of the Multi-Ref-corrected double difference misclosures and the respective improvement for FRAN to LIMO, AGUA to SJRP, and REGI to BOTU baselines for August 11 and 13, 1999, using the original covariance functions, and the ones for troposphere, satellite orbits and ionosphere in non-directional and directional components [1]

Baseline	Length (km)	L1 (m)		WL (m)	
		Corr. Diff.	Imp. Diff.	Corr. Diff.	Imp. Diff.
Original covariance functions versus the ones for the troposphere, satellite orbits and ionosphere in non-directional components (Table 4.14 versus Table 5.11)					
FRAN - LIMO	122				
August 11		0.007	-4%	0.006	-2%
August 13		0.001	0%	0.003	-1%
AGUA - SJRP	146				
August 11		-0.004	1%	-0.007	2%
August 13		-0.007	2%	-0.009	2%
REGI - BOTU	193				
August 11		0.001	0%	0.000	0%
August 13		-0.006	2%	-0.008	1%
Original covariance functions versus the ones for the troposphere, satellite orbits and ionosphere in directional components (Table 4.14 versus Table 5.12)					
FRAN - LIMO	122				
August 11		0.006	-3%	0.002	-1%
August 13		0.016	-5%	0.020	-5%
AGUA - SJRP	146				
August 11		-0.009	3%	-0.011	3%
August 13		0.003	-1%	0.004	-1%
REGI - BOTU	193				
August 11		0.006	-2%	0.007	-2%
August 13		0.004	-1%	0.007	-1%

1: a positive improvement difference means better performance using the covariance functions for the troposphere, satellite orbits and ionosphere

The covariance matrix of the reference stations' corrections and the *a posteriori* variance of unit weight were also computed for the Brazilian network when using the covariance functions for the troposphere/satellite orbits and ionosphere in non-directional components. Figures 5.22 to 5.27 show the mean variance for every epoch for the three

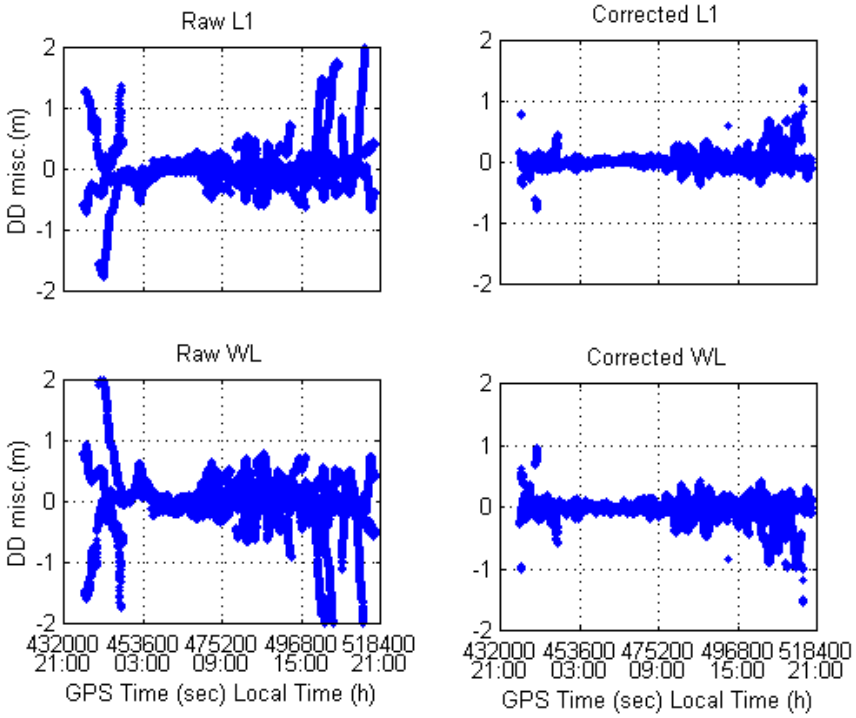

Figure 5.20: Raw and Multi-Ref-corrected L1 and WL double difference misclosures for the AGUA to SJRP baseline (146 km) for August 13, 1999, using August 13, 1999, covariance functions for the troposphere, satellite orbits and ionosphere in non-directional components

scenarios for both days (on the top). These figures also show the *a posteriori* variance (in the middle) and the corresponding scaled mean variances at the bottom. On the top of each graph, the mean of each quantity over time is also shown.

These figures are analogous to Figures 4.50 to 4.55, respectively, except that they include IF and IS_{L1} plots instead of L1 and WL ones. Similar to what was done with the St. Lawrence network, one can compare the bottom right plot in Figures 5.22 to 5.27 (mean IS_{L1} variances scaled by the *a posteriori* variance) with the bottom left one in

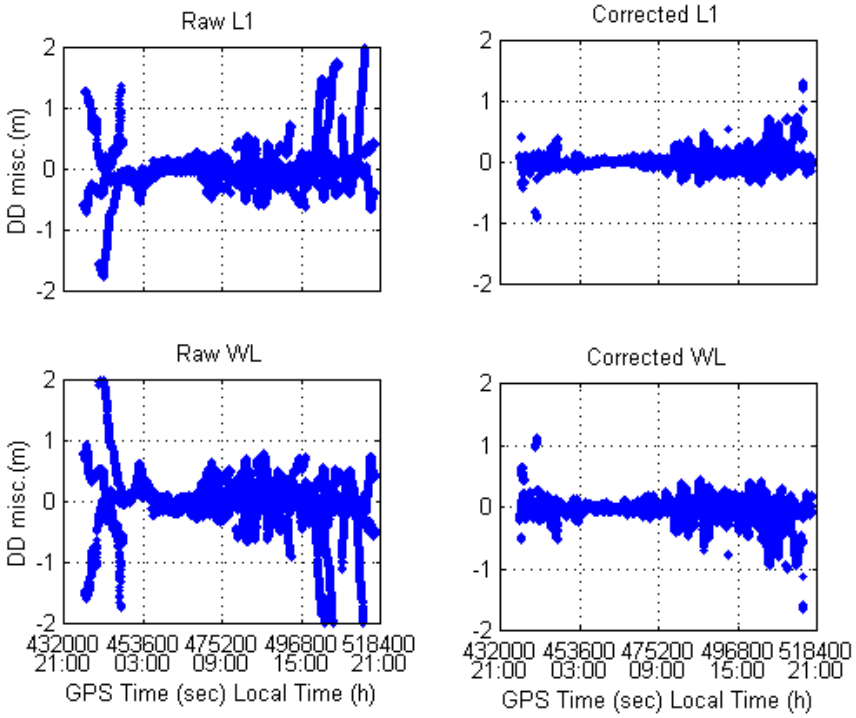

Figure 5.21: Raw and Multi-Ref-corrected L1 and WL double difference misclosures for the AGUA to SJRP baseline (146 km) for August 13, 1999, using August 13, 1999, covariance functions for the troposphere, satellite orbits and ionosphere in directional components

Figures 4.50 to 4.55 (mean L1 variances scaled by the *a posteriori* variance). The vertical scale of the plots was made the same for this comparison. Hence it can be seen that the corresponding plots are very similar. However the IS_{L1} mean scaled variances are slightly greater than the ones for L1, which was not observed in the St. Lawrence results. This can be explained by the poorer quality of the L2 carrier phase measurements in the Brazilian network. Most of GPS receivers used were Trimble 4000SSi™, which use the codeless cross-correlation technique [Lachapelle, 1997] to track signals on L2. This technique causes a 13dB loss in signal to noise ratio with respect to the semi-codeless

cross-correlation one, used in the NovAtel MiLLennium™ and Ashtech Z-12™ receivers utilised in the St. Lawrence network. Hence the noisier L2 measurement causes the IS_{L1} observable to be noisier too, as it is a linear combination of L1 and L2 carrier phase measurements.

From these figures, one can see the smaller values for the IF variances, as it was also observed in the St. Lawrence network results. In addition, the mean variances for the IS_{L1} are much larger than the ones for L1 (graphs on the top), as the quantity used to fit the IF and IS_{L1} covariance functions was the differential error, whereas the double difference was used in the L1 case, as was explained for the St. Lawrence case.

Analogous to what was seen before, the *a posteriori* variance values for the IS_{L1} reflect the situation of the ionosphere at each epoch, showing spikes during periods of time when an increased ionospheric activity occurred, whereas the *a posteriori* variances for the IF observable vary much less.

The covariance matrix of the reference stations' corrections and the *a posteriori* variance of unit weight were also computed when using the covariance function for the ionosphere in directional components. As the results were very similar to the ones with the non-directional case, the corresponding figures are not shown here. Table 5.14 summarises the correction variance means scaled by the *a posteriori* variances for L1 and

IS_{L1} using the three covariance functions computed for the Brazilian network, namely the original one for L1 (from Figures 4.50 to 4.55), the one for the ionosphere in non-directional components (from Figures 5.22 to 5.27), and the one for the ionosphere in directional components. Analysing this table, it can be seen that the values are similar, with the IS_{L1} ones for the non-directional case in general greater than the L1 ones, as explained before. The better modelling of the ionosphere in directional components seemed to have compensated for the higher noise, giving variances closer to the L1 values.

An important aspect related to the computation of the covariance matrix of the reference stations' corrections is that special care has to be taken when generating the covariance functions. In the Brazilian network, intermediate test results when computing the IF covariance function gave a negative value for the $\mathbf{k_1}$ coefficient. Despite the fact that the corrections themselves are not very sensitive to the covariance function chosen, the negative coefficient generated a covariance matrix of the observations - $C_{\delta l}$ - that was not positive definite [Mikhail, 1976]. This caused problems when computing the *a posteriori* variance of unit weight using Equation 3.21, as the $C_{\delta l}$ matrix needs to be inverted.

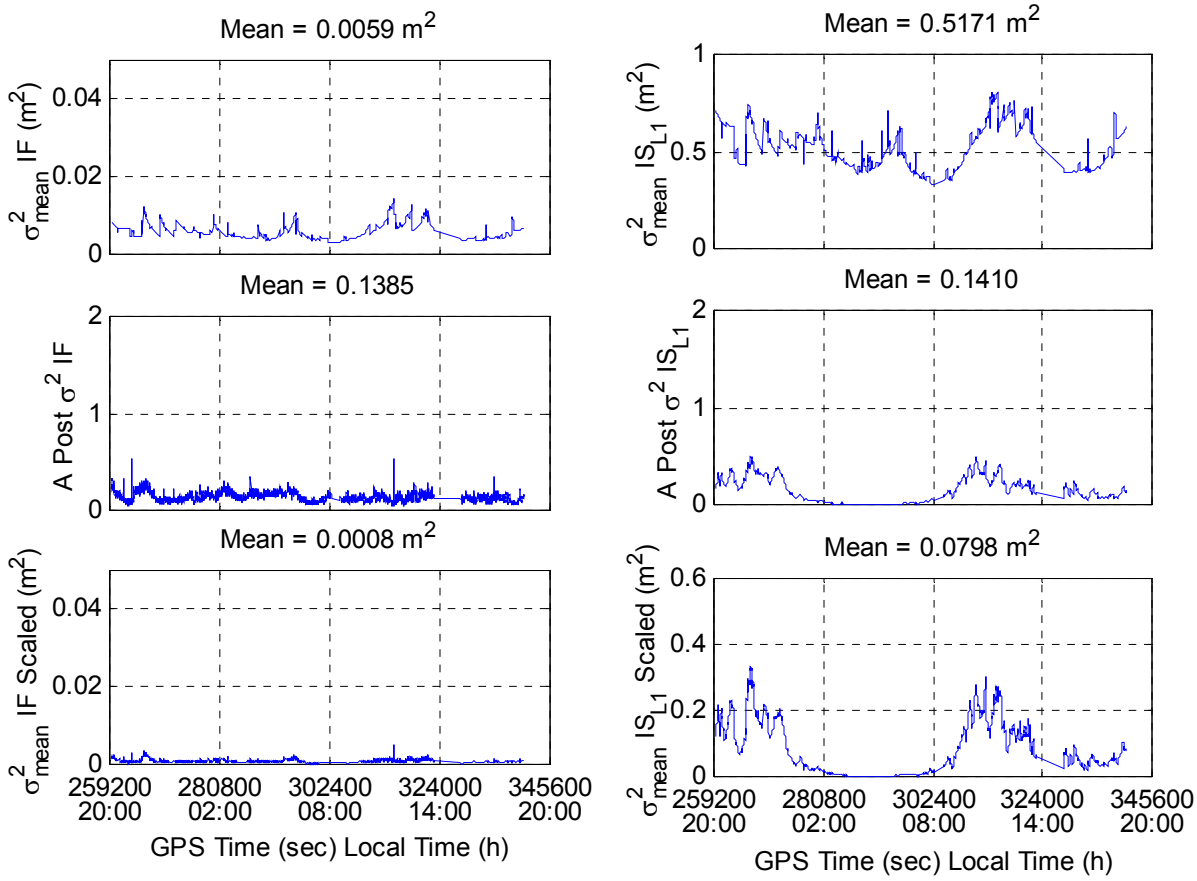

Figure 5.22: Quality estimation of the reference station's corrections for IF and IS_{L1} for the first scenario (LIMO as rover) for August 11, 1999, using the August 13, 1999 covariance functions for the troposphere/satellite orbits and ionosphere in non-directional components: mean variance (top graphs), *a posteriori* variance of unit weight (graphs in the middle), and mean variance scaled by the *a posteriori* variance (bottom graphs)

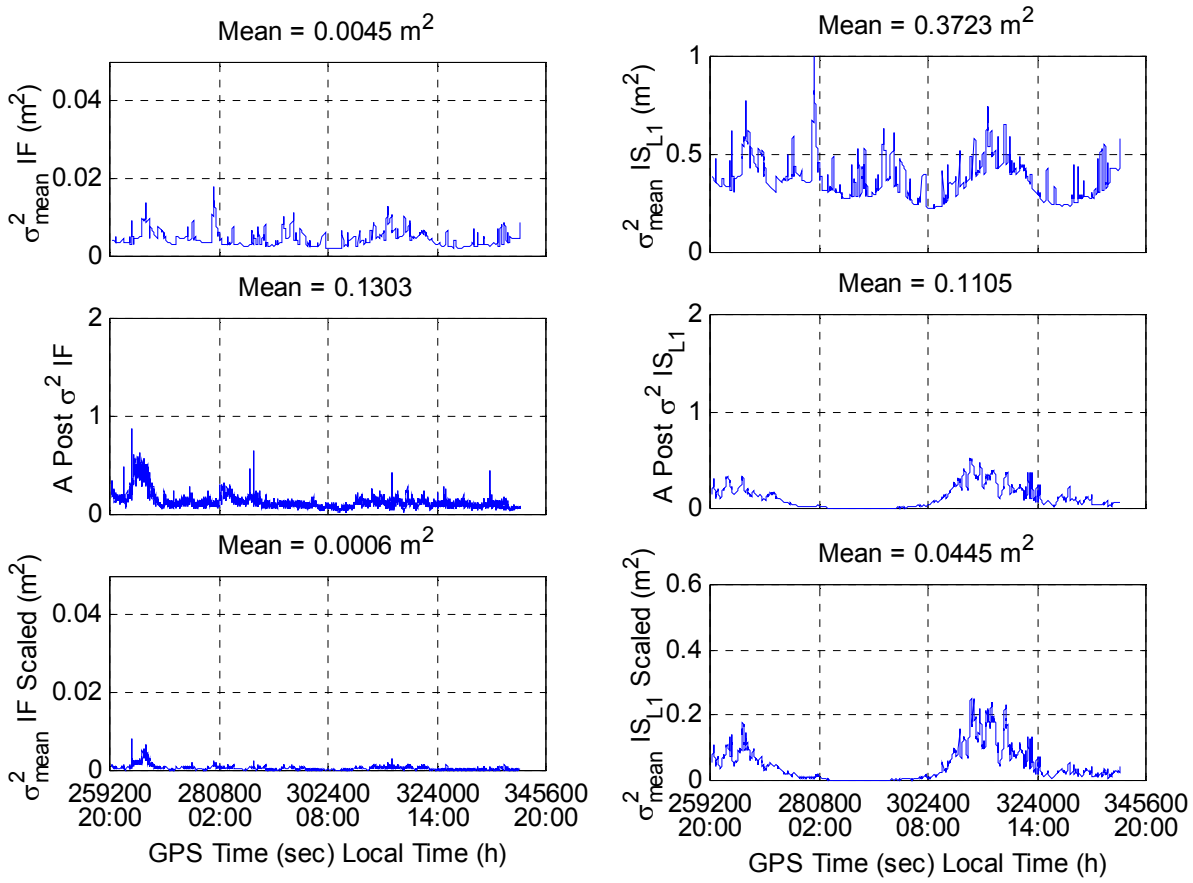

Figure 5.23: Quality estimation of the reference station's corrections for IF and IS_{L1} for the second scenario (SJRP as rover) for August 11, 1999, using the August 13, 1999 covariance functions for the troposphere/satellite orbits and ionosphere in non-directional components: mean variance (top graphs), *a posteriori* variance of unit weight (graphs in the middle), and mean variance scaled by the *a posteriori* variance (bottom graphs)

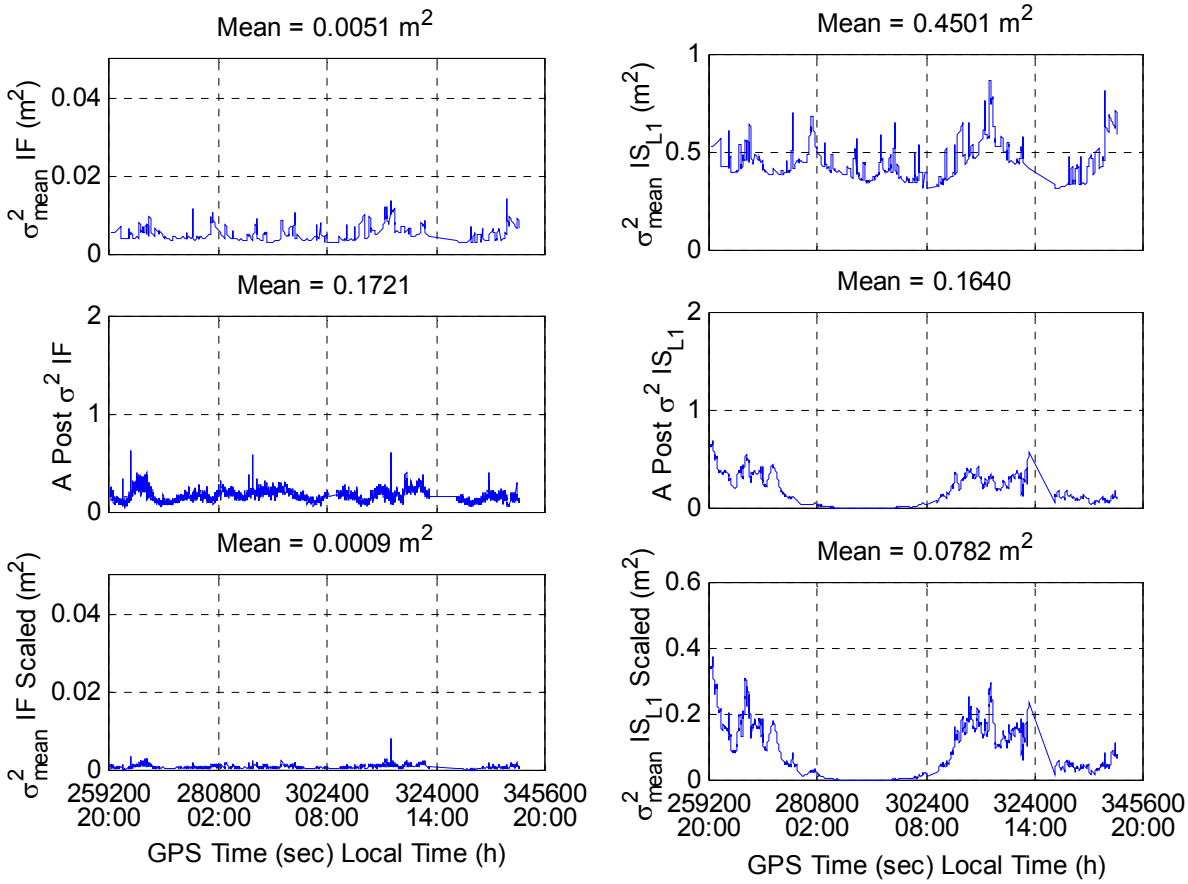

Figure 5.24: Quality estimation of the reference station's corrections for IF and IS_{L1} for the third scenario (BOTU as rover) for August 11, 1999, using the August 13, 1999 covariance functions for the troposphere/satellite orbits and ionosphere in non-directional components: mean variance (top graphs), *a posteriori* variance of unit weight (graphs in the middle), and mean variance scaled by the *a posteriori* variance (bottom graphs)

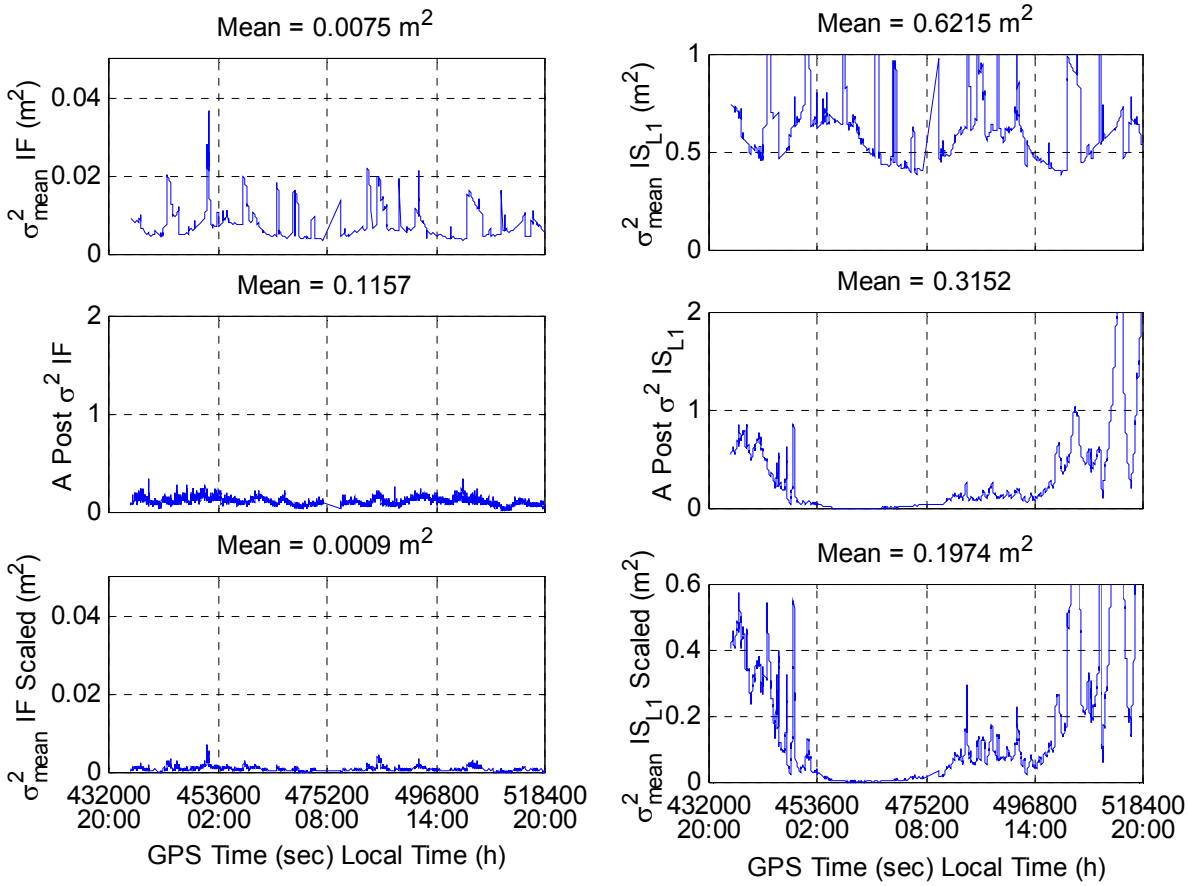

Figure 5.25: Quality estimation of the reference station's corrections for IF and IS_{L1} for the first scenario (LIMO as rover) for August 13, 1999, using the August 13, 1999 covariance functions for the troposphere/satellite orbits and ionosphere in non-directional components: mean variance (top graphs), *a posteriori* variance of unit weight (graphs in the middle), and mean variance scaled by the *a posteriori* variance (bottom graphs)

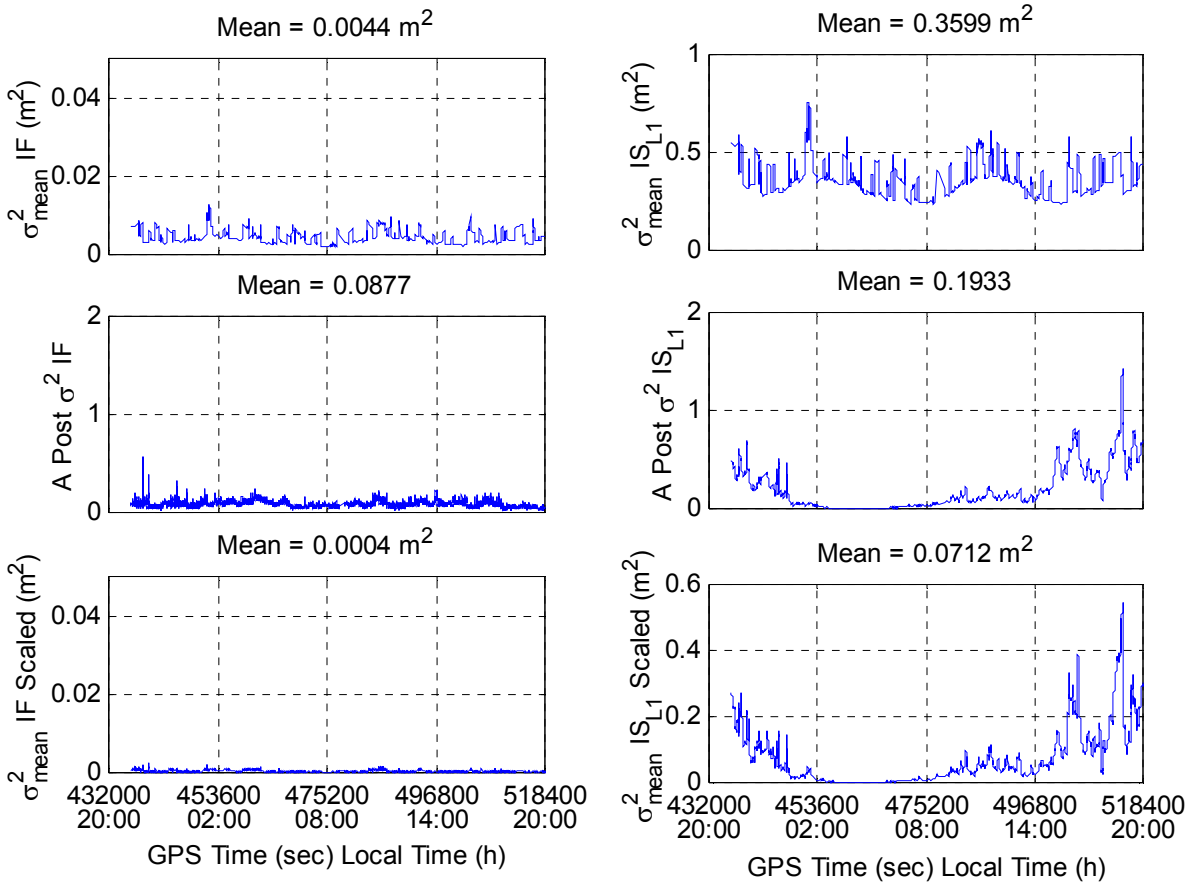

Figure 5.26: Quality estimation of the reference station's corrections for IF and IS_{L1} for the second scenario (SJRP as rover) for August 13, 1999, using the August 13, 1999 covariance functions for the troposphere/satellite orbits and ionosphere in non-directional components: mean variance (top graphs), *a posteriori* variance of unit weight (graphs in the middle), and mean variance scaled by the *a posteriori* variance (bottom graphs)

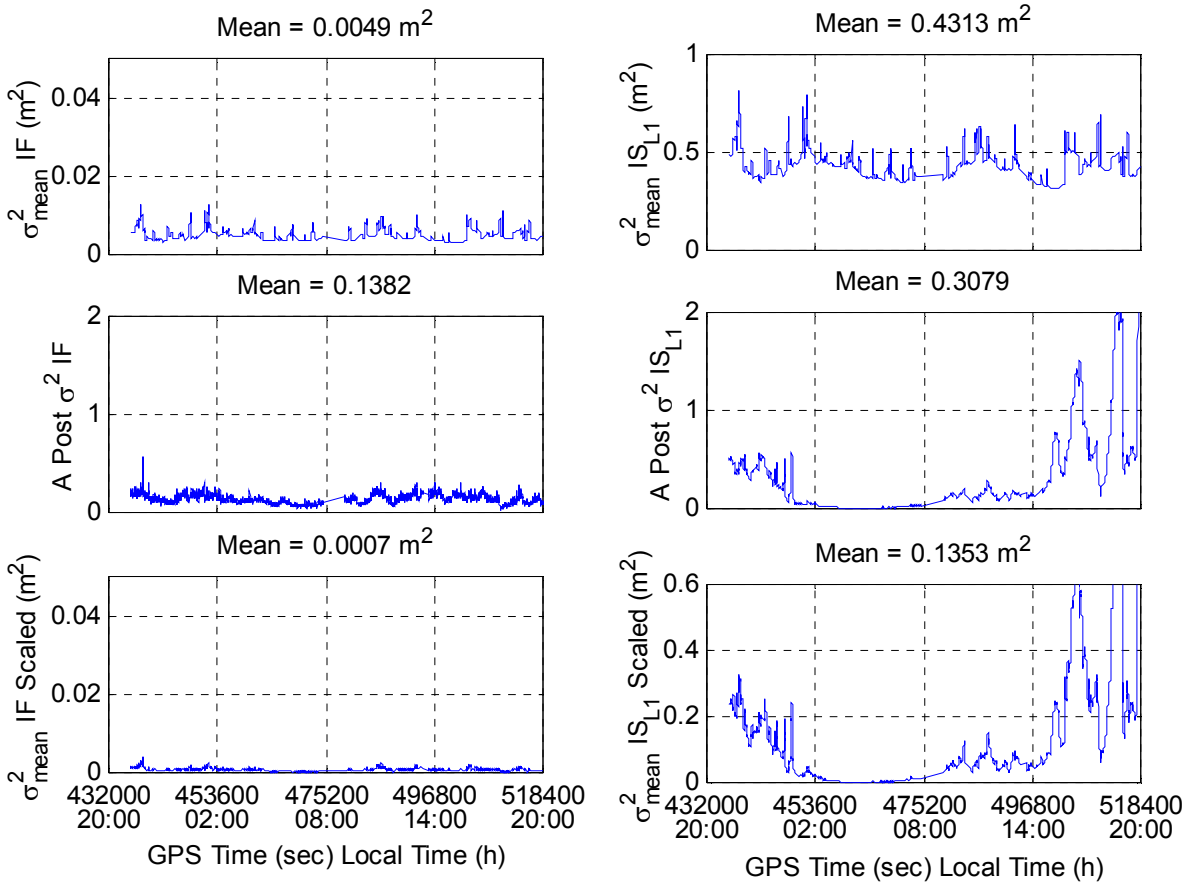

Figure 5.27: Quality estimation of the reference station's corrections for IF and IS_{L1} for the third scenario (BOTU as rover) for August 13, 1999, using the August 13, 1999 covariance functions for the troposphere/satellite orbits and ionosphere in non-directional components: mean variance (top graphs), *a posteriori* variance of unit weight (graphs in the middle), and mean variance scaled by the *a posteriori* variance (bottom graphs)

Table 5.14: Correction variance means scaled by the *a posteriori* variances for L1 and IS_{L1} using the three covariance functions (CF) computed for the Brazilian network using data collected on August 13, 1999

Baseline	Length (km)	Original CF for L1 (m^2)	CF for the Ionosphere in Non-directional Components (m^2)	CF for the Ionosphere in Directional Components (m^2)
FRAN-LIMO	122			
August 11		0.0444	0.0798	0.0425
August 13		0.0962	0.1974	0.1130
AGUA-SJRP	146			
August 11		0.0300	0.0445	0.0334
August 13		0.0486	0.0712	0.0849
REGI-BOTU	193			
August 11		0.0429	0.0782	0.0474
August 13		0.0687	0.1353	0.1174

5.5 Remarks on Multi-Ref Code Error Modelling

In the previous sections of this chapter an attempt was made in terms of modelling the correlated errors that affect GPS positioning, as the main objective was to correct the prominent errors that are present in carrier phase observations. A side benefit of modelling the errors separately is that they could be also used to correct errors that occur to code observations, based on the application of Equation 5.51, for instance. However, the dominant errors that affect code observations are noise and multipath, a fact that reduces the effectiveness of applying the mentioned corrections to code observations. In order to generate corrections that account for code noise and multipath, one can apply the

approach derived by Raquet [1998], which used the variances of the double difference code misclosures for each baseline to derive the variances of the uncorrelated errors for each station in the network ($\sigma^2_{u_z}$). To compute the variance of the uncorrelated errors for code observations, a Least-Squares adjustment is performed using either one of the following observation equations:

$$E\{(\Delta\nabla\delta l^{xy}_{ab_z})^2\} = 2\sigma^2_{u_z}(a) + 2\sigma^2_{u_z}(b) \tag{5.58}$$

$$E\{(\Delta T_{ab_z})^2\} = \sigma^2_{u_z}(a) + \sigma^2_{u_z}(b) \tag{5.59}$$

depending if the zenith differential error (double or single difference) is computed using Equation 3.41 or 5.8, respectively. Equations 5.58 and 5.59 can be deduced from 3.42 and 5.10, respectively, after neglecting the terms corresponding to correlated errors, i.e. the terms that are function of the baseline length, as the dominant errors, in this case, are the uncorrelated ones. The covariance matrix elements are then computed in the same way as for carrier phase observations, using Equation 3.27, and properly combining the computed variance of the uncorrelated errors for each station with the variance of the correlated errors computed using the functions for the troposphere, satellite orbits and ionosphere given by Equation 3.33. However, one has to consider that applying the Multi-Ref approach to correct for the code noise and multipath only partially resolves the problem, because the errors to be corrected are the ones of the reference stations. Hence

the same type of error that happens to the user observations is not accounted for (contrary to the correlated errors, the uncorrelated ones can not be predicted at the user). This approach can be particularly ineffective, if one considers that the reference stations are generally equipped with very good geodetic receivers, which use narrow correlator-like technologies [Lachapelle, 1997], and multipath-resistant antennas (chokering [Seeber, 1993], for instance), and are installed on specially selected locations, obstruction-free, in order to minimise multipath. On the other hand, the user receiver may not match the same quality standard and most likely is surrounded by a more sub-optimal environment.

Another option to mitigate code multipath at the reference stations would be to use an approach based on Ray [2000], which implies the necessity of installing multiple antennas in close proximity to determine multipath parameters (reflection coefficient, multipath delay and multipath phase) at each station. These parameters are then used to correct the observation data. However the same limitations in terms of the effectiveness of this method are valid here, as the user data is not corrected.

5.6 Summary of Multi-Ref Optimisation based on Refining the Covariance Functions

In this chapter and in Chapter 4, an optimisation of the Multi-Ref method was attempted throughout refinements implemented to the covariance functions. Data sets collected in

August 1999 in Canada and Brazil were used, in order to assess the impact on two different parts of the world and, as such, subjected to different characteristics of the ionosphere and troposphere.

The first test (Chapter 4) assessed the impact of using different data sets to compute the original covariance functions for L1 and WL derived by Raquet [1998]. Initial results in applying the Multi-Ref method to both networks were obtained using covariance functions derived using data collected in the St. Lawrence region in November, 1998. After re-computing the covariance functions using data collected in both regions during August, 1999, the Multi-Ref approach gave results with the same percentage improvement in the observation domain for the St. Lawrence network. It is important to emphasise that the previous covariance functions had been computed using data from the same region and that the baseline lengths to assess the improvement brought by the Multi-Ref method were short (30 and 46 km), which can have contributed to get the same level of improvement. However, in the Brazilian network, using covariance functions computed with data collected during the campaign increased the improvement brought by Multi-Ref up to 9%, or 3.1 cm, in L1 and up to 14%, or 5.8 cm, in WL in the observation domain (in terms of the RMS of the double difference misclosures). The fact that the previous results were obtained using covariance functions derived using data from another region of the world and that longer baselines were present in the Brazilian network seem to have contributed to the improvement of

performance. Nevertheless, the main differences were observed in some double difference misclosures which corresponded to the situation when the remote satellite was observed by only few reference stations, as it was rising or setting with a low elevation, i.e. the observability was not good. This issue is addressed in Chapter 6 and a strategy is proposed to overcome the cases when the remote satellite is setting.

The results mentioned in the previous paragraph indicated that the Multi-Ref method is not very sensitive to the original covariance functions utilised. In order to confirm this, very extreme (high and low) error conditions were simulated for the correlated error functions, giving results similar to those obtained using covariance functions computed using real data (differences at the millimetre level only). Consequently the covariance functions do not seem to have a large impact on the improvement brought by the Multi-Ref approach for the data sets used herein.

The second test (this chapter) was related to try improving the Multi-Ref performance by modelling separately the correlated errors that affect GPS positioning. Hence, different covariance functions were computed for the tropospheric/satellite orbit errors and for the ionospheric ones, using respectively the ionospheric-free and the geometric-free (scaled to L1) linear combinations. For the ionosphere, modelling the errors in directional components (North-South and East-West) was also tried, considering the expected different error decorrelation along those directions, particularly in the

equatorial region where the Brazilian network is located. The results for both networks did not show a significant improvement with respect to the original covariance functions (only at the millimetre level in some cases), even with the directional modelling of the ionosphere using corrected geomagnetic coordinates, showing that the extra effort for sophisticating the model did not prove to have value. It was known from Moritz [1972] that the results of Least-Squares Collocation were not so sensitive to the covariance function, but as the case here was to completely redefine the function by error source, a greater impact on the results was expected. Actually, just using data from each campaign to recompute the original covariance functions improved the results more than changing the covariance functions themselves.

As seen in Chapter 3, the computation of corrections to the reference station observations using the Multi-Ref approach is equivalent to a Least-Squares Conditional adjustment, and consequently the observation corrections force that the adjusted double difference misclosures between any pair of reference stations to be always zero, independent of the covariance function adopted. The Multi-Ref method then gives a tool to distribute the misclosures among the single observations, for which the covariance function plays a role (of course it is also important for predicting the corrections at the rover positions). These properties help to understand why the method is not so sensitive to the covariance functions chosen.

On the other hand, these results emphasise the Multi-Ref method robustness, as a simpler lumped model gives good results. This characteristic is very important if one thinks of a real time service, as there will be no need for frequent covariance function updates. Comparing the original covariance functions to those that models the errors separately, the second ones may have the advantage of reducing the number of corrections to be transmitted to users, as the tropospheric/satellite orbit corrections and the ionospheric corrections are applicable to both code and phase observations. In addition, transmitting corrections separated by error source gives more flexibility, as different update rates can be used for each correction according to the error behaviour.

A second degree polynomial was used in the tests mentioned above, showing a good fit to the data. In addition, other functions were tried, but none of them with better performance than that. When a third degree polynomial was used to fit the geometric-free misclosures to model the ionosphere, very bad results were obtained, even worse than the ones with raw observation. Later, it was found out that the normal matrix to be inverted to compute the corrections (term $BC_{\delta l}B^T$ in Equations 3.15 and 3.16) was not positive definite. The same situation happened when a second degree polynomial with $\mathbf{k_1}$ equal to zero was tried. This makes evident that special care has to be taken in terms of testing if the normal matrix satisfies that condition when trying different covariance functions.

The covariance matrix of the reference stations' corrections and the *a posteriori* variance of unit weight were also computed in all tests for both networks. Using different covariance functions did change the estimated accuracy of the corrections, as mentioned by Moritz [1976]. However, when the correction variances were scaled by the *a posteriori* variance of unit weight, the corrections estimated accuracies were very similar in all cases. This confirms that the *a posteriori* variance converts the precision of the corrections (internal), based on the covariance functions, to an estimation of their accuracy (external), based on the real data. Other results later in Chapter 6 confirm that the scaled standard deviation of the corrections is a very good estimate of the real error of the corrections.

The *a posteriori* variance was also shown to be useful to detect when the actual conditions of the errors in the network deviate from the ones predicted by the covariance functions. For instance, when the ionosphere is more active than it was when the covariance function was derived, the *a posteriori* variance values are greater than 1 (corresponding to accentuated observation residuals), as the observation weights given by the covariance function are relatively large (optimistic). The *a posteriori* variance therefore is an indicator to portrait the error behaviour in a real time service, which can help to issue alerts to users, for example.

Due to the fact that the *a posteriori* variances reflect the situation of the errors in the network, it is important to interpret properly the meaning of the scaled variances of the corrections. As mentioned previously, the scaled variances are estimates of the external accuracy of the corrections. Therefore, a large correction variance means that the corresponding correction is not as accurate, which normally occurs under active ionospheric conditions (when the corrections are not expected to have the same quality as during quiet times, due to greater variability of the ionospheric errors across the reference network), or when the specific satellite has observability problems, as discussed in Chapter 6. Based on this fact, the estimated accuracy of the corrections is very useful information that can be used along with the corrections in order to help subsequent processes, e.g. ambiguity resolution (in the network and to the user) and user positioning.

To compute the *a posteriori* variance of unit weight, the observation covariance matrix has to be inverted. In some cases (mainly when modelling the tropospheric and satellite orbit errors, as they decorrelate slowly), the $\mathbf{k_1}$ coefficient was negative, generating a non-positive definite observation covariance matrix $C_{\delta l}$. Hence special care has to be taken in terms of testing if the covariance matrix satisfies that condition before inverting it.

CHAPTER 6

OPTIMISING MULTI-REF APPLYING A KALMAN FILTER TO THE CORRECTIONS

Results of optimising the Multi-Ref method by improving the covariance functions (see Chapters 4 and 5) showed the influence that the observability has on the correction computation. Normally when the satellite elevation is very close to the elevation mask used in the data processing (15° in the present case) - which happens when the satellite is rising or setting - the number of reference stations that can observe that satellite is reduced, as the satellite is below the elevation mask for some stations. This reduces the number of reference stations contributing to the correction computation. Depending on the magnitude of the raw measurement errors (due to the ionosphere, for instance), this can make a difference in the value and quality of the computed corrections. Figure 6.1 shows the raw and corrected L1 double difference misclosures for PRN 1 as the remote satellite for the AGUA to SJRP baseline (146 km) of the Brazilian network, using data collected on August 13, 1999 and the original covariance functions computed for the same day (so it is a detail of Figure 4.48). This satellite was rising during the time shown. There are five labelled time windows in this figure, separated by vertical lines, which

define the instant when an additional baseline started to observe PRN 1. The windows were labelled as follows:

- Window ‘1’: PRN 1 was visible by only one baseline from the reference network. Hence Multi-Ref was unable to correct for all of the raw error;
- Window ‘2’: PRN 1 was visible by two baselines. It can be seen the significant improvement this additional baseline brought to the quality of the corrections;
- Window ‘3’: PRN 1 was observed by three and then four baselines from the reference network. As the fourth additional baseline was located at almost the same azimuth as the third baseline, it did not bring any discontinuity to the misclosures, as the new added information was already very correlated with the one provided by the third baseline;
- Window ‘4’: PRN 1 was observed by five baselines;
- Window ‘5’: PRN 1 was visible by six baselines, i.e. all baselines in the reference network.

In Figure 6.2, the baselines contributing to the correction computations in each time window of Figure 6.1 are shown, using the same colour scheme that was used in the window numbers in Figure 6.1. For the sake of completeness, the AGUA to SJRP baseline was also shown. The baselines used in each window always included all the ones from the previous window.

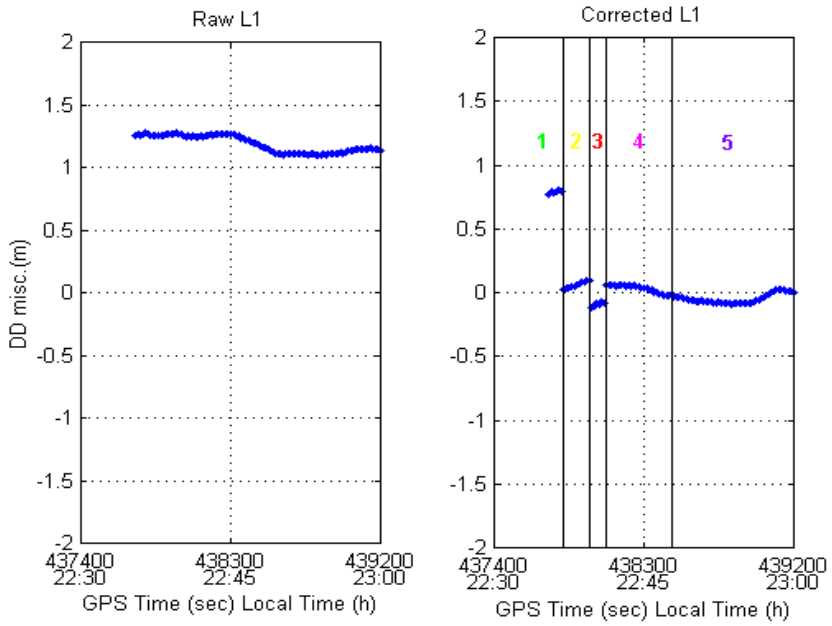

Figure 6.1: Raw and Multi-Ref-corrected L1 double difference misclosures for the AGUA to SJRP baseline (146 km) for PRN 1 as the remote satellite for August 13, 1999, using August 13, 1999, original covariance functions. The vertical lines delimit time windows when additional baselines from the reference network observed this rising satellite

Analysing Figure 6.1 it is clear the influence of observability on the quality of the corrections. In order to correlate that with the formal covariance matrix of the corrections, Figure 6.3 shows the L1 correction values for PRN 1 at the AGUA station and the corresponding standard deviations scaled by $\hat{\sigma}_0$. The correlation between them is evident. Every time a new baseline from the reference network was added to the computation, a correction with a lower standard deviation was obtained.

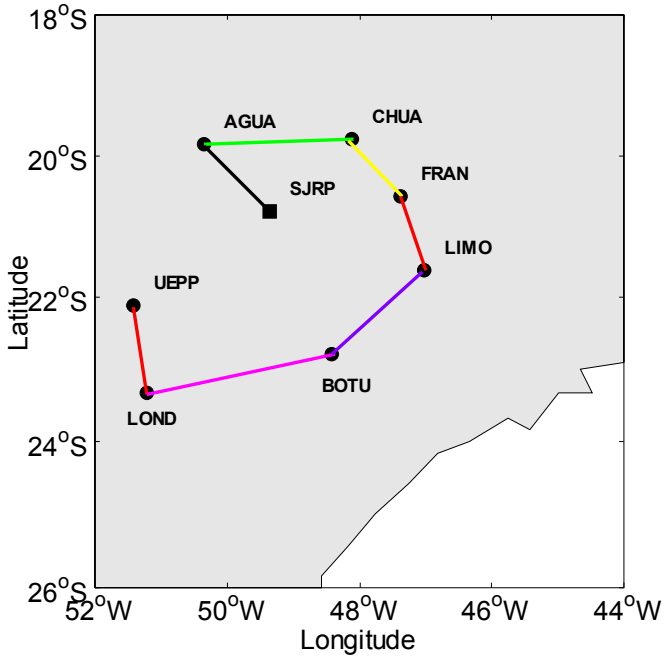

Figure 6.2: Baselines observing the rising PRN 1 for each time window: first time window (green), second one (green and yellow), third one (green, yellow and red), fourth one (green, yellow, red and magenta), and fifth one (all previous baselines plus purple)

The characteristic discussed in previous paragraphs for a rising satellite also holds for a setting satellite. In this last case, information from past epochs can be used in a Kalman filter approach [Gelb, 1974] to help improve the quality of the corrections. Townsend et al. [1999] showed that the corrections are highly correlated in time using data collected in Norway in November, 1998. The quality of the double difference corrected misclosures started to degrade only with correction latencies of 600 seconds. Despite the fact that the ionosphere was not as active as in 1999, those results indicate that the information from previous epochs can be used to strengthen the quality of the corrections.

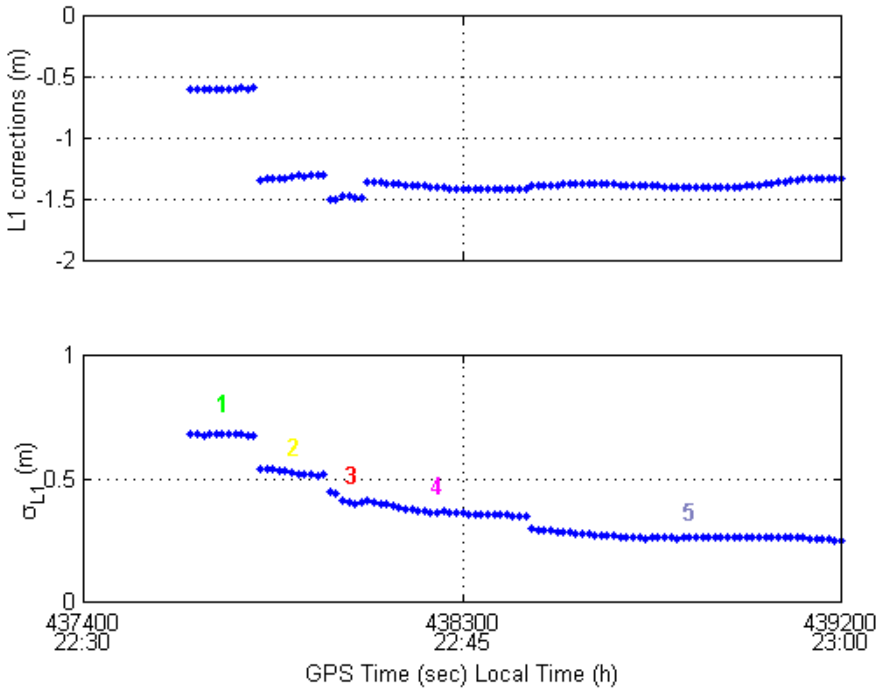

Figure 6.3: Multi-Ref L1 corrections and corresponding standard deviations scaled by $\hat{\sigma}_0$ for PRN 1 at AGUA for August 13, 1999, using August 13, 1999, original covariance functions. The numbers indicate again the time windows when additional baselines from the reference network observed this rising satellite

6.1 Kalman Filtering the Multi-Ref Corrections

The Kalman filter uses a measurement model, describing the functional relationship between observations and unknowns (also known as states), and a system model, describing the temporal variations of the unknowns [Gelb, 1974]. In the present case, the unknowns at each epoch are the "filtered" Multi-Ref corrections. The observations are the corrections computed at every epoch using the original Multi-Ref approach, i.e. using

information restricted to each epoch without considering any data provided by other epochs. Hence the observation model is simple and can be written as:

$$z(t_j) = cor(t_j) + v(t_j) \tag{6.1}$$

where $\mathbf{z(t_j)}$ is the observation (i.e. the original Multi-Ref correction) at epoch $\mathbf{t_j}$; $\mathbf{cor(t_j)}$ is the corresponding filtered correction and $\mathbf{v(t_j)}$ is the zero mean random residual.

To select the proper system model it is necessary to know how the corrections change in time. Considering that their time variations depend very much on the physical characteristics of each source of error, it is more reasonable to separately use the tropospheric/satellite orbit corrections and the ionospheric corrections rather than the lumped L1 and WL values to study their behaviour. Both random walk (RW) and Gauss-Markov (GM) stochastic processes have been used to model the temporal variations of the troposphere and ionosphere. Liao [2000] used a RW process to model the ionosphere, whereas Skone [1998] used a first order GM; Tralli and Lichten [1990] used RW and GM processes to model the troposphere, whereas Zhang [1999] used a first order GM. In this thesis, stationary, zero-mean, first order GM processes [Gelb, 1974] were used to model both troposphere and ionosphere, as it showed a good fit to the data (see Section 6.2). Hence the system model used was the following:

$$cor(t_{j+1}) = e^{-\beta(t_{j+1}-t_j)} cor(t_j) + w(t_j) \tag{6.2}$$

where $\mathbf{1/\beta}$ is the correlation time, $\mathbf{\Delta t = t_{j+1}-t_j}$ is the prediction interval, and $\mathbf{w(t_j)}$ is a white noise sequence with variance $\mathbf{q(t_j)}$, known as the process noise, given by:

$$q(t_j) = \sigma^2[1 - e^{-2\beta(\Delta t)}] \tag{6.3}$$

where $\mathbf{\sigma^2}$ is referred to as the process variance.

From Equations 6.2 and 6.3, it can be seen that the system model is determined if β and σ are known. They can be evaluated for a specific process using auto-correlation techniques [Gelb, 1974]. The auto-correlation function of a stationary random process is defined as:

$$\varphi_{xx}(\tau) = E[x(t_1)x(t_1 + \tau)] \tag{6.4}$$

As an auto-correlation function of the stationary process **x**, $\varphi_{\mathbf{xx}}$ does not depend on $\mathbf{t_1}$, but only on the time increment τ. In the case of a discrete process, with **N** samples of data taken at constant intervals $\Delta\mathbf{t}$, Equation 6.4 becomes:

$$\varphi_{xx}(k\Delta t) = \sum_{i=0}^{N-1} x(t_i)x(t_i + k\Delta t) \tag{6.5}$$

where **k** varies from 0 to N-1. This function, scaled by 1/N, was used in the computation of β and σ in Section 6.2.

After determining the values of β and σ, the Kalman filter solution for the Multi-Ref corrections for epoch $\mathbf{t_{k+1}}$ was given using the following steps:

- Prediction from time $\mathbf{t_k}$ to $\mathbf{t_{k+1}}$:

$$\mathrm{cor}^{-}(t_{k+1}) = \Theta\, \mathrm{cor}^{+}(t_k) \tag{6.6}$$

$$P^{-}(t_{k+1}) = \Theta\, P^{+}(t_k)\, \Theta^{T} + Q(t_k) \tag{6.7}$$

- Update at time $\mathbf{t_{k+1}}$:

$$\mathrm{cor}^{+}(t_{k+1}) = \mathrm{cor}^{-}(t_{k+1}) + K[z(t_{k+1}) - H(t_{k+1})\mathrm{cor}^{-}(t_{k+1})] \tag{6.8}$$

$$P^{+}(t_{k+1}) = [I - KH]\, P^{-}(t_{k+1}) \tag{6.9}$$

where the superscripts '-' and '+' represent predicted and updated values, respectively. The matrices included in Equations 6.6 to 6.9 are described as:

$$\Theta = e^{-\beta(\Delta t)}\ I \tag{6.10}$$

$$Q = \sigma^2\ [1 - e^{-2\beta(\Delta t)}]\ I \tag{6.11}$$

$$K = P^{-}(t_{k+1})\ H^{T}[H\ P^{-}(t_{k+1})\ H^{T} + R]^{-1} \tag{6.12}$$

$$H = I \tag{6.13}$$

$\boldsymbol{\Theta}$ is the transition matrix; **Q** is the process noise matrix; **I** is the identity matrix; **K** is the gain matrix; **H** describes the relationship between observations (**z**) and unknowns (**cor**), referred to as the design matrix, equal to **I** in this case (see Equation 6.1); **R** is the covariance matrix of the Multi-Ref corrections, computed using Equations 3.18 and 3.19 (and scaled by the *a posteriori* variance of unit weight - Equation 3.21), depending on if the corrections at the predicted points or at the reference stations are being filtered, respectively; and **P** is the covariance matrix of the filtered corrections.

An important remark has to be made regarding the use of the scaled version of the covariance matrix of the Multi-Ref corrections (matrix **R**). Intermediate tests using **R** not scaled by the *a posteriori* variance generated filtered corrections that were delayed with respect to the unfiltered corrections, demonstrating that the variances of the corrections were too small when compared with the elements of the process noise matrix, **Q**. However, when scaling **R** by the *a posteriori* variance, the delay was eliminated, confirming that the scaled version of **R** is a better estimate of the external accuracy of the

corrections. In order to exemplify this fact, the real quality of the Multi-Ref corrections for PRN 1 (graph on the top of Figure 6.3) was assessed inspecting the double difference corrected misclosures in Figure 6.1, which shows the raw and corrected L1 misclosures for the AGUA to SJRP baseline for the same time window with PRN 1 as the remote satellite. Despite the fact that the corrected misclosures in this figure were computed with the contribution of corrections at both stations AGUA *and* SJRP, their values match well the (scaled) standard deviations given in the bottom graph of Figure 6.3, particularly at the beginning of the satellite pass.

The Kalman filter approach described previously was applied to the Brazilian network. The initial conditions assumed in the filtering were:

- Elements of the vector $\mathbf{cor}(\mathbf{t_0})$ = 0 m;
- Diagonal elements of $\mathbf{P}(\mathbf{t_0})$ = 9999 m^2; non-diagonal elements = 0 m^2;

in order to have the first filtered correction for a specific satellite converge to the first "observation" (i.e. to the Multi-Ref correction).

The time increment ($\mathbf{\Delta t}$) adopted in the filter was the time interval between consecutive corrections. Considering that the GPS data was processed at 15 seconds, $\mathbf{\Delta t}$ was equal to this value, unless a data gap occurred.

The next section describes the computation of β and σ using auto-correlation techniques applied to real data.

6.2 Determination of the Correlation Time and the Process Variance in the Brazilian Network

The auto-correlation function of a zero-mean first order Gauss-Markov process is given by the following formula [Gelb, 1974]:

$$\varphi_{xx}(\tau) = \sigma^2 e^{-\beta|\tau|} \tag{6.14}$$

Using data collected on August 13, 1999, by the Brazilian network, auto-correlation functions were computed for the tropospheric/satellite orbit corrections and for the ionospheric corrections for 18 satellites observed from station AGUA. Special care was taken to select sequences of data that did not include any gap, in order to properly calculate the auto-correlation functions. Consequently, satellites which had data gaps were not used (PRNs 1, 6, 10, 17, 18, 19, 21, 27 and 29). After that, a Least-Squares adjustment was carried out to fit the function given by Equation 6.14 to the auto-correlation functions computed using corrections for the 18 satellites. As Equation 6.14 is

not linear in $\boldsymbol{\beta}$ and $\boldsymbol{\sigma^2}$, it had to be linearised before applying the Least-Squares algorithm. The corresponding linear model is given by:

$$\varphi_{xx}(\tau) + v = e^{-\beta_0|\tau|}\begin{bmatrix} 1 & -\sigma^2 \mid \tau \mid \end{bmatrix}\begin{bmatrix} \bar{\sigma}^2 - \sigma_0^2 \\ \bar{\beta} - \beta_0 \end{bmatrix} + \sigma_0^2 e^{-\beta_0|\tau|} \tag{6.15}$$

where $\mathbf{v}$ stands for residuals, $\bar{\boldsymbol{\beta}}$ and $\bar{\boldsymbol{\sigma}}^{\boldsymbol{2}}$ are adjusted values, and $\boldsymbol{\beta_0}$ and $\boldsymbol{\sigma_0^2}$ are initial values of an iterative process, evaluated as:

- $\beta_0 = 1/1000$ Hz;
- $\sigma_0^2 = \varphi_{xx}(0)$.

Considering that the auto-correlation function values belonged to finite-length data series, the greater the time-lag absolute values ($|\boldsymbol{\tau}|$) the worse the quality of the function values ($\varphi_{\mathbf{xx}}(\boldsymbol{\tau})$). In order to take this into account, the auto-correlation function for each satellite was limited to time lags of up to 10,000 seconds. In addition, the function values were weighted inversely to $|\boldsymbol{\tau}|$. Figures 6.4 and 6.5 show the auto-correlation functions for the tropospheric/satellite orbit corrections and for the ionospheric corrections for PRNs 16 and 30, respectively, as well as the adjusted curves. PRN 16 corresponds to a time period of quiet ionosphere, as the data was collected

during the early morning hours, whereas the data corresponding to PRN 30 was collected during the afternoon, then under an active ionosphere. These figures are similar to the ones obtained by Fotopoulos [2000], also showing the higher process variance for the ionospheric corrections during active times. It can be seen that in general the quality of the fit is very good, except for larger $|\tau|$ in some cases, due to the poorer quality of the corresponding auto-correlation values.

Table 6.1 lists the $\mathbf{1/\beta}$ and σ^2 adjusted values for the 18 satellites utilised. σ^2 values for the ionospheric corrections are, most of time, at least two orders of magnitude greater than the ones for the tropospheric/satellite orbit corrections, confirming that the ionosphere changes more over time, as mentioned in Chapter 2. The significant variability of $\mathbf{1/\beta}$ and σ^2 values among the satellites for both types of corrections can also be seen in this table. In order to try to satisfy all cases, the mean values of these parameters were used in the correction filter shown in the next section.

Despite the fact that using the mean values may not look so conservative, one should remember that the main focus was to filter corrections of low satellites setting during active ionospheric periods. When the mean process variance is smaller than the ones computed for individual satellites, more weight is assigned to corrections calculated in previous epochs than to current corrections computed using poorer observability. On the other hand, during periods of quiet ionosphere, the mean process variance is greater

than the individual ones, causing the filter results to be based more on current corrections than on previous ones, which is not a problem (a small process variance means that the corresponding corrections do not vary much over time, which shows that the filter would not be so necessary in these cases).

6.3 Filtering Corrections in the Brazilian Network

The approach described in Section 6.1 was applied to the three Brazilian scenarios for August 11 ad 13, 1999, using the correlation time and the process variance values listed in Section 6.2 to filter the tropospheric/satellite orbit corrections as well as the ionospheric corrections.

An important detail is that only corrections to reference station observations were filtered here. This is justified by the fact that the prediction points were always selected to be coincident with the $\mathbf{p_0}$ point (see Sections 4.3.1.1 and 4.3.2.1), a fact that caused all the predicted corrections and their variances to be equal to zero – then eliminating the need of filtering. Despite the fact that this represents a particular case, all conclusions drawn here can be applied to the general case, as there is no reason that restrict them.

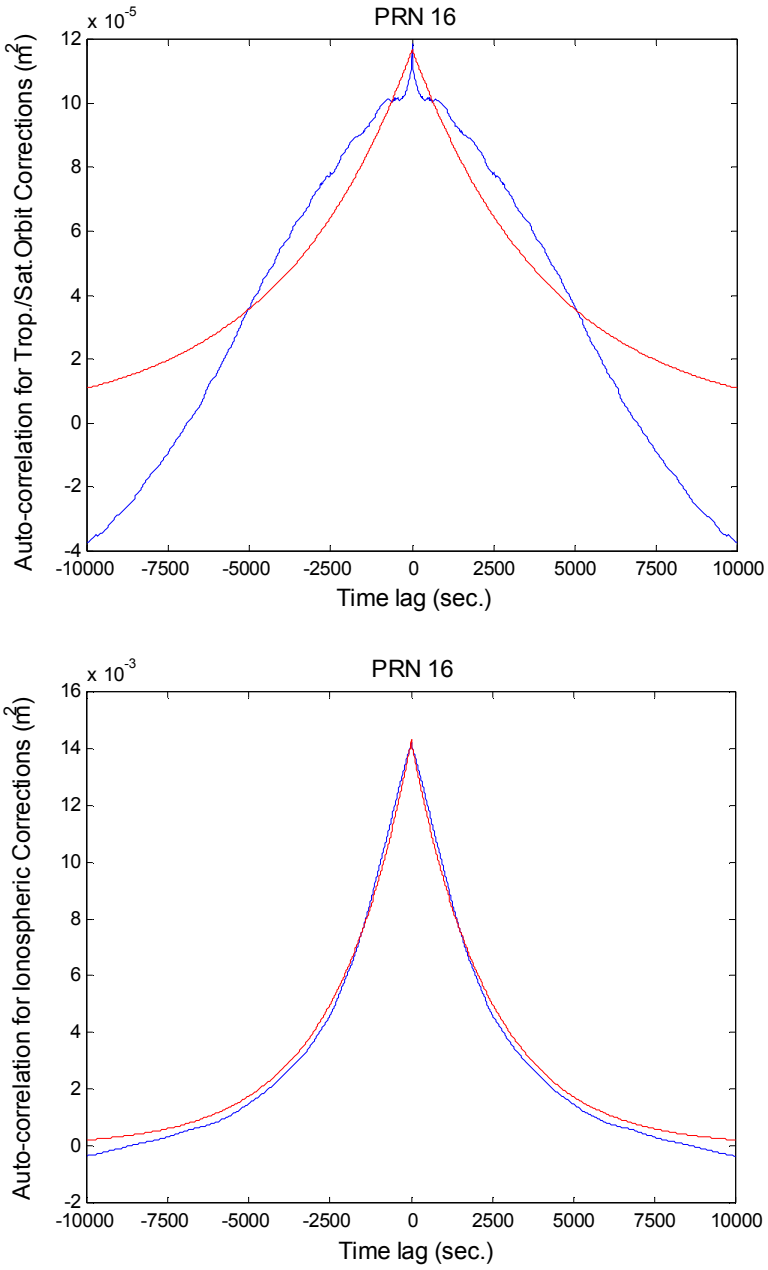

Figure 6.4: Auto-correlation functions for the tropospheric/satellite orbit corrections and for the ionosphere for PRN 16 (in blue) computed using data collected in the early morning of August 13, 1999 (quiet ionosphere), at AGUA station. The zero-mean first order Gauss-Markov auto-correlation function fit to them are shown in red

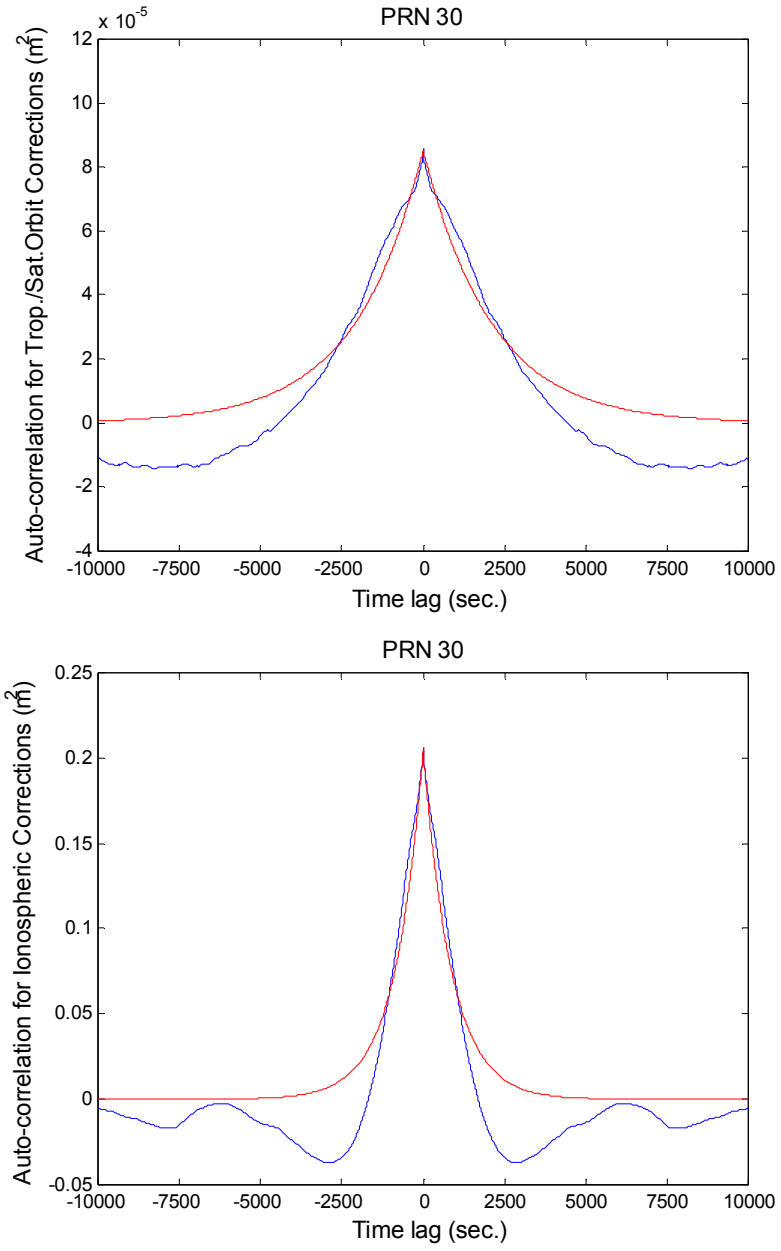

Figure 6.5: Auto-correlation functions for the tropospheric/satellite orbit corrections and for the ionosphere for PRN 30 (in blue) computed using data collected in the afternoon of August 13, 1999 (active ionosphere), at AGUA station. The zero-mean first order Gauss-Markov auto-correlation function adjusted to them are shown in red

Table 6.1: Adjusted correlation time (1/β) and process variance (σ^2) for 18 satellites using data collected at AGUA station on August 13, 1999

PRN	Trop./Sat.Orbit Corrections		Ionospheric Corrections	
	1/β (sec.)	σ^2 (m^2)	1/β (sec.)	σ^2 (m^2)
2	2287	0.000060	6070	0.008673
3	1850	0.000049	6015	0.119173
4	1053	0.000053	4133	0.060260
5	2920	0.000146	4347	0.086197
7	2627	0.000178	1887	0.010354
8	8010	0.000403	1967	0.179057
9	666	0.000040	1762	0.161585
13	521	0.000048	880	0.000691
14	3405	0.000698	1515	0.001942
15	3350	0.000143	2884	0.196723
16	4218	0.000117	2382	0.014288
22	3149	0.000234	4013	0.004379
23	2554	0.000081	2504	0.024439
24	8335	0.000438	2487	0.032830
25	9132	0.000572	1716	0.017361
26	3586	0.000205	3791	0.047642
30	2088	0.000085	866	0.205801
31	2149	0.000134	3084	0.123367
Mean	**1960**	**0.000205**	**2156**	**0.071931**

After filtering the corrections, they were applied to L1 and WL phase observations using Equations 5.52 and 5.54 before recomputing the double difference misclosures. Table 6.2 shows the improvement in the observation domain brought by the Multi-Ref filtered corrections, whereas Table 6.3 shows the difference with respect to the results obtained before filtering the corrections (from Table 5.11). As can be seen by analysing these two tables, in general the improvement is at the same level as before, as expected. That happened because the filter improved the corrections only in a few cases, mainly when a satellite was setting under a high ionospheric condition, causing little or

no impact on the overall statistics of the entire 24-hour period. Nevertheless, the RMS values were slightly reduced in most of cases when the filtered corrections were applied. For the baselines AGUA to SJRP and REGI to BOTU on August 13, 1999, the filtered corrections slightly deteriorated the quality of the results. Possible reasons for this are based on the quality of the corrections for rising satellites and some extreme setting satellites' cases, as is going to be discussed later in this section. Hence the overall improvement for each scenario was a trade-off between the cases improved by the filter and the ones deteriorated by the filter. Figure 6.6 plots the raw double difference misclosures for the FRAN to LIMO baseline (122 km) for August 13, 1999, and the Multi-Ref corrected values using unfiltered and filtered corrections. One can see that many of the isolated dots present in the unfiltered case – mainly at the end of the day - were eliminated when using filtered corrections, thereby improving the results.

To actually assess the improvement brought by the filtered corrections, individual satellite cases had to be investigated. Figure 6.7 shows the unfiltered and filtered tropospheric/satellite orbit corrections to observations of PRN 30 collected at the FRAN reference station on August 13, 1999, whereas Figure 6.8 plots the corresponding unfiltered and filtered ionospheric corrections. Once more the consequences of the poor observability in the network when the satellite was setting can be seen, causing discontinuities in the unfiltered ionospheric corrections. As the tropospheric/satellite orbit corrections were much smaller (as normally happens), those discontinuities were masked

by the correction noise – mainly at low elevations - in this case. Analysing Figure 6.8, it can be seen that some corrections close to 20:00h local time changed by almost one metre after the filter was applied.

Table 6.2: Raw and Multi-Ref-corrected double difference misclosures RMS and respective improvement for the FRAN to LIMO, AGUA to SJRP, and REGI to BOTU baselines for August 11 and 13, 1999, using filtered corrections for the troposphere, satellite orbits and ionosphere

Baseline	Length (km)	L1 (m)			WL (m)		
		Raw	Corr.	Improv.	Raw	Corr.	Improv.
FRAN - LIMO	122						
August 11		0.191	0.104	46%	0.258	0.133	48%
August 13		0.327	0.148	55%	0.418	0.192	54%
AGUA - SJRP	146						
August 11		0.284	0.100	65%	0.364	0.131	64%
August 13		0.350	0.129	63%	0.440	0.168	62%
REGI - BOTU	193						
August 11		0.239	0.117	51%	0.312	0.157	50%
August 13		0.407	0.176	57%	0.516	0.214	59%

Table 6.3: Differences between Multi-Ref-corrected double difference misclosures RMS and respective improvement for the FRAN to LIMO, AGUA to SJRP, and REGI to BOTU baselines for August 11 and 13, 1999, using filtered and unfiltered corrections for the troposphere, satellite orbits and ionosphere[1]

Baseline	Length (km)	L1 (m)		WL (m)	
		Corr. Diff.	Imp. Diff.	Corr. Diff.	Imp. Diff.
FRAN - LIMO	122				
August 11		-0.004	3%	-0.004	1%
August 13		-0.003	1%	-0.003	1%
AGUA - SJRP	146				
August 11		-0.004	2%	-0.004	1%
August 13		0.006	-2%	0.007	-1%
REGI - BOTU	193				
August 11		-0.003	1%	-0.006	2%
August 13		0.004	-1%	0.005	0%

1: a positive improvement difference means better performance using the filtered corrections

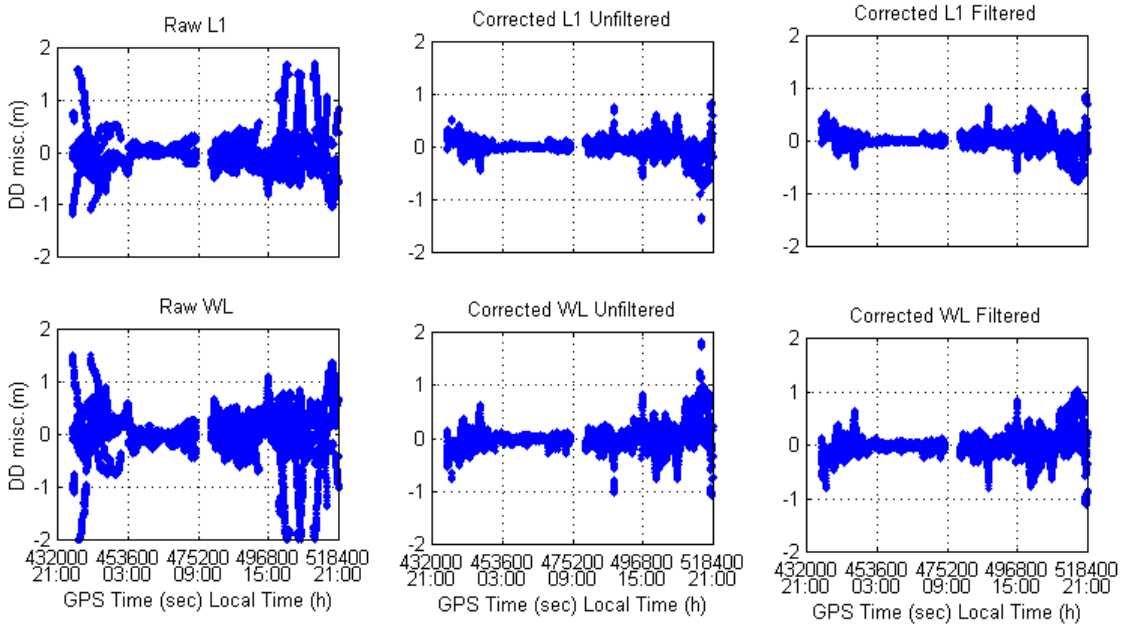

Figure 6.6: Raw (left column) and Multi-Ref-corrected L1 and WL double difference misclosures for the FRAN to LIMO baseline (122 km) for August 13, 1999, using unfiltered (middle column) and filtered (right column) corrections for the troposphere, satellite orbits and ionosphere

One can also see in this figure that the unfiltered corrections shown small discontinuities during the entire data set (for example, just before 16:00 and 19:00 local time), which corresponded to epochs when the total number of reference network misclosures used in the correction computation changed, with the added or removed misclosures not including PRN 30. These small discontinuities were smoothed out after filtering.

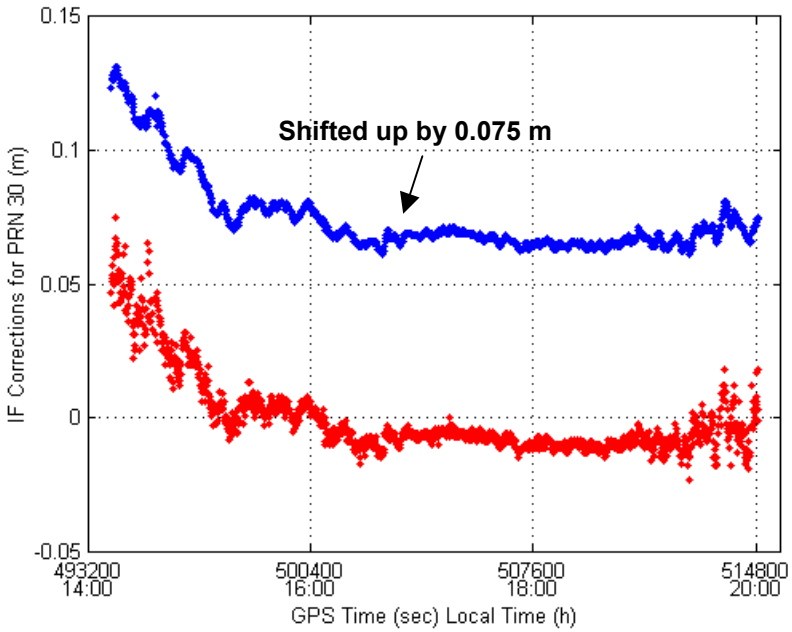

Figure 6.7: Unfiltered (red) and filtered (blue) tropospheric/satellite orbit corrections to observations of PRN 30 collected at the FRAN reference station on August 13, 1999. The filtered corrections were shifted up by 0.075 m for comparison purposes

To confirm that the filtered corrections are actually of better quality than the unfiltered ones, it was necessary to analyse the double difference misclosures that have PRN 30 as the remote satellite. Figure 6.9 plots these raw misclosures and the ones obtained using unfiltered and filtered corrections (actually these misclosures are embedded into Figure 6.6 as well). It can be seen that the misclosures corrected by the filtered corrections are much smaller than the ones obtained using unfiltered corrections.

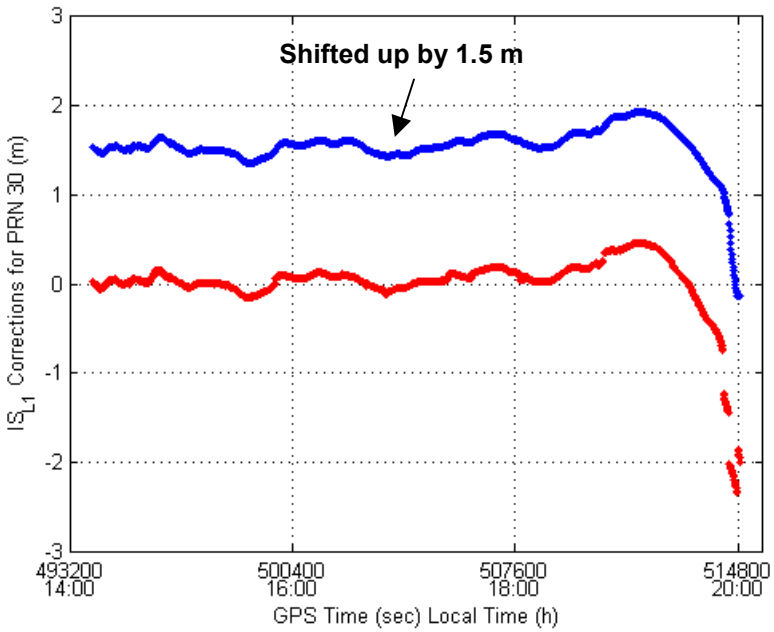

Figure 6.8: Unfiltered (red) and filtered (blue) ionospheric corrections to observations of PRN 30 collected at the FRAN reference station on August 13, 1999. The filtered corrections were shifted up by 1.5 m for comparison purposes

Table 6.4 lists the RMS of the L1 and WL raw and corrected misclosures and corresponding improvement using unfiltered and filtered corrections computed individually for some satellites of the six scenarios of the Brazilian network. The differences between the unfiltered and filtered results are also included in this table. The use of filtered corrections improved the Multi-Ref performance up to 44%, or 0.111 m, in L1, and up to 43%, or 0.139m, in WL (corresponding to PRN 30 of Figure 6.9).

Although these represent very good results, they did not repeat for all satellites. This happened because the actual improvement given by the filtered corrections

depended on the situation of the specific satellite. If the satellite was rising or setting during the night, the filtered corrections did not have an impact on the results. If the satellite was setting under high ionosphere, the filtered corrections improved the results in most cases. A few exceptions occurred at extreme situations – i.e. the corresponding raw misclosures were very large (> 0.60 m) - when the use of filtered corrections caused the results to be up to 5% (equivalent to a few centimetres) worse than the ones given by unfiltered corrections. In these cases, a fine-tuning of the correlation time and process variance may be required. In addition, the filter did not outperform the unfiltered case in some situations when the corresponding satellite was rising under high ionosphere. Figure 6.10 plots the raw misclosures and the ones obtained using unfiltered and filtered corrections with PRN 15 as the remote satellite for the AGUA to SJRP baseline (146 km) for August 13, 1999. This satellite was rising under high ionospheric conditions just after 23:30 local time. It can be seen that the misclosures were pulled out from the zero line in the beginning of the data set, as the filter forced the corresponding corrections to follow the ones from previous epochs, obtained with poor observability. The general improvement given by the unfiltered corrections was 81% for L1 and 83% for WL, whereas these values were slightly degraded to 80% and 82%, respectively, when the filtered corrections were applied. These results show that in general the filtered corrections should not be applied to observations corresponding to initial rising portions of the satellite pass.

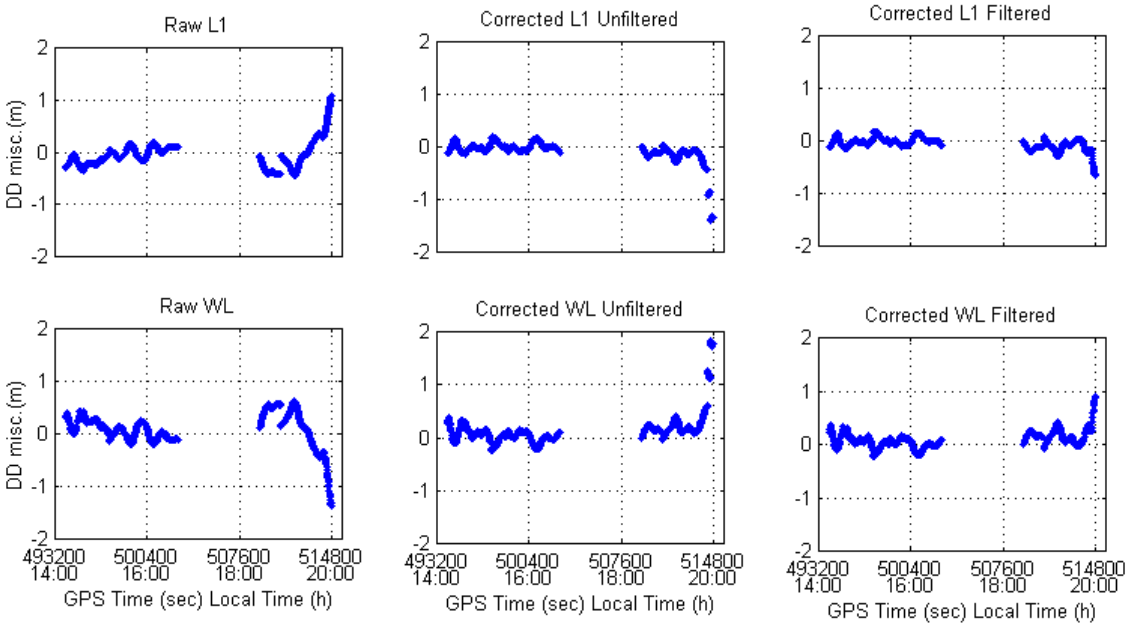

Figure 6.9: Raw (left column) and Multi-Ref-corrected L1 and WL double difference misclosures for the FRAN to LIMO baseline (122 km) for August 13, 1999, using unfiltered (middle column) and filtered (right column) corrections for the troposphere, satellite orbits and ionosphere, with PRN 30 as the remote satellite (setting under high ionospheric conditions)

Table 6.4: Raw and Multi-Ref-corrected double difference misclosures RMS and respective improvement, using unfiltered and filtered corrections for the troposphere, satellite orbits and ionosphere, for some satellites in each scenario

PRN	Corrections	L1 (m)			WL (m)		
		Raw	Corr.	Improv.	Raw	Corr.	Improv.
FRAN → LIMO (122 km), August 11							
9	Unfiltered (U)	0.243	0.156	36%	0.354	0.188	47%
	Filtered (F)	0.243	0.143	41%	0.354	0.172	51%
	Difference (F-U)	**0**	**-0.013**	**5%**	**0**	**-0.016**	**4%**
19	Unfiltered (U)	0.109	0.067	39%	0.140	0.075	46%
	Filtered (F)	0.109	0.059	46%	0.140	0.068	51%
	Difference (F-U)	**0**	**-0.008**	**7%**	**0**	**-0.007**	**5%**
22	Unfiltered (U)	0.308	0.258	16%	0.407	0.269	34%
	Filtered (F)	0.308	0.238	23%	0.407	0.251	38%
	Difference (F-U)	**0**	**-0.020**	**7%**	**0**	**-0.018**	**4%**
26	Unfiltered (U)	0.227	0.204	10%	0.294	0.261	11%
	Filtered (F)	0.227	0.191	16%	0.294	0.244	17%
	Difference (F-U)	**0**	**-0.013**	**6%**	**0**	**-0.017**	**6%**
FRAN → LIMO (122 km), August 13							
25	Unfiltered (U)	0.277	0.113	59%	0.341	0.135	60%
	Filtered (F)	0.277	0.103	63%	0.341	0.124	64%
	Difference (F-U)	**0**	**-0.010**	**4%**	**0**	**-0.011**	**4%**
27	Unfiltered (U)	0.130	0.102	22%	0.158	0.122	23%
	Filtered (F)	0.130	0.089	32%	0.158	0.105	34%
	Difference (F-U)	**0**	**-0.013**	**10%**	**0**	**-0.017**	**11%**
30	Unfiltered (U)	0.252	0.232	8%	0.323	0.311	4%
	Filtered (F)	0.252	0.121	52%	0.323	0.172	47%
	Difference (F-U)	**0**	**-0.111**	**44%**	**0**	**-0.139**	**43%**
AGUA → SJRP (146 km), August 11							
10	Unfiltered (U)	0.385	0.174	55%	0.459	0.228	50%
	Filtered (F)	0.385	0.150	61%	0.459	0.196	57%
	Difference (F-U)	**0**	**-0.024**	**6%**	**0**	**-0.032**	**7%**
22	Unfiltered (U)	0.646	0.235	64%	0.790	0.308	61%
	Filtered (F)	0.646	0.213	67%	0.790	0.284	64%
	Difference (F-U)	**0**	**-0.022**	**3%**	**0**	**-0.024**	**3%**

(continues)

Table 6.4 (continued): Raw and Multi-Ref-corrected double difference misclosures RMS and respective improvement, using unfiltered and filtered corrections for the troposphere, satellite orbits and ionosphere, for some satellites in each scenario

AGUA → SJRP (146 km), August 13							
1	Unfiltered (U)	0.472	0.102	78%	0.584	0.134	77%
	Filtered (F)	0.472	0.096	80%	0.584	0.120	79%
	Difference (F-U)	**0**	**-0.006**	**2%**	**0**	**-0.014**	**2%**
5	Unfiltered (U)	0.205	0.166	19%	0.246	0.230	7%
	Filtered (F)	0.205	0.158	23%	0.246	0.218	11%
	Difference (F-U)	**0**	**-0.008**	**4%**	**0**	**-0.012**	**4%**
BOTU → REGI (191 km), August 11							
2	Unfiltered (U)	0.313	0.162	48%	0.467	0.232	50%
	Filtered (F)	0.313	0.126	60%	0.467	0.176	62%
	Difference (F-U)	**0**	**-0.036**	**12%**	**0**	**-0.056**	**12%**
6	Unfiltered (U)	0.253	0.109	57%	0.392	0.165	58%
	Filtered (F)	0.253	0.099	61%	0.392	0.154	61%
	Difference (F-U)	**0**	**-0.010**	**4%**	**0**	**-0.011**	**3%**
9	Unfiltered (U)	0.338	0.302	11%	0.561	0.429	24%
	Filtered (F)	0.338	0.291	14%	0.561	0.409	27%
	Difference (F-U)	**0**	**-0.011**	**3%**	**0**	**-0.020**	**3%**
BOTU → REGI (191 km), August 13							
8	Unfiltered (U)	0.436	0.139	68%	0.522	0.165	68%
	Filtered (F)	0.436	0.121	72%	0.522	0.154	70%
	Difference (F-U)	**0**	**-0.018**	**4%**	**0**	**-0.011**	**2%**
9	Unfiltered (U)	0.372	0.234	37%	0.547	0.263	52%
	Filtered (F)	0.372	0.182	51%	0.547	0.197	64%
	Difference (F-U)	**0**	**-0.052**	**14%**	**0**	**-0.066**	**12%**
19	Unfiltered (U)	0.180	0.101	44%	0.179	0.089	50%
	Filtered (F)	0.180	0.086	52%	0.179	0.069	61%
	Difference (F-U)	**0**	**-0.015**	**8%**	**0**	**-0.020**	**11%**
30	Unfiltered (U)	0.820	0.217	74%	0.987	0.261	74%
	Filtered (F)	0.820	0.200	76%	0.987	0.239	76%
	Difference (F-U)	**0**	**-0.017**	**2%**	**0**	**-0.022**	**2%**

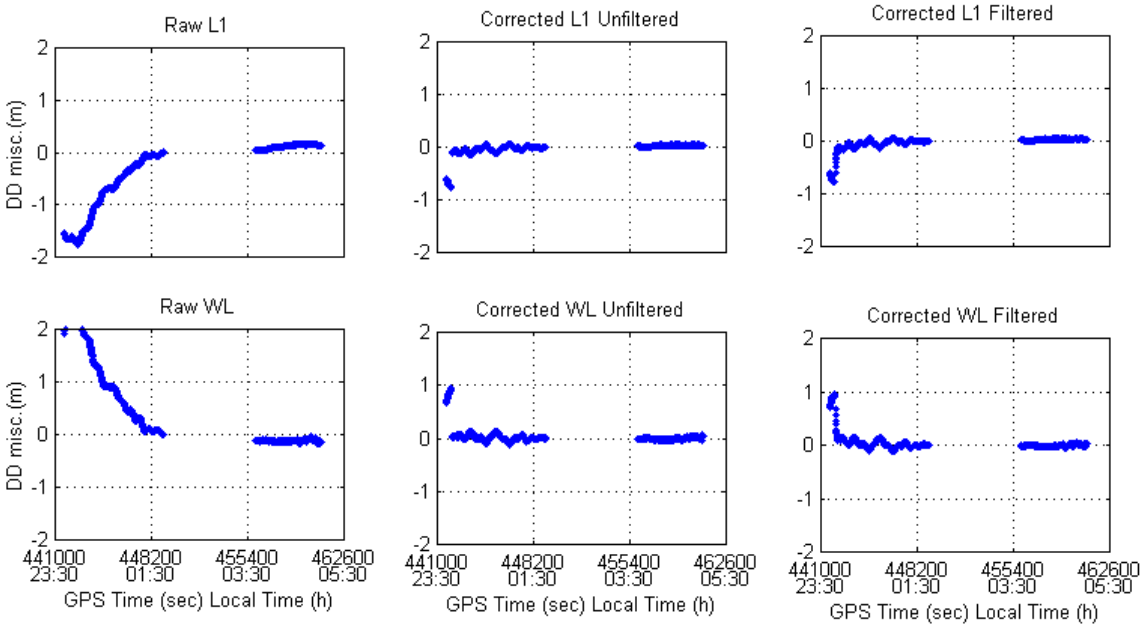

Figure 6.10: Raw (left column) and Multi-Ref-corrected L1 and WL double difference misclosures for AGUA to SJRP baseline (146 km) for August 13, 1999, using unfiltered (middle column) and filtered (right column) corrections for troposphere, satellite orbits and ionosphere, with PRN 15 as the remote satellite (rising under high ionosphere)

CHAPTER 7

CONCLUSIONS, RECOMMENDATIONS AND FUTURE RESEARCH

In this thesis, an optimisation of the Multi-Ref method was attempted through refinements and extensions implemented to the covariance functions, including separate modelling of the correlated errors. A detailed study was also carried out in terms of the impact of the various covariance functions on the estimated variances of the corrections. In addition, filter techniques were applied to the tropospheric/satellite orbit corrections and to the ionospheric corrections, in order to use information from previous epochs to improve their quality. Data sets collected in August 1999 in the St. Lawrence region, Canada, and in Southeastern Brazil were used to assess the impact of the derived approaches on two different regions of the world, subjected to different characteristics of the ionosphere and troposphere. The conclusions and recommendations related to this work are described in the next section, whereas areas for future research are recommended in Section 7.2.

7.1 Conclusions and Recommendations

7.1.1 Optimisation Based on Re-computing the Original Covariance Functions

The impact of using different data sets to compute the original covariance functions for L1 and WL derived by Raquet [1998] was assessed. Initial results in applying the Multi-Ref method to both networks were obtained using covariance functions derived using data collected in the St. Lawrence region in November, 1998. The original covariance functions were then re-computed using data collected in both regions during August, 1999. For the St. Lawrence network, the Multi-Ref approach generated results with the same percentage improvement in the observation domain as before. The fact that the previous covariance functions had been computed using data from the same region, combined with the short baselines in the network (30 and 46 km), may have contributed to get the same level of improvement. For the Brazilian network, using covariance functions re-computed with data collected during the campaign increased the improvement brought by Multi-Ref in the observation domain (RMS of the double difference misclosures) up to 9%, or 3.1 cm, in L1 and up to 14%, or 5.8 cm, in WL. The longer baselines present in the Brazilian network seem to have contributed to this performance improvement. The main differences were observed in some double difference misclosures, which corresponded to the situation when the remote satellite was observed by only a few reference stations, as it was rising or setting. This characteristic

motivated the derivation of the correction filtering, in order to overcome these cases of poor observability of low elevation satellites.

The results mentioned above indicated that the Multi-Ref method is not very sensitive to the original covariance functions utilised. In order to confirm this, very extreme (high and low) error conditions were simulated for the correlated error functions, giving results similar to those obtained using covariance functions computed using real data (differences at the millimetre level only). Consequently the covariance functions do not seem to have a large impact on the improvement brought by the Multi-Ref approach for the data sets used in this research.

7.1.2 Optimisation Based on Separate Modelling of the Errors

The next step was to improve the Multi-Ref performance by separate modelling of the correlated errors that affect GPS positioning. Hence, different covariance functions were computed for the tropospheric/satellite orbit errors and for the ionospheric errors, using respectively the ionospheric-free and the geometric-free (scaled to L1) linear combinations. For the ionosphere, the errors were also modelled in directional components (North-South and East-West), considering the expected different error decorrelation along those directions, mainly in the equatorial region where the Brazilian network is located. The results for both networks did not show a significant improvement

with respect to the original covariance functions (only at the millimetre level in some cases), even with the directional modelling of the ionosphere using corrected geomagnetic coordinates, demonstrating that the extra effort for generating a more sophisticated model did not prove to have value. It was known from Moritz [1972] that the results of Least-Squares Collocation are not so sensitive to the covariance function, but as the case here was to completely redefine the function by error sources – including the use of completely different mapping functions, a greater impact on the results was expected. Using data from each campaign to re-compute the original covariance functions improved the results more than changing the covariance functions themselves.

Considering the variation of the ionospheric effects with local time, an attempt was made in terms of using an adaptive covariance function for the ionosphere, recomputing it every 30 or 60 minutes. The improvement brought by the Multi-Ref method in this case was worse than using the original covariance functions, probably due to the lack of redundant observations when computing the covariance function for each time interval.

Analysing from a conservative perspective, the results mentioned in Section 7.1.1 and above indicate that the covariance functions should be calculated using data collected by the reference network to be used when starting this kind of service. After that,

recomputing them about three times during each 11-year solar cycle (at the peak, in the middle and at the bottom of the cycle) is probably enough.

The Multi-Ref approach is equivalent to a Least-Squares Conditional adjustment with respect to the computation of corrections to the reference station observations. Consequently, the corrections force the adjusted double difference misclosures between any pair of reference stations to always be zero, independent of the covariance function used. The Multi-Ref method then gives a tool to distribute the misclosures among the single observations, for which the covariance function plays a role. The covariance function is also important to predict the corrections at the rover positions. These properties help to understand why the method is not so sensitive to the covariance functions chosen.

On the other hand, the results emphasise the Multi-Ref method robustness, as a simpler lumped model gives good results. This characteristic is very important if one thinks of a real time service, as there will be no need for frequent covariance function updates. Comparing the original covariance functions to those that model the errors separately, the second ones may have the advantage of reducing the number of corrections to be transmitted to users, as the tropospheric/satellite orbit corrections and the ionospheric corrections are applicable to both code and phase observations. In addition, transmitting corrections separated by error source gives more flexibility, as

different update rates can be used for each correction according to the error behaviour. When implementing the filter approach, it makes more sense to use corrections for each type of error, as the intrinsic characteristics of the error sources can be isolated more effectively. These advantages suggest that it is preferable to use the separate model of the errors over the lumped model in such services.

The covariance matrix of the reference stations' corrections and the *a posteriori* variance of unit weight were computed in all tests for both networks. Using different covariance functions changed the estimated accuracy of the corrections, as mentioned by Moritz [1976]. However, when the correction variances were scaled by the *a posteriori* variance of unit weight, the corrections' estimated accuracies were very similar in all cases. This confirmed that the *a posteriori* variance converts the precision of the corrections (internal), based on the covariance functions, to an estimation of their accuracy (external), based on the real data. Filter results (see next section) confirmed that the scaled standard deviations of the corrections are a very good estimate of the real errors of the corrections. This fact was again confirmed by comparing the actual quality of the corrections (based on the double difference corrected misclosures) with their estimated accuracy.

The *a posteriori* variance was also shown to be useful to detect when the actual conditions of the errors in the network deviate from the ones predicted by the covariance

functions, working to some extent as an “adaptive” approach to calibrate the covariance functions. For instance, when the ionosphere was more active than it was when the covariance function was derived, the *a posteriori* variance values were greater than 1 (corresponding to accentuated observation residuals), as the observation weights given by the covariance function were relatively large (optimistic). The *a posteriori* variance therefore is an indicator to portrait the error behaviour in a real time service, which can help to issue alerts to users, for example.

Due to the fact that the *a posteriori* variances reflect the actual situation of the errors in the network, it is important to properly interpret the meaning of the scaled variances of the corrections. As mentioned previously, the scaled variances are estimates of the external accuracy of the corrections. Therefore, a large correction variance means that the corresponding correction is not as accurate, which normally occurs under active ionospheric conditions (when the corrections are not expected to have the same quality as during quiet times, due to greater variability of the ionospheric errors across the reference network), or when the specific satellite has observability problems. Based on this fact, the estimated accuracy of the corrections is very useful information that can be used along with the corrections in order to help subsequent processes, e.g. ambiguity resolution (in the network and to the user) and user positioning. It could also be used to generate criteria to reject poor corrections, in the case of rising satellites, for instance.

Second degree polynomials were used for the covariance functions in all cases, as they showed a good fit to the data. Other functions were also tried, but none had a better performance. Some of them generated very poor results, e.g. a third degree polynomial used to fit the geometric-free misclosures to model the ionosphere, even worse than with raw observations. Later, it was found out that the normal matrix to be inverted to compute the corrections (term $BC_{\delta l}B^T$ in Equations 3.15 and 3.16) was not positive definite. The same situation happened when a second degree polynomial with the coefficient of the first order term ($\mathbf{k_1}$) equal to zero was tried. This makes evident that special care has to be taken in terms of testing if the normal matrix satisfies that condition when trying different covariance functions.

To compute the *a posteriori* variance of unit weight, the observation covariance matrix has to be inverted. In some cases (mainly when modelling the tropospheric and satellite orbit errors, as they decorrelate slowly), the $\mathbf{k_1}$ coefficient was negative, generating a non-positive definite observation covariance matrix $C_{\delta l}$. Hence special care has to be taken in terms of testing if the covariance matrix satisfies this condition before inversion.

7.1.3 Optimisation Based on Filtering the Corrections

In order to try to overcome the poor quality of the corrections in the Brazilian network in cases when the remote satellite was rising or setting – due to a bad observability from the reference network - a Kalman filter approach applied to the Multi-Ref corrections was implemented. The tropospheric/satellite orbit corrections as well as the ionospheric corrections were modelled as first-order Gauss-Markov processes, which seemed adequate when analysing real data. The corresponding correlation time and process variance for each process were derived using actual corrections computed for one observation day. The raw L1 and WL double difference misclosures for each of the six scenarios were corrected using filtered corrections. In general, the filtered corrections improved the performance of the method for setting satellites under high ionospheric conditions up to 44%, or 0.111 m, in L1, and up to 43%, or 0.139 m, in WL. This shows that the filter must be applied to improve the corrections in such cases. The same level of improved results was not obtained for rising satellites under the same ionospheric conditions, as the filter in general degraded the corrections in these cases, indicating that it should not be applied in such situations. In a few other extreme cases, when the raw double difference misclosure were too large (> 0.60 m), the filter did not improve the performance for setting satellites. It is believed that the correlation time and process variance – for the ionospheric corrections - would have to be fine-tuned in these cases.

Intermediate tests using a covariance function of the corrections not scaled by the *a posteriori* variance generated filtered corrections that were delayed with respect to the unfiltered corrections, demonstrating that the variances of the corrections were too small when compared with the elements of the process noise matrix. However, when scaling it by the *a posteriori* variance, the delay was eliminated, confirming that the scaled version of the covariance matrix is a better estimate of the external accuracy of the corrections.

7.2. Future Research

The current implementation of the covariance functions in the Multi-Ref approach – either the original lumped ones or the ones separated by error source - does not include correlations between different satellites. When attempted in this research, this alternative generated unsuccessful results, as the resultant covariance matrix of the observations, based on the current functional form of the covariance functions, was not positive definite. This topic requires further investigation, as the inclusion of correlations between satellites could improve the method in some aspects, such as the quality of the corrections for new (i.e. rising) satellites.

It was detected that the reference network observability is an issue that affects the Multi-Ref performance. In order to overcome this problem, even in extreme cases, it is recommended to extend the procedure described in Section 7.1.3 by applying an adaptive

filter to the corrections. This approach could improve the quality of the corrections for rising satellites as well. Another option would be to model the ionospheric corrections as a second order Gauss-Markov process, as the results for some satellites indicated this possibility. In addition, adding more stations to the reference network (despite the fact that it is not a cost-effective solution), decreasing the inter-reference station distances, would make a low-elevation satellite be observed by more reference stations and, as such, also improve the quality of the corrections for both rising and setting periods of time.

With respect to the geometry of the reference network, no specific investigation was carried in this research. The scenarios used in the St. Lawrence and Southeastern Brazil tests always included a prediction point located inside the network. It is expected that for points located outside the network, the Multi-Ref performance decreases. In addition, Fortes et al. [2000] attempted to apply the Multi-Ref approach using a reference network whose stations were practically aligned along the same azimuth, and showed that observations from satellite positions located across the reference network were not properly corrected. This fact indicates that a reference network with "good" geometry should have its baselines covering the 0°-360° azimuth range. The high correlation between differential ionospheric errors for baselines with similar azimuths in the Brazilian network (see Section 5.2.1) corroborates this indication. Nevertheless, a rigorous study of the impact of the reference network geometry on the Multi-Ref performance is recommended.

The Multi-Ref approach is strongly based on the ability of fixing ambiguities in the reference network. In the present dissertation, this task was accomplished in post-mission mode using the Bernese GPS Software. The real time solution of these ambiguities represents a field of study that still requires further investigation. With respect to this matter, an optimised solution, which combines the ambiguity resolution approach with the correction generation, is envisaged, as the observation corrections (and their estimated accuracy) could be used to improve the ambiguity resolution in subsequent data epochs. Considering the proximity to the last solar maximum, occurred during the 2000-2001 period, the adoption of a stochastic model for the ionosphere [Odijk, 2000] seems to be also a valuable tool to help ambiguity resolution in the network.

In terms of error modelling, a field that requires further investigation is related to using the observations collected by the reference network stations to derive post-mission and predicted local/regional ionospheric models (i.e. maps) to be used to correct the ionospheric errors in the region. The Multi-Ref approach could then be used to model the residual errors, similar to what is done with the tropospheric effects. In this thesis, this approach was attempted using the CODE global ionospheric maps, but it showed not to be beneficial in this case, since those maps only model the long wavelengths of the errors.

REFERENCES

Aarons, J. *Global Morphology of Ionospheric Scintillations*. Proceedings of the IEEE, Vol. 70, No. 4, pp. 360-378, April 1982.

Advanstar Communications, Inc. *GPS Constellation*. GPSWorld Showcase, Technology and Product Innovation for the Global Positioning System, August 1999.

Appleton, E. V. *The Anomalous Equatorial Belt in the F2-layer*. Journal of Atmospheric and Terrestrial Physics, 5, pp. 348-351, 1954.

Aquino, M. H. O. de. *Regional Approach to Wide Area DGPS*. PhD Thesis, Institute of Engineering Surveying & Space Geodesy, University of Nottingham, 1998.

Beutler, G. *Panel Discussion: The Civil and Military Issues Facing GPS and GNSS*. Proceedings of the 10th International Technical Meeting of the Satellite Division of the Institute of Navigation, pp. 3-20, Kansas City, September 1997.

Beutler, G., Weber, W., Hugentobler, U., Rothacher, M., and Verdun, A. *GPS for Geodesy*. Chapter 2: GPS Satellite Orbits, pp. 43-109. Springer-Verlag, 1998.

Blais, J. A. R. *Estimation and Computational Analysis*. ENGO 699.78 Lecture Notes, Department of Geomatics Engineering, The University of Calgary, 2002.

Cannon, M. E. *Carrier Phase Kinematic Positioning: Fundamentals and Applications*. Geodetic Applications of GPS, Lecture Notes for Nordic Autumn School, pp 157-179. National Land Survey, Sweden, 1997.

CODE. *Global Ionosphere Maps Produced by CODE*. http://www.cx.unibe.ch/aiub/ionosphere.html. Centre for Orbit Determination in Europe, Astronomical Institute, University of Berne, 2001.

DMA. *World Geodetic System 1984 (WGS84) – Its Definition and Relationships with Local Geodetic Systems*. Defense Mapping Agency Technical Report 8350.2, Second Edition, 1991.

Dodson, A. H., Bingley, R. M., Penna, N. T., and Aquino, M. H. O. *A National Network of Continuously Operating GPS Receivers for the UK*. Geodesy Beyond 2000:

The Challenges of the First Decade, International Association of Geodesy Symposia, Vol. 121, pp. 367-372, Springer-Verlag, 1999.

Falvey, M., and Beavan, J. *Real-Time Estimation of Precipitable Water Using New Zealand's Continuous GPS Network*. Paper presented at the General Assembly of the International Union of Geodesy and Geophysics, Birmingham, UK, July 1999.

Feltens, J., and Schaer, S. *1999 IGS Activities in the Area of the Ionosphere*. IGS 1999 Technical Reports, pp. 263-268, IGS Central Bureau, Pasadena, 2000.

Ferland, R. *IGSMail-2899: Original / New Realization of ITRF97*. http://igscb.jpl.nasa.gov/mail/igsmail/2000/msg00245.html. June 23, 2000.

Fortes, L. P. S.; Luz, R. T.; Pereira, K. D.; Costa, S. M. A., and Blitzkow, D. *The Brazilian Network for Continuous Monitoring of GPS (RBMC): Operation and Products*. Advances in Positioning and Reference Frames, International Association of Geodesy Symposia, Vol. 118, pp. 73-78, Springer-Verlag, 1998.

Fortes, L. P., Lachapelle, G., Cannon, E., Ryan, S., Marceau, G., Wee, S., and Raquet, J. *Use of a Multi-Reference GPS Station Network for Precise 3D Positioning in*

Constricted Waterways. International Hydrographic Review, Vol. 1 No. 1 (New Series), pp. 15-29, July 2000.

Fotopoulos, G. *Parameterization of DGPS Carrier Phase Errors Over a Regional Network of Reference Stations*. MSc Thesis, UCGE Report Number 20142, Department of Geomatics Engineering, The University of Calgary, 2000.

Frei, E., and Beutler, G. *Rapid Static Positioning based on the Fast Ambiguity Resolution Approach "FARA": Theory and First Results*. Manuscripta Geodaetica, Vol. 15, pp. 325-356, Springer-Verlag, 1999.

Gao, Y., Li, Z., and McLellan, J. F. *Carrier Phase Based Regional Area Differential GPS for Decimeter-Level Positioning and Navigation*. Proceedings of the 10th International Technical Meeting of the Satellite Division of the Institute of Navigation, 1305-1313, Kansas City, September 1997.

Gao, Y., and Li., Z. *Ionosphere Effect and Modeling for Regional Area Differential GPS Network*. Proceedings of the 11th International Technical Meeting of the Satellite Division of the Institute of Navigation, pp. 91-97, Nashville, September 1998.

Gelb, A. (Ed.). *Applied Optimal Estimation*. The M.I.T. Press, 1974.

Gemael, C. *Introdução ao Ajustamento de Observações: Aplicações Geodésicas*. Editora da UFPR, Curitiba, 1994.

Georgiadou, Y. *The impact of GPS technology on National Mapping Organisations*. Invited Paper 7.3, Proceedings of Cambridge Conference, pp. 12, Ordnance Survey, UK, July 1999.

GEOsurv. *Flykin Suite™ & Flykin Suite+ User's Manual, Rev. 112*. GEOsurv Inc., Nepean, Ontario, 1999.

GSD. *Canadian Active Control System*. http://www.geod.nrcan.gc.ca/site/index_e/products_e/cacs_e/cacs_e.html. Geodetic Survey Division of Geomatics Canada, 2002.

GSI. *Crustal Deformation of Japan Detected by GEONET - GPS Earth Observation Network of Geographical Survey Institute*. http://mekira.gsi.go.jp/ENGLISH/index.html. Geographical Survey Institute, Japan, 2002.

Gustafsson, G., Papitashvili, N. E., and Papitashvili, V. O. *A Revised Corrected Geomagnetic Coordinate System for Epochs 1985 and 1990*. Journal of Atmospheric and Terrestrial Physics, Vol. 54, pp. 1609-1631, 1992.

Haw, D. *SP3 Format*. http://www.ngs.noaa.gov/GPS/SP3_format.html. 2001.

Hay, C. *The GPS Accuracy Improvement Initiative*. GPSWorld, pp. 56-61, Advanstar Communications, June 2000.

Hedling, G., and Jonsson, B. *SWEPOS – Design, Applications and Future Development*. Paper presented at the General Assembly of the International Union of Geodesy and Geophysics, Birmingham, UK, July 1999.

Hermit Eclipse. *Total Eclipse of the Sun – August 11, 1999 – Cornwall UK, Europe, and Asia*. http://www.hermit.org/Eclipse/1999-08-11/. 2001.

Hopfield, H. S. *Two-quartic Tropospheric Refractivity Profile for Correcting Satellite Data*. Journal of Geophysical research, Vol. 74, No. 18, 4487-4499, 1969.

Hugentobler, U., Schaer, S., and Fridez, P. *Bernese GPS Software, Version 4.2*. Astronomical Institute, University of Bern, 2001.

IBGE. *SIRGAS Final Report, Working Groups I and II*. Departamento de Geodésia, Instituto Brasileiro de Geografia e Estatística, Rio de Janeiro, 1997.

IGS. *IGS Product Table*. International GPS Service, http://igscb.jpl.nasa.gov/components/prods.html. 2001a.

IGS. *International GPS Service: Monitoring Global Change by Satellite Tracking*. http://igscb.jpl.nasa.gov/. 2001b.

IGS ACC. *General Information About the IGS Products*. http://www.aiub.unibe.ch/acc.html. IGS Analysis Centre Coordinator website at the Astronomical Institute, University of Bern, 2001.

Kaplan, E. D, Leva, J. L., and Pavloff, M. S. *Understanding GPS Principles and Applications*. Chapter 2: Fundamentals of Satellite Navigation, pp. 15-57. Artech House, 1996.

Kylkilahti, A., Koivula, H., and Poutanen, M. *The Antenna Calibration of the Finnish Permanent GPS Network (FINNREF)*. Paper presented at the General Assembly of the International Union of Geodesy and Geophysics, Birmingham, UK, July 1999.

Klobuchar, J. A. *Global Positioning System: Theory and Applications*. Volume I, Chapter 12: Ionospheric Effects on GPS, pp. 485-515. American Institute of Aeronautics and Astronautics, Inc., 1996.

Krakiwsky, E. J. *The Method of Least Squares: A Synthesis of Advances*. Technical Report, UCGE Report Number 100003, Department of Geomatics Engineering, The University of Calgary, 1990.

Lachapelle, G. *GPS Theory and Applications*. ENGO 625 Lecture Notes, Department of Geomatics Engineering, The University of Calgary, 1997.

Lachapelle, G., Cannon, M. E., Fortes, L. P., and Stephen, J. *Feasibility Study on the use of a Multi-Reference Station Approach for OTF Ambiguity Resolution in a Constricted Waterway (St. Lawrence)*. Department of Geomatics Engineering's Report under contract with the Canadian Coast Guard, The University of Calgary, 1999.

Lachapelle, G., Alves, P., Fortes, L. P., Cannon, E., and Townsend, B. *DGPS RTK Positioning Using a Reference Network*. Proceedings of the 13th International

Technical Meeting of the Satellite Division of the Institute of Navigation, pp. 1165-1171, Salt Lake City, September 2000.

Landau, H., Vollath, U., Deking, A., and Pagels, C. *Virtual Reference Station Networks – Recent Innovations by Trimble*. Proceedings of the GPS Symposium 2001, Japan Institute of Navigation, pp. 39-52, Tokyo, Japan, November 2001.

LAREG. *The International Terrestrial Reference Frame - ITRF*. http://lareg.ensg.ign.fr/ITRF/. Laboratory for Research in Geodesy, 2001.

Larson, K. M. *Global Positioning System: Theory and Applications*. Volume II, Chapter 20: Geodesy, pp. 539-558. American Institute of Aeronautics and Astronautics, Inc., 1996.

Leick, A. *GPS Satellite Surveying*. John Wiley and Sons, Inc., 2nd edition, 1995.

Liao, X. *Carrier Phase Based Ionosphere Recovery Over a Regional Area GPS Network.* MSc Thesis, UCGE Report Number 20143, The University of Calgary, 2000.

Lu, G., Cannon, M. E., Chen, D., and Lachapelle, G. *FLYKIN™ Operator's Manual, Version 2.0*. Department of Geomatics Engineering, The University of Calgary, 1994.

Luo, N. *Precise Relative Positioning of Multiple Moving Platforms Using GPS Carrier Phase Observables*. PhD Thesis, UCGE Report Number 20147, Department of Geomatics Engineering, The University of Calgary, 2001.

McArthur, D. J., and Steeves, R. R. *On the Impact of the Active Control System on Survey Control Networks*. Geodetic Survey Division, Canada Centre for Surveying, Ottawa, 1988.

Maybeck, P. S. *Stochastic Models, Estimation, and Control, Volume I*. Navtech Book and Software Store, Arlington, 1994.

Mendes, V. de B. *Modeling the Neutral-Atmosphere Propagation Delay in Radiometric Space Techniques*. PhD Thesis, Technical Report No. 199, Department of Geodesy and Geomatics Engineering, University of New Brunswick, 1999.

Mikhail, E. M. *Observations and Least-Squares*. IEP-A Dun-Donnelley Publisher, New York, 1976.

Moritz, H. *Advanced Least-Squares Methods*. Report 175, Department of Geodetic Sciences, Ohio State University, 1972.

Moritz, H. *Covariance Functions in Least-Squares Collocation*. Report 240, Department of Geodetic Sciences, Ohio State University, 1976.

Moritz, H. *Advanced Physical Geodesy*. Abacus Press, Tunbridge Wells, 1980.

Mueller, T. *Wide Area Differential GPS*. GPSWorld, pp. 36-44, Advanstar Communications, June 1994.

NASA/GSFC. *Total Solar Eclipse of 1999 August 11*. http://sunearth.gsfc.nasa.gov/eclipse/TSE1999/TSE1999.html. Goddard Space Flight Center, NASA, 2001.

NASA/NSSDC. *Corrected Geomagnetic Coordinates*. http://nssdc.gsfc.nasa.gov/space/cgm/cgmm_des.html. National Space Science Data Center, NASA, 2001a.

NASA/NSSDC. *IGRF/DGRF Model Parameters and Corrected Geomagnetic Coordinates*. http://nssdc.gsfc.nasa.gov/space/cgm/cgm.html. National Space Science Data Center, NASA, 2001b.

NGDC. *Geomagnetic Kp and Ap indexes*. http://www.ngdc.noaa.gov/stp/GEOMAG/kp_ap.html. National Geophysical Data Center, NOAA, 2001.

NGS. *Welcome to the National CORS*. http://www.ngs.noaa.gov/CORS/. National Geodetic Survey, NOAA, 2002.

NIMA. *Current GPS Satellite Data*. http://164.214.2.59/GandG/sathtml/satinfo.html, National Imagery and Mapping Agency, 2001.

Odijk, D. *Stochastic Modelling of the Ionosphere for Fast GPS Ambiguity Resolution*. Geodesy Beyond 2000: The Challenges of the First Decade, International Association of Geodesy Symposia, Vol. 121, pp. 387-392, Springer-Verlag, 2000.

Papitashvili, V. *Personal Communication*. Space Physics Research Laboratory, The University of Michigan, 2001.

Parkinson, B. W., and Enge, P. K. *Global Positioning System: Theory and Applications*. Volume II, Chapter 1: Differential GPS, pp. 3-50. American Institute of Aeronautics and Astronautics, Inc., 1996.

Raquet, J. F. *Development of a Method for Kinematic GPS Carrier-Phase Ambiguity Resolution Using Multiple Reference Receivers*. PhD Thesis, UCGE Report Number 20116, Department of Geomatics Engineering, The University of Calgary, 1998.

Raquet, J., Lachapelle, G., and Melgård, T. *Test of a 400 km x 600 km Network of Reference Receivers for Precise Kinematic Carrier-Phase Positioning in Norway*. Proceedings of the 11th International Technical Meeting of the Satellite Division of the Institute of Navigation, pp. 407-416, Nashville, September 1998.

Ray, J. K. *Mitigation of GPS Code and Carrier Phase Multipath Effects Using a Multi-Antenna System*. PhD Thesis, UCGE Report Number 20136, Department of Geomatics Engineering, The University of Calgary, 2000.

Remondi, B. W. *The NGS GPS Orbital Formats*. http://www.ngs.noaa.gov/GPS/Utilities/format.txt, 2001.

Rothacher, M., and Mervart, L. *Bernese GPS Software, Version 4.0*. Astronomical Institute, University of Bern, 1996.

Roulston, A., Talbot, N., and Zhang, K. *An Evaluation of Various GPS Satellite Ephemerides*. Proceedings of the 13th International Technical Meeting of the Satellite Division of the Institute of Navigation, pp. 45-54, Salt Lake City, September 2000.

Schaer, S. *Mapping and Predicting the Earth's Ionosphere Using the Global Positioning System*. PhD Thesis, Astronomic Institute, University of Bern, 1999.

Schaer, S., Beutler, G., Rothacher, M., Brockmann, E., Wiget, A., and Wild, U. *The Impact of the Atmosphere and Other Systematic Errors on Permanent GPS Networks*. Geodesy Beyond 2000: The Challenges of the First Decade, International Association of Geodesy Symposia, Vol. 121, pp. 373-380, Springer-Verlag, 1999.

Seeber, G. *Satellite Geodesy Foundations, Methods, and Applications*. Walter de Gruyer, 1993.

SIDC. *Sunspot Index Graphics*. http://sidc.oma.be/html/wolfmms.html. Sunspot Index Data Center, Royal Observatory of Belgium, 2001.

Skone, S. *Wide Area Ionosphere Grid Modelling in the Auroral Region.* UCGE Report Number 20123, Department of Geomatics Engineering, The University of Calgary, 1998.

Skone, S. *Atmospheric Effects on Satellite Navigation Systems*. ENGO 699.56 Lecture Notes, Geomatics Engineering, The University of Calgary, 1999.

Skone, S. *Wide Area Ionosphere Modeling in the Equatorial Region During a Magnetic Storm Event*. Proceedings of the National Technical Meeting of the Institute of Navigation, pp. 481-489, San Diego, January 2000a.

Skone, S. *Wide Area Ionosphere Modeling at Low Latitudes – Specifications and Limitations*. Proceedings of the 13th International Technical Meeting of the Satellite Division of the Institute of Navigation, pp. 643-652, Salt Lake City, September 2000b.

Skone, S., and deJong, M. *The Impact of Geomagnetic Substorms on GPS Receiver Performance, and Correlation with Space Weather Indices*. Paper presented at the International Symposium on GPS, Tsukuba, Japan, October 1999.

Slater, J. A., and Malys, S. *WGS84 – Past, Present and Future*. Advances in Positioning and Reference Frames, International Association of Geodesy Symposia, Vol. 118, pp. 1-7, Springer-Verlag, 1998.

Spilker Jr., J. A. *Global Positioning System: Theory and Applications*. Volume I, Chapter 13: Tropospheric Effects on GPS, pp. 517-546. American Institute of Aeronautics and Astronautics, Inc., 1996.

Springer, T. *IGSMail-2904: IGS ITRF97 Realization*. http://igscb.jpl.nasa.gov/mail/igsmail/2000/msg00250.html. June 27, 2000a.

Springer, T. *IGSMail-3088: IGS Ultra-Rapid Products*. http://igscb.jpl.nasa.gov/mail/igsmail/2000/msg00435.html. November 3, 2000b.

Sun, H., Cannon, M.E., and Melgård, T. *Real-time GPS Reference Network Carrier Phase Ambiguity Resolution*. Proceedings of the National Technical Meeting of the Institute of Navigation, pp. 193-199, San Diego, January 1999.

Talaya, J., and Bosch, E. *CATNET, a Permanent GPS Network With Real-Time Capabilities*. 12th International Technical Meeting of the Satellite Division of the Institute of Navigation, pp. 33-39, Nashville, September 1999.

Townsend, B., Lachapelle, G., Fortes, L. P., Melgård, T., Nørbech, T., and Raquet, J. *New Concepts for a Carrier Phase Based GPS Positioning Using a National Reference Station Network*. Proceedings of the National Technical Meeting of the Institute of Navigation, pp. 319-326, San Diego, January 1999.

Tralli, D. M., and Lichten, S. M. *Stochastic Estimation of Tropospheric Path Delays in Global Positioning System Geodetic Measurements*. Bulletin Géodésique, Vol. 64, No. 2, pp. 127-159, 1990.

U.S. Assistant Secretary of Defense for Command, Control, Communications, and Intelligence. *Global Positioning System Standard Positioning Service Performance Standard*. http://www.igeb.gov/SPS-2001-final.pdf. October 2001.

van der Marel, H. *Virtual GPS Reference Stations in the Netherlands*. Proceedings of the 11th International Technical Meeting of the Satellite Division of the Institute of Navigation, pp. 49-58, Nashville, September 1998.

Varner, C. C. *DGPS Carrier Phase Networks and Partial Derivative Algorithms*. PhD Thesis, UCGE Report Number 20129, Department of Geomatics Engineering, The University of Calgary, 2000.

Varner, C. C., and Cannon, M. E. *The Application of Multiple Reference Stations to the Determination of Multipath and Spatially Decorrelating Errors*. Proceedings of the National Technical Meeting of the Institute of Navigation, pp. 323-333, Santa Monica, January 1997.

Vollath, U., Deking, A., Landau, H., and Pagels, C. *Long-Range RTK Positioning Using Virtual Reference Stations*. Proceedings of the International Symposium on Kinematic Systems in Geodesy, Geomatics and Navigation, pp. 470-474, Banff, Canada, June 2001.

Wanninger, L. *Effects of the Equatorial Ionosphere on GPS*. GPSWorld, pp. 48-54, Advanstar Communications, July 1993.

Wanninger, L. *Improved Ambiguity Resolution by Regional Differential Modelling of the Ionosphere*. Proceedings of the 8th International Technical Meeting of the Satellite Division of the Institute of Navigation, pp. 55-62, Palm Springs, September 1995.

Wanninger, L. *Real-Time Differential GPS Error Modelling in Regional Reference Station Networks*. Advances in Positioning and Reference Frames, International Association of Geodesy Symposia, Vol. 118, pp. 86-92, Springer-Verlag, 1998.

Wanninger, L. *The Performance of Virtual Reference Stations in Active Geodetic GPS-networks under Solar Maximum Conditions*. Proceedings of the 12th International Technical Meeting of the Satellite Division of the Institute of Navigation, pp. 1419-1427, Nashville, September 1999.

Wdowinski, S., Bock, Y., Forray, Y., Melzer, Y., Baer, G., Levitte, D. *The GIL Network of Continuous GPS Monitoring in Israel for Geodetic and Geophysical Applications*. Paper presented at the General Assembly of the International Union of Geodesy and Geophysics, Birmingham, UK, July 1999.

Weber, R. *IGSMail-3605: Towards ITRF2000*. http://igscb.jpl.nasa.gov/mail/igsmail/2001/msg00450.html, November 20, 2001.

Wells, D., Beck, N., Delikaraoglou, D., Kleusberg, A., Kraviwisky, E.J., Lachapelle, G., Langley, R., Nakiboglu, M., Schwarz, K.P., Tranquilla, J.M., and Vanícek, P. *Guide to GPS Positioning*. Canadian GPS Associates, Fredericton, 1986.

Wiederholt, L. F. and Kaplan, E. D. *Understanding GPS Principles and Applications*. Chapter 13: GPS System Segments, pp. 59-81. Artech House, 1996.

Woo, K. T. *Optimum Semi-Codeless Carrier Phase Tracking of L2*. Proceedings of the 12th International Technical Meeting of the Satellite Division of the Institute of Navigation, pp. 289-305, Nashville, September 1999.

Wild, U., Hug, R., Signer, T., and Wiget, A. *The Automated GPS Network for Switzerland (AGNES)*. Paper presented at the General Assembly of the International Union of Geodesy and Geophysics, Birmingham, UK, July 1999.

Wübbena, G., and Seeber, G. *Developments in Real-Time Precise DGPS Applications: Concepts and Status*. GPS Trends in Precise Terrestrial, Airborne and Spaceborne Applications, International Association of Geodesy Symposia, Vol. 115, pp. 212-216, Springer-Verlag, 1996.

Wübbena, G., Bagge, A., Seeber, G., Böder, V., and Hankemeier, P. *Reducing Distance Dependent Errors for Real-Time Precise DGPS Applications by Establishing Reference Station Networks*. Proceedings of the 9th International Technical Meeting of the Satellite Division of the Institute of Navigation, pp. 1845-1852, Kansas City, September 1996.

Wübbena, G., Bagge, A., and Schmitz, M. *RTK Networks Based on Geo++® GNSMART – Concepts, Implementation, Results*. Proceedings of the 14th International

Technical Meeting of the Satellite Division of the Institute of Navigation, pp. 368-378, Salt Lake City, September 2001.

Zhang, J. *Investigations into the Estimation of Residual Tropospheric Delays in a GPS Network*. PhD Thesis, UCGE Report Number 20132, The University of Calgary, 1999.

Zumberge, J. F., and Bertiger, W. I. *Global Positioning System: Theory and Applications*. Volume I, Chapter 16: Ephemeris and Clock Navigation Message Accuracy, pp. 585-599. American Institute of Aeronautics and Astronautics, Inc., 1996.

APPENDIX A

RE-VISITING LEAST-SQUARES PREDICTION (COLLOCATION)

The Least-Squares Prediction (Collocation) method has been used for interpolation and extrapolation of gravity anomalies for long time. In Chapter 3, its application to the derivation of the Multi-Ref approach was shown. This appendix re-visits the method, according to Moritz [1980].

Consider the random variable **l** corresponding to the set of **q** measured quantities:

$$\mathbf{l} = [l_1 \quad l_2 \quad ... \quad l_q]^T \tag{A.1}$$

and the random variable **s** corresponding to the set of **m** unknown signals:

$$\mathbf{s} = [s_1 \quad s_2 \quad ... \quad s_m]^T \tag{A.2}$$

where the superscript **T** denotes transposition, so that **l** and **s** are column vectors.

It is assumed that each of the random variables has an expected value equal to zero:

$$E\{l\} = 0 \; ; \; E\{s\} = 0 \tag{A.3}$$

where the expectation **E** is, for a continuous random variable **x**, of the form:

$$E\{x\} = \int_{-\infty}^{+\infty} x\phi(x)dx \tag{A.4}$$

where $\boldsymbol{\phi(x)}$ is the Probability Density Function (PDF) of **x**.

Also consider the following covariance matrices:

$$C_{ll} = \mathrm{cov}(l, l) \tag{A.5}$$

$$C_{ss} = \mathrm{cov}(s, s) \tag{A.6}$$

$$C_{sl} = \mathrm{cov}(s, l) \tag{A.7}$$

where $\mathbf{C_{ll}}$ and $\mathbf{C_{ss}}$ are the covariance matrices of the measurements and signals, respectively, and $\mathbf{C_{sl}}$ is the cross-covariance matrix between them. From probability theory:

$$C_{ll} = E\{(l - E\{l\})(l - E\{l\})^T\}. \quad (A.8)$$

However, according to Equation A.3, Equation A.8 becomes:

$$C_{ll} = E\{ll^T\} \quad (A.9)$$

Analogously:

$$C_{ss} = E\{ss^T\} \quad (A.10)$$

and consequently:

$$C_{sl} = E\{sl^T\}. \quad (A.11)$$

It is assumed that, in addition to the measurement vector **l**, the covariance matrices are also known and that they have full rank. The functional relation between **s** and **l** is not known, only the covariance matrices.

The question that arises is: what is the best estimate of **s** based on **l**? In this case the linear minimum variance unbiased estimate is applied, with the form:

$$\hat{s} = Hl \tag{A.12}$$

where the **H** matrix, with **m** rows and **q** columns, is to be determined. First of all, it is necessary to show that $\hat{\mathbf{s}}$, given by Equation A.12, is an unbiased estimate of **s**. Applying the expectation operator **E** to Equation A.12, the following can be obtained:

$$E\{\hat{s}\} = E\{Hl\} = HE\{l\} = H.0 = 0 = E\{s\}\ . \tag{A.13}$$

Thus $\hat{\mathbf{s}}$ is an unbiased estimate of **s**.

The error vector **ε** is given by:

$$\varepsilon = \hat{s} - s \tag{A.14}$$

and its covariance matrix is:

$$C_{\varepsilon\varepsilon} = \mathrm{cov}(\varepsilon, \varepsilon) = E\{\varepsilon\varepsilon^T\} \tag{A.15}$$

as Equations A.13 and A.14 imply that $E\{\varepsilon\}=0$. Using Equations A.12 and A.14:

$$\varepsilon\varepsilon^T = (\hat{s}-s)(\hat{s}-s)^T = (Hl-s)(Hl-s)^T = (Hl-s)(l^TH^T-s^T) = \\ = Hll^TH^T - sl^TH^T - Hls^T + ss^T \tag{A.16}$$

Applying the expectation operator **E** to Equation A.16, one gets:

$$E\{\varepsilon\varepsilon^T\} = E\{Hll^TH^T - sl^TH^T - Hls^T + ss^T\} = \\ = E\{Hll^TH^T\} - E\{sl^TH^T\} - E\{Hls^T\} + E\{ss^T\} = \\ = HE\{ll^T\}H^T - E\{sl^T\}H^T - HE\{ls^T\} + E\{ss^T\} \tag{A.17}$$

Substituting Equations A.9, A.10 and A.11 into A.17, using A.15 and noting that:

$$C_{ls} = E\{ls^T\} = E\{(sl^T)^T\} = (E\{sl^T\})^T = C_{sl}^T\ , \tag{A.18}$$

the following is obtained:

$$C_{\varepsilon\varepsilon} = HC_{ll}H^T - C_{sl}H^T - HC_{sl}^T + C_{ss}\,. \tag{A.19}$$

Now it is necessary to use an additional step to get the final form of $C_{\varepsilon\varepsilon}$ by adding and subtracting the term $C_{sl}\,C_{ll}^{-1}C_{ls}$ to Equation A.19, giving:

$$C_{\varepsilon\varepsilon} = C_{ss} - C_{sl}\,C_{ll}^{-1}C_{ls} + HC_{ll}H^{T} - HC_{sl}^{T} - C_{sl}H^{T} + C_{sl}\,C_{ll}^{-1}C_{ls}\,. \qquad (A.20)$$

Noting that $C_{ll}C_{ll}^{-1} = C_{ll}^{-1}C_{ll} = I$, where **I** is the identity matrix, with **q** rows and columns, Equation A.20 can be re-written inserting it in the fourth, fifth and sixth terms, taking into account Equation A.18, and carrying out operations in the scope of matrix algebra:

$$\begin{aligned}
C_{\varepsilon\varepsilon} &= C_{ss} - C_{sl}\,C_{ll}^{-1}C_{ls} + HC_{ll}H^{T} - HC_{ll}\,C_{ll}^{-1}C_{sl}^{T} - \\
&\quad - C_{sl}\,C_{ll}^{-1}C_{ll}H^{T} + C_{sl}\,C_{ll}^{-1}C_{ll}\,C_{ll}^{-1}C_{ls} = \\
&= C_{ss} - C_{sl}\,C_{ll}^{-1}C_{ls} + HC_{ll}(H^{T} - C_{ll}^{-1}C_{sl}^{T}) - \\
&\quad - C_{sl}\,C_{ll}^{-1}C_{ll}(H^{T} - C_{ll}^{-1}C_{ls}) = \\
&= C_{ss} - C_{sl}\,C_{ll}^{-1}C_{ls} + (HC_{ll} - C_{sl}\,C_{ll}^{-1}C_{ll})(H^{T} - C_{ll}^{-1}C_{sl}^{T}) = \\
&= C_{ss} - C_{sl}\,C_{ll}^{-1}C_{ls} + (H - C_{sl}\,C_{ll}^{-1})C_{ll}(H^{T} - C_{ll}^{-1}C_{sl}^{T}) = \\
&= C_{ss} - C_{sl}\,C_{ll}^{-1}C_{ls} + (H - C_{sl}\,C_{ll}^{-1})C_{ll}(H - C_{sl}C_{ll}^{-1})^{T}
\end{aligned} \qquad (A.21)$$

The right side of Equation A.21 is formed by the addition of two matrices **A** and **B**, where:

$$A = C_{ss} - C_{sl}\, C_{ll}^{-1} C_{ls} \tag{A.22}$$

$$B = (H - C_{sl}\, C_{ll}^{-1}) C_{ll} (H - C_{sl}\, C_{ll}^{-1})^{T}. \tag{A.23}$$

The matrix **A** does not depend on **H**. Thus, the matrix **H** that minimises the covariance of the errors $\mathbf{C_{\varepsilon\varepsilon}}$ is the one that minimises **B**, i.e. that makes **B** equal to zero. Then:

$$H = C_{sl}\, C_{ll}^{-1}. \tag{A.24}$$

Substituting Equation A.24 into A.12, the final form for the estimate of the signals, based on the measurement vector and on the covariance matrices, is given by:

$$\hat{s} = C_{sl}\, C_{ll}^{-1} l. \tag{A.25}$$

So knowing the measurement of a random variable at some points and how it propagates spatially (throughout the knowledge of the covariance matrices) it is possible to predict its value at a point where there is no measurement.

The covariance matrix of the predicted signals is obtained by substituting the expression for **H**, given by Equation A.24, into A.21, noticing that the covariance matrix of the errors is equal to the covariance matrix of the predicted signals [Moritz, 1980]:

$$C_{\hat{s}\hat{s}} = C_{ss} - C_{sl}\, C_{ll}^{-1} C_{ls} \tag{A.26}$$

The necessary covariance matrices in Equation A.25 are generally computed using covariance functions, which express the error behaviour in the region of interest. These covariance functions can be evaluated using real data, for example according to the procedures described in Chapters 3, 4 and 5 of this thesis. Generally it is necessary to assume that the stochastic processes represented by the covariance functions satisfy certain characteristics. The first one is stationarity, which happens when all moments of the process are independent of time. The second one is ergodicity, which means that time (or space) averages are equivalent to ensemble averages over the probability space [Blais, 2002]. In most practical cases, the evaluation of the covariance functions is carried out through averaging the error values over time and space, which indicates the implicit assumption of these characteristics. In addition, Moritz [1976] describes some properties the covariance functions have to satisfy in order to generate proper covariance matrices. They are: isotropy, which means that the covariance values do not depend on the azimuth; homogeneity, when the covariances do not depend on the location of the point; harmonicity, when the covariance function is harmonic, i.e. satisfies the Laplace's

equation; and positive definiteness, i.e. when the generated covariance matrices are always positive definite. Mathematically, the last property can be verified through the Fourier transform of the covariance function, which must always be greater than or equal to zero. Moritz [1976] also describes three essential parameters that characterise a covariance function **C(d)**, where **d** is the distance between two points: the variance $\mathbf{C_0}$, which is the value of the covariance function for **d** equal to zero; the correlation length, which is the value of the argument for which **C(d)** is decreased to half of its value at **d** equal to zero; and the curvature parameter, which is related to the curvature of the covariance curve at **d** equal to zero (see Moritz [1976] for more details).

It is important to emphasise that the properties and parameters referred to in the previous paragraph were described by Moritz [1976] regarding applications in the field of physical geodesy. Except for the positive definiteness, they do not necessarily need to be satisfied for other applications (like Multi-Ref), as this depends on the particular characteristics of each application. For instance, if the stochastic process to be model is not isotropic, one should not expect to use a covariance function that is isotropic.

APPENDIX B

DETERMINATION OF PRECISE COORDINATES AND INTEGER AMBIGUITIES OF THE REFERENCE NETWORKS IN ST. LAWRENCE, CANADA, AND SOUTHEASTERN BRAZIL

As mentioned in Chapter 3, it is necessary to know the precise coordinates of the reference stations and the integer ambiguities between them to apply the Multi-Ref method. This task was accomplished in this research for the St. Lawrence and the Brazilian data sets in post-mission, using the Bernese GPS Software Version 4.0 [Rothacher and Mervart, 1996] and Version 4.2 [Hugentobler et al., 2001], respectively. Although several improvements were implemented by the group at the University of Bern in Version 4.2, the use of Version 4.0 to obtain the results for the St. Lawrence data set did not impact their quality, as the version used at the University of Calgary was "enhanced", with many of the Version 4.2 improvements already implemented.

Operationally, if one thinks about the implementation of the Multi-Ref approach as a service, the resolution of the integer ambiguities between the reference stations has to be done in real-time as per Sun et al. [1999] and Lachapelle et al. [2000].

In Bernese, the resolution of the integer ambiguities is carried out in the scope of determination of the coordinates. Before describing the computation of each network, it is necessary to mention the basic steps of the Bernese processing.

B.1 Bernese Processing

The Bernese GPS software is a powerful tool and suited for the following tasks [Hugentobler et al., 2001]:

- Permanent network processing;
- Rapid processing of small-size single and dual frequency surveys;
- Ambiguity resolution on long baselines (up to 2000 km using high accuracy orbits);
- Ionosphere and troposphere modelling;
- Clock estimation;
- Combination of different receiver types, taking into account antenna phase centre variations;
- Orbit determination and estimation of Earth rotation parameters.

For the purpose of this thesis, the following steps were taken when computing coordinates and ambiguities with the Bernese software. For each day of data:

- Orbit generation, based on the integration of IGS rapid orbits, in the St. Lawrence network (as they were the best ones available at the processing time), and IGS final orbits, in the Brazilian network;
- Ionospheric-free point-positioning code solution for each station in the network, in order to compute precise receiver clock offsets and to refine initial coordinates included in the RINEX observation files;
- Computation of between-receiver single difference carrier phase observations, based on the selection of the independent baselines to be processed by Bernese; as a general criterion, the shortest baselines were preferably chosen, in order to facilitate ambiguity resolution;
- L1 and L2 carrier phase pre-processing to detect and repair cycles slips, unpaired observations, etc;
- Ionospheric-free double difference carrier phase float solution of the entire network, including the determination of residual tropospheric zenith delays every two hours after applying the Saastamoinen model, in order to generate refined coordinates for each station;
- Resolution of the L1 and L2 integer ambiguities of baselines in the network, fixing the coordinates of all stations obtained in the previous step. CODE GIM maps [CODE, 2001] were used in this step, which demonstrated to slightly help the ambiguity resolution process;

- Ionospheric-free double difference carrier phase fixed solution (using the L1 and L2 integer ambiguities fixed in the previous step as input), including again the determination of residual tropospheric zenith delays, saving the normal equations.

After generating a set of normal equations for each daily solution, a final solution was computed based on the combination of the normal equations, when the coordinates of one of more stations were constrained. To apply the Multi-Ref approach, it is estimated that the coordinates of the reference stations must be known with an accuracy of 1-2 cm or better.

B.2 St. Lawrence Network

Two days of data (August 4 and 5, 1999) were used in the Bernese processing of the St. Lawrence network. The independent baselines formed are shown in Figure 4.1, reproduced again in Figure B.1. As it can be seen, the baseline lengths varied from 30 to 82 km.

As the coordinate accuracy requirements to apply Multi-Ref are predominantly internal, which means that the whole network can be shifted by centimetres without affecting the results of the method, the coordinates of only one station (Trois-Rivières)

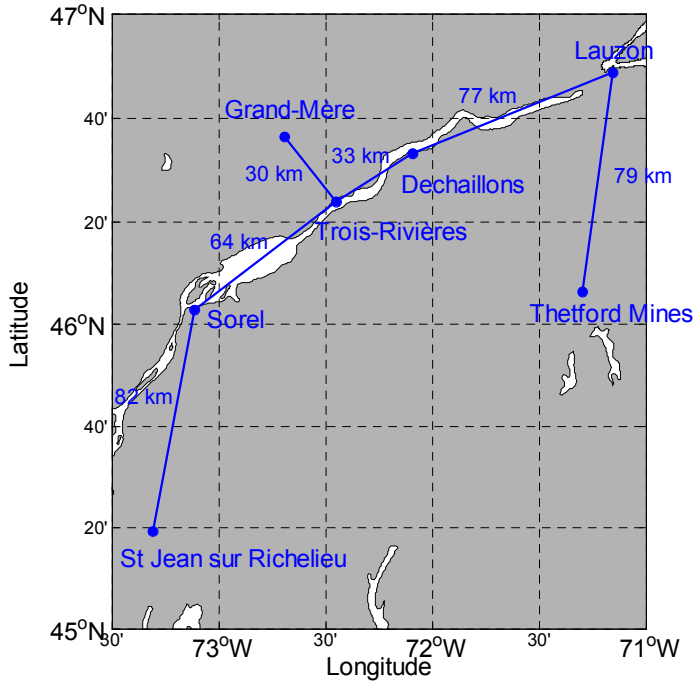

Figure B.1: Independent baselines (6) of the St. Lawrence reference network processed by Bernese

were constrained to the values given by the Canadian Coast Guard. The coordinates of all remaining stations were determined in the adjustment.

The SIGMA strategy [Hugentobler et al., 2001] was used to resolve ambiguities in the independent baselines shown in Figure B.1 for the two days of data, being applied first to fix WL ambiguities and then to fix the L1 ones. This strategy was selected considering that the baseline lengths were not long and because it was the most used at that time. It is based on the Fast Ambiguity Resolution Approach (FARA) [Frei and

Beutler, 1990], where the float double difference ambiguities and every difference between them are used in the search of the integer values.

Besides the independent baselines shown in Figure B.1, ambiguities were also resolved for additional baselines in order to generate necessary files to be supplied to the Multi-Ref correction computation as well as to support the determination of the covariance functions (see Chapters 4 and 5). As a result, ambiguities for the 18 baselines listed in Table 4.1 were resolved. For longer baselines, the Quasi Ionospheric-Free (QIF) strategy was used instead of SIGMA, as it normally gives better results in this case, especially under an active ionosphere. In the QIF strategy, L1 and L2 double difference float ambiguities are first resolved using a stochastic model for the ionosphere, similar to what was described by Odijk [2000]. The L1 and L2 integer ambiguities were then searched and the integer set that minimises the distance between the ionospheric-free ambiguities computed using the float and the integer L1 and L2 values was selected as the integer solution. Analogous to SIGMA, differences in ambiguities were also computed and searched in the QIF strategy.

Figure B.2 shows the percentage of L1 and L2 ambiguities fixed to integers in each baseline, with different colours used according to the strategy and to the processed day. It can be seen that at least 75% of ambiguities were resolved in each baseline, with a tendency of higher percentages for smaller baselines when using the SIGMA strategy

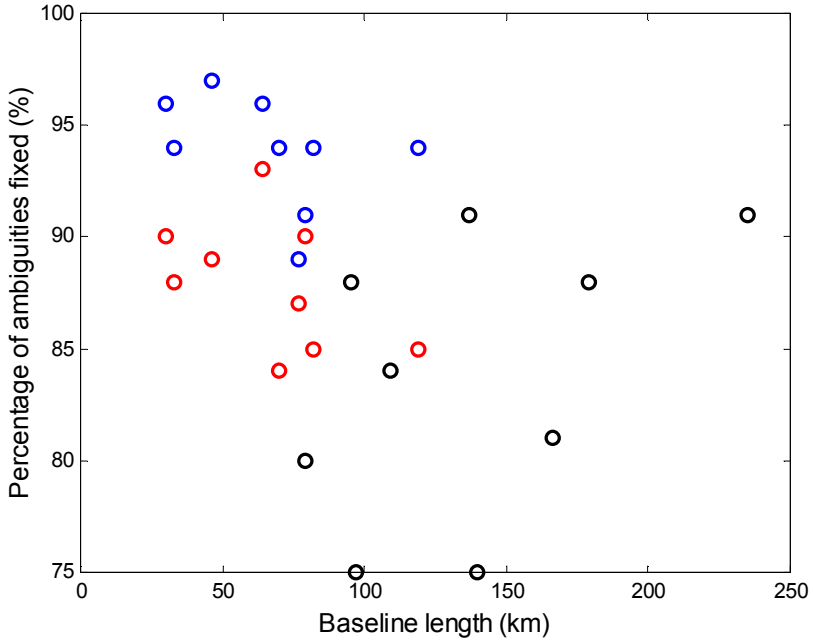

Figure B.2: Percentage of L1 and L2 ambiguities fixed by Bernese to integer values in the St. Lawrence network, using the SIGMA strategy for August 4, 1999 (in blue) and August 5 (in red) and using the QIF strategy for August 4 (in black)

(which does not model the ionosphere), as expected. For the conditions of the St. Lawrence network, there is no reduction in the percentage values for longer baselines when using the QIF strategy, showing that the model compensated the spatial decorrelation of the ionosphere. It should be emphasised that these percentage values correspond to the number of ambiguities fixed and not to the percentage time of fixing, as Bernese is a batch processing software. The ambiguities that were not fixed to integers normally were valid for a short period of time only and, as such, did not have enough observations to be reliably determined. One should notice that the percentages for August 5 were systematically smaller than the ones for August 4 for the same baselines using the

SIGMA strategy. That happened because more cycle slips occurred on August 5, some of them were not recovered, which created a greater number of short-time ambiguities to be resolved.

To verify the quality of the integer ambiguities, tests were performed using network constraints, analogous to the procedure described by Luo [2001]. In all cases tested, the closed loops' sum of the ambiguities was always equal to zero.

As previously mentioned, the normal equations for August 4 and 5 were combined in order to generate the final solution for the station coordinates. Table B.1 shows a comparison of station coordinates of each daily solution with respect to the combined solution. It can be seen that the agreement between daily solutions was very good, at the millimetre level. Table B.2 contains the final coordinates and respective estimated accuracy. As the fixed coordinates of Trois-Rivières are referred to NAD83, it is assumed that the coordinates of all remaining stations are, nominally, referred to this system.

B.3 Brazilian Network

Two days of data (August 11 and 13, 1999) were used in the Bernese processing of the Brazilian network. In this case, an additional day was also processed (August 14) in order

to supply ambiguities for the computation of double difference misclosures (see Section 4.2.2) as well as to generate one more daily solution to assess the quality of the final coordinates. The independent baselines formed for each day are shown in Figures B.3 to B.5. The change in configuration for each day was based on the availability of data. As it can be seen, the baseline lengths were much longer than the ones in the St. Lawrence network, varying from 118 (CHUA – FRAN) to 423 km (BRAZ – CHUA).

Table B.1: Comparison of station coordinates of each daily solution with respect to the combined solution in the St. Lawrence network

Station	Coord.	Aug. 4 sol. versus Combined (mm)	Aug. 5 sol. versus Combined (mm)
Deschaillons	N	-1.4	1.4
	E	-1.6	1.5
	U	-0.3	0.0
Grand-Mère	N	0.7	-0.7
	E	0.4	-0.4
	U	4.3	-4.2
Lauzon	N	-3.2	3.1
	E	1.0	-0.9
	U	5.2	-4.8
Sorel	N	0.1	-0.1
	E	0.7	-0.6
	U	-1.4	1.5
St-Jean-sur-Richelieu	N	-0.3	0.3
	E	0.6	-0.5
	U	3.5	-3.5
Thetford Mines	N	-3.0	2.8
	E	1.1	-1.0
	U	2.2	-1.9
Trois-Rivières	N	0.0	0.0
	E	0.0	0.0
	U	0.0	0.0

Table B.2: Final adjusted (NAD83) coordinates of the St. Lawrence stations, referred to L1 phase centres

Station	Coordinates		σ (m)
Deschaillons	Lat.	46° 33' 11.572853"	0.0001
	Lon.	-72° 5' 35.583368"	0.0001
	Ellip. h	28.7520 m	0.0006
Grand-Mère	Lat.	46° 36' 29.054932"	0.0001
	Lon.	-72° 41' 35.919271"	0.0001
	Ellip. h	124.7006 m	0.0006
Lauzon	Lat.	46° 48' 44.681719"	0.0001
	Lon.	-71° 9' 33.429908"	0.0001
	Ellip. h	91.8332 m	0.0006
Sorel	Lat.	46° 2' 47.705452"	0.0001
	Lon.	-73° 6' 51.548132"	0.0001
	Ellip. h	-6.1456 m	0.0006
St-Jean-sur-Richelieu	Lat.	45° 19' 16.773251"	0.0001
	Lon.	-73° 18' 37.193883"	0.0001
	Ellip. h	15.3553 m	0.0006
Thetford Mines	Lat.	46° 6' 24.030799"	0.0001
	Lon.	-71° 18' 4.110197"	0.0001
	Ellip. h	308.1580 m	0.0006
Trois-Rivières	Lat.	46° 23' 48.792300"	0.0000
	Lon.	-72° 27' 11.654200"	0.0000
	Ellip. h	-12.8600 m	0.0000

The coordinates of five stations, namely BRAZ, CACH, PARA, UEPP, and VICO, were constrained to their SIRGAS values [IBGE, 1997], as they belong to a very accurate continental network. As all stations are located on the same South American tectonic plate and they are not close to any deformation zone (i.e. to the plate edges), no velocities were applied to update the constrained coordinates (originally referred to ITRF94, epoch 1995.4) to the campaign epoch.

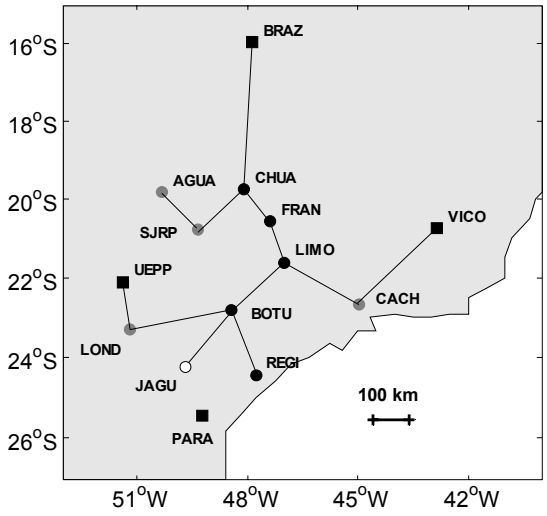

Figure B.3: August 11, 1999, independent baselines (12) of the Brazilian reference network processed by Bernese

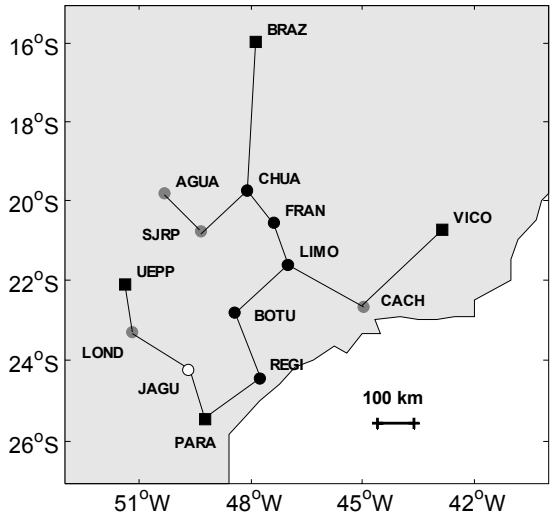

Figure B.4: August 13, 1999, independent baselines (13) of the Brazilian reference network processed by Bernese

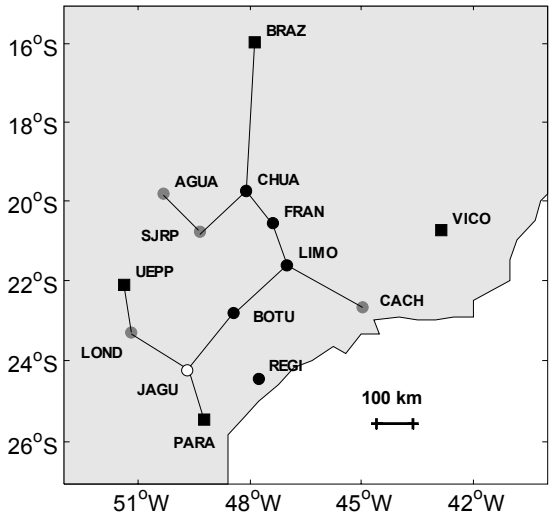

Figure B.5: August 14, 1999, independent baselines (11) of the Brazilian reference network processed by Bernese

The final solution was generated by combining the normal equations corresponding to daily solutions for August 11 and 13. Table B.3 shows a comparison of the station coordinates of the August 11 and 13 daily solutions with respect to the combined solution. It can be seen that the agreement was very good, at the millimetre level in practically all cases. Table B.4 contains the final coordinates and respective estimated accuracy for all stations. As mentioned previously, the daily solution for August 14 was used for checking the combined solution. Table B.5 lists the differences between them, all at the millimetre level.

The QIF strategy was used to fix ambiguities in all baselines shown in Figures B3 to B.5, in addition to the remaining ones necessary for computing the Multi-Ref corrections and for determining the covariance functions. Figure B.6 shows the

percentage of L1 and L2 ambiguities fixed to integers in each baseline observed for more than 12 hours (all listed in Table 4.2), with different colours used according to the processed day. It can be seen that at least 60% of ambiguities were resolved in each baseline. There was only a slight tendency for the percentage values to decrease for longer baselines, showing that the QIF strategy also worked well in the Brazilian case. Similar to what happened in the processing of the St. Lawrence network, the ambiguities that were not fixed to integers normally were valid for a short period of time only (less than an hour). It can be seen that the percentages for August 14 were generally smaller than the ones for the other two days, due to more occurrences of unreconstructed cycle slips, which increased the number of ambiguities valid for a short period of time.

Network constraints were also used in the Brazilian network to test the quality of the ambiguities. In all tests, the double difference integer ambiguity misclosures were always equal to zero in the closed loops summations.

One interesting aspect of the data set was the large number of losses of L2 tracking at many stations. This can be explained by problems some receivers experienced in maintaining satellite tracking under scintillation (see Chapter 2). Table B.6 shows the number of unpaired (L1 without L2) single difference carrier phase observations for some baselines for different types of receivers, obtained by Bernese in the pre-processing step. Notably, the correlation with receiver technology is evident, despite some differences that

happen due to the specific location of each site. These results match the ones obtained by Skone and deJong [1999].

Table B.3: Comparison of station coordinates of the August 11 and 13 daily solutions with respect to the combined solution in the Brazilian network

Station	Coord.	Aug. 11 sol. versus Combined (mm)	Aug. 13 sol. versus Combined (mm)
AGUA	N	2.4	-1.9
	E	-1.2	0.5
	U	-4.1	3.2
BOTU	N	1.0	-0.7
	E	-2.5	1.9
	U	-5.4	4.7
BRAZ	N	0.2	0.2
	E	-0.8	0.4
	U	-0.1	0.0
CACH	N	0.0	0.2
	E	0.7	-1.1
	U	-0.4	-0.1
CHUA	N	0.6	-0.1
	E	-2.4	1.7
	U	-2.7	1.9
FRAN	N	0.1	0.3
	E	-2.0	1.3
	U	-4.5	3.9
JAGU	N	-0.3	0.0
	E	-1.4	0.5
	U	11.3	-3.7

(continues)

Table B.3 (continued): Comparison of station coordinates of the August 11 and 13 daily solutions with respect to the combined solution in the Brazilian network

Station	Coord.	Aug. 11 sol. versus Combined (mm)	Aug. 13 sol. versus Combined (mm)
LIMO	N	1.4	-1.1
	E	-2.4	1.8
	U	-7.1	6.9
LOND	N	0.9	-0.5
	E	-1.3	0.2
	U	2.3	-4.1
PARA[1]	N		-0.4
	E		0.7
	U		0.1
REGI	N	1.3	-1.1
	E	-2.1	1.4
	U	-3.7	2.6
SJRP	N	1.1	-0.7
	E	-2.4	1.7
	U	-3.3	2.7
UEPP	N	-0.2	0.0
	E	0.3	0.0
	U	0.5	0.0
VICO	N	0.2	0.1
	E	-0.3	-0.1
	U	-0.2	0.0

1: PARA station was not observed on August 11, 1999

Table B.4: Final adjusted (SIRGAS) coordinates of the Brazilian stations, referred to L1 phase centres

Station	Coordinates		σ (m)
AGUA	Lat.	-19° 50' 31.817785"	0.0002
	Lon.	-50° 20' 5.782592"	0.0003
	Ellip. h	390.4711 m	0.0003
BOTU	Lat.	-22° 48' 17.252672"	0.0002
	Lon.	-48° 25' 38.769704"	0.0003
	Ellip. h	745.4714 m	0.0002
BRAZ	Lat.	-15° 56' 50.913240"	0.0001
	Lon.	-47° 52' 40.327350"	0.0001
	Ellip. h	1106.1442 m	0.0001
CACH	Lat.	-22° 41' 13.060619"	0.0001
	Lon.	-44° 59' 3.434919"	0.0001
	Ellip. h	620.4723 m	0.0001
CHUA	Lat.	-19° 45' 43.338110"	0.0002
	Lon.	-48° 6' 5.693422"	0.0003
	Ellip. h	755.3498 m	0.0003
FRAN	Lat.	-20° 34' 54.865699"	0.0002
	Lon.	-47° 22' 51.438612"	0.0003
	Ellip. h	1005.1864 m	0.0002
JAGU	Lat.	-24° 14' 30.809956"	0.0002
	Lon.	-49° 42' 17.358285"	0.0003
	Ellip. h	915.1945 m	0.0003

(continues)

Table B.4 (continued): Final adjusted (SIRGAS) coordinates of the Brazilian stations, referred to L1 phase centres

Station	Coordinates		σ (m)
LIMO	Lat.	-21° 37' 30.589318"	0.0002
	Lon.	-47° 1' 4.846714"	0.0003
	Ellip. h	580.1458 m	0.0002
LOND	Lat.	-23° 19' 21.768043"	0.0002
	Lon.	-51° 12' 7.739462"	0.0003
	Ellip. h	583.5309 m	0.0002
PARA	Lat.	-25° 26' 54.129211"	0.0001
	Lon.	-49° 13' 51.436565"	0.0001
	Ellip. h	926.0252 m	0.0001
REGI	Lat.	-24° 26' 31.764403"	0.0002
	Lon.	-47° 46' 58.637595"	0.0003
	Ellip. h	44.4480 m	0.0002
SJRP	Lat.	-20° 47' 4.765928"	0.0002
	Lon.	-49° 21' 29.463972"	0.0003
	Ellip. h	520.9405 m	0.0003
UEPP	Lat.	-22° 7' 11.659401"	0.0001
	Lon.	-51° 24' 30.721485"	0.0001
	Ellip. h	431.0577 m	0.0001
VICO	Lat.	-20° 45' 41.404190"	0.0001
	Lon.	-42° 52' 11.961101"	0.0001
	Ellip. h	666.0789 m	0.0001

Table B.5: Comparison of station coordinates of August 14 daily solution with respect to the combined solution in the Brazilian network

Station	Coord.	Aug. 14 sol. versus Combined (mm)
AGUA	N	2.4
	E	2.2
	U	-4.0
BOTU	N	-0.2
	E	-1.3
	U	-4.9
BRAZ	N	1.1
	E	-0.7
	U	-0.2
CACH	N	0.0
	E	-0.6
	U	0.2
CHUA	N	1.5
	E	-0.7
	U	2.1
FRAN	N	-0.3
	E	1.8
	U	0.5
JAGU	N	-1.2
	E	-0.2
	U	-7.9
LIMO	N	0.3
	E	0.5
	U	2.8
LOND	N	0.7
	E	-0.7
	U	-0.4
PARA	N	-2.0
	E	2.3
	U	-0.2
SJRP	N	-6.1
	E	-1.4
	U	-2.1
UEPP	N	0.9
	E	-1.0
	U	0.4

REGI and VICO were not observed on Aug. 14

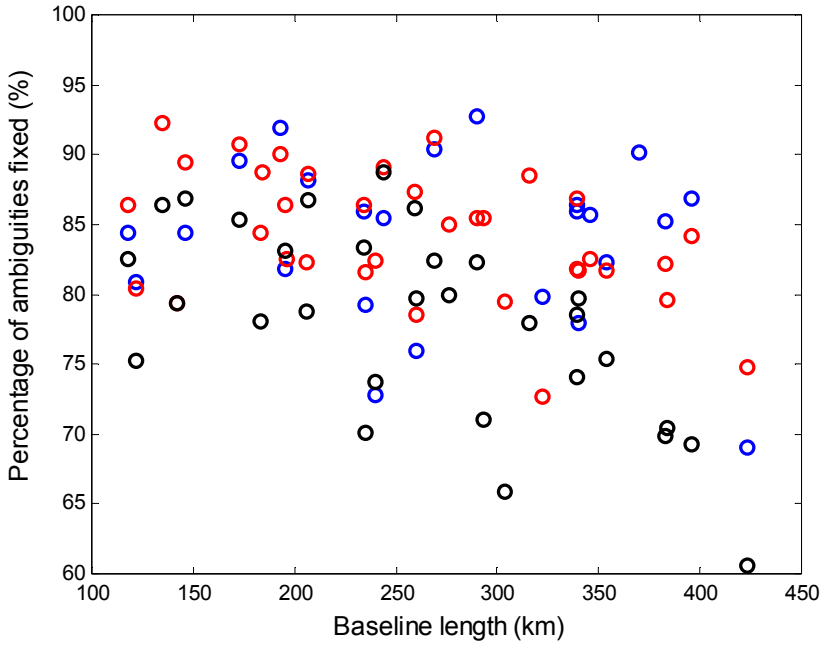

Figure B.6: Percentage of L1 and L2 ambiguities fixed by Bernese to integer values in the Brazilian network for August 11 (in blue), August 13 (in red) and August 14 (in black), using the QIF strategy

Table B.6: Number of unpaired single difference carrier phase observations for 24-hour sessions[1]

Baseline	GPS Receivers used	L2 Tracking Technique	Number of Unpaired Single Diff. Obs.
AGUA – SJRP on Aug 11	Asthech Z-XII	Semi-codeless	5
AGUA – SJRP on Aug 13	Asthech Z-XII	Semi-codeless	7
BOTU – REGI on Aug 11	Trimble 4000SSi	Codeless	1394
BRAZ - CHUA on Aug 11	Trimble 4000SSi	Codeless	1645
BRAZ - CHUA on Aug 13	Trimble 4000SSi	Codeless	1573
CACH – LIMO on Aug 11	Ashtech Z-XII Trimble 4000SSi	Semi-codeless codeless	973
CACH – LIMO on Aug 13	Ashtech Z-XII Trimble 4000SSi	Semi-codeless codeless	994
CHUA – FRAN on Aug 11	Trimble 4000SSi	Codeless	2841
CHUA – FRAN on Aug 13	Trimble 4000SSi	Codeless	2826
FRAN – LIMO on Aug 11	Trimble 4000SSi	Codeless	2018
FRAN – LIMO on Aug 13	Trimble 4000SSi	Codeless	2039
JAGU – LOND on Aug 13	Javad Legacy Ashtech Z-XII	? Semi-codeless	142

1: The total number of observations per session (at 15 seconds) is about 30000

APPENDIX C

Table C.1: GPS satellite antenna phase centre offsets, with respect to the satellite centre of mass, in the SCSF system (ref. August, 1999)

PRN	Block	Antenna Offsets (m)		
		Δx	Δy	Δz
1	IIA	0.2794	0.0000	1.0230
2	II	0.2794	0.0000	1.0230
3	IIA	0.2794	0.0000	1.0230
4	IIA	0.2794	0.0000	1.0230
5	IIA	0.2794	0.0000	1.0230
6	IIA	0.2794	0.0000	1.0230
7	IIA	0.2794	0.0000	1.0230
8	IIA	0.2794	0.0000	1.0230
9	IIA	0.2794	0.0000	1.0230
10	IIA	0.2794	0.0000	1.0230
13	IIR	0.0000	0.0000	0.0000
14	II	0.2794	0.0000	1.0230
15	II	0.2794	0.0000	1.0230
16	II	0.2794	0.0000	1.0230
17	II	0.2794	0.0000	1.0230
18	II	0.2794	0.0000	1.0230
19	II	0.2794	0.0000	1.0230
21	II	0.2794	0.0000	1.0230
22	IIA	0.2794	0.0000	1.0230
23	IIA	0.2794	0.0000	1.0230
24	IIA	0.2794	0.0000	1.0230
25	IIA	0.2794	0.0000	1.0230
26	IIA	0.2794	0.0000	1.0230
27	IIA	0.2794	0.0000	1.0230
29	IIA	0.2794	0.0000	1.0230
30	IIA	0.2794	0.0000	1.0230
31	IIA	0.2794	0.0000	1.0230

Source: Rothacher and Mervart [1996]; Hugentobler et al. [2001]